# SEARCH FOR EXTRASOLAR PLANETS THROUGH HIGH CONTRAST DIFFRACTION LIMITED INTEGRAL FIELD SPECTROSCOPY

Jacopo Antichi, Kjetil Dohlen

# SEARCH FOR EXTRASOLAR PLANETS THROUGH HIGH CONTRAST DIFFRACTION LIMITED INTEGRAL FIELD SPECTROSCOPY

Jacopo Antichi
Department of Astronomy
University of Padova

Thesis submitted towards the degree of
Doctor of Philosophy

April 2007

**UNIVERSITÀ DEGLI STUDI DI PADOVA,**
**DIPARTIMENTO DI ASTRONOMIA**

Coordinatore: Ch.mo Prof. Giampaolo Piotto

Relatori: Dott. Raffaele Gratton, INAF-Osservatorio Astronomico di Padova

Dott. Massimo Turatto, INAF-Osservatorio Astronomico di Padova

Controrelatore: Dr. Kjetil Dohlen, Laboratoire d'Astrophysique de Marseille & Observatoire Astronomique de Marseille Provence

Data della Discussione: 26 Aprile 2007

# Subject

This Dissertation is devoted to high contrast diffraction limited Integral Field Spectroscopy for the direct imaging of extrasolar planets. The aim is to describe this subject in the domain of signals dominated by Speckles residual. This latter being the specific working case of the Integral Field Spectrograph (IFS) planned for the next Planet Finder instrument of the Very Large Telescope facility (SPHERE). In the effort of realizing the Integral Field Unit of this instrument, we found a new optical concept (BIGRE) allows to overcome all the features affecting the Slit Functions of a 3D-Spectrograph working in this optical regime. As a consequence, the proposed IFS is a complete BIGRE oriented instrument, optimized for the SPHERE system. More generally, the presented theory on diffraction limited Integral Field Spectroscopy is largely new and could contribute in advancing the field of high contrast imaging.

# Summary

Nowadays the extrasolar planet research can be raised to the level of a new chapter of Astrophysics, combining different domains of science: Physics of sub-stellar objects, Planetology, Astrobiology and Optics in an interdisciplinary way; in this sense, this matter "rides the wave" of the evolutive epoch we are leaving, the one of the interdisciplinary information.

The statistics on the properties of planets and their parent stars is increasing monthly, and is opening the way to the next step of this research, the direct detection. The first direct detection of a stellar companion with a planetary mass, occurred only in 2004, when distinct images of a star 2M1207 and of its low-mass companion were finally obtained, exploiting a few among the best astronomical facilities available today: VLT/NACO and HST/NICMOS. After the first detection, the ones of GQ Lup b and AB Pictoris b followed in 2005. However, these cases should be considered the first pioneering efforts to try to collect separately the light of a planet from the one of the parent star and, at present, it remains a non-standard technique in Astronomy.

Direct detection techniques, such the ones based on high contrast imaging or interferometry, could overcome the limits of the in-direct approaches. The Transit technique - for instance - provides the radius of a low-mass companion only. Derivation of the planet mass by the periodic variation of the stellar light curve is impossible unless Radial Velocity measures are available: the object may be a planet, but also a low mass star or a brown dwarf or a white dwarf, whose radii are similar to the Earth one. The Radial Velocity technique - in turn - is sensitive only to extrasolar planets with relatively small orbits, typically corresponding to objects at a distance smaller than a few AU from their parent star, or with high eccentricity. These limitations lead to ambiguous interpretations on the properties of what has been actually detected, biasing both single-object and statistical analyses.

Simultaneous Differential Imaging (SDI) is a high contrast differential calibration technique, allowing to create several images taken at different wavelengths of the same field of view around a target star. Subtraction of simultaneous monochromatic images is a way to remove the Speckle Noise which dominates over any other optical pattern inside the angular separation boundary, where a suitable Adaptive Optics system restores the diffraction limit fixed by the telescope aperture. This calibration technique has produced already a number of important scientific results in the realm of sub-stellar objects, reaching star vs. planet Contrast of order of $10^4$-$10^5$ with the NACO-SDI facility at the VLT. Presently, the Contrast threshold allowing to detect (young) Jupiter-like planets - around $10^7$ - is the challenge for the next ground based Planet Finder projects as the European one SPHERE.

SPHERE will mount the first Integral Field Spectrograph aimed to the direct detection of extrasolar planets. The theory joining 3D-Spectroscopy and extrasolar planets direct detection represents what, in this Dissertation, we defined as Spectroscopical Simultaneous Differential Imaging (S-SDI). In this frame, diffraction limited Integral field Spectroscopy is needed to obtain monochromatic images over the entire field of view around a target star. Then, through 3D-Spectroscopy, simultaneous difference of monochromatic images should exceed the standard Simultaneous Differential Imaging, based on chromatic filters only.

The work presented in this Dissertation is entirely devoted to high contrast diffraction limited Integral Field Spectroscopy. The aim is to describe this subject, leading the reader to

approaching step by step the domain of diffraction limited Integral Field Spectroscopy, from the ideal case, up to the real case of a Speckle dominated input signal. This latter being the specific case of the SPHERE Integral Field Spectrograph (IFS). Design of a diffraction limited IFS requires careful consideration of a number of subtle effects, including not uniform illumination of the entrance aperture (causing diffraction patterns different from the classical Airy disk), cross talk between adjacent spaxels (i.e. pixels in the spatial dimension) caused by the wings of the diffraction profiles, and correct sampling in both spatial coordinates and wavelength. Appropriate consideration of these effects should be combined in a design where the largest field of view, spectral resolution and coverage are obtained at the cheapest possible cost (this being mainly driven by the number of detector pixels).

In the effort of realizing the Integral Field Unit of this instrument, we found that a new optical concept - BIGRE - allows to overcome all the features affecting the Slit Functions of a 3D-Spectrograph working in this optical regime. As a consequence, the SPHERE Integral Field Spectrograph presented in this Dissertation is a complete BIGRE oriented instrument. The theory of a diffraction limited IFS presented in this Dissertation is largely new, and it is the most important original contribution of this work.

Finally, this Dissertation ends describing the contribution we gave for the 3D-Spectroscopy facility foreseen within the EPICS instrument. EPICS is a feasibility study for a Planet Finder for the OWL Telescope promoted by ESO in 2005. It was based on a collaboration of expertises from all over Europe; the design explored different possible frameworks for the future European ELT.

The structure of the Dissertation is as follows: in Section 1 we introduce the topic of extrasolar planet research; special emphasis is given to the model atmosphere for extrasolar giant planets, on which both Simultaneous Differential Imaging and the Spectroscopical Simultaneous Differential Imaging achieve their scientific reasons. Section 2 is dedicated to a panoramic description of the detection methods useful to the search for planets; here special emphasis is given in the comparison between direct and in-direct detection methods. The fact that in-direct detection method will remain fundamental even after direct detection techniques will be operative is clearly stated. In Section 3 Simultaneous Differential Imaging and Spectroscopical Simultaneous Differential Imaging are defined, described and compared. The important aspect here is that - in principle - S-SDI is much powerful that the standard SDI, and that the Integral Field Spectrograph of SPHERE could reach Constrast values as high as $10^7$, i.e. the (young) Jupiter Contrast size. In Section 4 the SPHERE project is described as a whole, except for the Integral Field Spectrograph. Sections 5 and 6 are fully dedicated to this subject. Specifically, Section 5 is dedicated to the general description of the classical TIGER and the new BIGRE devices, and to the optimization of the BIGRE Integral Field Unit of this Integral Field Spectrograph. Results of laboratory prototyping are presented; they confirm that BIGRE is the right optical solution in order to achieve the science goals of this Integral Field Spectrograph. Section 6 describes the IFS optical design, and Section 7 finally, the work we did for the 3D-Spectroscopy channel foreseen for EPICS.

# Sommario

La ricerca di pianeti extrasolari oggi può essere considerata come un nuovo capitolo della Astrofisica che riunisce differenti campi scientifici: Fisica degli oggetti sub-stellari, Planetologia, Astrobiologia ed Ottica in modo interdisciplinare; in questo senso questa materia "cavalca l'onda" dell'epoca in cui viviamo, quella della conoscenza interdisciplinare.

L'inferenza statistica riguardante le proprietà dei pianeti e delle loro stelle ospiti migliora di mese in mese e sta aprendo la strada per il passo successivo di questa ricerca, la rivelazione tramite metodi diretti. La prima scoperta diretta di un compagno stellare di massa planetaria è avvenuta solo nel 2004, quando, finalmente, sono state ottenute immagini distinte della stella 2M1207 e del suo compagno di piccola massa, usufruendo di un paio dei migliori strumenti per l'Astronomia disponibili oggi: VLT/NACO e HST/NICMOS. Dopo questo primo ritrovamento, nel 2005 sono seguiti quelli di GQ Lup b ed AB Pictoris b. Tuttavia, questi casi devono essere considerati come esempi pionieristici dell'intento di rappresentare separatamente la luce di un pianeta e quella della sua stella madre. Al momento, in Astronomia questi casi rimangono esempi di rivelazione non standardizzati in una tecnica consolidata.

Le tecniche per la scoperta diretta, come quelle basate sull'Imaging ad alto contrasto o l'Interferometria, possono superare i limiti propri degli approcci indiretti. La tecnica dei Transiti - per esempio - fornisce come informazione fisica solo il raggio del compagno di piccola massa. Ricavare la massa del pianeta attraverso la variazione periodica della curva di luce della stella ospite è impossibile a meno che siano disponibili anche misure di Velocità Radiale: l'oggetto in questione potrebbe essere un pianeta ma anche una stella di piccola massa, oppure una nana bruna od una nana bianca, il cui raggio è simile a quello della Terra. A sua volta, la tecnica delle Velocità Radiali è sensibile alla presenza di un pianeta, nel caso in cui esso abbia orbita relativamente stretta - tipicamente essa corrisponde ad oggetti con distanza più piccola di qualche UA dalla stella madre -, oppure nel caso in cui la sua orbita abbia un valore di eccentricità alto. Questi limiti comportano interpretazioni ambigue su ciò che effettivamente è stato rivelato, pregiudicando l'analisi sul singolo oggetto, come quella sull'intero campione statistico.

L'Imaging Differenziale Simultaneo (SDI) è una tecnica di calibrazione differenziale ad alto contrasto che permette di creare alcune immagini di diversa lunghezze d'onda e dello stesso campo di vista attorno ad una stella target. La sottrazione simultanea di immagini monocromatiche è utilizzata come metodo per rimuovere il rumore di Speckle. Esso domina su ogni altro "pattern ottico" compreso nell'intervallo di separazione angolare dove un sistema di Ottica Adattiva opportuno restaura il limite ottico di diffrazione, fissato a sua volta dall'apertura del telescopio. Questa tecnica di calibrazione ha già prodotto importanti risultati scientifici nel regno degli oggetti sub-stellari, arrivando a valori di Contrasto stella vs. pianeta dell'ordine di $10^4$-$10^5$ con lo strumento NACO-SDI al VLT. Al momento, la soglia di Contrasto che permette di rivelare pianeti gioviani (giovani) - dell'ordine di $10^7$ - rappresenta la sfida per i prossimi progetti da terra per la rivelazione diretta dei pianeti extrasolari, tra cui quello Europeo SPHERE.

SPHERE monterà il primo Spettrografo a Campo Integrale indirizzato alla rivelazione diretta di pianeti extrasolari. La teoria che collega Spettroscopia 3D e la rivelazione diretta di pianeti extrasolari è ciò che, in questa Dissertazione, noi definiamo come Imaging Differenziale Simultaneo Spettroscopico (S-SDI). In questa prospettiva, la Spettroscopia a

Campo Integrale al limite ottico di diffrazione è necessaria per ottenere immagini sull'intero campo di vista attorno ad una stella target. Poi, sempre attraverso la Spettroscopia 3D, la differenza simultanea di immagini monocromatiche dovrebbe superare l'Imaging Differenziale Simultaneo standard, che è basato solo su filtri cromatici.

Il lavoro qui presentato è interamente dedicato alla Spettroscopia a Campo Integrale al limite ottico di diffrazione in condizione di alto contrasto. La volontà è di descrivere questo argomento, portando il lettore ad avvicinarsi passo dopo passo al domino della Spettroscopia a Campo Integrale al limite ottico di diffrazione, partendo dal caso ideale, fino al caso reale di un segnale di ingresso dominato dal rumore di Speckle. Specificamente, quest'ultimo è il caso in cui opererà lo Spettrografo a Campo Integrale montato su SPHERE. La progettazione di uno Spettrografo a Campo Integrale ottimizzato per lavorare al limite ottico di diffrazione richiede di fare attenzione a fenomeni ottici complessi, ad esempio l'illuminazione non uniforme delle fenditure di ingresso (questo causa profili di diffrazione diversi dal classico disco di Airy), cross talk tra spaxel adiacenti (cioè pixel nella dimensione spaziale) causato dalle ali dei profili di diffrazione, ed il corretto campionamento del segnale di ingresso sia nelle coordinate spaziali che in lunghezza d'onda. L'esame opportuno di questi effetti deve essere combinato in un progetto ottico dove il massimo campo di vista e la giusta risoluzione spettrale siano ottenute con il minimo costo possibile (quest'ultimo dipende principalmente dal numero di pixel del rivelatore).

Nell'intento di realizzare l'Unità a Campo Integrale di questo strumento, abbiamo messo a punto un nuovo concetto ottico - BIGRE - che permette di superare tutti gli effetti che intaccano le Funzioni di Fenditura di uno Spettrografo 3D, operante in questa condizione ottica. Come conseguenza, lo Spettrografo a Campo Integrale di SPHERE, presentato in questa Dissertazione, è completamente orientato al concetto ottico BIGRE. La teoria di uno uno Spettrografo a Campo Integrale ottimizzato per lavorare al limite ottico di diffrazione è in gran parte nuova e rappresenta il contributo originale più importante di questo lavoro.

Infine, questa Dissertazione termina con la descrizione del contributo che abbiamo dato alla realizzazione dello Spettrografo 3D previsto all'interno dello strumento EPICS. EPICS è uno studio di fattibilità per un Planet Finder - adatto al Telescopio OWL - promosso da ESO nel 2005. Questo lavoro si è basato sulla collaborazione di esperti provenienti da tutta Europa; nella progettazione si sono esplorati possibili adattamenti per il futuro Extremely Large Telescope Europeo.

La struttura di questa Dissertazione è la seguente: nella Sezione 1 introduciamo l'argomento dei pianeti extrasolari; è data particolare enfasi ai modelli di atmosfera relativi ai pianeti extrasolari giganti, sui quali sia l'Imaging Differenziale Simultaneo e l'Imaging Differenziale Simultaneo Spettroscopico traggono la loro ragione scientifica. La Sezione 2 è dedicata ad una descrizione panoramica dei metodi utili nella rivelazione dei pianeti extrasolari; particolarmente sottolineata è la comparazione tra metodi diretti e metodi indiretti. E' spiegato chiaramente il fatto che i metodi indiretti rimarrano fondamentali una volta che le tecniche di detezione diretta saranno operative. Nella Sezione 3 sono definite, descritte e comparate le tecniche di Imaging Differenziale Simultaneo ed Imaging Differenziale Simultaneo Spettroscopico. Il fatto importante qui è che - di principio - la tecnica S-SDI è più potente della tecnica SDI standard, e che lo Spettrografo a Campo Integrale di SPHERE è in grado di raggiungere valori di Contrasto dell'ordine di $10^7$, cioè i valori di Contrasto tipici dei pianeti gioviani (giovani). Nella Sezione 4 è descritto l'intero progetto SPHERE, eccetto lo Spettrografo a Campo Integrale. Le Sezioni 5 a 6 sono completamente dedicate a questo argomento. Specificamente, la Sezione 5 riguarda la descrizione generale del classico dispositivo TIGER e del nuovo dispositivo BIGRE, e

l’ottimizzazione della Unità a Campo Integrale di questo Spettrografo 3D. Inoltre, sono presentati i risultati del prototipo di laboratorio; essi confermano che BIGRE è la soluzione ottica vincente per soddisfare il caso scientifico di questo strumento. La Sezione 6 ne descrive il disegno ottico e la Sezione 7 - infine - presenta il lavoro svolto per il canale di Spettroscopia 3D previsto per EPICS.

# Contents

# List of Figures

# List of Tables

# Abbreviations: A-M

ACS = Advance Camera for Surveys

ADC = Atmospheric Dispersion Corrector

AEOS = Advanced Electro Optical System

ALC = Apodized Lyot Coronagraph

AO = Adaptive Optics

AOTF = Atmospheric Optical Transfer Function

AR-C = Anti Reflection Coating

BS = Beam Splitter

CCD = Charge Counting Device

CCT = Coherent CrossTalk coefficient

CFHT = Canada France Hawaii Telescope

CGRO = Compton Gamma-Ray Observatory

CHEOPS = CHaracterizing Extrasolar planets by Opto-infrared Polarimetry and Spectroscopy

CLC = Classical Lyot Coronagraph

CNES = Centre National d'Etudes Spatiales

COROT = COnvection, ROtation et Transits Planétaires

DENIS = Deep Survey of Southern Sky

DI = Differential Imaging

DM = Deformable Mirror

DRSW = Data Reduction Software

EE = Encircled Energy

EF = Electric Field

ELT = Extremely Large Telescope

EPICS = Exoplanets Imaging Camera and Spectrograph

EROS = Experience de Recherche d'Objects Sombres

ES = Exit Slit Function

ESA = European Space Agency

ESO = European Southern Observatories

EUV = Extreme UltraViolet

F = Focal Ratio

FIR = Far InfraRed

FOV = Field Of View

4Q = four-Quadrant

4QPMC = four-Quadrant Phase Mask Coronagraph

FT = Fourier Transform

FTS = Fourier Transform Spectrograph

FWHM = Full width at Half Maximum

# Abbreviations: N-Z

NACO = NAOS-CONICA

NAOS-CONICA = Nasmyth Adaptive Optics System for Near-InfraRed Imager and Spectrograph

NASA = National Aeronautics and Space Administration

NICS = Near Infrared Camera-Spectrometer of the TNG

NIR = Near InfraRed

OAPD = Osservatorio Astronomico di PaDova

OGLE = Optical Gravitational Lensing Experiment

OHP = Observatoire de Haute-Provence

OMM = Observatoire du Mont Megantic

OPD = Optical Path Difference

OPDR = Optical Preliminary Design Review

OTF = Optical Transfer Function

OWA = Outer Working Angle

OWL = Overwhelmingly Large

P-DI = Polarimetric-DI

PIAA = Phase Induced Amplitude Apodization

PRIMA = Phase-Reference Imaging and Micro-Arcsecond Astrometry

PSD = Power Spectral Density

PSF = Point Spread Function

RAOTF = Residual Atmospherical Optical Transfer Function

RMS = Root Mean Square

RTC = Real Time Computer

SARG = Spettrografo ad Alta Risoluzione per telescopio Galileo

SAURON = Spectroscopic Areal Unit for Research on Optical Nebulae

SCUBA = Submillimetre Common User Bolometer Array

SDI = Simultaneous Differential Imaging

SDSS = Sloan Digital Sky Survey

SED = Spectral Energy Distribution

SF = IFS Slit Function

SIM = Space Interferometry Mission

SNR = Signal to Noise Ratio

SP = Spectral Purity

SMF = Spectrograph Pupil Mask

GTO = Guarantee Time for Observations

HARPS = High Accuracy Radial velocity Planets Searcher

HATnet = Hungarian-made Automated Telescope network

HST = Hubble Space Telescope

HWHM = Half width at Half Maximum

HWP = Half Wave Plate

ICT = Incoherent CrossTalk coefficient

IFS = Integral Field Spectroscopy/Spectrograph

IFU = Integral Field Unit

IR = InfraRed

IRAC = InfraRed Array Camera

ISCCP = International Satellite Cloud Climatology Project

IWA = Inner Working Angle

JCMT = James Clerk Maxwell Telescope

JPL = Jet Propulsion Laboratories

JWST = James Webb Space Telescope

LAM = Laboratoire d'Astrophysique de Marseille

LSF = Line Spread Function

MACHO = Massive Compact Halo Objects

MIPS = Multiband Imaging Photometer for Spitzer

MIR = Mid InfraRed

MMT = Multi Mirror telescope

MOS = Multi Object Spectrograph

MPM = MicroPupil Mask

MTF = Modulated Transfer Function

SPHERE = Spectro-Polarimetric High contrast Exoplanets Research

SPIE = International Society for Optical Engineering

SR = Strehl Ratio

S-SDI = Spectroscopic-SDI

STIS = Space Telescope Imaging Spectrograph

TBD = To Be Defined

TIGER = Traitement Integral des Galaxies par l'Etude de leur Raies

TLR = Top Level Requirement

TNG = Telescopio Nazionale Galileo

TrES = Trans-Atlantic Exoplanets Research

TPF = Terrestrial Planet Finder

TPF-C = Terrestrial Planet Finder Coronagraph

TPF-I = Terrestrial Planet Finder Interferometer

TTM = Tip Tilt Mirror

2MASS = 2 Micron All Sky Survey

UT = Universal Time

VLT = Very Large Telescope

VLTI = Very Large Telescope Interferometer

WASP = Wide Angle Search for Planets

WFS = Wave-Front Sensor

WHT = William Herschel Telescope

XAO = eXtreme Adaptive Optics

# Useful Symbols and Quantities

$AU \equiv$ Astronomic Unit $\sim 1.5 \times 10^{11}$ [m]

$Z_{SUN} \equiv$ Sun metallicity $\sim 0.02$

$pc \equiv$ Parsec $\sim 31 \times 10^{16}$ [m]

$Kpc \equiv$ Kiloparsec $\sim 31 \times 10^{19}$ [m]

$M_{SUN} \equiv$ Sun mass $\sim 2.0 \times 10^{30}$ [kg]

$M_{JUPITER} \equiv$ Jupiter mass $\sim 9.5 \times 10^{-4} M_{SUN}$

$M_{SATURN} \equiv$ Saturn mass $\sim 2.9 \times 10^{-4} M_{SUN}$

$M_{URANUS} \equiv$ Uranus Mass $\sim 4.4 \times 10^{-5} M_{SUN}$

$M_{EARTH} \equiv$ Earth mass $\sim 10^{-3} M_{JUPITER}$

$R_{SUN} \equiv$ Sun radius $\sim 6.96 \times 10^{8}$ [m]

$atm = 1.01325 \times 10^{5}$ [$N \cdot m^{-2}$]

$arcsec \equiv \sim 4.85 \times 10^{-6}$ [Radians]

$erg = 10^{-7}$ [Joule]

$Jy = 10^{-26}$ [$Watt \cdot m^{-2} \cdot Hz^{-1}$]

$mmag = 10^{-3}$ mag

$C_n^2 \equiv$ Integrated Atmospheric Turbulence Profile

$L_0 \equiv$ Atmospheric Turbulence Outer Scale

$r_0 \equiv$ Atmospheric Turbulence Coherence Length

$\sigma_\chi^2 \equiv$ logarithm of the Variance of the Electric Field Amplitude due to the Atmospheric Turbulence

$\sigma_I^2 \equiv$ Variance of the Intensity due to the Atmospheric Turbulence

$\tau_0 \equiv$ Atmospheric Turbulence Coherence Time

# 1 The extrasolar planets research

Just over a decade ago the discovery of the first extrasolar planet surrounding a main sequence star by Michael Mayor and Didier Queloz (Mayor and Queloz 1995) opened an entire new chapter of Astrophysics which now is living its infancy, capturing more and more the attention of the scientific community. Anticipated by the serendipitous discovery of two terrestrial-mass companions around the 6.2-ms pulsar PSR 1257+12 (Wolszczan and Frail 1992), the first extrasolar planet hosted by a solar-type star identified by Mayor and Queloz - 51 Pegasi - has shown that formation and evolution of planets is possible out of the Solar-System, around main sequence stars and probably is quite common in the Galaxy, as suggested by the increasing number of confirmed extrasolar planets (http://exoplanets.org, cfr. Butler et al. 2006). The last decade (1995-2005) has seen a real explosion in the science of extrasolar planets through the development of theoretical models to explain the unexpected features shown by these objects and the development of techniques for their detection. Presently, the theoretical models are still far from a self-consistent picture of the mechanisms leading the formation and the evolution of a planet, but statistics on the properties of planets and their parent stars are increasing month by month, opening the way to the next step of the research i.e. the direct detection.

## 1.1 The realm of sub-stellar objects

Before 1995 no object was known in the mass range between Jupiter (~$9.5 \times 10^{-4}$ $M_{SUN}$) and the lowest-mass stars. Gl 229B was the first discovery of a sub-stellar object covering this mass gap (Nakajima et al. 1995, Oppenheimer et al. 1995). Indeed, according to Kumar (1963) there is a lower mass limit depending on metallicity (~0.08 $M_{SUN}$ for $Z=Z_{SUN}$) for a full luminosity stabilization by hydrogen burning in the core of the stars. Specifically, stars are defined as those objects where this stabilization may occur while brown dwarfs are properly defined as the object comprised between the lower mass limit of the stars and the minimum mass for which the Deuterium burning is allowed (~$12 \times 10^{-3}$ $M_{SUN}$, see Figure 1-1). Objects of even lower mass are considered to be planets.

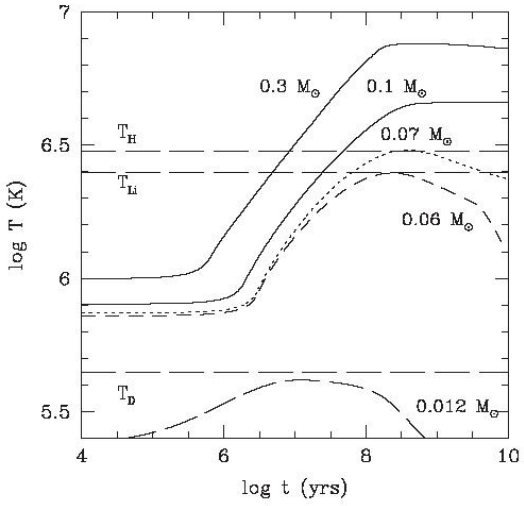


**Figure 1-1: Central temperature as a function of age for different masses. $T_H$ ,$T_{Li}$ and $T_D$ indicate the hydrogen, lithium and deuterium burning temperatures, respectively (cfr. Chabrier and Baraffe 2000).**

The existence of brown dwarfs was predicted by Kumar (1962). However, in the following thirty years no evidence of this kind of objects emerged until 1995 when three independent discoveries were announced: the methane-dwarf Gl 229B and the two brown dwarfs in the Pleiades, PPl 15 (Stauffer et al. 1994) and Teide 1 (Rebolo et al. 1995). Up to now more than 300 brown dwarfs have been detected in different environments of our Galaxy: in star forming regions (Comeron et al. 2000), in young stars clusters (Martin et al. 2000) and in the field by the largest-field surveys in the IR domain (e.g. 2MASS[1], cfr. Kirkpatrick et al. 2000), in the NIR domain (e.g. DENIS, cfr. Tokunaga et al. 1999) and in the VISible domain (e.g. SDSS, cfr. Hawley et al. 2002).

### 1.1.1 Proper characteristics of brown dwarfs and giant planets evolution

The temperature of stars rises in the pre-main sequence phase due to the contraction along the Hayashi track until the interior is hot and dense enough to burn sufficient hydrogen to stabilize the central temperature and balance gravitational pressure on the hydrogen burning main sequence phase.

For brown dwarfs, the central temperature also increases due to gravitational contraction in the first million to a few hundred million years. As the density increases part of the electron gas in the interior becomes degenerate. The compression of the degenerated fraction of the gas subtracts enough energy to the system so that the temperature remains constant for a small fraction of the evolutive time and then starts to decrease. When the gas is completely degenerated no further contraction is possible and the brown dwarf reaches its final radius and cools without other thermodynamics compensations (see Figure 1-2).

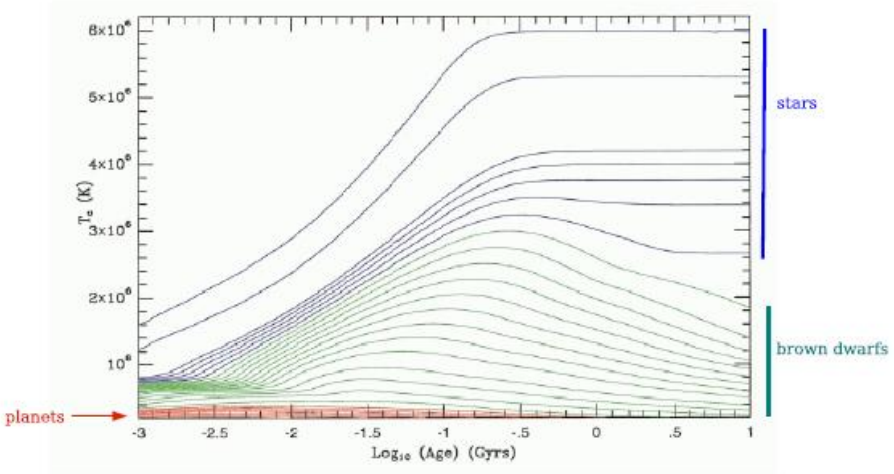


**Figure 1-2: Theoretical evolution of the central temperature for stars, brown dwarfs and planets from 0.3 $M_{JUPITER}$ to 0.2 $M_{SUN}$. Notice the increase (Maxwell-Bolzmann plasma), maximum and decrease (Fermi-Dirac plasma) of the central temperature for brown dwarfs. The red lines indicate sub-stellar objects with mass lower than 12 x $10^{-3}$ $M_{SUN}$ that represents the sharpest criterion in distinguishing planets and brown dwarfs (cfr. Burrows et al. 2001).**

[1]For the definition of all the abbreviations adopted in this Section see the opening list.

Today the mass range beyond the hydrogen burning limit has been covered by various instruments in different wavelength domains (for example 2MASS, DENIS, SDSS), and hundred of objects are classified now as brown dwarfs or extrasolar planets.

Quantitatively, the distinction between the realms of brown dwarfs and extrasolar giant planets should lie on the different processes leading to their formation rather than on the minimum mass criterion for the deuterium burning (~$12 \times 10^{-3}$ $M_{SUN}$). This latter should be considered only as the minimum mass allowed to an object following the same evolutive path of a star but with different final results due to the different initial mass budget. Then, it is to be considered only as a lower mass limit for the brown dwarfs population. Eventually, the distinction between the realms of brown dwarfs and extrasolar giant planets could be appreciated through the study of their atmospheres, which in turn present substantial differences with respect to the realm of stellar objects.

### 1.1.2 Model atmospheres for brown dwarfs

Since the first discovery, a sound number of objects less massive and cooler than true M dwarf stars, but more massive than extrasolar giant planets such as Jupiter, has become known through the 2MASS, DENIS and SDSS sky searches. The discovery of these objects requires an extension of the spectral sequence of stars to fainter and lower mass object. By 1999 two new classes, L and T, were added to the spectral classification (Kirkpatrick et al. 1999, Martin et al. 1999, Burrows et al. 2001). The introduction of the L and T classes is relatively new; the distinction among M, L, T types, the definition of the L and T sub-types and an understanding of the physical condition in the atmospheres of cool stars and sub-stellar systems are among the new challenges of stellar atmospheres Astrophysics. Both infrared and optical spectral features and colours have been used in order to distinguish between M dwarfs and L dwarfs, and to disentangle the complicated infrared spectral energy distributions of the dwarf population beyond the M spectral type in a discrete and increasing number of sub-types: L1-L9 and T0-T9. The M dwarfs threshold - for example - is defined spectroscopically by the presence of bands of oxides such as TiO and VO (Jones and Tsuji 1997), while a clear spectroscopic distinction between L and T dwarfs is still an open issue (Burrows et al. 2006).

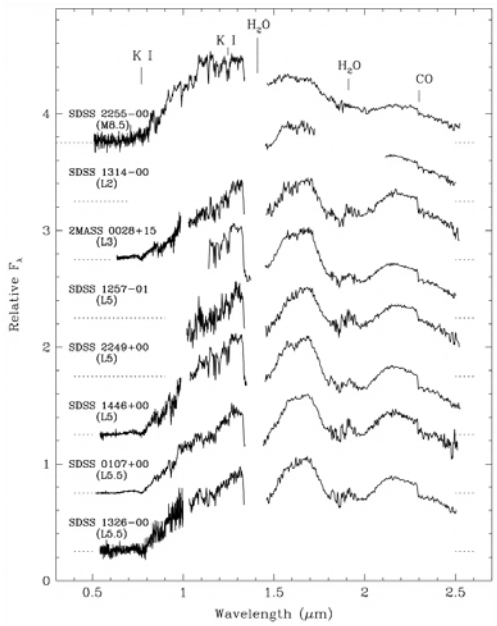

**Figure 1-3: Example of observed M and L dwarf spectra in the range 0.5-2.5 [micron] from M9 to L 5.5. SDSS or 2MASS identifications are given above the dashed line that corresponds to the zero flux level for each spectrum (cfr. Geballe et al. 2002).**

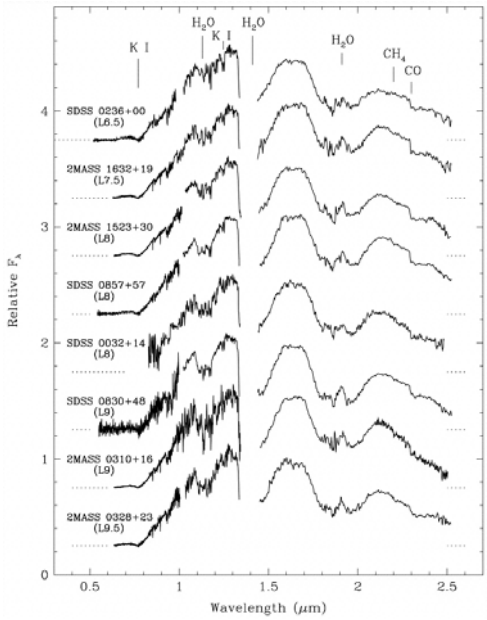


**Figure 1-4: Example of observed L dwarf spectra in the range 0.5-2.5 [micron] from L 6.5 to L 9.5. SDSS or 2MASS identifications are given above the dashed line that corresponds to the zero flux level for each spectrum (cfr. Geballe et al. 2002).**

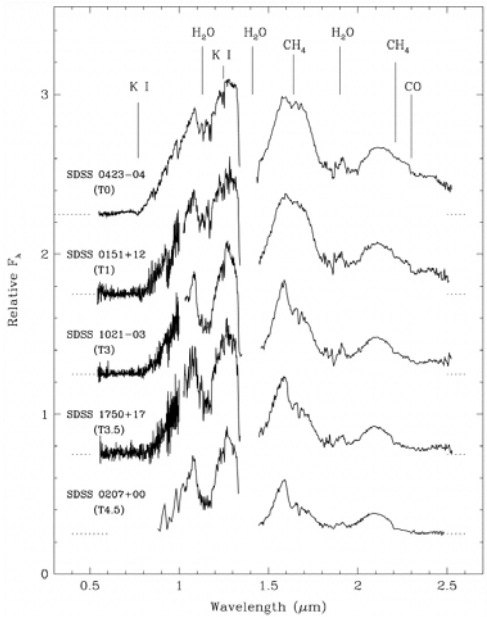


**Figure 1-5: Example of observed T dwarf spectra in the range 0.5-2.5 [micron] from T 0 to T 4.5. SDSS or 2MASS identifications are given above the dashed line that corresponds to the zero flux level for each spectrum (cfr. Geballe et al. 2002).**

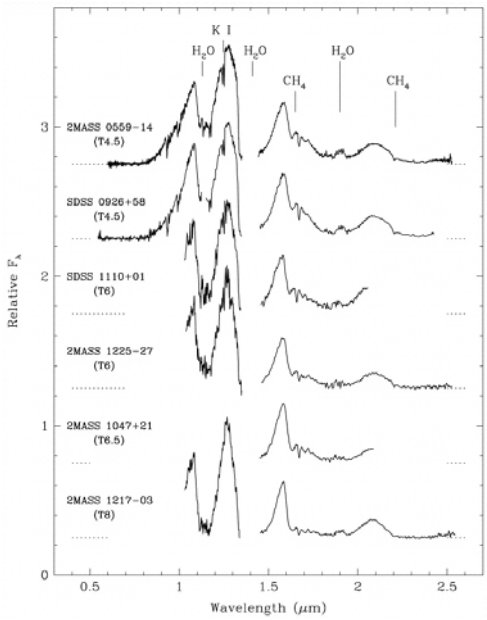


**Figure 1-6: Example of observed T dwarf spectra in the range 0.5-2.5 [micron] from T 4.5 to T 8. SDSS or 2MASS identifications are given above the dashed line that corresponds to the zero flux level for each spectrum (cfr. Geballe et al. 2002).**

L and T sub-types span an effective temperature range from 2300 K to 750 K and encompass the edge of the hydrogen-burning main sequence, this latter corresponding to an effective temperature of about 1700 K, which is proper of the sub-types L5 and L6. The L-dwarf sequence is characterized by the growth of near infrared FeH and CrH features, the emergence of $CH_4$ features in the K-band (~1.8-2.2 [micron]), and the progressive reddening of the J-K colours. The T dwarfs are distinguished by the presence of strong $CH_4$ features in the H (~1.4-1.8 [micron]) and K bands, and anomalously blue infrared colours (Burrows et al. 2006). It is thought that the L-T transition occurs near 1300 K and that all the T dwarfs are brown dwarfs with sub-stellar masses, but many L dwarfs could be stars with masses above the main sequence edge.

Theoretical models of L and T dwarfs atmospheres are still evolving and the extraction of physical quantities such as the effective temperature, the gravity and the metallicity from the growing library of well-calibrated spectra remains imprecise. In particular, the most difficult challenge confronting theorists designing models of L dwarfs is to incorporate the condensation of clouds in the numerical codes producing the final templates of synthetic spectral energy distributions. Cloud formation in a cooling atmosphere seems unavoidable; formation of clouds layers leads to drastic compositional and morphological atmospheric changes by removal of potential absorbers from the observable atmosphere and by blocking and scattering the emerging spectral flux, depending on how close the clouds are to the photosphere. So in addition to chemical effects - due to the presence of alkali elements (Na, K, Rb, Cs) and molecules (FeH, CrH, CO, $CH_4$ and $H_2O$) - the models needed to compute spectra should include also the physical effects of clouds (both number and size of cloud layers and size of cloud particles).

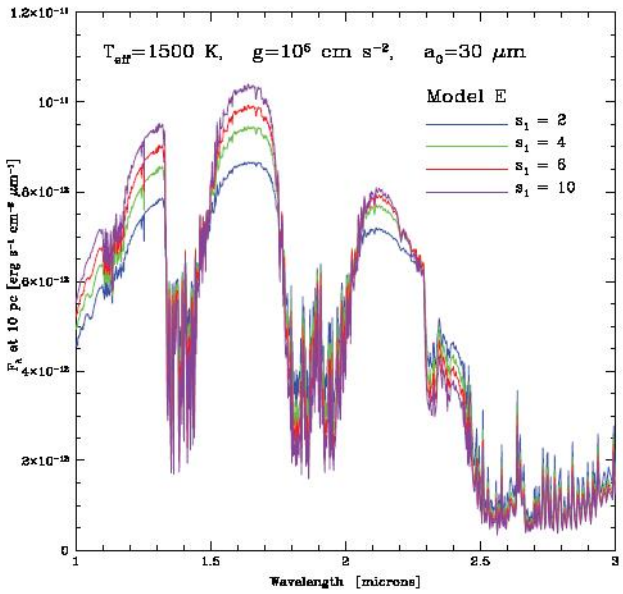


**Figure 1-7: Dependence of a model of dwarf spectrum on the vertical extent of the condensate cloud. A sharper cloud-top cut off - parameterized by the scalar $s_1$ and by the size of the single cloud particle $a_0$ - results in a bluer infrared spectrum (cfr. Burrows et al. 2006).**

### 1.1.3 Insight on the brown dwarfs formation mechanisms

The sub-stellar border defined by the hydrogen burning mass is a crucial dividing line with respect to further evolution of a candidate brown dwarf. Anyhow, there is no physical reason suggesting that this mass boundary should be related to their formation mechanism. Rather, the correct frame to deal with the possible formation scenarios is in elaborating theories working continuously from the low-mass stars regime to the one of sub-stellar objects.

In the traditional picture of low-mass stars formation, collapse and hierarchical fragmentation of molecular clouds (Shu et al. 1987) is assumed. This process involves the formation of circumstellar disk due to conservation of the angular momentum. The disk in turn is the birth place for extrasolar planets (see Section 1.2).

Brown dwarfs might either be the high-mass extension of extrasolar giant planets in the protostellar disk (first paradigm), or they form like stars, i.e. by direct gravitational collapse of molecular clouds and then fragmentation out of cloud cores, which should be cold and dense enough to become Jeans-unstable for the brown dwarfs masses range (second paradigm). The first formation paradigm (Stepinski and Black 2000) nowadays is attacked by a highly constrained observational feature: the so-called *Brown Dwarfs Desert* (see Section 1.1.4). Instead, the second paradigm is supported by the spectroscopic classification of the coolest stars population encompassing the range appropriate to sub-stellar objects (see Section 1.1.2). However, the small cloud cores by which a brown dwarf should form have not yet been detected by radio observations, and - on the theoretical ground - there is an important constraint regarding the opacity limit for a fragmentation process which can become Jeans-unstable. More in detail, when a critical mass density is reached during the collapse, the gas becomes optically thick and thereafter the Jeans-mass increases (Low and Lynden-Bell 1976). This phenomenon should prevent the formation of brown dwarfs by direct collapse of clouds. Nevertheless, assuming that brown dwarfs form in this way, they would be the low-mass extension of the stellar population and should share the properties of the low-mass young stellar objects, such as T Tauri stars. These latter have a very high multiplicity fraction (Kohler et al. 2000), indicating that the majority of low-mass stars is

formed in binaries or high order multiple systems. The same high multiplicity fraction would then be expected for the brown dwarfs population. Furthermore, young brown dwarf should have circumstellar disks - due to the preservation of the angular momentum - and should harbor planetary systems as their stellar counterparts. Another possibility is that brown dwarfs formed by direct but aborted collapse of the core of clouds of larger masses, which stopped the accretion at an early stage due to some external process, before the object has accreted enough mass to finally become a star. The general expectation of this last formation scenario is a low binary frequency, the absence of wide brown dwarf binaries and the presence of close-in circumstellar disks only. Various observational works aiming to constrain these different formation scenarios are underway, studying the stellar kinematics in different star forming regions of the Galaxy, through direct imaging (Proper Motion) and high-resolution spectroscopy (Radial Velocities: see - for example - Neuhäuser et al. 2002 and Joergens 2006).

### 1.1.4 Brown dwarfs statistics

Galactic sky surveys (for example 2MASS, DENIS and SDSS) together with specific observations in different environments such as the solar neighborhood (Grether and Lineweaver 2006), the star forming regions ChaI (Joergens 2006) and the Pleiades (Bihain et al. 2006), have allowed to construct numerous enough samples of brown dwarfs for statistical analysis, and then to better constrain models of their formation.

#### 1.1.4.1 The companion mass function

A deficit in the frequency of brown dwarf companions to stars relative to the frequency of companions of lower and higher mass is known since a few years (Marcy and Butler 2000). This observational feature is called *Brown Dwarfs Desert*. The Brown Dwarf Desert is described by the companion mass function i.e. the numerical density of the companions of different mass to a solar type star discretized in mass bins. Figure 1-8 shows the companion mass function for stars in the solar neighborhood (from Grether and Lineweaver 2006).

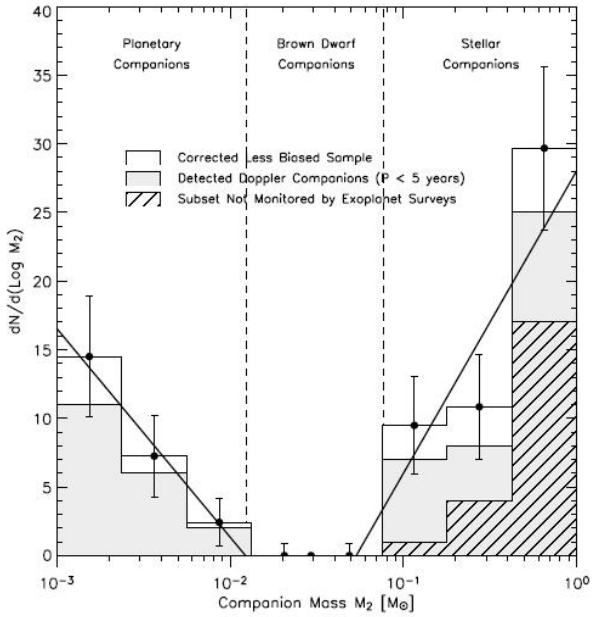


**Figure 1-8: Companions ($M_2$) mass function of the Sun-like stars closer than 25 pc, plotted against mass (cfr. Grether and Lineweaver 2006).**

As this Figure explains, there is a sharp drop in this function when the mass of the companions goes below one solar mass - at least two orders of magnitude - and then a sharp rising toward the range of the Jupiter-mass planets. Constraints on the formation mechanisms can be inferred by the opposite signs of the slopes of this observable when one considers separately its high and low-mass tails. For example, if two distinct processes are responsible for the formation of the stellar and planetary secondaries one would expect a well-defined slope of the companion mass function in these mass ranges and a sharp Brown Dwarf Desert as observed (Grether and Lineweaver 2006). The Brown Dwarf Desert can be described by another observational feature i.e., the extremely small percentage of brown dwarfs companions with orbital periods lower than five years. This fact indicates that the formation process of brown dwarfs is likely different from that of extrasolar giant planets else because one should find them in close-in orbits around their host star as planets do.

#### 1.1.4.2 The brown dwarf mass function

The mass function of the brown dwarf population as a whole is another observable related to the possible formation processes. Nowadays this research is only at its beginning. For example we are far from discriminating between different shapes of the brown dwarfs mass function when the astrophysical environment changes; we have then poor constrains on the distributions of the mass density amplitude perturbations, which are related to the kind of gravitational instabilities that lead to the formation mechanism.

Bihain et al. (2006) addressed this issue in the case of the Pleiades. They selected cluster small mass members using proper motion. This allowed identifying a clear sequence of confirmed brown dwarfs in the J vs. (I-J) colour-magnitude diagram. Thus, by matching observations with model isochrones (see Figure 1-9 for details) the masses of the brown dwarfs were obtained, and then an estimate of their mass function (see Figure 1-10) was produced.

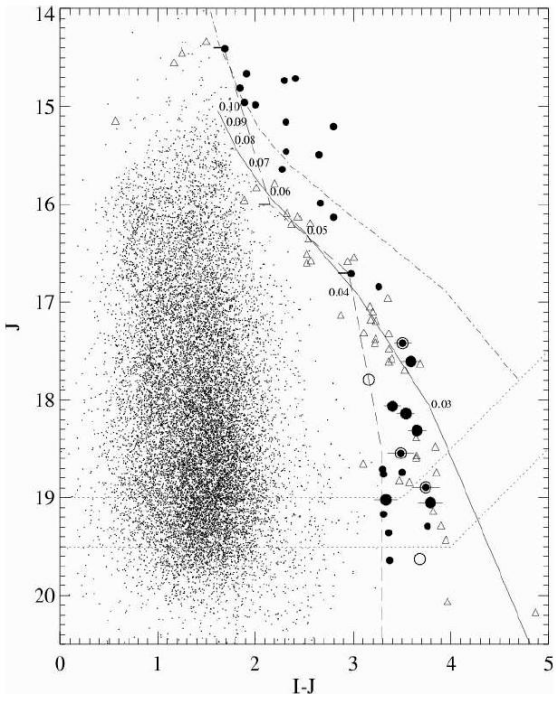

**Figure 1-9: The faint part of the I vs. (I-J) colour-magnitude diagram for the Pleiades. Points represent field stars, while the large filled circles are the confirmed brown dwarfs cluster population (indicated as redder than the dash colour-magnitude boundary). Triangles represent known field brown dwarfs, shifted to the distance of the cluster. The solid line and the dash-dotted line represent respectively the ~120 [Myr] DUSTY isochrones (Chabrier et al. 2000) and the ~125 [Myr] NextGen isochrones (Baraffe et al. 1998), shifted to the distance of the cluster. Finally, upper and the lower dotted lines at the bottom of the diagram indicate the completeness and limiting magnitude of the survey (cfr. Bihain et al. 2006).**

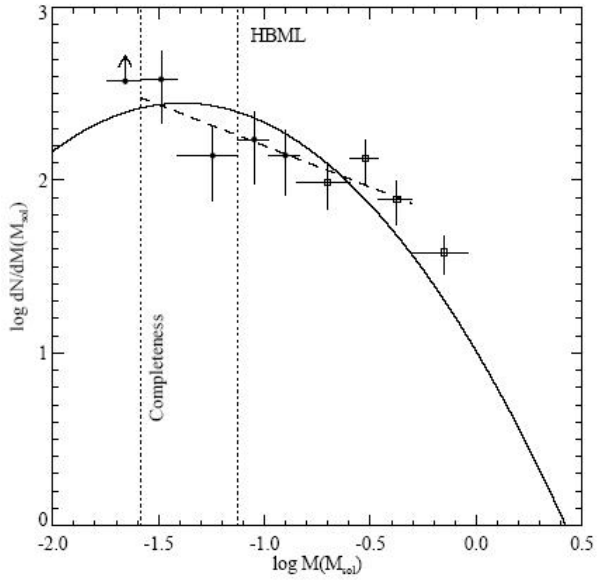


**Figure 1-10: The derived mass function for the Pleiades (cfr. Bihain et al. 2006). Filled circles are cumulative data obtained by the counts of the observed brown dwarf population and open circles are the data points obtained by Deacon and Hambly (2004). The solid line - over imposed to the data points - represents the log-normal mass function obtained by Deacon and Hambly (2004), normalized to the total number of object in this survey between 0.5 $M_{SUN}$ down to the completeness mass limit of this survey (0.026 $M_{SUN}$). The dashed line represents a power law fit to the data points.**

## 1.2 Theories of planetary system formation

A number of theories on the origin of our Solar System - and by inference on the planetary formation in general - have been proposed. They can be grouped in two main formation scenarios: the Solar Nebula paradigm - based on the Laplace (1796) - and the Capture paradigm - based on Jeans (1917). These share a common theoretical frame, i.e. the intimate connection between the formation of the Sun and of the protoplanetary disk, which is the environment where planets form.

The formation of a star begins from a cloud with some initial rotation that becomes Jeans-unstable and then collapses - maintaining the same amount of angular momentum - up to a flattened system, with a high proportion of double ad multiple stars arising from the subsequent fragmentation process (see e.g. Bonnell 1999). The minimum mass for star formation via fragmentation is determined by the minimum Jeans mass along the evolutive track of the collapsing cloud, which occurs when it becomes optically thick. The minimum mass that can be obtained by this process appears to be in the range 7-20 $M_{JUPITER}$ (Bodenheimer 1998).

### 1.2.1 The Solar Nebula formation scenario

In this scenario planet formation proceeds through several sub-phases. The first phase is the settlement of the dust grains into a dense layer in the mid-plane of the disk. The grains begin to stick together as they collide and form macroscopic objects of typical size of order 0.01-10 [m], all orbiting in the same direction and in the same plane, analogous to the Saturn ring pattern. The dust disk can survive against the so-called *orbital decay* (cfr. Goldreich et al. 1973) for a period of time of order of $10^5$ [yr], depending on various disk parameters as the angular velocity, the orbital distance and the kinematical viscosity. The second phase is the formation of the so-called *Planetesimals*, i.e. object having size of around 10-1000 [m], over a period of $10^4$-$10^5$ [yr]. Driven by gravitational interaction Planetesimals can discretize the allowed orbits inside the protoplanetary disk. The final result is an ensemble of empty gaps between the orbits where Planetesimals are accumulating. The third phase is the collision among Planetesimals sharing the same bounded orbits between two consecutive gaps. Statistically, the process can produce some larger objects. These objects- with a limiting mass of about $10^{23}$ [kg] - are called Embryos. The fifth is the onset of the runaway growth of Embryos induced by dynamical friction and three-body effects. Runaway growth of the Embryos requires $10^5$ [yr] within 1 AU and more than $10^6$ [yr] beyond 1 AU. Then, a rocky core can forms by the gravitational pull of the remaining largest Planetesimals over a timescale of $10^7$-$10^8$ [yr] (Wetherill 1990).

At least in our Solar System, a few rocky cores in the outer parts of the protoplanetary disk should have become large enough (~10-30 $M_{EARTH}$) to accrete residual gas (H and He), giving rise to the Giant Planets: Jupiter, Saturn, Uranus, Neptune (Pollack et al. 1996). However, the big problem of the Solar Nebula paradigm remains the longer formation timescale demanded with respect to the Capture formation paradigm.

### 1.2.2 The Capture formation scenario

The Capture Theory considers tidal interactions between the Sun and a diffuse cold protoplanetary disk which cause distortion, and then escape of filaments of material. Dormand and Woolfson (1971) confirmed the validity of the capture process and through simulations showed that the calculated distribution of planetary material agrees with that of the Solar System. Moreover, Dormand and Woolfson (1988) modeled the filament fragmentation - by Smoothed Particle Hydrodynamics codes - showing that protoplanets move toward the aphelia of eccentric orbits, and if their collapse time is less than their orbital period, then they would condense before the dispersing action of tidal forces at perihelion becomes too effective. Thus, this disk instability may give rise to trailing spiral arms, which can form high density clumps with sufficient mass to be self graviting and tidally stable, forming protoplanets in a much shorter time range with respect to the Solar Nebula paradigm. The short time for the planet formation is one of the main characteristics of the Capture formation scenario; and its recent update - the Disk Instability mechanism, see Section 1.2.3 - has been proposed as the appropriate formation scenario for planets orbiting stars where the protoplanetary disk is likely to dissipate in a time lower than the one needed for the dust grains growth to the Planetesimals regime (cfr. Boss et al. 2006). However, the Disk Instability mechanism lacks of experimental evidences which otherwise promote the Solar Nebula scenario and its modern update (i.e. the Core Accretion mechanism see Section 1.2.3) - as the standard scenario of planetary formation. Among these experimental evidences are: the relation between the star metallicity of and the frequency of stars with planets (cfr. Marcy et al. 2005), and the fact that planets formation prefers the lowest masses, according the updated mass function of 167 detected extrasolar planets (cfr. Butler et al. 2006). At contrary, the Capture formation scenario should foreseen

a decrement in the planets mass function towards the low masses range. This feature has not been already observed. Much further, the physical processes leading the planets formation in the Disk Instability mechanism depend on the gravitational instability of the gas contained in the protoplanetary disk only, independently on the dust grains growth, that in turn lead the formation of Planetesimals. In this sense, the Capture formation scenario is independent from the Planetesimals formation and evolutions, than planets without rocky cores are expected in this scenario. The case of HD 149026 b (cfr. Charbonneau et al. 2006) represents experimental evidence against this conclusion.

### 1.2.3 Insight on the present-day theoretical approaches to planetary system formation

These planetary formation scenarios presented above succeed to explain some characteristics observed in the Solar System but they fail in explaining the exotic features recently found in the realm of extrasolar planets. These include for instance the large range of eccentricities (from small values - like e.g. 47 UMa b - up to large ones, like e.g. 70 Vir b), or the existence of giant planets - the "Hot-Jupiters" - in almost circular orbits with semi-major orbital axis shorter than 0.1 AU (for example 51 Pegasi). These features pointed out the need to revise former theories and develop new models able to explain the origin of planets with a broad range of characteristics.

The updated catalog of nearby extrasolar planets contains 172 low-mass companions (cfr. Butler et al. 2006) with orbits established through Radial Velocity and Transit measurements around stars within 200 pc, with an upper limit for the Minimum Mass (hereafter **M·sin(i)**, see Section 2.1.1 for this definition) equal to 24 $M_{JUPITER}$. The growth of this research is shown by the discovery of over 100 planets in six years since the publication of the first complete list containing 57 extrasolar planets (cfr. Butler et al. 2002). Additionally, other candidates extrasolar planets were detected with direct imaging: 2M1207 (Chauvin et al. 2004) and GQ Lup b (Neuhäuser et al. 2005), AB Pic b (Chauvin et al. 2005), but presently their classification should remain suspended due to the considerably uncertainty on orbital periods, eccentricities and masses (Butler et al. 2006). Finally, a few planets around stars at large distances from the sun have been discovered using the Gravitational Microlensing technique (see Bond et al. 2004, Udalski et al. 2005, Beaulieu et al. 2006 and Gould et al. 2006).

The sample of Butler et al. (2006) - excluding the few ones already found through direct imaging - can be divided broadly in three groups without necessarily implying a clear distinction of different formation processes between them: Jupiter analogous in term of period (**P**) and semi-major orbital axis of the orbit (**a**) with respectively low and highly eccentricities (**e**); and the close-in giant planets with **a** < 0.1 AU and **e**~0 i.e. the *Hot-Jupiters*. Up to now no further "planetary species" have been found outside the Solar System. Actually, considering the variety observed in the Solar System, further "planetary species" are expected to exist also in extrasolar systems. For example: Earth-like planets in different physical configurations up to the warm equivalent of our Earth i.e. the Hot-Earths, and finally the lightest i.e. the atmosphere-free rocky planets such as our Mercury and Mars, up to possible Moon-like objects orbiting their extrasolar planet. The bridge between the present taxonomy of extrasolar planets and the one expected by the modern exo-Planetology lies on the future techniques of detection. A lot of promises are expected by them, not only the direct imaging of a planet, but even the direct imaging of its surface, up to the extremely challenging goal to find new habitable Earths and finally to detect the presence of life.

A robust formation mechanism must explain the planet mass distribution, the large eccentricities, and the large number of planets with the small semi-major orbital axis (**a** <0.03 AU, cfr. Butler et al 2006), and then with very short orbital periods (see Figure 1-11).

Both the local high temperature and the shortage of protostellar matter available for their agglomeration should inhibit formation *in situ* for this sub-population of extrasolar planets (Bodenheimer et al. 2000).

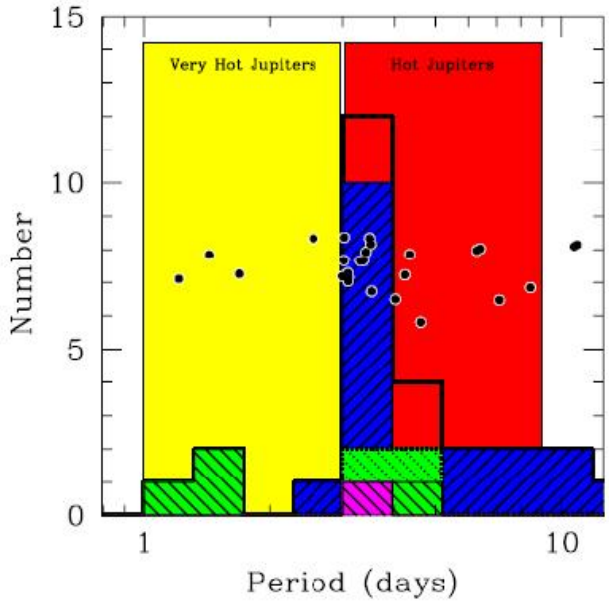


**Figure 1-11: Period distribution of the short period extrasolar giant planets. The blue shaded histogram shows planets with mass M sin(i) > 0.2 $M_{JUPITER}$ detected via Radial Velocities surveys, the green-shaded histogram shows planets detected via OGLE-TRansit surveys and magenta shaded histogram shows the planet detected via the TrES survey. The yellow and the red bands indicate the fiducial period ranges of the Very-Hot-Jupiter and the Hot-Jupiters, while the black points show the individual periods of the planets (cfr. Gaudi et al. 2005).**

The existence of the Hot-Jupiters has focused attention on some earlier predictions that Jupiter-mass planets could have formed further from the star, and then migrated by some non-destructive process. The inward migration could be driven by tidal interaction with the protoplanetary disk (Ward and Hourigan 1989) and subject to tidal circularization (Lie et al. 2000). On the other hand, direct radial migration is expected due to inward torques between the planet and the disk or to outward torques between the planet and the star or finally to outward torques due to Roche lobe overflow and consequent mass loss of the planet (Trilling et al. 1998). The discovery of many systems with small orbital radii represents a serious challenge to these kinds of induced migration. This is because orbital migration timescale is proportional to the orbital period, leading to a rapid orbital decay for the smaller orbits. This physical constraint suggests that inward migration is halted at some radial distance until the disk evaporates. Alternatively, gravitational encounters in post-disk environment could perturb a planet orbit and pushing it into a close-in orbit. Such an event should be followed by the tidal interactions with the host star allowing the circularization of the final orbit.

The theoretical models should also explain the occurrence of planets with high orbital eccentricity at separations larger than those of the Hot-Jupiters. In fact, orbital migration in a viscous gaseous environment - as a protoplanetary disk should be - is expected to preserve circular orbits: planets like that orbiting 70 Vir are then unexpected. This observation forces toward the distinction of four different kinds of migration: the first is the so-called *Jumping Jupiter model* (Weidenschilling and Marzari 1996). In this theory planet encounters via multiple-body gravitational scattering can move a single planet very far from the central star

but maintaining the elliptical-signature of its orbit and then the requested high eccentricity. The second is the Accretion Disk model (Artymowicz 1993) in which the protoplanet exerts gravitational forces on the disk that launch in the intra-planet medium spiral density waves which in turn exert a gravitational back-reaction on the planet. The third is the Companion Star model (Holman et al. 1997) in which the high eccentricity depends on tidal interaction with another star. The fourth is the Young Star Cluster model (Laughlin and Adams 1998) where stellar encounters in a young star cluster could modify the orbits of a planet bound to one of the encountering object.

Presently, all the new theoretical topics (in situ formation, migration, circularization etc.) are matter of debate between two main formation scenarios which in turn represent the thoughtful update of the old Solar Nebula and Capture ones (see Sections 1.2.1 and 1.2.2 for details): the Core Accretion and the Disk Instability mechanisms. The basic distinction between the two theories is on the different explication of how a giant planet could accrete its gas content. In the Core Accretion Mechanism the cores were sufficiently massive to capture gravitationally the gas from the surrounding disk. For the Disk Instability Mechanism a sufficiently cold gas in the disk is gravitationally unstable and can collapse directly into giant gaseous planets. Jupiter and Saturn could have formed in this way, but only if the surface density was greater than the value of the so-called *Minimum Mass Solar Nebula* (cfr. Hayashi 1981 for its definition) by more than a factor of 10 (Guillot and Gladman 2000). On the other hand, some extrasolar planets might indeed have formed in this manner, for example the two Super-Earth (5.5 $M_{EARTH,}$ cfr Beaulieu et al. 2006, and 13 $M_{EARTH}$, cfr. Gould et al. 2006) orbiting distant (i.e. d >> 200 pc) M-dwarf stars, and detected by Microlensing events during the ongoing OGLE survey. Indeed, Boss et al. (2006) proposed that these Super-Earth failed to become gas giant planets because the growth of solid cores by collisional accumulation proceeds considerably slower at a fixed orbital radius around a M-dwarf star than around a G-dwarf star, and the disk gas is likely to have been dissipated in ~$3x10^6$ [yr], well before such a core cloud could accrete a significant gaseous envelope. On the contrary, around our Sun (a G2V star), Uranus and Neptune are likely to be formed via coagulation i.e. the process - expected in the Core Accretion theory - by which bodies in a circumsolar disk grow up by accreting each other and damping each other's velocities through viscous stirring and dynamical friction (cfr. Goldreich et al. 2004).

## 1.3 Model atmospheres for extrasolar giant planets

To date, there are ~170 known extrasolar giant planets i.e. those with **M·sin(i)** ranging from a lower limit of around 1 $M_{JUPITER}$ up to an upper limit of 24 $M_{JUPITER}$ (cfr. Butler et al. 2006). Most of these detections were obtained by extraction of the Radial Velocity profile of the primary star moving around the center of mass of the star-planet/s system through high-resolution spectroscopy (see Section 2.1.1 for details on this technique). To date, 13[2] extrasolar giant planets have been found to transit their parent star. The observation of planetary Transits (see Section 2.2 for details on this technique) allows determination of the fundamental parameters of a planet - mass and the radius - then enabling the study of its physical properties. Furthermore, the measures of duration of the Transits at different wavelengths led to the first hints about the composition of an extrasolar giant planet atmosphere. Through this approach, Charbonneau et al. (2002) detected the sodium D-lines in the Transit spectrum of HD 209458 b. This work was followed by the detection of atomic hydrogen (by $Ly_\alpha$) providing indications of a wind around the planetary surface (cfr. Vidal-

[2] Cfr. Section 2.2 for specifications about the updated list of planets detected with this technique.

Madjar et al. 2003). In the near future, the challenge is to characterize the whole spectrum of an extrasolar giant planet using a direct chromatic analysis of its light which, in turn, could be disentangled from the emission of its parent star by direct imaging with the new class of ground based ELTs or with the future space based observatory concepts envisaged by NASA and ESA. Additionally, extrasolar giant planets could be detected exploiting their own spectroscopic features by intriguing techniques like the Closure-Phase Interferometry (foreseen for the VLTI on 2007 by the new PRIMA facility, cfr. Quirrenbach 2004), the AO assisted SDI (already undertaken at VLT with the NACO-SDI facility, cfr. Lenzen at al. 2005, and at the CFHT with the TRIDENT camera, cfr. Marois et al. 2005) or the brand new S-SDI technique obtained with IFS (cfr. this Dissertation), and foreseen for the novel VLT Planet Finder facility (SPHERE) which is expected to begin operation in 2010 (cfr. Beuzit et al. 2006). All these projects should be supported by theoretical models of extrasolar giant planets spectra upon which all the instrumental requirements and specifications depend.

Various groups are constructing model atmospheres suitable for extrasolar giant planets (among others, we may cite Baraffe and its group in France; Sudarsky and its group in the US). Hereafter we will mostly follow the approach of Surdarsky's group, although similarly important contributions are given by the others. Sudarsky et al. (2000) modeled albedo and reflection spectra for a full range of extrasolar giant planets, exploiting the latest atomic and molecular cross-sections, the Mie's theory treatment of scattering and absorption condensates, and an extension of the Feautrier's technique for building a general treatment of the scattering phase function. Surdarsky's team distinguished the theoretical spectral albedos in five classes, defined only by the different range of atmospheric temperature of the planet. This classification has been improved in Sudarsky et al. (2003), obtaining the spectral profile of the whole energy (i.e. the sum of the reflected and internal - blackbody-like - radiations) emitted by the atmospheres of irradiated extrasolar giant planets. An important output of this study is the suggestion of which spectral features are most useful diagnostics of giant planet atmospheres and which bands are best for detection and characterization of planets from their spectroscopic features.

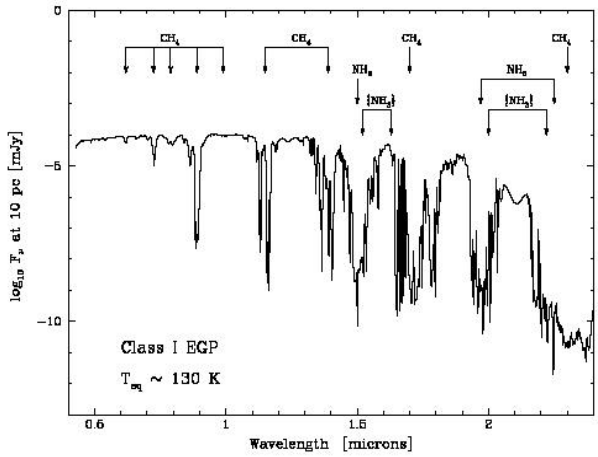


**Figure 1-12: Emergent spectrum of a class I ($T_{eq}$~130 K, cfr. Sudarsky et al. 2003) extrasolar giant planet placed at 10 pc from the Earth.**

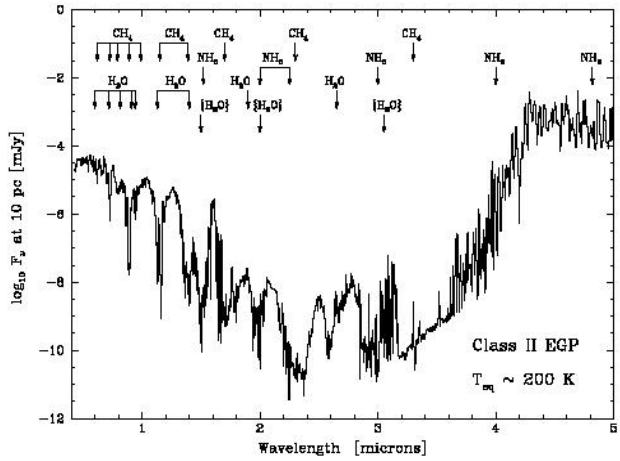


**Figure 1-13: Emergent spectrum of a class II ($T_{eq}$~200 K, cfr. Sudarsky et al. 2003) extrasolar giant planet placed at 10 pc from the Earth.**

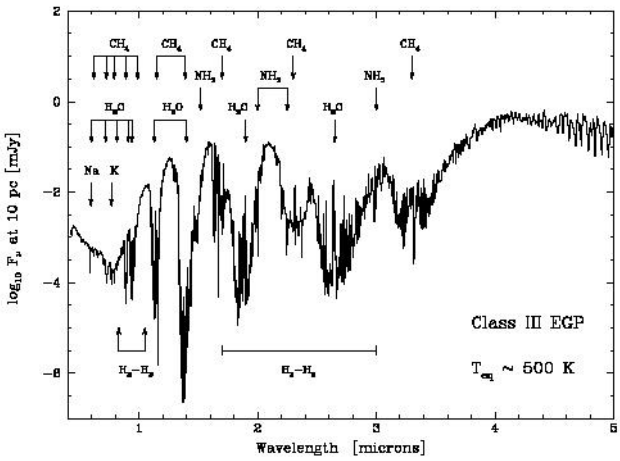


**Figure 1-14: Emergent spectrum of a class III ($T_{eq}$~500 K, cfr. Sudarsky et al. 2003) extrasolar giant planet placed at 10 pc from the Earth.**

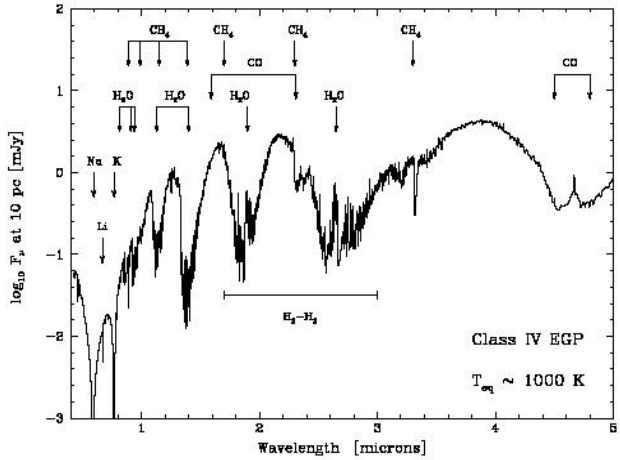


**Figure 1-15: Emergent spectrum of a class IV ($T_{eq}$~1000 K, cfr. Sudarsky et al. 2003) extrasolar giant planet placed at 10 pc from the Earth.**

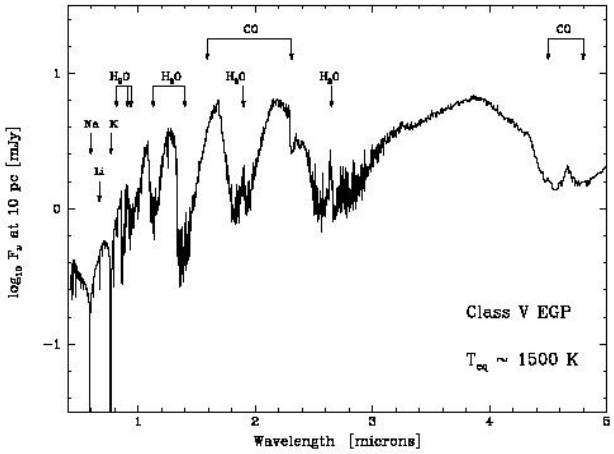


**Figure 1-16: Emergent spectrum of a class V ($T_{eq}$~1500 K, cfr. Sudarsky et al. 2003) extrasolar giant planet placed at 10 pc from the Earth.**

The specifications of the Sudarsky's spectral classification of extrasolar giant planets are properly described in Sudarsky et al. (2003). A detailed discussion of this topic is beyond the intention of this Dissertation. For this reason in the following only a qualitatively description of the differences among the Sudarsky's classes is given.

The so-called *Jovian objects* (class I) have the lowest temperature and get tropospheric ammonia clouds. Class II objects are warmer and the spectra are strongly influenced by the presence of water clouds in the atmosphere. For Class I and II the absorption features of gaseous methane are prevalent. Moreover, Class II objects are expected to have the highest VISible albedos of any class. When the upper atmosphere is too hot for $H_2O$ to condense, radiation generally penetrates more deeply. These objects are designated class III. Absorption lines of alkali, sodium and potassium characterize their spectral albedos, which become negligible toward the NIR. In those extrasolar giant planets with the smallest orbital distance - named in literature *Roaster* or Very-Hot-Jupiters - the irradiation by the host star produces tropospheric silicate layers in the temperature range 900 -1500 K (class IV). When the temperature exceeds 1500 K (class V), the silicate layers move to the highest zone of the atmosphere, reflecting much of the incident radiation. Hence, class V objects have much higher spectral albedos than those of class IV.

## 1.4 Earth's atmosphere and models for extrasolar terrestrial planets

The search for life on extrasolar planets is a basic cornerstone of the Astronomical research for the XXI century. At present this is considered beyond the possibilities of the present and near-future observatories by the scientific community (cfr. Perryman et al. 2005). But the mood of the scientific community is definitively changing on this topic. Indeed, the NASA has re-defined his so-called *Origins Program* (i.e. the multi-wavelength vision of the Universe with the spatial observatories: CGRO, Chandra, HST and Spitzer) in a larger ensemble of missions that - step by step - should allow to find life on extrasolar terrestrial planets. In this sense, the First Generation missions (including the spatial observatories JWST and SIM) should find the candidate exo-Earths. The Second Generation missions (including the spatial observatory TPF) should examine the presence of life through the spectroscopic signatures of biomarkers. Once habitable planets will be identified, a Third Generation mission could detect life exploiting future technologies like hyper-telescopes (cfr. Labeyrie 1996).

In this subject, the important question is what type of biosignatures will unveil the possible presence of life. Spectral signatures can be of two kinds. A first type consists of biological activity by-products, such as oxygen and ozone, in association with water vapor, methane and carbon dioxide (Lovelock 1975; Owen 1980; Angel et al. 1986). These biogenic molecules present attractive narrow molecular bands. This lead in 1993 to concept of the ESA/Darwin project (Leger et al. 1996), followed by the NASA/TPF project (Beichman et al. 1999). But oxygen is not a universal by-product of biological activity, as demonstrated by the existence of anoxygenic photosynthetic bacteria (Blankenship et al. 1995). A second type of biosignature is provided by signs of stellar light transformation into biochemical energy, such as the planet surface colouring by vegetation. This may translate into a characteristic spectral feature. This signature is in principle a more reliable biomarker than any biogenic gas such as oxygen, since it is a general feature of photosynthetic activity. However its appearance may depends on the kind of irradiated spectrum, i.e. on the spectral type of the host star (cfr. Tinetti et al. 2006). On the Earth spectrum, this pattern is revealed as a strong increase of the spectral albedo beyond 0.7 [micron] (see Figure 1-17) and then is named the *Red-Edge*.

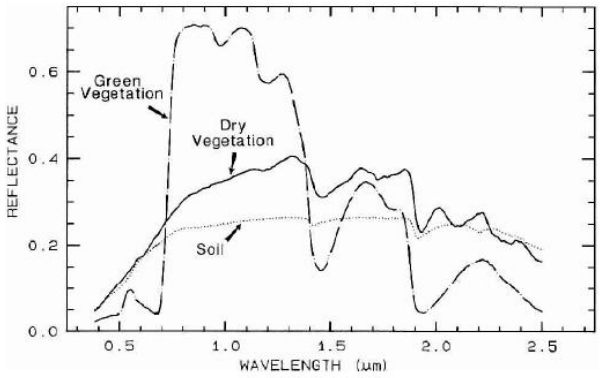


**Figure 1-17: Spectral albedo of photosynthetic (green), non-photosyntetic (dry) vegetations and the Earth's soil according to Clark (1999).**

In these years different observation of the Earthshine - i.e. the part of the Sunlight reflected form the Earth on the dark side of the Moon and then reflected back again to Earth - and of the Moonlight - i.e. the intrinsic radiation of the Moon - have been undertaken (for example see Arnold et al. 2002, Woolf et al. 2002, Montenez-Rodriguez 2005), in order to obtain the spectrum of the Earth as it would be seen from outside the Solar-System. The results apparently do not confirm the high reflectivity at wavelengths longer than 0.7 [micron], as expected for a pure-vegetation albedo profile dominated by the Red-Edge feature. Rather, this behaviour is well reproduced by models containing different contributions to the final Earth's spectral albedo including the Ocean surface reflection, the Ocean green-pigmented phytoplankton and the Aerosol scattered light. Moreover, this latter contribution depends on the amount of clouds, which in turn is related strongly to the global Earth's weather and then changes with time.

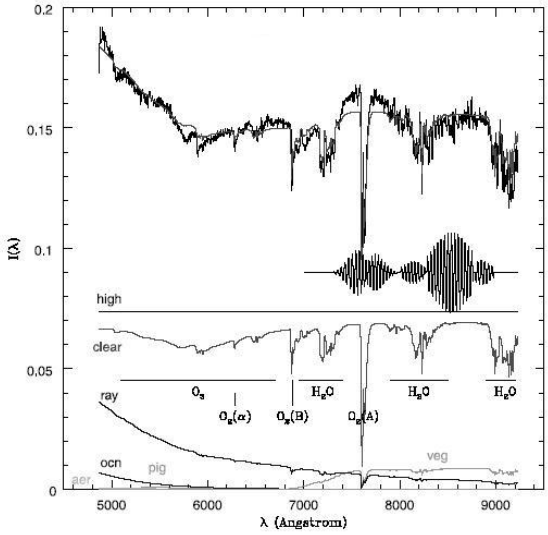


**Figure 1-18: Spectral albedo of the Earth as determined by the Earthshine measure of Woolf et al. (2002), with a model spectrum super-imposed. This latter is the sum of the various contributions as the Figure shows. The interferometric pattern on the right-center of the Figure is the CCD fringing by which the instrumental spectrum produced by the detector was divided.**

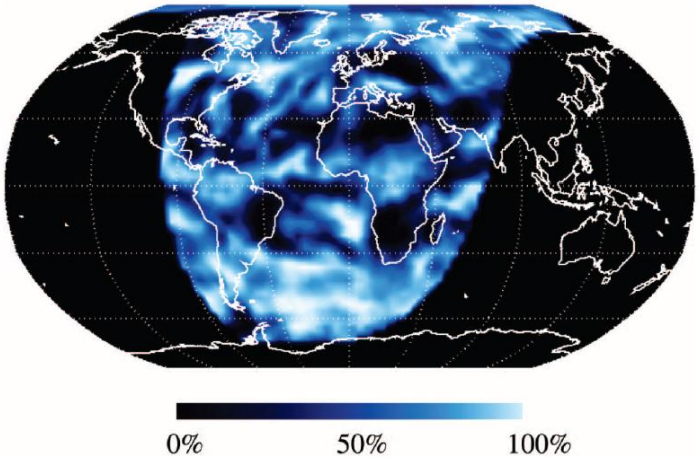


**Figure 1-19: Earthshine contributing area of the Earth during the observation of Montanez-Rodriguez et al. (2005) (2003 November 19-th, 10.47-13.08 UT hour). The super-imposed colour map represents the mean cloud distribution form the ISCCP data over this area.**

## 1.5 Statistical properties of the observed planetary systems

The first direct detection of stellar companions with a planetary mass finally occurred with the two Camera VLT/NACO and HST/NICMOS. Specifically, an image of the star 2M1207 and of its low-mass companion, located at 54 AU to the central object, was obtained by Chauvin et al. (2004). The system likely has an age of about 8 [Myr] and it is a member of the TW Hydrae association. The IR photometry implies a companion's mass in the range 2-5 $M_{JUPITER}$. Second epoch HST observations confirmed that the companion is bound to the primary, making it the first object with planetary mass ever imaged. However, up to now all the observed properties in the other planets were obtained via in-direct methods. Among these, the Radial Velocity technique allowed to discover more than 90 % of the known extrasolar planets and only nine of them are known to cross the disk of their star and to be

detectable via the Transit technique (cfr.Charbonneau et al. 2006). Among this group, HD 209458 b, HD 149026 b and HD 189733 b were found first with the Radial Velocity technique. By combining Radial Velocity and Transit observations, a direct estimation of mass and radius and then of the density is possible, with resulting values ranging from 0.2 to 1.5 [g·cm$^{-3}$] (see Figure 2-9). These values verify the expectation that these planets are gaseous, with liquid hydrogen in their interiors. Remarkable are the observations with Spitzer/MIPS of HD 209458 b (Deming et al. 2005) and with Spitzer/IRAC of TrES-1 (Charbonneau et al. 2005), which showed the eclipse of the planet by the star: the diminished flux of the star-planet system allowed to measure the temperature of their atmosphere.

With the rather large number of planetary systems detected presently, we can begin to shed light on their statistical properties, which in turn is a basic tool for constraining the formation models.

### 1.5.1 Properties of the observed exoplanets

As explained in Section 1.1.4.2, an important diagnostic for a statistical ensemble of planets is the mass function, because it is closely related to the formation mechanism. In this specific case, the observable is the numerical density of extrasolar planets discretized in mass bins. This density distributes according to a power law with index equal to $\alpha$= -1.10 (see Figure 1-20).

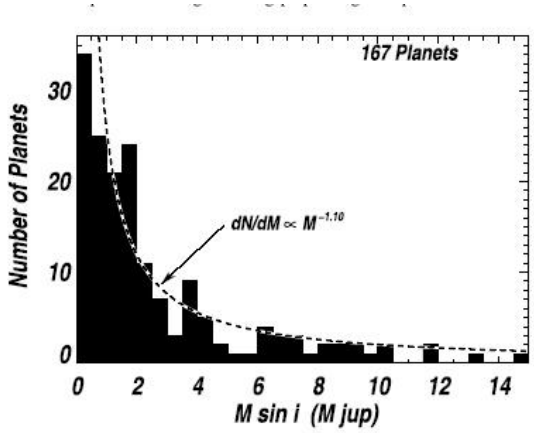


**Figure 1-20: Histogram of Minimum Mass for 167 known extrasolar planets found with M·sin(i)<15 $M_J$ (cfr. Butler et al. 2006).**

This indicates that planets formation prefers the lowest masses; behaviour expected as a result of the Core Accretion mechanism (Marcy et al. 2005). However, the Core Accretion model fails to explain the duration of the accretion process for giant planets at large distances from the star. This mechanism is slowed by the diminishing amounts of local gas in the outer regions of the circumstellar disk and the time predicted for this accretion ranges 5-10 [Myr]. This is too much with respect to the observed circumstellar disk lifetimes (~3 [Myr]).

The distribution of orbital semi-major axis for the known planets peaks in the range 1-5 AU, (see Figure 1-21) but selection effects may be important for semi-major orbital axis larger than 5 AU where the orbital period of a planet - according the third Kepler's law- can become larger than 10 [yr]. This value is greater than the time coverage of all the dedicated surveys undertaken on this subject up to now.

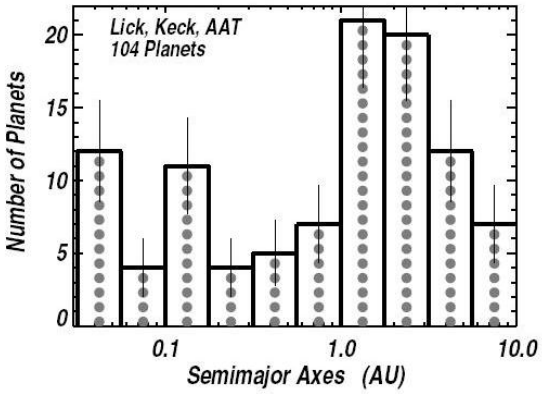


**Figure 1-21: Histogram of the semi-major orbital axis distribution for the 104 planets found in the uniform Doppler survey (accuracy ~3 [m·sec$^{-1}$]) of 1330 star conducted by the Lick, Keck, Anglo-Australian telescopes with a duration of ~8 [yr] (cfr. Marcy et al. 2005).**

It has been emphasized that the observed decrement of planets in the range 0.1-1 AU, in the histogram of the orbital semi-major axis, corresponds to a *period valley* in the range 10-100 [days], in the equivalent histogram of the orbital periods. This statistical trend has been interpreted as an indicator of the lack of massive planets on short-period orbits. More in details, in the context of the migration scenario, several processes have been proposed to explain this feature such as type II migration[3] - which is less effective for massive planets - or planet-star interactions that could provoke mass transfer from the planet to the star - deceasing the mass of the former - or leads massive planets to fall in to the central star (cfr. Udry et al. 2003).

Planets with semi-major orbital axis shorter than 0.1 AU have systematically quasi-circular orbits (see Figure 1-22) and the lowest masses (see Figure 1-23). This also may be a selection effect: small planets can be detected easily by the Radial Velocity technique if they have small semi-major orbital axis. Indeed, the lower detectable value of **M·sin(i)** goes down for orbits with the smallest semi-major orbital axis (see Section 2.1.1 for details).

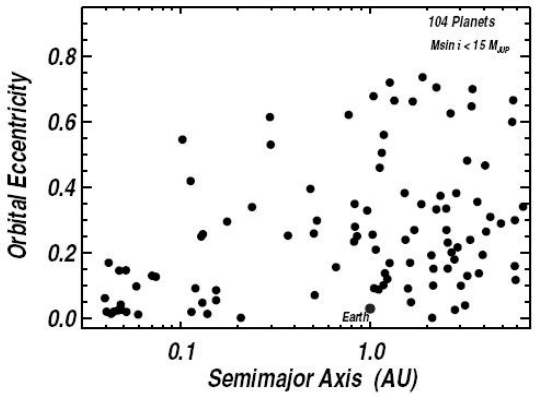


**Figure 1-22: Eccentricity vs. semi-major orbital axis distribution for the 104 planets in the sample of Marcy et al. (2005).**

[3] Type II migration is a dynamical model where the circumstellar disk accretes viscously onto the star, dragging planets with them toward close-in orbits, see for example Artymowicz (2006) for a detailed description.

Presently, the Zone of Avoidance observed in the diagram correlating orbital eccentricity and semi-major orbital axis (see Figure 1-22) is interpreted as a manifestation of the gravitational tidal circularization of the orbits, induced by the host star. On the other hand, the Zone of Avoidance observed in the diagram correlating **M·sin(i)** and the orbital semi-major axis (see Figure 1-23) can be due to a possible correlation between the mass distribution of extrasolar planets and the orbital distance.

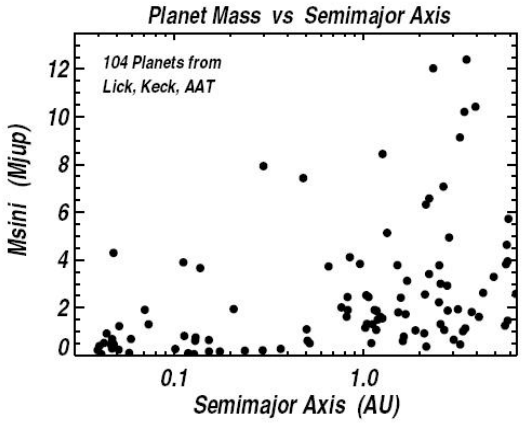


**Figure 1-23: M·sin(i) vs. semi-major orbital axis distribution for the 104 planets in the sample of Marcy et al. (2005).**

On the contrary there is no strong correlation between eccentricity and the planet mass. Although the most massive planets i.e. beyond **M·sin(i)** > 5 $M_{JUPITER}$ exhibit eccentricities systematically higher than the planets of lower mass (see Figure 1-24).

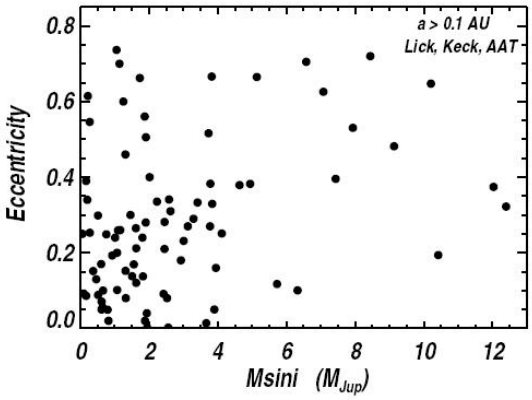


**Figure 1-24: Orbital eccentricity vs. M·sin(i) distribution for the 104 planets in the sample of Marcy et al. (2005).**

Then, if planets form initially in circular orbits, the high eccentricities of the most massive planets pose a puzzle that both Core Accretion and Disk Instability model are not able to explain. Gravitational interaction between different bodies in a phase following that of formation seems more successful to justify this feature, as induced by N-body gravitational scattering (cfr. Marzari et al. 2002). Alternatively, massive planets form by a process in which they move on orbits not as round as the smallest ones do.

### 1.5.2 Properties of the stars hosting observed exoplanets

The wide sample of Marcy et al. (2005) - ~1330 FGKM main sequence stars - allows to infer some statistical properties of the stars that harbor planetary systems. In this sample there are 88 stars hosting planets, giving a crude occurrence frequency of 6.6 %; 12 stars get two or more planets, and then the multiple occurrence frequency is ~1 %[4]. In the same sample there is a well defined trend for the metallicity distribution function: the number of stars with planets is higher when their metallicity is higher, apparently with a square dependence (see Figure 1-25).

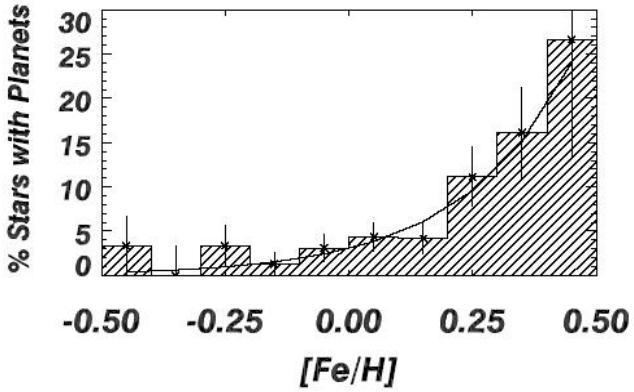


**Figure 1-25: Frequency of extrasolar planets in bins of different metallicity in the sample of Marcy et al. (2005).**

This trend favors the Core Accretion mechanism because the Planetesimals growth is enhanced and accelerated in a metal rich environment, and the timescale for accretion should indeed decrease with the square of the number of grains, that may be expected to be proportional to the metal content. However, it is important to note here that a planetary system identical to our own Sun should however classified as a star without planets in the sample of Marcy et al. (2005), then it is clear that the inferred statistics are biased.

Moreover, the so-called *Sozzetti's diagram* (see Figure 1-26) reveals another intriguing correlation. When the star metallicity is plotted against the planet orbital period (**P**), Very-Hot-Jupiters (**P** < 5 days) are found more likely around stars with higher metallicity. In the framework of the Core Accretion scenario, this statistical trend could be interpreted as the evidence that planetary migration depends on the star metallicity, and then on the protoplanetary disk metallicity. In this case, the Very-Hot-Jupiter vs. metallicity occurrence could be linked with the primeval disk. This is a behaviour expected in the type II migration model.

[4] The search is assumed to be complete for planets with mass >1 $M_J$ and orbital period <5 [yr]. Hence, the occurrence frequencies are for planets with mass larger than 1 $M_J$ and orbital periods shorter than 5 [yr].

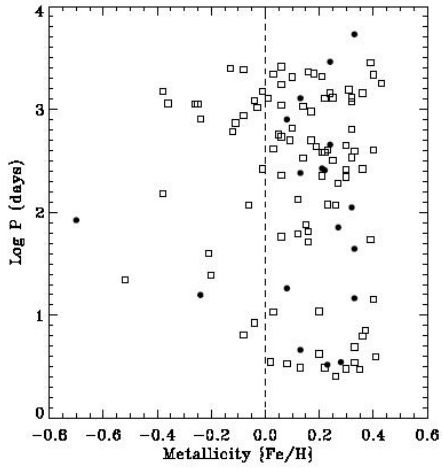


**Figure 1-26: Occurrence of Very-Hot-Jupiters vs. metallicity in the sample (cfr. Sozzetti 2004).**

## 1.6 Properties of the observed circumstellar disks

According to Artymowicz (1999), planetary formation begins right after the protostellar collapse, and continues through the T Tauri/HerbigAeBe stage of stellar evolution. These evolutive phases - proper of young stellar objects - are characterized by the presence of circumstellar disks, which in turn evolve, modifying their content of gas and dust. In the Core Accretion mechanism, the circumstellar disks behaviour is related to the formation and the growth of Planetesimals, i.e. to the seeds of planetary formation. Moreover, dust-dominated disks (or debris disks) should be the final phase of evolution of circumstellar disks, in which collisions among solid residuals of the planetary formation or low erosion of long lived Planetesimals occur (cfr. Augereau 2004).

The circumstellar disks research is active since several decades. Theoretical and observational breakthroughs have been accomplished in the realm of protoplanetary disks (see Natta et al. 2006 for a detailed discussion), and more recently, dusty disks in the IR-emitting (Vega-type) planetary systems have been discovered. The first example of this new population is the debris disk around β Pictoris (see e.g. Mouillet et al. 1997).

### 1.6.1 Protoplanetary disks

Protoplanetary disks - see Figure 1-27 - might be extremely large (up to 1000 AU) with respect to the standard distances of sub-stellar objects to the host star, and the surface area of the particles making up the disk may be many order of magnitude larger than that of a planet. Protoplanetary disks are strong thermal emitters in the range 2-1000 [micron], with SEDs much broader than any single-temperature black body. This is because the observed spectrum is the sum of the thermal emissions from material spanning a wide range of temperatures, from 30 K - in the outer region - to 1000 K very close to the star.

In the specific context of the exoplanets research, improvements in our understanding of the protoplanetary disks physics have important consequences for the planetary formation models too. In this subject, the fundamental component in a circumstellar disk is the dust grains content, even though the mass of a protoplanetary disk is dominated by its gas content. Dust grains play an active role in determining the structure of the disks because their opacity dominates over the gas opacity. Furthermore dust grains shield the disk mid-plane from the star energetic radiation, and possibly led to a dead zone were magneto-rotational instability can operate and contribute to form planets (cfr. Natta et al. 2006). One of the basic features of the dust grains in circumstellar disks is the evidence of their growth, from sizes below the micron scale - dominated by the Polycyclic Aromatic Hydrocarbons contribution - up to the tail of 1 [cm] where silicates dominate. The evidence of growth is not present in the interstellar medium and in the molecular clouds dusty environments; this characteristic could be the origin of the Planetesimals growth inside a circumstellar disk. More in detail, models of grain growth by coagulation and sedimentation - which constitute the building block of the Core Accretion mechanism - predict the grain growth on very short timescales (cfr. Dullemond and Dominik 2005). Presently, this expectation is not consistent with observations showing that stars as old as $10^7$ [yr] get a dust grains growth well beyond the Planetesimals regime (cfr. Dullemond et al. 2006).

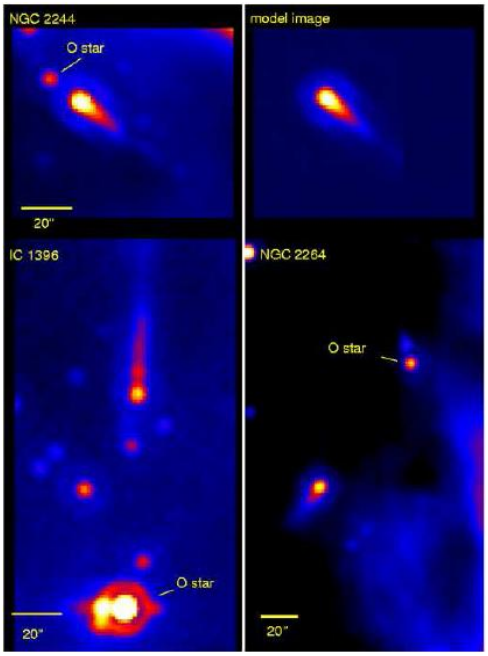


**Figure 1-27: 24 [micron] Spitzer/MIPS images of three protoplanetary disks around high mass O type stars (NGC 2244, NGC2264, IC 1396) together with a model image for the tail in NGC 2244 (upper right panel), cfr. Balog et al. 2006.**

### 1.6.2 Dusty disks

Optically thin disks around main sequence stars should consist of debris from catastrophic collisions among residual rocky products of the Core Accretion mechanism, or should come from low erosion of primeval Planetesimals. Nowadays, this scenario is able to explain the observed features of the dusty disks population. For example, the IR-flux excesses observed in a large fraction of nearby main sequence stars is explained as the thermal emission of a disk made by cool and solid material which in turn derives from the dissipation of the initial massive protoplanetary disk (cfr. Lagrange et al. 2000). Moreover, the observed large spread of the so-called *disk fractional luminosity* is well explained by the presence of planetary Embryos which can stir up Planetesimals through gravitational interaction, thereby increasing the rate of collisions and resulting in stochastic brightness spikes of the dusty disks (cfr. Kenyon and Bromley 2002).

Only a sparse set of dusty disks around main sequence stars bas been spatially resolved up to now. However, this set should be considered as an impressive improvement compared to the situation of a few years ago, when only β Pictoris was known. In particular, the images of β Pictoris revealed the disk-shaped and flat geometry of a system seen almost edge-on. Now, images of different resolved dusty disk environments are available; the images in the VISible of HD 141569 and HR 4796 have been obtained with HST/STIS (Mouillet et al. 2001 and Schneider et al. 2001), while a NIR image of β Pictoris has been obtained from the ground with AO technique (Mouillet et al. 1997). The 3 oldest disks: Fomalhaut, Vega, ε Eridani, have been resolved in thermal emission with JCMT/SCUBA in the submillimetre (Holland et al. 1998, 2003, and Greaves et al. 1998). These images display a wealth of structures: ring-shaped disks accompanied with gaps (all the systems surveyed), spiral structures and arcs (HD 141569), clumps or blobs (β Pictoris, ε Eridani, Vega and Fomalhaut), offset asymmetries (HD 141569 and HR 4796) and warps or offset inclinations (β Pictoris), see Figure 1-28.

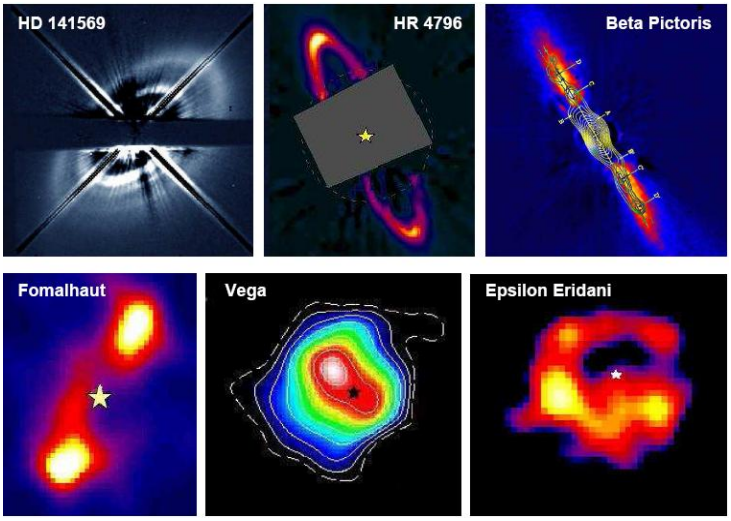


**Figure 1-28: Montage of resolved dusty disk around mains sequence stars in ascending order from left to right, top to bottom (from Augereau et al. 2004). The 3 top panels display disks seen is scattered light using coronagraphic techniques to mask the central bright star. The 3 bottom panels display disks seen in IR and FIR emitted light.**

Similar structures in the dusty Solar System are related to the presence of the planets; for this reason the observed structures in extra-solar dusty disks have raised the idea that they could as well be due to yet undetected distant exoplanets in these systems (cfr. Augereau et al. 2004). Furthermore, such disks may contain comparable amounts of dynamically coupled gas and dust, and - in the case of embedded planets - this feature could allow the direct detection of planet-disk dynamical interactions by which it should be possible to shed light on the planetary migration processes (cfr. Artymowicz 1999).

## 1.7 Bibliography


Angel, J. R. P.; Cheng, A. Y. S.; Woolf, N. J., 1986, Nature (ISSN 0028-0836), vol. 322, p. 341-343.

Arnold, L.; Gillet, S.; Lardière, O.; Riaud, P.; Schneider, J., 2002, A&A., v.392, p.231-237.

Artymowicz, P., 1993, ApJ., v.419, p.166.

Artymowicz, P., *Planet formation and disk evolution*, Proceedings of the conference 'Darwin and astronomy - the infrared space interferometer', Stockholm, Sweden, 17-19 November 1999. Noordwijk, the Netherlands: European Space Agency, 2000, ESA SP 451, ISBN 92--9092-645-7., p.117.

Artymowicz, Pawel, *Planetary Systems*, Graduate School in Astronomy: X Special Courses at the National Observatory of Rio de Janeiro; X CCE, held 26-30 September, 2005 in Rio de Janeiro, Brazil. AIP Conference Proceedings, Vol. 843. Edited by Simone Daflon, Jailson Alcaniz, and Eduardo Telles. Melville, NY: American Institute of Physics, 2006., p.3-34.

Augereau, J.-C., *Extrasolar Planets: Today and Tomorrow*, ASP Conference Proceedings, Vol. 321, held 30 June - 4 July 2003, Institut D'Astrophysique de Paris, France. Edited by Jean-Philippe Beaulieu, Alain Lecavelier des Etangs and Caroline Terquem. ISBN: 1-58381-183-4, 2004, p.305.

Balog Z., Rieke G. H., Su K. Y. L., Muzerolle J., Young E. T., ***astro-ph/0608630*** (Accepted for publication in The Astrophysical Journal Letters).

Baraffe, I.; Chabrier, G.; Allard, F.; Hauschildt, P. H., 1998, A&A, v.337, p.403-412.

Beaulieu, J.-P.; Bennett, D. P.; Fouqué, P.; Williams, A.; Dominik, M.; Jorgensen, U. G.; Kubas, D.; Cassan, A.; Coutures, C.; Greenhill, J.; and 63 coauthors, 2006, Nature, Volume 439, Issue 7075, pp. 437-440.

Beichman, C. A.; Woolf, N. J.; Lindensmith, C. A, **The Terrestrial Planet Finder (TPF): a NASA Origins Program to search for habitable planets / the TPF Science Working Group**; edited by C.A. Beichman, N.J. Woolf, and C.A. Lindensmith. [Washington, D.C.]: National Aeronautics and Space Administration ; Pasadena, Calif. : Jet Propulsion Laboratory, California Institute of Technology, [1999] (JPL publication ; 99-3).

Beaulieu, J.-P.; Bennett, D. P.; Fouqué, P.; Williams, A.; Dominik, M.; Jorgensen, U. G.; Kubas, D.; Cassan, A.; Coutures, C.; Greenhill, J.; and 63 coauthors, 2006, Nature, Volume 439, Issue 7075, pp. 437-440.

Beuzit, J.-L.; Feldt, M.; Mouillet, D.; Moutou, C.; Dohlen, K.; Puget, P.; Fusco, T.; Baudoz, P.; Boccaletti, A.; Udry, S.; and 17 coauthors, *Direct Imaging of Exoplanets: Science & Techniques*. Proceedings of the IAU Colloquium #200, Edited by C. Aime and F. Vakili. Cambridge, UK: Cambridge University Press, pp.317-322, 2006.

Bodenheimer, Peter; Hubickyj, Olenka; Lissauer, Jack J., 2000, Icarus, Volume 143, pp. 2-14.

Bihain G., Rebolo R., Bejar V. J. S., Caballero J. A., Bailer-Jones C. A. L., Mundt R., Acosta-Pulido J. A., Manchado Torres A., ***astro-ph/0608255*** (accepted for publication in Astronomy and Astrophysics).

Blankenship, R. E., Madigan, M. T., & Bauer, C. E. 1995, **Anoxygenic Photosynthetic Bacteria** (Kluwer Academic Publishing, Dordrecht, The Netherlands).

Bodenheimer, P., *Brown dwarfs and extrasolar planets*, Proceedings of a Workshop held in Puerto de la Cruz, Tenerife, Spain, 17-21 March 1997, ASP Conference Series #134, edited by Rafael Rebolo; Eduardo L. Martin; Maria Rosa Zapatero Osorio, p. 115.

Bond, I. A.; Udalski, A.; Jaroszyński, M.; Rattenbury, N. J.; Paczyński, B.; Soszyński, I.; Wyrzykowski, L.; Szymański, M. K.; Kubiak, M.; Szewczyk, O.; and 22 coauthors, 2004, ApJ., Volume 606, Issue 2, pp. L155-L158.

Bonnell, Ian A, **The Origin of Stars and Planetary Systems**. Edited by Charles J. Lada and Nikolaos D. Kylafis. Kluwer Academic Publishers, 1999, p.479.

Boss, Alan P., 2006, ApJ, Volume 644, Issue 1, pp. L79-L82.

Burrows, Adam; Hubbard, W. B.; Lunine, J. I.; Liebert, James, 2001, Reviews of Modern Physics, vol. 73, Issue 3, pp. 719-765.

Burrows, Adam; Sudarsky, David; Hubeny, Ivan, 2006, ApJ., Volume 640, Issue 2, pp. 1063-1077.

Butler, R. Paul; Marcy, Geoffrey W.; Vogt, Steven S.; Tinney, C. G.; Jones, Hugh R. A.; McCarthy, Chris; Penny, Alan J.; Apps, Kevin; Carter, Brad D., 2002, ApJ., Volume 578, Issue 1, pp. 565-572.

Butler, R. P.; Wright, J. T.; Marcy, G. W.; Fischer, D. A.; Vogt, S. S.; Tinney, C. G.; Jones, H. R. A.; Carter, B. D.; Johnson, J. A.; McCarthy, C.; Penny, A. J., 2006, ApJ., Volume 646, Issue 1, pp. 505-522.

Chabrier, G.; Baraffe, I.; Allard, F.; Hauschildt, P, 2000, ApJ, Volume 542, Issue 2, pp. L119-L122.

Chabrier, G.; Baraffe, I.; Allard, F.; Hauschildt, P. H., *11th Cambridge Workshop on Cool Stars, Stellar Systems and the Sun*, ASP Conference, Proceedings, Vol. 223., 2001, Edited by Ramon J. Garcia Lopez, Rafael Rebolo, and Maria Rosa Zapaterio Osorio. San Francisco: Astronomical Society of the Pacific, ISBN: 1-58381-055-2, p.49.

Charbonneau, David; Brown, Timothy M.; Noyes, Robert W.; Gilliland, Ronald L., 2002, ApJ., Volume 568, Issue 1, pp. 377-384.

Charbonneau, David; Allen, Lori E.; Megeath, S. Thomas; Torres, Guillermo; Alonso, Roi; Brown, Timothy M.; Gilliland, Ronald L.; Latham, David W.; Mandushev, Georgi; O'Donovan, Francis T.; Sozzetti, Alessandro, 2005, ApJ., Volume 626, Issue 1, pp. 523-529.

Charbonneau D., Brown T. M., Burrows A., Laughlin G., ***astro-ph/0603376*** (Review Chapter for Protostars and Planets V).

Chauvin, G.; Lagrange, A.-M.; Dumas, C.; Zuckerman, B.; Mouillet, D.; Song, I.; Beuzit, J.-L.; Lowrance, P., 2004, A&A., v.425, p.L29-L32.

Chauvin, G.; Lagrange, A.-M.; Zuckerman, B.; Dumas, C.; Mouillet, D.; Song, I.; Beuzit, J.-L.; Lowrance, P.; Bessell, M. S., 2005, A&A., Volume 438, Issue 3, pp.L29-L32.

Clark, R. N. 1999, **Manual of Remote Sensing**, ed. A. Rencz (J.Wiley and Sons, NewYork).

Comerón, F.; Neuhäuser, R.; Kaas, A. A, 2000, A&A., v.359, p.269-288.

Deacon, N. R.; Hambly, N. C., VizieR On-line Data Catalog: J/A+A/416/125.

Deming, Drake; Seager, Sara; Richardson, L. Jeremy; Harrington, Joseph, 2005, Nature, Volume 434, Issue 7034, pp. 740-743.

Dormand, J. R.; Woolfson, M. M., 1971, MNRAS, Vol. 151, p. 307.

Dormand, J. R.; Woolfson, M. M., **The physics of the planets: Their origin, evolution and structure** (A88-52201 22-91). John Wiley and Sons, 1988, p. 371-383.

Dullemond, C. P.; Dominik, C., 2005, A&A., Volume 434, Issue 3, pp.971-986.

Dullemond, C. P.; Natta, A.; Testi, L., 2006, ApJ., Volume 645, Issue 1, pp. L69-L72.

Gaudi, B. Scott; Seager, S.; Mallen-Ornelas, Gabriela, 2005, ApJ., Volume 623, Issue 1, pp. 472-481.

Geballe, T. R.; Knapp, G. R.; Leggett, S. K.; Fan, X.; Golimowski, D. A.; Anderson, S.; Brinkmann, J.; Csabai, I.; Gunn, J. E.; Hawley, S. L.; and 19 coauthors, 2002, ApJ., Volume 564, Issue 1, pp. 466-481.

Goldreich, Peter; Keeley, Douglas A.; Kwan, John Y., 1973, ApJ., Vol. 182, pp. 55-66.

Goldreich, Peter; Lithwick, Yoram; Sari, Re'em, 2004, ARA&A., vol. 42, Issue 1, pp.549-601.

Gould, A.; Udalski, A.; An, D.; Bennett, D. P.; Zhou, A.-Y.; Dong, S.; Rattenbury, N. J.; Gaudi, B. S.; Yock, P. C. M.; Bond, I. A.; and 26 coauthors, 2006, ApJ., Volume 644, Issue 1, pp. L37-L40.

Greaves, J. S.; Holland, W. S.; Moriarty-Schieven, G.; Jenness, T.; Dent, W. R. F.; Zuckerman, B.; McCarthy, C.; Webb, R. A.; Butner, H. M.; Gear, W. K.; Walker, H. J., 1998, ApJ., Volume 506, Issue 2, pp. L133-L137.

Grether, Daniel; Lineweaver, Charles H., 2006, ApJ., Volume 640, Issue 2, pp. 1051-1062.

Guillot, T.; Gladman, B., *Disks, Planetesimals, and Planets*, ASP Conference Proceedings, Vol. 219, 2000, Edited by F. Garzón, C. Eiroa, D. de Winter, and T. J. Mahoney. Astronomical Society of the Pacific, ISBN 1-58381-051-X, 2000, p.475.

Hawley, Suzanne L.; Covey, Kevin R.; Knapp, Gillian R.; Golimowski, David A.; Fan, Xiaohui; Anderson, Scott F.; Gunn, James E.; Harris, Hugh C.; Ivezić, Željko; Long, Gary M.; and 22 coauthors, 2002, AJ, Volume 123, Issue 6, pp. 3409-3427.

Hayashi, C., *Fundamental problems in the theory of stellar evolution*; Proceedings of the Symposium, Kyoto, Japan, July 22-25, 1980. (A82-34012 16-90) Dordrecht, D. Reidel Publishing Co., 1981, p. 113-126; Discussion, p. 127, 128.

Holland, W. S.; Greaves, J. S.; Zuckerman, B.; Webb, R. A.; McCarthy, C.; Coulson, I. M.; Walther, D. M.; Dent, W. R. F.; Gear, W. K.; Robson, I., 1998, Nature, 392, 788-790.

Holland, W. S.; Greaves, J. S.; Dent, W. R. F.; Wyatt, M. C.; Zuckerman, B.; Webb, R. A.; McCarthy, C.; Coulson, I. M.; Robson, E. I.; Gear, W. K., 2003, ApJ., Volume 582, Issue 2, pp. 1141-1146.

Holman, M.; Touma, J.; Tremaine, S., 1997, DPS meeting #29, #28.05; Bulletin of the American Astronomical Society, Vol. 29, p.1025.

Joergens, V, 2006, A&A., Volume 448, Issue 2, March III 2006, pp.655-663.

J. H. Jeans. *The part played by rotation in cosmic evolution,* 1917, MNRAS, 77:186-199.

Jones, Hugh R. A.; Tsuji, Takashi, 1997, ApJ-Lett., v.480, p.L39.

Kenyon, Scott J.; Bromley, Benjamin C., 2002, ApJ., Volume 577, Issue 1, pp. L35-L38.

Kirkpatrick, J. Davy; Allard, France; Bida, Tom; Zuckerman, Ben; Becklin, E. E.; Chabrier, Gilles; Baraffe, Isabelle, 1999, ApJ., Volume 519, Issue 2, pp. 834-843.

Kirkpatrick, J. Davy; Reid, I. Neill; Liebert, James; Gizis, John E.; Burgasser, Adam J.; Monet, David G.; Dahn, Conard C.; Nelson, Brant; Williams, Rik J., 2000, AJ., Volume 120, Issue 1, pp. 447-472.

Köhler, R.; Kunkel, M.; Leinert, C.; Zinnecker, H., 2000, A&A., v.356, p.541-558.

Krist, John E.; Ardila, D. R.; Golimowski, D. A.; Clampin, M.; Ford, H. C.; Illingworth, G. D.; Hartig, G. F.; Bartko, F.; Benítez, N.; Blakeslee, J. P.; and 31 coauthors, 2005, AJ., Volume 129, Issue 2, pp. 1008-1017.

Kumar, Shiv Sharan, Thesis (Ph.D.), University of Michigan, 1962. Source: Dissertation Abstracts International, Volume: 23-01, page: 0023.

Kumar, Shiv S., 1963, ApJ., vol. 137, p.1121.

Labeyrie, A., 1996, A&AS., v.118, p.517-524.

Lagrange, A.-M.; Backman, D. E.; Artymowicz, P., 2000, **Protostars and Planets IV** (Tucson: University of Arizona Press; eds Mannings, V., Boss, A.P., Russell, S. S.), p. 639.

Laplace, Pierre; *Exposition du Sisteme du Monde* Paris. Imprimiere Cercle-Social,1796.

Laughlin, Gregory; Adams, Fred C, 1998, ApJ., Volume 508, Issue 2, pp. L171-L174.

Léger, A.; Mariotti, J. M.; Puget, J. L.; Rouan, D.; Schneider, J., *Circumstellar Habitable Zones*, Proceedings of The First International Conference. Edited by Laurance R. Doyle. Menlo Park, CA: Travis House Publications, 1996., p.265.

Lenzen, Rainer; Close, Laird; Brandner, Wolfgang; Hartung, Markus; Biller, Beth, *Science with Adaptive Optics*, Proceedings of the ESO Workshop Held at Garching, Germany, 16-19 September 2003. Edited by W. Brandner and M. E. Kasper. 387 p. Library of Congress Catalog Card No. 200592215. ISBN: 3-540-25034-4. Published by Springer, Berlin 2005, p.46.

Lovelock, J. 1975, Proc. Roy. Soc. London, B 189, 167.

Low, C.; Lynden-Bell, D., 1976, MNRAS, vol. 176, p. 367-390.

Marcy, Geoffrey W.; Butler, R. Paul, 2000, PASP., Volume 112, Issue 768, pp. 137-140.

Marcy, G.; Butler, R. P.; Fischer, D.; Vogt, S.; Wright, J. T.; Tinney, C. G.; Jones, H. R. A., Progress of Theoretical Physics Supplement, No. 158, pp. 24-42.

Marois, Christian; Doyon, René; Nadeau, Daniel; Racine, René; Riopel, Martin; Vallée, Philippe; Lafrenière, David, 2005, PASP., Volume 117, Issue 833, pp. 745-756.

Martín, Eduardo L.; Delfosse, Xavier; Basri, Gibor; Goldman, Bertrand; Forveille, Thierry; Zapatero Osorio, Maria Rosa, 1999, AJ., Volume 118, Issue 5, pp. 2466-2482.

Martín, E. L.; Brandner, W.; Bouvier, J.; Luhman, K. L.; Stauffer, J.; Basri, G.; Zapatero Osorio, M. R.; Barrado y Navascués, D., 2000, ApJ., Volume 543, Issue 1, pp. 299-312.

Marzari, F.; Weidenschilling, S. J., 2002, Icarus, Volume 156, Issue 2, pp. 570-579.

Mayor, M.; Queloz, D., 1995, Nature V.378, NO.6555/NOV23, P. 355.

Montañés-Rodriguez, P.; Pallé, E.; Goode, P. R.; Hickey, J.; Koonin, S. E., 2005, ApJ., Volume 629, Issue 2, pp. 1175-1182.

Mouillet, D.; Larwood, J. D.; Papaloizou, J. C. B.; Lagrange, A. M., 1997, MNRAS., vol. 292, p. 896.

Mouillet, D.; Lagrange, A. M.; Augereau, J. C.; Ménard, F., 2001, A&A., v.372, p.L61-L64.

Nakajima, T.; Oppenheimer, B. R.; Kulkarni, S. R.; Golimowski, D. A.; Matthews, K.; Durrance, S. T., 1995, Nature V.378, NO.6556/NOV30, P. 463.

Natta A., Testi L., Calvet N., Henning Th., Waters R., Wilner D., ***astro-ph/0602041*** (Protostars and Planets V, in press).

Neuhäuser, R.; Brandner, W.; Alves, J.; Joergens, V.; Comerón, F., 2002, A&A., v.384, p.999-1011.

Neuhäuser, R.; Guenther, E. W.; Wuchterl, G.; Mugrauer, M.; Bedalov, A.; Hauschildt, P. H., 2005, A&A., Volume 435, Issue 1, pp.L13-L16.

Oppenheimer, B. R.; Kulkarni, S. R.; Matthews, K.; Nakajima, T., SCIENCE V.270, NO. 5241/DEC1, P.1478, 1995.

Owen, T. 1980, in Proc., **Strategies for the search for life in the universe**, ed. M. Papagiannis (Reidel), 177.

Perryman M., Hainaut O., Dravins D., Leger A., Quirrenbach A., Rauer H., Kerber F., Fosbury R., Bouchy F., Favata F., Fridlund M., Gilmozzi R., Lagrange A-M., Mazeh T., Rouan D., Udry S., Wambsganss J., ***astro-ph/0506163*** (ESA-ESO Working Groups Report No. 1, A printed version (A5 booklet) is available in limited numbers from Space Telescope-European Coordinating Facility (ST-ECF) on request: stdesk@eso.org).

Pollack, James B.; Hubickyj, Olenka; Bodenheimer, Peter; Lissauer, Jack J.; Podolak, Morris; Greenzweig, Yuval, 1996, Icarus, Volume 124, Issue 1, pp. 62-85.

Quirrenbach, Andreas; Henning, Thomas; Queloz, Didier; Albrecht, Simon; Bakker, Eric J.; Baumeister, Harald; Bizenberger, Peter; Bleuler, Hannes; Dandliker, Rene; de Jong, Jeroen A.; and 24 coauthors, *New Frontiers in Stellar Interferometry*, Proceedings of SPIE Volume 5491. Edited by Wesley A. Traub. Bellingham, WA: The International Society for Optical Engineering, 2004.

Rebolo, R.; Zapatero-Osorio, M. R.; Martin, E. L, 1995, Nature V.377, NO.6545/SEP14, P. 129.

Schneider, G., 2001, American Astronomical Society, 198th AAS Meeting, #83.01; Bulletin of the American Astronomical Society, Vol. 33, p.911.

Shu, Frank H, 1987, ApJ, Part 1 (ISSN 0004-637X), vol. 316, May 15, 1987, p. 502-504.

Sozzetti, A., 2004, MNRAS., Volume 354, Issue 4, pp. 1194-1200.

Stauffer, John R.; Hamilton, Donald; Probst, Ronald G., 1994, AJ., vol. 108, no. 1, p. 155-159.

Stepinski, T. F.; Black, D. C, 2000, A&A., v.356, p.903-912.

Sudarsky, David; Burrows, Adam; Pinto, Philip, 2000, ApJ., Volume 538, Issue 2, pp. 885-903.

Sudarsky, David; Burrows, Adam; Hubeny, Ivan, 2003, ApJ., Volume 588, Issue 2, pp. 1121-1148.

Tinetti, Giovanna; Rashby, Sky; Yung, Yuk L., 2006, ApJ., Volume 644, Issue 2, pp. L129-L132.

Tokunaga, A. T.; Kobayashi, N., 1999, AJ.,Volume 117, Issue 2, pp. 1010-1013.

Trilling, D. E.; Benz, W.; Guillot, T.; Lunine, J. I.; Hubbard, W. B.; Burrows, A, 1998, ApJ., v.500, p.428.

Udalski, A.; Jaroszyński, M.; Paczyński, B.; Kubiak, M.; Szymański, M. K.; Soszyński, I.; Pietrzyński, G.; Ulaczyk, K.; Szewczyk, O.; Wyrzykowski, Ł.; and 23 coauthors, 2005, ApJ., Volume 628, Issue 2, pp. L109-L112.

Udry, S.; Mayor, M.; Santos, N. C., 2003, A&A., v.407, p.369-376.

Vidal-Madjar, A.; Lecavelier des Etangs, A.; Désert, J.-M.; Ballester, G. E.; Ferlet, R.; Hébrard, G.; Mayor, M., 2003, Nature, Volume 422, Issue 6928, pp. 143-146.

Ward, William R.; Hourigan, Kerry, 1989, ApJ, Part 1 (ISSN 0004-637X), vol. 347, p. 490-495.

Weidenschilling, S. J.; Marzari, F., 1996, DPS meeting #28, #12.14; Bulletin of the American Astronomical Society, Vol. 28, p.1113.

Wetherill, George W., AREPS, Volume 18 (A91-15219 04-46), Annual Reviews, Inc., 1990, p. 205-256.

Wolszczan, A.; Frail, D. A., 1992, Nature (ISSN 0028-0836), vol. 355, Jan. 9, p. 145-147.

Woolf, N. J.; Smith, P. S.; Traub, W. A.; Jucks, K. W., 2002, ApJ., Volume 574, Issue 1, pp. 430-433.

# 2 Detecting extrasolar planets

The most obvious extrasolar planet detection is its imaging close to the parent star; even beyond, the detection of details on its disk might provide the most exciting information about the physical status on its surface. Unfortunately, both these prospects i.e. the image of point source representing the light of a planet and the planet surface imaging, are far to be considered standard techniques in Astronomy today.

The direct detection era started with the observation of planets 2M1207 b (cfr. Chauvin et al. 2004), GQ Lup b (cfr. Neuhäuser et al. 2005) and AB Pictoris b (cfr. Chauvin et al. 2005). These works have to be considered the first pioneering efforts trying to collect separately the light of a planet from to the one of the parent star. Additionally, the observations with Spitzer/MIPS[5] of HD 209458 b (Deming et al. 2005) and with Spitzer/IRAC of TrES-1 (Charbonneau et al. 2005), during the planet Eclipse phase allowed a direct photometric measure of planetary fluxes and then the first inference on the effective temperatures of planetary atmospheres. These detections were possible thanks to intrinsic properties of these planetary systems: for example the high star vs. planet separation (~54 AU) and the small star vs. planet Luminosity ratio of 2M1207 b (equal to $10^{1.85}$, following the model of Chabrier et al. 2000, or equal to $10^{1.88}$, following the one of Baraffe et al. 2002) or the significant IR emission of HD 209458 b - the underlying detection techniques won the challenge of the direct imaging. However, these spectacular measures were obtained pushing to extreme the possibilities of the adopted instrumentations. Direct detection remains a challenge because of physical characteristics of planets (Luminosity Contrast, Separation etc.) that make it extremely difficult. This is why direct methods represent an entire new chapter of planets finding. On the other hand, most of the ongoing adopted techniques are based on detection of a perturbation into standard observables obtained from the light of the candidate star induced by the planet presence (see Sections 2.1, 2.2 and 2.3 for a description of the more used among these latter).

The challenge of direct detection is well represented in terms of star vs. planet Luminosity ratio (hereafter indicated as Contrast[6] and/or **C**). If we consider our Solar System as the reference for this quantity, a set of basic conclusions arise from this analysis. The first is that - as a whole - the star vs. planet Contrast in general is enormous, as indicated in Figure 2-1 (**C**=$10^9$ in the VISible and NIR domains for of a Jupiter-like planet, while is **C**=$10^{10}$ in the VISible and NIR domains in the case of an Earth-like planet). The second is that contrary to the standard black-body shape of the star continuum, old bodies - like the planets inside our Solar System - are dominated by two distinct contributions in the continuum of their spectrum: a black-body contribution in the FIR, and the reflected light contribution in the VISible and NIR. This last depends on the characteristics of the spectral albedo, which in turn depends on physical and chemical parameters of the planet atmosphere (effective temperature, pressure, chemical composition, cloud pattern, aerosol pattern, etc.). The third is that departures from black-body in the spectrum of a planet are important even when the spectral resolution (**R**) is very low. Contrary, the spectrum of a solar type star is dominated

[5] For the definition of all the abbreviations adopted in this Section see the opening list.

[6] Throughout this Dissertation, both scalar and vector variables appearing in the text body are specified using boldface font types. If "vector" is not explicitly specified, a quantity appearing in the text body is to be thought as a scalar. In equations, however, scalars and vectors are indicated as it is customary.

by the pattern of its continuum and not by differential absorption lines that are detectable only when **R** gets much higher values. The fourth and final conclusion is that the near-infrared flux from a planet could be a powerful tool for both the two big goals of planets finding i.e. direct detection and characterization of the physical parameters. Indeed - as Figure 2-1 shows - the spectra of planets with atmospheres are dominated by broad absorption features in the VISible and NIR domains. These features are exploited by the direct detection technique named SDI (see Section 3 for a detailed description of this technique) and the brand new S-SDI technique explained in details is this Dissertation (starting from Section 3.5). Moreover - as Figure 2-2 shows - at higher spectral resolution a lot of features due to different molecular flavors might be detected in the spectrum of a planet atmosphere. These ones might represent the door towards the spectral characterization of the extrasolar planets that future space-based instruments like TPF-C (cfr. Traub et al. 2006) or ground-based instrument like the one described in this Dissertation - EPICS (see Section 7) - will try to open in the next future.

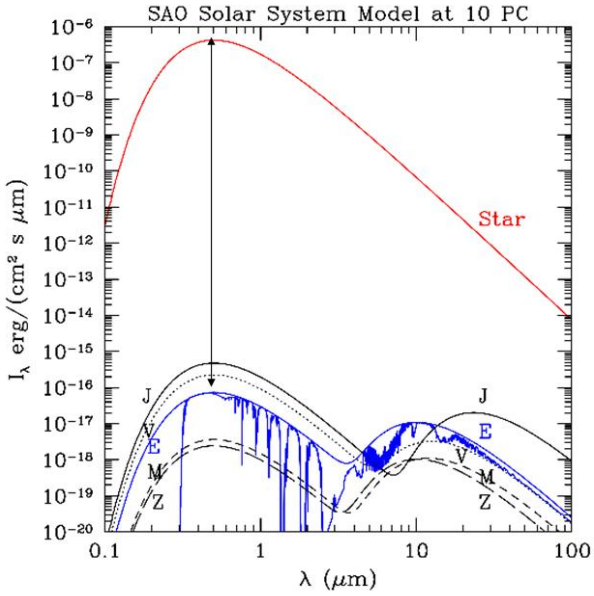


**Figure 2-1: Comparison between the flux emitted by the Sun (a G2V star) and those coming from the planets of the Solar System (J=Jupiter, V=Venus, E=Earth, M=Mars). Z represents the spectral distribution of the zodiacal light. The two peaks in the VIS-NIR-MIR correspond to the maxima of reflected light and intrinsic emission respectively (from Vérinaud et al. 2006).**

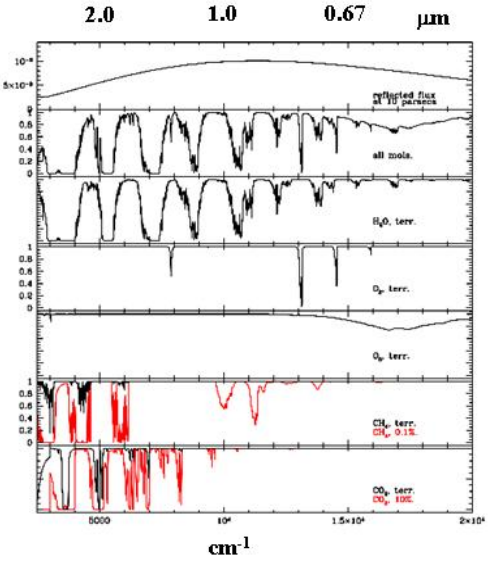


**Figure 2-2: Main features in the VISible-Near IR spectra of the most important molecules expected to be present in planetary atmospheres ($H_2O$, $O_2$, $O_3$, $CH_4$, $CO_2$, $N_2O$), from Traub and Jucks (2002) and Des Marais et al. (2002).**

By now, all detections of extrasolar planetary systems - except for the few ones cited before - derive from the achievement of a handful of observational techniques by which Astronomers were able to infer - via in-direct conclusions - the presence of planet/s in the proximity of the hosting star. These techniques exploit different features like the dynamical perturbation of the star e.g. the Radial Velocity Variation, the Astrometric Perturbation and the Timing Delay (see Sections 2.1.1, 2.1.2 and 2.1.3 respectively), the Transit technique (see Section 2.2) or the perturbation of the space-temporal metric close to the star induced by a planet (e.g. the Gravitational Microlensing technique, see Section 2.3). Actually, this handful of in-direct techniques belongs to the rich detection techniques ensemble that Perryman collected and differentiated carefully through distinct methods in his *Planets Detection Tree* (see Figure 2-3).

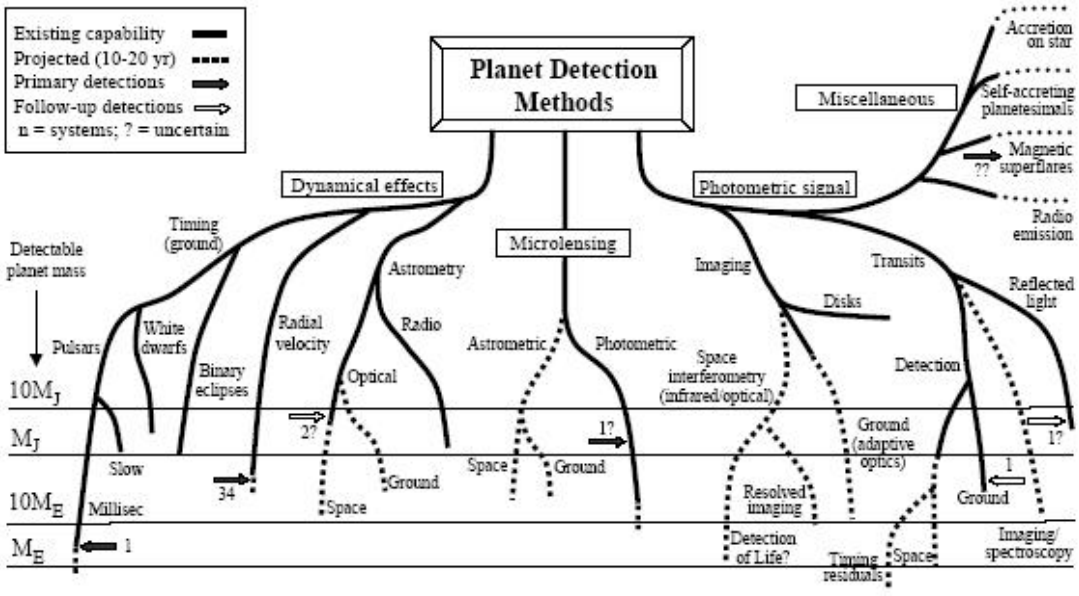

**Figure 2-3: Detection methods for extrasolar planets. The lower extent of the lines indicates, roughly, the detectable masses that are in principle within reach of present measurements (solid lines), and those that might be expected within the next 10-20 [yr] (dashed). The (logarithmic) mass scale is shown at left. The miscellaneous signatures to the upper right are less well quantified in mass terms. Solid arrows indicate (original) detections according to approximate mass, while open arrows indicate further measurements of previously-detected systems. '?' indicates uncertain or unconfirmed detections (cfr. Perryman 2000)[7].**

## 2.1 Dynamical perturbation of the star

The motion of a planet in orbit around a star causes the star to move around the star-planet barycentre, with orbital semi-major axis $\mathbf{a_S}$:

$$a_S = a \cdot \left( \frac{M_P}{M_S} \right) \qquad \textbf{Equation 2-1}$$

and orbital period **P**.

This feature produces a periodic perturbation of three observables: the Radial Velocity of the star along the line of sight of the observer, the Astrometric Perturbation in the sky plane orthogonal to the line of sight of the observer and the Timing Delay of a periodic reference signal.

### 2.1.1 The Radial Velocity technique

The semi-amplitude **K** of the Radial Velocity variation along the line of sight of the observer of a star of mass $\mathbf{M_S}$ due to a companion with mass $\mathbf{M_P \cdot sin\ (i)}$ with orbital period **P** and eccentricity **e** is given by:

$$K = \left( \frac{2\pi \cdot G}{P} \right)^{\frac{1}{3}} \cdot \frac{M_P \cdot \sin(i)}{(M_P + M_S)^{\frac{2}{3}}} \cdot \frac{1}{(1 - e^2)^{\frac{1}{2}}} \qquad \textbf{Equation 2-2}$$

where **(i)** is the orbital inclination angle between the normal to the orbital plane and the line of sight (see Figure 2-4) and **G** is the Newton's constant. On the other hand, by the Kepler's third law, the orbital period may be expressed as:

$$P = \left( \frac{4\pi^2 \cdot a^3}{G \cdot (M_P + M_S)} \right)^{\frac{1}{2}} \qquad \textbf{Equation 2-3}$$

where **a** is the semi-major axis of the companion orbit. Then, the semi-amplitude **K** of the Radial Velocity variation along the line of sight of the observer can be given in term of only **a**, **e**, $\mathbf{M_S}$ and the companion Minimum Mass: $\mathbf{M_P sin\ (i)}$ merging Equations 2-2 and 2-3. Considering a circular orbit (i.e. **e**=0) seen edge-on (i.e. **i**=90 [deg]), Equation 2-2 becomes:

$$K = M_P \cdot \left( \frac{G}{a \cdot (M_P + M_S)} \right)^{\frac{1}{2}} \qquad \textbf{Equation 2-4}$$

[7] Notice that Figure 2-3 was drawn a few years ago; in the mean time, much more detections were obtained through various techniques. Moreover, the same Figure takes no account of the numbers of planets that may be detectable by each method.

where of course, in the case of planets $\mathbf{M_P << M_S}$.

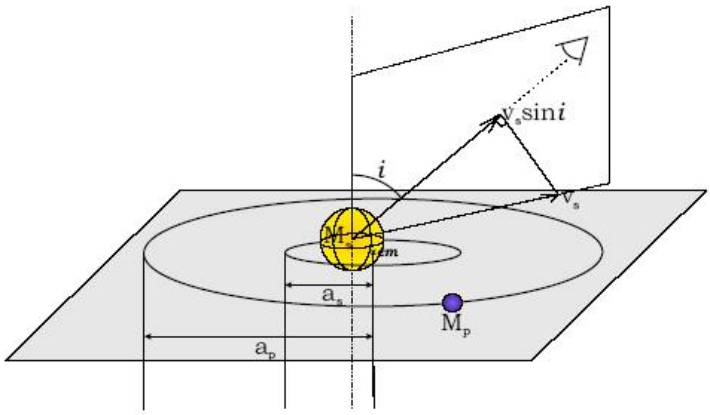


**Figure 2-4: Orbital parameters of a planet-star system. In this Figure, the star (s) and the planet (p) are assumed to be in circular orbit around the center of mass (cm) of the system (more in general, the orbit would be elliptical). The orbital radii are $a_s$ for the star and $a_p$ for the planet. These are plotted along the orbital plane. The orbital inclination angle (i) between the normal to the orbital plane and the line of sight determines the orbital inclination angle. The Radial Velocity $V_s$ of the star as measured along the line of sight (from the upper right in the diagram) depends on the sine of the orbital inclination angle.**

It helps to give an idea about the magnitude of **K** in our Solar system: **K**=12.5 [m·sec$^{-1}$] for the case of Jupiter if the orbit would be seen edge-on. Since the Radial Velocity variation increases with planet mass and decrease with semi-major axis (roughly with the square root), giant planets of few Jupiter masses in close-in orbits (i.e. smaller than 1 AU) are easy to be measured. An example of detection of a planet using this technique is shown in Figure 2-5, where the Radial Velocity variation of 51 Pegasi is clearly visible (notice that the observations shown here are not those which provided the first detection of 51 Pegasi by Mayor and Queloz 1995).

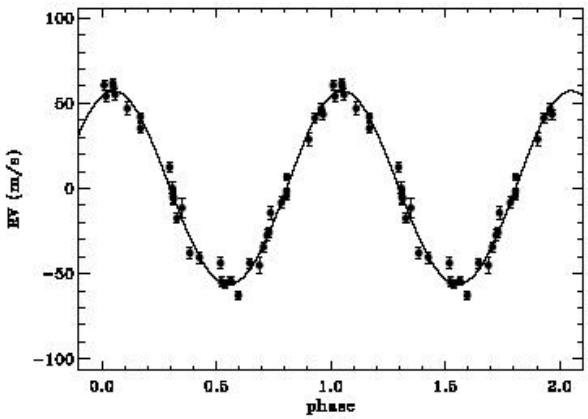


**Figure 2-5: Radial Velocity signal of the star 51 Pegasi as measured with SARG.**

By the equations above one can easily deduce the limits of this detection technique. The first limit depends purely on geometry, i.e. planets are not visible in the case of zero orbital inclination (i.e. orbits seen edge-on). The second is that planet with larger masses are more easily detectable than others. The third is that the amplitude of the Radial Velocity variation

depends on the orbital parameters (e.g. when **P** is large - and then by the third Kepler's law the semi-major axis is large - or when **e** is large). Considering all these limitations, it is clear the extrasolar planets population detectable by Radial Velocity measurements is biased towards those with the highest masses and the closest orbits.

Almost all extrasolar planets around normal main sequence stars discovered insofar have been detected with this technique. In order to detect the planetary signal, accuracies of around 15 [m·sec$^{-1}$] or better are needed. If we express these Radial Velocity variations in term of light velocity, we see that wavelength measures accurate to 1 part over 20 millions - or better - are required. This is challenging because stars are only faint sources of light, so that large telescope and long integration time are needed for acquisition of the required high signal-to-noise high-resolution spectra. Furthermore, various instrumental effects, like inaccurate centering of the star images on the spectrograph entrance aperture or temperature and pressure variations within the spectrograph, may easily introduce systematic spectrum shifts comparable to or larger than the planet signal. This is why very accurate instrumental and wavelength calibrations are demanded. Typically, spectrograph with spectral resolution of around **R**=60000 are operated in the VISible region (450-700 [nm]) using two different techniques in order to maintain the instrument extremely stable with time. The first is the Iodine Cell technique (cfr. Marcy and Butler 1992), exploited for example in the SARG instrument at TNG (cfr. Gratton et al. 2001, see Figure 2-5). The second is the Fiber-Fed technique adopted for instruments like Elodie at OHP (cfr. Baranne et al. 1996) and Coralie and HARPS at ESO-la Silla (cfr. Queloz et al. 2000 and Pepe et al. 2000). This latter technique revealed as the most successful in achieving accuracies even below 1 [m·sec$^{-1}$] (cfr. Mayor et al. 2003). Results of similar accuracy have been also obtained with the Iodine Cell technique; however the efficiency of the Fiber-Fed technique is potentially higher. Ultimately, the accuracy of the Radial Velocity variations is limited by the Signal-to-Noise ratio (hereafter **S/N**) of the spectra - ideally the errors given by the Poisson statistic of the photons detected by the CCD - and by intrinsic characteristics of the stellar spectrum like number, depth and width of the spectral lines (see. Bouchy et al. 2001 for an in-depth discussion). Solar type stars are optimal for planet detection from Radial Velocities, because lines are too broad in (generally rapidly rotating) early-type stars, and small-mass stars are generally too faint for high **S/N** observations. The natural limit imposed by photons statistics can be achieved by adequate modeling of the procedures of Radial Velocity measurements in stellar spectra. Radial velocity accuracies in the range 3-1 [m·sec$^{-1}$] imply - in the case of circular orbit and edge-on geometry - detection limits in the range 0.01-0.1 $M_{JUPITER}$ - depending on the orbital period -. On the other hand detection of an Earth-like planet in the Habitable Zone[8] (see Figure 2-6) would require accuracies of 0.03 [m·sec$^{-1}$]. Unluckily, what is actually measured by this technique is not the Radial Velocity of the stellar barycentre, but rather the average velocity of the stellar photosphere. The offset of these two velocities is not exactly constant; this difference is called *Jitter*. The Jitter of the star is due to different causes including convective motions in the stellar photospheres, activity, etc. The Radial Velocity variations related to Jitters have typical amplitudes from a few up to tens [m·sec$^{-1}$], and timescales from hours to months. Larger values are found for low-gravity and young stars. Furthermore oscillations are also presents, again with amplitudes that can be as large as 0.3 [m·sec$^{-1}$] for solar-type stars (on timescales of minutes), and of tens of [m·sec$^{-1}$] for low-gravity stars, on weeks to month timescales. The Jitter phenomenon - has a whole - limits the accuracy of the determination of the star barycentre to a few meter per·second,

[8] Habitable Zone is a region of space around a star where conditions are favourable for the creation of life (cfr. http://en.wikipedia.org/wiki/Habitable_zone)

typically. Observations from space will not improve these limits and no high-precision Radial Velocity measurements from space have been proposed up to now. With HARPS, an individual measurements precision of about 0.5 [m·sec$^{-1}$] is reached, as illustrated by asteroseismology results on μ Arae with 250 observations each (cfr. Perryman et al. 2005). A strategy considering many Radial Velocities measures over a suitable timescale could considerably lower the threshold for detection of extrasolar planets using the Radial Velocity technique. However, such a technique is very costly in terms of telescope time. The possibility of having a reference threshold of about 0.02 [m·sec$^{-1}$] for the Radial Velocity amplitude variation suggests that follow up Radial Velocity programs should be considered for new technology Earth-like planet finders like the space-based TPF-C.

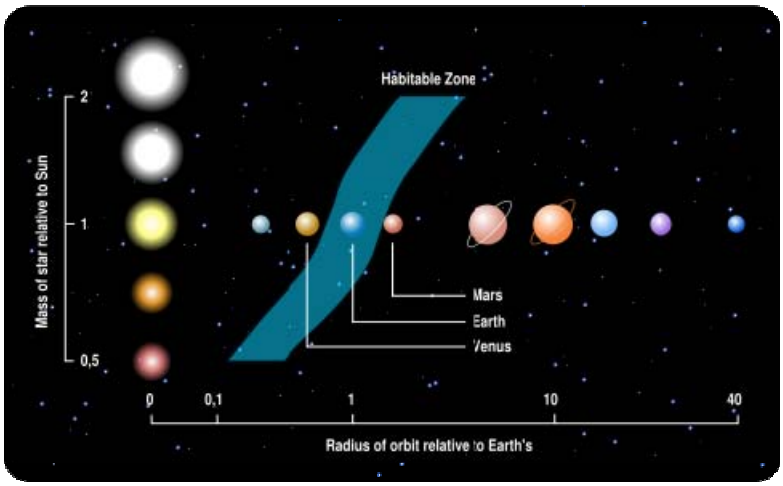


**Figure 2-6: Habitable Zone distance and width vs. mass of the hosting star expressed in $M_{SUN}$ unit.**

### 2.1.2 The Astrometric Perturbation technique

The path of a star orbiting the star-planet barycentre appears projected on the plane of the sky as an ellipse with angular semi-major orbital axis $\alpha$:

$$\alpha = \left(\frac{M_P}{M_S}\right) \cdot \left(\frac{a}{d}\right) \qquad \textbf{Equation 2-5}$$

where $\alpha$ is in arcsec, **a** is in AU**,** the distance of the star from the Sun **d** is in pc, $\mathbf{M_P}$ and $\mathbf{M_S}$ are in the same units. This angular signature is therefore proportional to both planet mass and orbital radius, and inversely proportional to the distance of the star from the Sun. The aim of the Astrometric Perturbation technique is to measure the photocentric displacement of the star in the plane orthogonal to the line of sight of the observer. For comparison, the motion of the Sun around the barycentre of the Solar System viewed from a distance of 10 pc, produce a maximum angular displacement of 500 [microarcsec], while the effect due to the Earth when seen from the same distance is 0.3 [microarcsec]. Even in favourable cases, the Astrometric accuracy required to detect planets through this reflex motion therefore lies in the microarcsec scale as Figure 2-7 clearly shows.

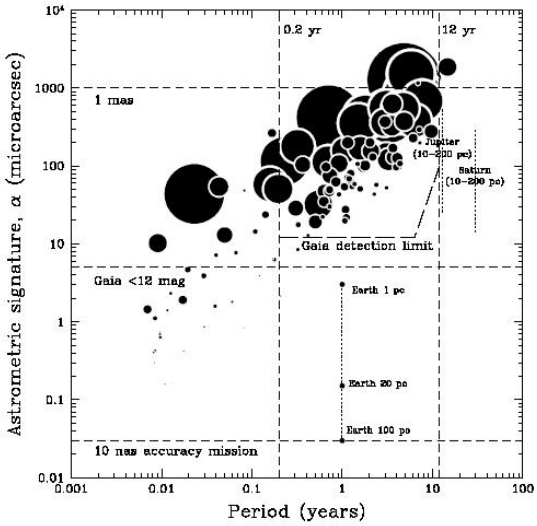


**Figure 2-7: Astrometry Variation (α) induced on the parent star for the known planetary systems, as a function of orbital period. Circles are shown with a radius proportional to $M_P \cdot \sin(i)$. Astrometry at the milliarcsec level has negligible power in detecting these systems, while the situation changes dramatically for microarcsec measurements. Effects of Earth, Jupiter, and Saturn are shown at the distances indicated. The Gaia detection limit is also shown, from ESA/ESO report on extrasolar planets: Perryman et al. (2005).**

The Astrometric Perturbation technique is particularly sensitive to planets on orbits with relatively long semi-major orbital axis, and then - according the third Kepler's law - to relatively long orbital periods (**P**>1 [yr]). Hence, this technique is complementary with respect to the Radial Velocity one. Moreover the method is applicable to stars with rapid rotation or with magnetic activity in their atmospheres, for which the Radial Velocity technique can produce false alarms. If **a** is known from spectroscopic measurements, **d** from the star parallax, $\mathbf{M_S}$ by the spectral type or from evolutionary models, the Astrometric Perturbation allows to obtain $\mathbf{M_P}$ directly. Additionally, if combined with available Radial Velocity measures, this technique allows deriving all the planet orbital parameters too. On this subject, remarkable are the observations conducted by Benedict et al. (2002) in which they exploited the HST Fine Guiding System for Astrometric measures in combination with the measures obtained by the Radial Velocity technique for the planet orbiting Gliese 876. These efforts led to measure the mass of ε Eridani b (1.55± 0.24 $M_{JUPITER}$) and the inclination angle of its orbital plane (**i**=30.1 ± 3.8 [deg]) by Benedict et al. (2006).

However, Astrometric detection demands very accurate positional measurements within a well-defined reference system at different epochs. This represents still an enormous difficulty on non AO-assisted ground based instruments - due to the atmospheric optical phase fluctuation - and is challenging even for space based instruments. Up to now, only a single instrument obtained a sound Astrometric catalogue (~120000 stars) at milliarcsec accuracy i.e. Hipparcos (cfr. Perryman et al. 1997). Measurements of microarcsec displacements are the targets of the new class of Astrometric instruments, both ground and space based. As for the case of ε Eridani b, this technological goal in combination with spectroscopic measurements should provide the direct determination of the planets mass, in a way independent to the orbital inclination up to Earth-size objects. Finally, if a significant fraction of the orbit is known or data could be combined with Radial Velocity measurements, the relative orbital inclinations of multi-planets system could be determined. The microarcsec accuracy together with the potential capability to make spectroscopy for low mass companions could be reached in a shorter time at ESO-Paranal within the VLTI

programme thanks to the PRIMA interferometric beams combiner (cfr. Quirrenbach 2004). However, interferometric measurements are quite slow, so that a limited number of stars will be targeted. On the other hand, very extensive data sets can be obtained by space observations programmed for the next decade. Two spatial observatories are planned by ESA and NASA/JPL in order to achieve this goal. They are respectively Gaia and SIM. Gaia is a survey-type instrument, with the launch foreseen for 2012 (Perryman et al. 2001). It will contribute to large-scale systematic detection of Jupiter-like planets up to 150-200 pc from the Earth. The science goals of SIM are focused on a list of target stars, with the aim to find planets down to the Earth mass (Extra-Solar Planet Interferometric Survey). Specifically, this survey will focus on 75 nearby main sequence stars within 10 pc from the Sun, one third of which will be G dwarfs and the remainder are inactive main sequence stars of other spectral types (mostly K an M types). While GAIA is one of the ESA cornerstones, SIM status is still suspended.

### 2.1.3 The Timing Delay technique

Although all orbital motion causes periodic change in the light travel time across the orbit, in general there is no time reference on which to base such measurements. The exception is represented by a peculiar type of evolved stars i.e. the Radio Pulsars. Attempts to exploit the same principle of pulsating white dwarfs (cfr. Mullally et al. 2005) have not been so far successful (see Mullally et al. 2006). Radio Pulsars are Neutron Stars with a strong magnetic field producing a beamed synchrotron emission centered in the direction of their magnetic dipole axis. The misalignment of the spin axis with respect to the magnetic dipole one produces a periodic radio signal on the Earth. Normal Pulsars get spin period of about 1 [sec] while the so-called *Millisecond Pulsars* have periods of about $10^{-3}$ [sec]. This fact produces an extreme accuracy on the frequency of the standard signal. According Wolszczan (1997), when a companion orbits a Millisecond Pulsar, the period of the radio-signal is modulated and - in the case of edge-on and circular orbit of the companion - the variation of the signal temporal period results proportional to the planet mass $\mathbf{M_P}$ and its orbital period **P**. More precisely:

$$\tau_P = 1.2 \cdot \left( \frac{M_P}{M_{EARTH}} \right) \cdot \left( \frac{P}{1\,yr} \right)^{\frac{2}{3}} \qquad \textbf{Equation 2-6}$$

where $\boldsymbol{\tau_P}$ is calculated in [millisecond]. The high accuracy of the Timing Delay technique allowed the detection of the two Earth mass objects around PSR 1257+12 (d~500 pc), which actually was the first detection of extrasolar planets (cfr. Wolszczan and Frail 1992). Continued monitoring of PSR 1257+12 provided evidence of a third companion with **P**=25.34 days (Wolszczan 1994) and a fourth with **P**~170 [yr] (Wolszczan 1997). Additionally, unconfirmed evidence of a companion (**a**=3.3 AU and $\mathbf{M_P \cdot sin(i)}$=1.7 $M_{EARTH}$) around the radio quiet Pulsar Geminga was reported from γ-ray observations by Mattox et al. (1998).

## 2.2 The Transit technique

Detection of extrasolar planets by measuring the photometric signature of the star due to the Transit of a planet is a method conceptually simple that - in the early 1970s - was considered as observationally more feasible than the prospects of detecting Astrometric Perturbation of around 0.0005 [arcsec], or Radial Velocity perturbations of around 10 [m·sec$^{-1}$] (cfr. Perryman 2000).

When a planet transits its parent star, we can accurately measure the orbital inclination (**i**). This allows to evaluate the planetary mass ($\mathbf{M_P}$) directly from the Minimum Mass ($\mathbf{M_P \cdot sin(i)}$) determined from the Radial Velocity technique, once an estimate of the mass of the parent star ($\mathbf{M_S}$) is available. Additionally, the planetary radius ($\mathbf{R_P}$) can be obtained by measuring the fraction of the parent star light that is occulted, once an estimate of the star radius ($\mathbf{R_S}$) is available. Figure 2-8 explains the usual Transit occurrence parameterization.

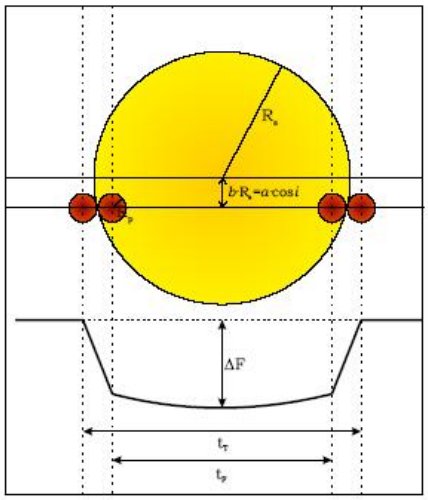


**Figure 2-8: Schematic representation of a transiting planet across the stellar disk. The planet is shown from first to fourth contact. The stellar flux (solid line) diminishes by ΔF during a Transit for a total time of $t_T$ while $t_F$ is the duration between to instants of the Transit called respectively Ingress and Egress. The curvature seen on the light curve during Transit is consequence of the star limb darkening of the stellar disk. The impact parameter (b) is shown also in term of the orbital inclination angle (i) and the orbital semi-major axis (a). Finally the stellar radius is indicated as $R_S$.**

Once the mass and the radius of the planet are known, we can estimate critical physical quantities as the average density and the surface gravity of the planet. Hence, the information obtained from a transiting planet - when all the requested parameters external to the planet are know - allows revealing the structure and the composition for planets detected with the Radial Velocity technique. Up to now[9], 13 planets have been detected both with the Radial Velocity technique and the Transit technique. Among these, only three planets (HD 209458 b, HD 149026 b and HD189733 b) were found before by the Radial Velocity variation. Figure 2-9 shows the Mass vs. Radius relation of 9 planets (from Charbonneau et al. 2006). This set has to be expanded with other 4 planets detected with the Transit

[9] In this Dissertation, the list of detected extrasolar planets is updated up to October 2006.

technique and confirmed via Radial Velocity measures: 2 planets discovered by the Super-WASP survey (cfr. Collier Cameron et al. 2006), a new planet discovered by the TrES survey (TrES-2, cfr. O'Donovan et al. 2006) and the first planet discovered in the HATnet project (HAT-P-1b, cfr. Bakos et al. 2006).

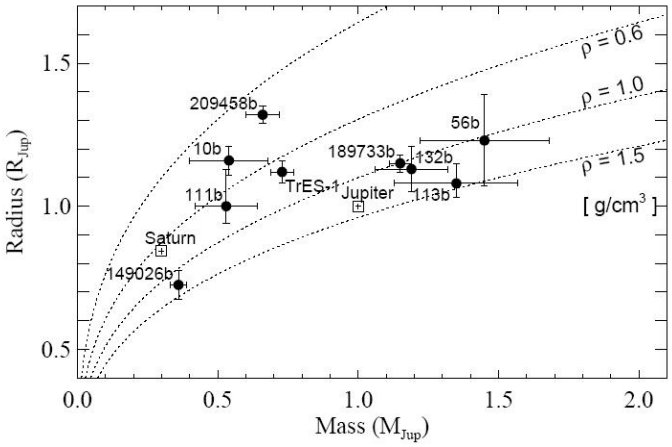


**Figure 2-9: Masses and radii for 9 transiting planets as well as Jupiter and Saturn. Dashed lines represent the radius vs. mass relation parameterized in term of the planets density (ρ), cfr. Charbonneau et al. (2006).**

This Figure indicates big deviations from the predictions for HD 209458 b and HD 149206 b: the first planet has a radius considerably larger than predicted, while the second has a too small radius. These discrepancies suggest that the physical structure of the transiting planets can depend significantly on factors other than radius and planet effective temperature. For example, Guillot and Showman (2002) proposed that a strong insolation-driven weather patterns on HD 209458 b leads to the conversion of kinetic energy into thermal energy at a pressure of tens of bars. This hypothesis predicts that other transiting planets with similar masses and at similar irradiation levels should be similar in size to HD 209458 b. The subsequent discovery of TrES-1 - with a considerably smaller radius despite its similar temperature, mass and parent star metallicity - was a clear evidence against this so-called *kinetic heating hypothesis*. On the other hand, the higher model density obtained for HD 149206 b (see Figure 2-9) suggests that this planets has a major fraction of heavy elements. This fact implies - potentially - interesting ramification for the theory of planets formation. In particular Sato et al (2005) argue that it would be difficult to form this giant planet by the Disk Instability mechanism. The predicted large core (see Figure 2-10) presents difficulties for conventional model of Core Accretion too. Specifically, in this framework it is difficult to prevent runaway gas accretion onto cores more massive than 30 $M_{EARTH}$ as seems to weigh the one of HD 149026 b, cfr. Charbonneau et al (2006).

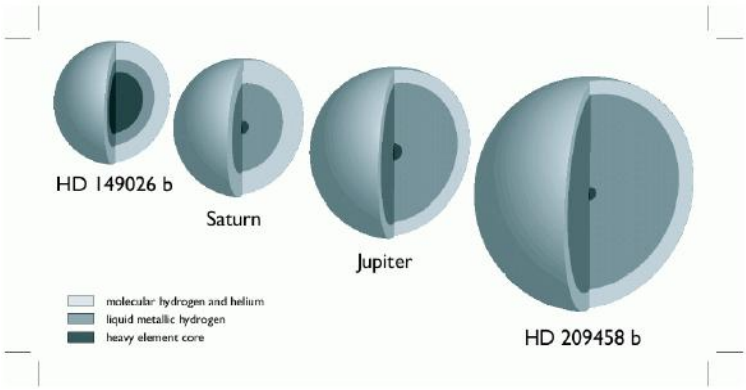


**Figure 2-10: Cut-away diagram of Jupiter, Saturn, the two exotic Hot-Jupiters (HD 209458 b and HD 149026 b) drawn to scale. The observed radius of HD 149026 b implies a massive core of heavy elements making perhaps 70% of the planetary mass. In contrast, the radius of HD 209458 b would indicate a coreless structural model or an additional energy source to explain its large value, cfr. Charbonneau et al. (2006).**

The understanding of the Hot-Jupiters evaporation physics has been improved by Lecavelier des Etangs (2006). In this work a new diagnostic diagram is proposed in order to describe the evaporation status of the extrasolar planets (Hot-Jupiters in particular), where the planet gravitational potential energy is plotted versus the EUV radiative energy received by its parent star (see Figure 2-11).

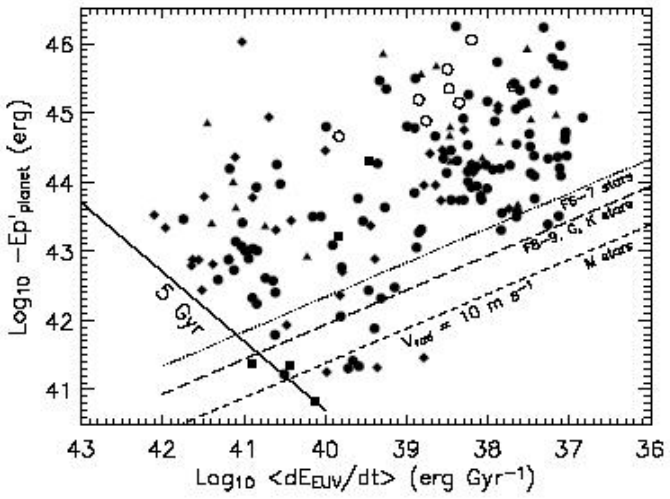


**Figure 2-11: Diagnostic diagram for the evaporation status of extrasolar planets. 182 identified planets are plotted with symbols depending on the spectral type of the central star: triangles for F type, filled circles for G type, diamonds for K type and squares for M type. The absence of planets below the line for which the Radial Velocity signal is lower than 10 [m·sec$^{-1}$] indicates a selection effect. While, the lifetime line at $t_2$=5 [Gyr] shows that there are no detected Hot-Jupiters in this part of the diagram because this is a forbidden evaporation region, cfr. Lecavelier des Etangs (2006).**

The striking result is to have pointed out the absence of Hot-Jupiters with high received EUV flux and small values of gravitational potential energy. More in detail, planets occupying that region of the Lecavalier des Etangs' diagnostic diagram, would receive more EUV energy than needed to fill the potential well of the planet, and evaporate in less than 5 [Gyr].

We can say then that the powerful combination of Radial Velocity and Transit techniques represents a strong advantage even with respect to the incoming direct detection sector of the planets finding research (see Section 2.4 for an overview on this topic). This is just because with direct detection we will be able - for example - to find different planets around a star in one (possibly with the characterization of their atmospheres too), and then we will increase seriously the statistics on the planets and the parent stars, but no information on the single object properties like its radius and its mass will be possible via direct detection techniques. This is why Radial Velocity and Transit techniques will be fundamental even in the next future when Astronomers - hoping routinely - will find planets via direct detection.

In the Transit technique the photometric precision determines the accuracy of the planet radius estimate. In order to have adequate photometrical precision, small telescopes can be used; on the other hand space observations are needful in order to detect planets with radii of the size of our Earth. The Transit probability depends on the planet-star distance and on the relative orientation to the observer. More in detail, a transiting planet should have an orbit oriented so that the observer on the Earth lies near its orbital plane: this one is a rather rare occurrence. Assuming a random orientation of planetary orbit in the statistical ensemble made by all the planetary orbits in the Galaxy, the probability that a planet with orbital semi-major axis (**a**), orbital eccentricity (**e**) and longitude of its periastron (**ϖ**) produces Transits visible from the Earth is:

$$P_{Tr} = 0.0045 \cdot \left(\frac{1\,AU}{a}\right) \cdot \left(\frac{R_P + R_S}{R_{SUN}}\right) \cdot \left[\frac{1 + e \cdot \cos\left(\frac{\pi}{2} - \varpi\right)}{1 - e^2}\right] \qquad \textbf{Equation 2-7}$$

This means that probability is inversely proportional to the orbital semi-major axis. In the case of circular orbit - usually a good approximation for very close orbits - the Transit Probability increases because the last factor in Equation 2-7 reduces to unity. Nevertheless, Transit is an event such rare that the following observing strategy is always requested:

- Time observing should be concentrated on large fields with high stellar concentration.
- Temporal sampling should be as long as possible (in particular, this is mandatory for planets with orbital period longer than few days).

An overall description of the Transit technique needs that the false alarms problem should be mentioned. Most ongoing Transit surveys are plagued by a high rate of candidate systems displaying light-curves that precisely mimic the searched signal, yet are not due to planetary Transits. One can divide the false alarms occurrence in three broad categories. The first is the so-called *astrophysical false positives category*, resulting from eclipse between members of double or multiple-star systems. The second is the instrumental false positive category, due to erroneous photometry, often resulting from leakage of signal between photometric apertures of nearby stars in crowded field. Finally, the third is the so-called *statistical false positives category*, resulting from selecting photometric thresholds overly-permissive that can induce the light-curves search algorithms to find events resulting purely by the photometric fluctuations of the signal due to photon counting statistic, cosmic-rays and Scintillation (cfr. Jenkins et al. 2002). In particular Scintillation - defined as the RMS of the

Intensity signal ($\sigma_I$) - is a phenomenon related purely to our atmosphere, vanishing when we the detector is located on space, as the following formalism[10] indicates:

$$\sigma_\chi^2 = 0.307 \cdot \left(\frac{2\pi}{\lambda}\right)^{\frac{7}{6}} \cdot L_0^{\frac{11}{6}} \cdot C_n^2 \qquad \textbf{Equation 2-8}$$

$$\sigma_I^2 = \exp\left(4\sigma_\chi^2\right) - 1 \qquad \textbf{Equation 2-9}$$

where $\sigma_\chi^2$ is the variance of the Amplitude signal in logarithmic scale, $\lambda$ is the monochromatic wavelength, $L_0$ is the atmospheric turbulence outer scale and $C_n^2$ is the integrated atmospheric turbulence profile. Out of the atmosphere $L_0$ is equal to zero, then Equations 2-8 and 2-9 imply that the Intensity-RMS will be equal to zero too. This is why space-based missions like the CNES/ESA-COROT and the NASA-Kepler can improve drastically the Transit detection up to the Earth-size mass threshold. Finally, for planets very close to the central star, a modulation in the light-curve due to the reflected light - in principle - could be observable. On this subject, the close-in planet hosted by $\tau$ Bootis (semi-major **a**=0.046 AU and $M_P \cdot \sin(i)$=3.89 $M_{JUPITER}$) has been studied by Charbonneau et al. (1999). The periodic phase-dependent (phase here indicates the planet orbital phase) flux ratio of Sobolev (1975) was adopted by the Authors and re-scaled to the planets parameters ($R_P$, **a**, and $\alpha$ i.e. the angle between the star and the observer as seen from the planet.) in order to identify possible secondary temporal frequencies. Anyhow, no pattern - induced by the reflected light - was obtained.

Among the ongoing surveys, the OGLE TRansit survey led to the detection of 5 planets: OGLE-TR-10 b, OGLE-TR-56 b, OGLE-TR-111 b, OGLE-TR-113 b and OGLE-TR-132 b. Other promising surveys are the ones exploiting multi-telescope facilities located in different place of the Earth in order to better monitoring the photometric variation of the candidate stars which increase the probability of detecting a Transit feature. At present, the biggest among these is TrES, with three telescope facilities placed at Palomar, Arizona and Teide Observatories, in order to have a good time-sampling on the light-curves of the target stars. Figure 2-12 shows the Transit of the first planet found in this survey project: TrES-1.

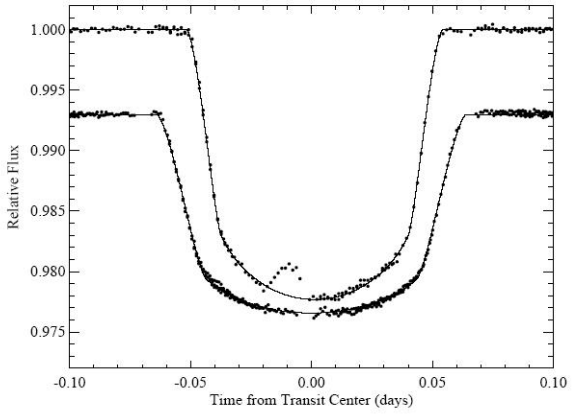


[10] Cfr. **Introduction to Adaptive Optics**, SPIE Tutorial Text in Optical Engineering Vol. TT41.

**Figure 2-12: HST photometric light-curves of the Transit of TrES-1 (top) and HD 209458 b (bottom). The shorter orbital period and the smaller size of the TrES-1 star result in a Transit that is shorter in duration than that of HD 209458 b. Similarly, the smaller star creates a deeper Transit for TrES-1, despite the fact that HD 209458 b gets a larger radius. TrES-1 light-curve shows a light-hump centred a time of -0.01 days from the light-curve minimum. This is likely the result of the planet occulting a star-spot on the stellar surface (cfr, Charbonneau et al. 2006).**

## 2.3 The Gravitational Microlensing

The term Microlensing was introduced by Paczynsky (1986) in order to describe Gravitational Lensing that can be detected by measuring the apparent brightness variation of a star due to the concentrating effect of an intervening massive object. This effect is distinguished from the usual Gravitational Lensing, because different images generated by the lens are too close each other to be separated spatially. Microlensing occurs when stellar mass objects (at typically a few Kpc distance from the Sun) lens the image of another star (the object) at a few times this distance. From this reason, Paczynsky proposed this method to search for dark stellar mass objects in the halo of our Galaxy.

The basics of Gravitational Microlensing lies on the same physics describing the Gravitational Lensing, exploited for example on Cosmology for studying the properties of Universe on the largest scales. Instead, the major differences of the Gravitational Lensing applied to extrasolar planets research are that the lens is a point-mass object - not an extended object like a Cluster of Galaxy - and the lensed object is a point-mass object too. This fact implies - when the object and the lens are perfectly co-aligned with the observer - that the resulting image becomes a ring of radius equal to the Einstein Radius $\mathbf{R_E}$:

$$R_E = \left[ \frac{4G \cdot M_L \cdot (D_S - D_L) \cdot D_L}{c^2 \cdot D_S} \right]^{\frac{1}{2}} \qquad \textbf{Equation 2-10}$$

(**G** is the Newton's constant, **c** is the speed of light, $\mathbf{D_S}$ and $\mathbf{D_L}$ are the distances of the object and the lens to the observer respectively), and the intensity magnification of this ring becomes - theoretically - infinite. While for single lensing objects the Microlensing effect is very simple (a symmetric curve with a single maximum), when the optical lens consists of two or more point-like objects the geometry of the phenomenon becomes more complex. In this case, is possible to define curves in the space where the magnifying effect of the lensing system becomes very large (*caustics*). When the magnified object crosses these curves, the light curve shows various secondary maxima. The position of caustic on the image plane and its shape depend on the planet vs. star mass-ratio ($\mathbf{M_P/M_S}$) and on their projected planet-lens separation ($\mathbf{x_P}$). From this physics it is possible to extrapolate a fundamental observable: the photometric lensing curve, where possible fine structures on the main pattern indicate the presence of small bodies orbiting the principal component of the lens, i.e. the central star. As Figure 2-13 shows, the photometric lensing curve is perfectly symmetric in the case of a single lens object, while it is a-symmetric on the other cases. Moreover, the main effect of a variation of the companion mass is to narrow the secondary maxima of the light curve. Then it is possible to discover planets with small masses in the case of a good sampling of the photometric lensing curve.

The photometric accuracy required by Microlensing is not as critical as for the Transit technique, because the amplitude of the light curve (i.e. the magnification) may be quite large, at least in the most favorable cases. This is the main advantage of the Microlensing technique with respect to the other techniques described above: this latter covers the Earth mass scale safely from ground with the current technology. This means that, when good

statistics will be available - hopefully within ten years - Gravitational Microlensing will give substantial contributions to the extrasolar planets research. However a disadvantage remains: Microlensing is an event that is unlikely to recur for the same system on any relevant timescale (Perryman 2000). Furthermore, the lensing star (hosting the detected planet) is generally faint and is projected towards a very dense field, so that its observation is very difficult. This indicates that recovery of the planets discovered by Microlensing is almost impossible, so that single-object physics is virtually forbidden by this technique.

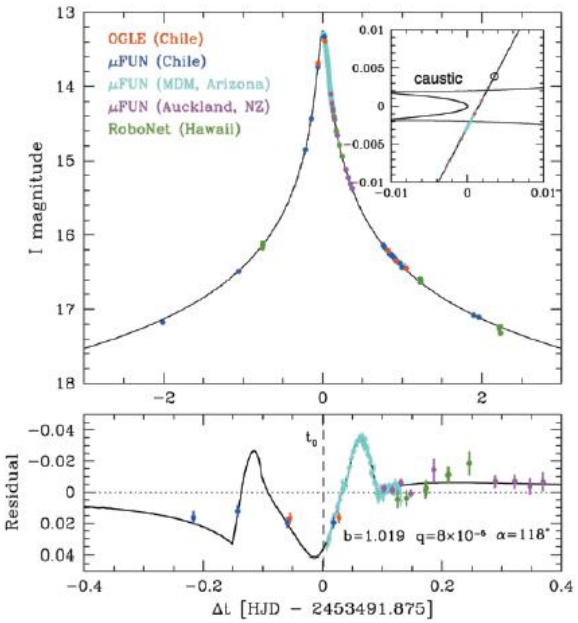


**Figure 2-13: (Top) data and best fit model for the OGLE-2005-BLG-169 event. (Bottom) the difference between this model and the classical form of a single-lens pattern. The extrapolated mass of the planet is ~13 $M_{EARTH}$, cfr. Gould et al. (2006).**

Gravitational Microlensing is a very rare phenomenon requiring very close alignment of the lens and the magnified object; hence the background field should be very rich of potential targets. Typical examples of such fields are the Galactic bulge or the Magellanic Clouds. Due to differential proper motion of the lens and of the magnified objects, Microlensing shows up as a symmetric brightening of the light curve; for single stars, the Microlensing episodes last typically of the order of a month so, continuous photometry of rich fields over this timescale is required for their detection.

Only since 1993 - when massive observational programs capable to surveying million of starts were underway - photometric Microlensing events have been observed by the survey EROS (cfr, Aubourg et al. 1993), MACHO (cfr. Alcock et al. 1993) and OGLE (cfr. Udalski et al. 1993) and the first results of this elegant techniques are coming out in this epoch. Specifically, 4 Microlensing events have been identified as extrasolar planets sources: OGLE 2003-BLG-235/MOA 2003-BLG-53 (Bond et al. 2004), OGLE-2005-BLG-071 (Udalski et al. 2005), OGLE-2005-BLG-390 (Beaulieu et al. 2006) and the late OGLE-2005-BLG169b (Gould et al. 2006) for which a 13 $M_{EARTH}$ object has been proposed (see Figure 2-13).

## 2.4 Direct detection of extrasolar planets

The detection techniques described above have proven to be efficient in detecting planets. In the next future, when good multi-techniques statistical samples will be available, comparative analysis will likely decrease the high level of bias - or event repeatability in the case of the Microlensing technique - that plague these in-direct approaches to the planet finding. However, the sound limitation they have with respect to any direct technique is that they provide limited information about a detected low-mass companion orbiting a star. This fact may lead to ambiguous interpretations on the properties of what has been actually detected and then biasing both single-object and statistical analyses. For instance, the Transit technique provides the radius of the low-mass companion, but without knowing the object mass it difficult to know whether the object is in fact a planet, or a small mass star or a brown dwarf (whose radii are similar to the one of giant planets) or a white dwarf (whose radii are similar to the Earth-size planets). Furthermore, the Radial Velocity technique is limited to only certain type of stars (see the related discussion in Section 2.1.1), and is sensitive only to extrasolar planets with relatively small orbits, typically corresponding to objects at distance smaller than a few AU from their parent star. The limitations of the Radial Velocity technique can be understood by noticing that we have not yet reached sensitivity enough to detect planets at separations comparable to those of Jupiter and Saturn in our Solar System if seen from a distance of ten parsec or more. In contrast, direct detection can survey - in theory - any type of star, including degenerates ones - like white dwarfs and brown dwarfs - for planetary mass companions. In principle, direct detection is more efficient for long-period planets than other techniques, since it requires only few observational runs at the telescope to confirm detection and to achieve spectra, rather than the multitude of observations over long periods of time necessary to the previous techniques. Summarizing, direct detection and spectroscopic analysis of the planetary radiation represents a great knowledge leap, as well as a rigorous maturation of this research field as the following list of motivation explains:

- Direct detection allows to remove the so-called **sin(i)** *ambiguity*, that plagues the mass estimation obtained with the Radial Velocity technique, and to test whether multi-planetary system generally have a single common orbital plane for all the planets - as seen in our solar system. This is a crucial aspect of the formation theories.
- The detection of planets around active stars is possible only through direct detection and - marginally - with Astrometric Perturbation and Transit techniques. In this subject, extremely important is the direct detection in particularly active objects like the young stars where - according to the common theoretical frame of the Core Accretion and Disk Instability scenarios - planet form.
- Planetary photometrical colours will constitute the first direct test of atmospheric models.
- The determination of the intrinsic luminosity of planets at various ages will yield additional constraints on models of planets evolution.
- Spectroscopy allows to obtain the spectral energy distribution - in principle providing information on the chemical composition (i.e. presence of molecules like $CH_4$, $NH_3$, $H_2O$) and the physical properties (i.e. presence clouds and/or aerosols) - for different atmospheric effective temperatures, and then to test model atmospheres of the extrasolar giant planets.
- The polarimetric signal of planets whose spectrum is dominated by the reflected light in the wavelength band where the observations are done it also provide crucial information

on planetary atmospheres. Although the fractional polarization from self-luminous planets is expected to be very small (typically lower than 1%), significant asymmetries in clouds distribution can induce higher polarization. In reflection, more than twenty percent polarization is seen at some orbital phases in the Solar System planets. More in detail, with simulations of Jupiter albedo-like planet at orbital distances lower that 0.3 AU (i.e. 0.1 [arcsec] at 2 pc) with 20% of polarization, a Constrast $\mathbf{C}=10^{7.4}$ is obtained with a strong dependence on orbital phase and system inclination. Such systems might be the first extrasolar planets imaged in reflected light (cfr. Beuzit et al. 2006).

Additionally, photometry of directly detected planets discloses the possibility to search for satellites using the Transit method, and finally, evidences for biomarkers and for biological activity could be searched for in the spectra. These last exciting motivations represent the challenging goals of future dedicated instruments mounted on the next class of ELTs (like the ESO/EPICS instrument) or mounted on dedicated space-based observatories (like the NASA/JPL TPF-C and TPF-I instruments).

### 2.4.1 Key scientific requirements for direct detection

Scientific requirements driving the design of instruments for direct detection of extrasolar planets are based on the properties of the planets in our Solar System and on theoretical models of extrasolar giant (see Section 1.3) and of Earth-like planets atmospheres (see Section 1.4). The projected planet distances from the star determine the angular resolution and the FOV needed to survey any fixed sample of stars within a given distance from the Sun, and expectations about the spectra of the planets allows an optimization of the search technique. Using these inputs the required star vs. planet Contrast scale - as a function of the wavelength, sizes and atmospheric planetary properties - can be estimated (see for example Figure 2-1).Using this approach, the basic requirements for direct detection instruments can be summarized as follows:

- From ground, the wavelength range from 0.6 to 2.5 [micron] should be preferred for various reasons. Giant gaseous planets are dominated by $CH_4$ features in the J and H bands, while for terrestrial planets, the wavelength range 0.7-0.9 [micron] is particularly interesting, due to the presence in this range of unique features like the $O_2$ bands. Wavelengths shorter than 0.7 [microns] have enhanced polarization in the Solar System objects, possibly allowing detection by the polarimetric signal. Observations beyond 2.5 [micron] from the ground are heavily hampered by the strongly thermal background due to the (warm) terrestrial atmosphere; this wavelength range is then best for space-based observations. Ground observations based on high contrast techniques - like SDI and S-SDI - in the J and H bands are competitive with space-based ones at these wavelengths due to the fact that the target star Background Noise[11] dominates over the Sky Noise[12] induced by our atmosphere (see Section 3 for a detailed description of SDI and S-SDI calibration techniques).
- Extremely high contrast: young extrasolar giant planets are believed to be typically 15 magnitudes (~ $\mathbf{C}=10^6$) fainter than their host stars, while an analog of the Earth is 25 magnitudes in the VISible wavelength range(~ $\mathbf{C}=10^{10}$, see. Figure 2-1).

[11] Hereafter Background Noise is defined as the Poisson noise of the target star whose signal is parallel to the optical axis of any direct detection instrument.

[12] Hereafter Sky Noise is defined as the Poisson noise due to the emitted spectral energy distribution of the Earth.

- Very high angular resolution: access to angular separations as small as 100 [microarcsec] is needed to resolve the radial scale of the Jupiter orbit at a distance of 25 pc, while the angular separation of the Earth is 5 times more critical. The scientific requirement on the angular resolution establishes the specification of the Coronagraphic-IWA[13].
- Total FOV extending from 2 [arcsec] up to 4 [arcsec] in diameter: a FOV of 2 [arcsec] corresponds to an exploration region of ~1.5 AU in radius at the distance to nearest star. A FOV of 4 [arcsec] covers a region similar to the scale of own Solar System at distances of around 20 pc.
- Relative Astrometry with 1 [milliarcsec] precision permits to discriminate the background objects with respect to the candidate planets and the accurate measurement of orbital motions on timescale of less than few years around stars within 10 pc.

The achievement of these requirements represents a strong motivation for new researches on the field of Instrumental Astronomy. For example, the research on narrow-angle Interferometry, the research on the sensitivity upgrading of all the AO approaches to obtain high spatial resolution - this latter is defined by the specialists as XAO research -, the research on signal cancellation - or Coronagraphy - that now is moving both towards the increase of capabilities on standard coronagraphic approaches (for example cfr. Sivaramakrishnan et al. 2001) and proposing new ones, as the ingenious PIAA technique by Guyon (2003), and - at last - the research on Differential Imaging techniques that is moving now towards the upgrading of the already tested techniques like SDI (see Section 3.4) and proposing new ones like S-SDI (see Section 3.5) through Integral Field Spectroscopy at the diffraction limit, this latter representing the core of this Dissertation. Ultimately, much of this works will have to be done for space-based instruments who get the remarkable property to be free from atmospheric turbulence and Sky Noise effects but whose strongest limit is the time duration of the related space mission which should maintain in operation the instruments themselves for adequate times. This fact means that ground-based instruments will always play a complementary role to the space-based ones.

### 2.4.2 Interferometry

Interferometry as a direct detection tool is to be distinguished from the interferometric methods by which the Astrometric Perturbation of the hosting star (see Section 2.1.2) is searched. Interferometry can be exploited to reveal the proper signal of a planet as this Section describes. In general these interferometric techniques have high angular resolution capabilities but suffer from signal-to-noise disadvantages since the net optical throughput is low due to the high complexity of the signal processing and reconstruction.

#### 2.4.2.1 Differential Phase technique

This interferometric direct detection technique exploits the phase shift and variation of the fringe Contrast (hereafter Visibility or **V**) that a planet around the central star induces on the total interferometric signal obtained with a fixed baseline vector (**b**) of slits. In the case of a planet around a central star, different flat wave fronts impinge on the slits and produce an interference pattern on an illuminated screen. Off-axis signals like those due to planets will

[13] IWA is defined as the smallest angle at which a planet can be detected, then the inner boundary of high contrast search area.

produce their own interference patterns with a phase shift proportional to the vector indicating the angular separation to the central star ($\delta$) and with a smaller amplitude with respect to the one corresponding to the central star. Then, the total interferometric pattern will be shifted in phase and with a lower Visibility with respect to that due to a single object. Figure 2-14 shows clearly the process through the famous Young's two-slit experiment.

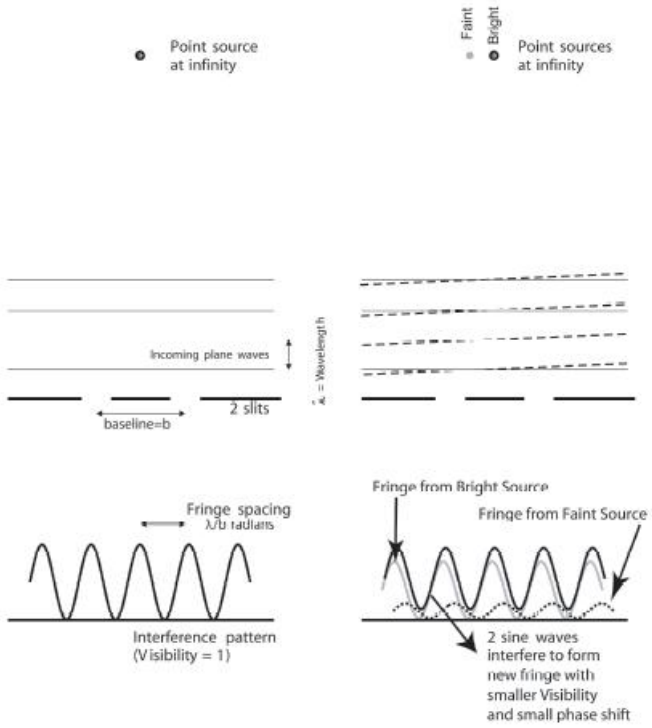


**Figure 2-14: Differential Phase technique explained through the Young's two-slit experiment (cfr. Born and Wolf 1965). The presence of a planet causes a phase shift in the stellar fringe observed by a long-baseline optical interferometer.**

In the limit of high star vs. planet chromatic Contrast ($\mathbf{C(\lambda)}$), observing wavelength ($\lambda$), planet vs. star vectorial separation $\delta$ and instrumental baseline vector $\mathbf{b}$, the normalized complex Visibility ($\mathbf{V}^*$) obtained by an interferometer is:

$$V^*(\lambda) = \frac{1 + C(\lambda) \cdot \exp\left(-\frac{2\pi}{\lambda} \cdot i \cdot \mathbf{b} \mid \boldsymbol{\delta}\right)}{1 + C(\lambda)}$$

**Equation 2-11**

In the limit of $\mathbf{C(\lambda)}$<<1 appropriate for extrasolar planet detection experiments, the Equation 2-11 takes a simpler form when one considers the modulus of the Visibility and its phase ($\mathbf{\Phi_V}$) separately:

$$\left|V^*(\lambda)\right| \approx 1 - 2 \cdot C(\lambda) \cdot \sin^2\left(\frac{\pi}{\lambda} \cdot \mathbf{b} \mid \boldsymbol{\delta}\right)$$

$$\varphi_V(\lambda) \approx C(\lambda) \cdot \sin\left(\frac{2\pi}{\lambda} \cdot \mathbf{b} \mid \boldsymbol{\delta}\right)$$

**Equation 2-12**

Hence, by measuring $\mathbf{\Phi_V}$ or alternatively the modulus of the Visibility for various baseline vectors $\mathbf{b}$ and wavelengths $\lambda$, both the chromatic Contrast $\mathbf{C(\lambda)}$ (then the total - i.e. the sum

of the emitted and reflected ones - planetary spectral energy distribution, if the star spectral energy distribution is known *a priori*) and the vectorial separation $\delta$ can be determined**.** In turn, this means to obtain a direct image of the planets itself.

To be applicable below the Earth atmosphere, this approach should deal with the atmospheric turbulence. This latter represents the main problem with respect to the pure formalism adopted above because difference in the path lengths between distinct slits due to different amounts of refraction index variation on top of them, should be taken into account and could drastically damage the final interferometric signal. In the illustrative case of Figure 2-14, the worst case is the one where differential path length - induced by the atmospheric turbulence - is half the wavelength $\lambda$. In this case the destructive interference will cancel the fringe pattern. The strategy adopted to overcome this evident show-stopper, is comparing the fringes at different wavelengths, in order to track the phase variations of the light on top of the slits and then to estimate the Differential Phase between them. This method is relatively insensitive to the atmospheric turbulence; moreover it benefits of the bright flux of the central star that works as natural guide-star for the wave front measurements. However, recent studies of line-of-sight variability of atmospheric water vapour indicate that the differential chromatic dispersion might be more difficult to calibrate for the Differential Phase technique than originally expected (cfr. Colavita et al. 2004). At present, this technique is still far from providing the Contrasts required to detect extrasolar planets.

#### 2.4.2.2 Closure Phase technique

There is another interferometric technique which is robust to both atmospheric phase shifts and also differential chromatic dispersion. Consider the right panel of Figure 2-15 in which a phase delay is introduced above telescope-2 in a 3-telescope interferometer. This causes a phase shift in the fringe detected between telescope-1 and telescope-2, as discussed in the Section 2.4.2.1. Notice that a phase shift is also induced for fringes between telescope-2 and telescope-3; however, this phase shift is equal but opposite to the one for telescope-1 and telescope-2. Hence, the sum of three fringe phases, between telescope-1 and telescope-2, telescope-2 and telescope-3, telescope-3 and telescope-1, is insensitive to the phase delay above telescope-2. This argument holds for arbitrary phase delays above any of the three telescopes. In general, the sum of three phases around a closed triangle of baselines, the *Closure Phase*, is a good interferometric observable; that is, it is independent of telescope-specific phase shifts induced by the atmosphere or optics. Then, the Closure Phase is formed by summing the interferometer phases on three baselines around a triangle of telescopes, and this quantity is immune to atmospheric phase delays.

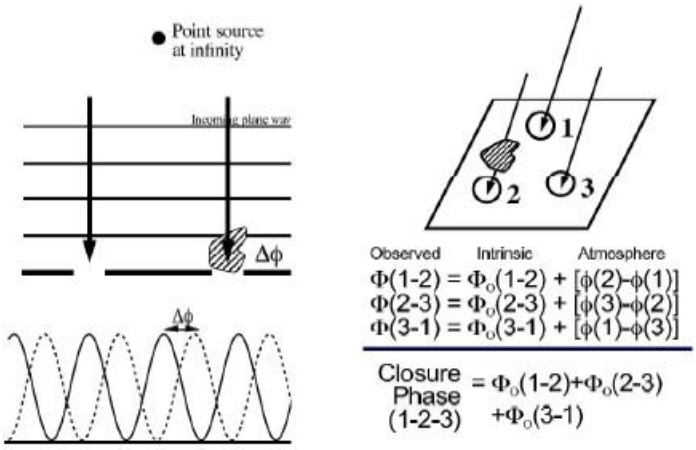


**Figure 2-15: In an interferometer, a phase delay above an aperture causes a phase shift in the detected fringe pattern (left panel). Phase errors introduced at any telescope causes equal but opposite phase shifts, cancelling out in the closure phase (right panel). Equations on the right panel are taken from Readhead et al. (1988).**

Segransan et al. (2000) and Monnier (2002) discussed how closure phases are immune to dominant calibration problems of differential phase and that they can also be used to solve for all the parameters of a binary system without needing to measure any visibility amplitudes. Unfortunately, the Closure Phase amplitude scales like the baseline to the third power for short baselines, making detection of partially-resolved systems difficult or quite impossible. At contrary, Differential Phase shift scales linearly with the baseline and thus it remains a viable planet detection method even for relatively short baselines (e.g., the 85-m Keck-Keck baseline).

#### 2.4.2.3 Nulling technique

The last approach to direct detect extrasolar planets through Interferometry is the Nulling technique. First demonstrated by Hinz et al. (1998) on the MMT facility, the Nulling interferometer introduces an extra (a-chromatic) phase delay in one of the arm of the interferometer so that light from the central star destructively interferes. Since the null depends on the incident angle of the starlight, one can tune the interferometer to selectively null out the star while allowing light from the planet to still be measured by the interferometer. Substantially, a Nuller is the Interferometry-equivalent of a Coronagraph on single aperture-telescope.

Nulling Interferometry is difficult to carry-out from ground-based telescopes due again to the impact of the atmospheric turbulence. In fact, not only differential path lengths between distinct points of the telescope Entrance Pupil have to be measured through wave front analysis, but also wave front correction is required in order to introduce the right amount of extra-phase in the optical signal. For this reason, significant gains using the Nulling technique will be obtained through space-based observatories devoted to planet finding, like the NASA/JPL TPF-I.

### 2.4.3 High contrast imaging

Interferometers may have a high spatial resolution advantage (see Figure 2-16) but they get the disadvantage of low signal-to-noise ratio - as explained in Section 2.4.2. The primary challenge in imaging extrasolar planets is the presence of a star at the center of the FOV which could be up to $10^{12}$ times brighter than the planet. Eliminating the light of this star without damaging that of planet represents the major challenge of high contrast techniques and requires new optical technology. In particular the challenges - and then their related new technologies - are:

- The Correction of the PSF with different purposes: to confine the disturbing stellar light into a coherent diffraction limited pattern that is understood and controlled; to concentrate the planetary flux making the planets peak brightness higher relative to the background due to the star light; and to reduce the in-coherent stellar halo.
- The Cancellation of the coherent part of the stellar PSF by Coronagraphy.
- The calibration of the residual (usually in-coherent) stellar halo including residuals of atmospheric and instrumental effects.

Actually, these three steps are closely entangled in any practical system design as in the case of SPHERE (see Section 4).

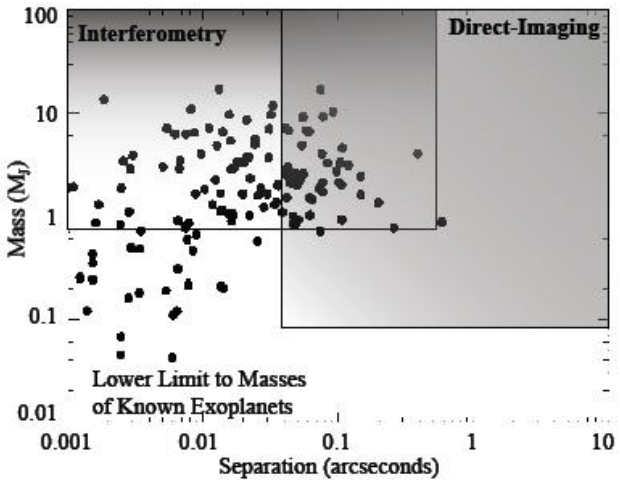


**Figure 2-16: Mass vs. separation diagram illustrating the complementarities of different techniques used for extrasolar planet direct detection. The black circles indicate known planets discovered through in-direct methods. The shaded regions show the approximate parameter space accessible to direct detection techniques employing Interferometry and high contrast imaging, from Beuzit et al. (2006).**

#### 2.4.3.1 Correction: Adaptive Optics

The primary source of disturbance to the PSF quality is due to wave front perturbation imposed during propagation through the atmosphere. AO is a technique that corrects these disturbances. The perturbations are measured with dedicated WFS and corrections are applied by an optically conjugated DM in real-time. The maximum performance for a given AO-system is limited by the number of actuators behind the DM, the servo-loop band pass and the overall stability and calibration accuracy. The whole system act as a spatio-temporal

filter, correcting most of the low temporal and spatial frequencies on the wave front perturbations. Remaining high spatial frequency defects translate in the image plane as a residual seeing-like halo extending outward from the Control Radius[14]. Within the AO Control Radius the departure from a pure diffraction limited pattern is due to remaining very fast wave front variations and high spatial frequency Aliasing[15].

With a reasonable inter-actuator spacing corresponding to **d**~10-20 [cm] (i.e. matching the $\mathbf{r_0}$ values on top of a fixed telescope facility), the corrected region of the image extends up to 0.8 [arcsec] for a minimum wavelength $\lambda$~0.7 [micron], which is well suited for planet searches. Progress on the WFS detector allows achieving correction on stars as faint as the 11-th absolute magnitude - depending on the wavelength used for guiding - even with the required spatial and temporal sampling. Finally, trying to reach the highest level of correction (**SR** >0.9), new limiting factors appear and must be taken into account like Scintillation, perturbation chromatism, etc. See for instance Dekany (2004) and Fusco et al. (2005) for in-depth discussions on these effects.

#### 2.4.3.2 Cancellation: Coronagraphy

The basic purpose of Coronagraphy (cfr. Lyot 1939) is to cancel the coherent part of the stellar signal over the observed FOV. In addition to the merit of reducing the Background Noise (by decreasing the number of photons in the image), Coronagraphy does the filtering of the high spatial frequencies corresponding to the on-axis signal, while out of the IWA the spatial frequency filtering is practically the same of the one already made by the telescope OTF (cfr. Sivaramakrishnan et al. 2001).

Considering a well corrected wave front - i.e. when the phase defects across the wave front remain small - the corresponding image can be approximated by the sum of a pure diffraction pattern (Airy profile in the case of circular apertures, $Sinc^2$ profile in the case of square apertures, cfr. Born and Wolf 1965) and of an in-coherent halo shaped as the FT of the phase defects Power Spectral Density (PSD). In a perfect Coronagraph the diffraction pattern is completely removed. In practice a trade-off must be made, as Figure 2-17 shows clearly.

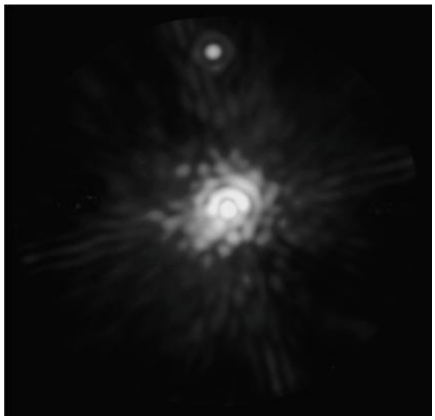

[14] The monochromatic Control Radius is defined as $\lambda/2\mathbf{d}$ where (**d**) is the inner actuator spacing as projected on the telescope primary mirror (cfr. Oppenheimer et al. 2003).

[15] In Optics, Aliasing refers to the distortion of the frequencies content of an electromagnetic signal being sampled in time (for a fixed point source) or in space (for a fixed time lag) and reconstructed as an alias of the original signal.

**Figure 2-17: An H-band image from one of best coronagraphic devices in the world today: the Lyot Project Coronagraph. This instrument is an optimized, diffraction limited, classical Coronagraph (i.e. Lyot-like) fitted behind an AO system with Control Radius =10 [cm] on the 3.67 [m] AEOS telescope on Mahui islands, currently the highest order AO correction available (cfr. Oppenheimer et al. 2004). The companion (confirmed through common proper motion Astrometry) to this nearby star gets a Contrast of $10^{-4.5}$ and a separation of 1.8 [arcsec].**

#### 2.4.3.3 Calibration: Differential Techniques

Several Differential Techniques have been proposed that combine AO-systems to instruments for Differential Imaging, for example NACO-SDI (cfr. Lenzen et al. 2005) and TRIDENT (cfr. Marois et al. 2005), exploiting Simultaneous Differential Imaging, SPHERE/ZIMPOL (cfr. Gisler et al. 2004) exploiting Polarimetric Differential Imaging and the new SPHERE/IFS, exploiting Spectroscopic Simultaneous Differential Imaging[16], whose optical concept and performances description represent the core of this Dissertation.

The following Sections are fully dedicated to Differential Imaging. More in detail, in Section 3 a description of the SDI technique is done, and the inner connection between SDI and S-SDI techniques is presented in Section 3.4, justifying the request of Integral Field Spectroscopy at the diffraction limit regime in Section 3.5. In Section 4, a global description of the high-integrated optical system SPHERE is presented. In Sections 5 and 6, the detailed optical concept and the description, both in terms of spatio-spectral frequencies and in term of optical performances, of the systems: SPHERE/IFU and SPHERE/IFS is given. Finally, Section 7 is dedicated to the description of the work we did on 3D-Spectroscopy, in the perspective of an European ELT Planet Finder instrument (EPICS, cfr Vérinaud et al. 2006), which foresees a S-SDI facility aimed at the direct detection of extrasolar planets.

[16] In this Dissertation the term Spectroscopic-SDI refers only to those optical concepts making SDI through a disperser device producing chromatical dispersion of the scientific beam before the image acquisition, see Section 3.5.

## 2.5 Bibliography


Alcock, C.; Akerloff, C. W.; Allsman, R. A.; Axelrod, T. S.; Bennett, D. P.; Chan, S.; Cook, C. H.; Freeman, K. C.; Griest, K.; Marshall, S. L.; and 8 coauthors, 1993, NATURE V.365, NO.6447/0CT14, P. 621.

Aubourg, E.; Bareyre, P.; Brehin, S.; Gros, M.; Lachieze-Rey, M.; Laurent, B.; Lesquoy, E.; Magneville, C.; Milsztajn, A.; Moscoso, L.; and 18 coauthors, 1993, NATURE V.365, NO.6447/0CT14, P. 623.

Bakos G. A., Noyes R. W., Kovacs G., Latham D. W., Sasselov D. D., Torres G., Fischer D. A., Stefanik R. P., Sato B., Johnson J. A., Pal A., Marcy G. W., Butler R. P., Esquerdo G. A., Stanek K. Z., Lazar J., Papp I., Sari P., Sipocz B., ***astro-ph/0609369*** (accepted for publication in ApJ.).

Baraffe, I.; Chabrier, G.; Allard, F.; Hauschildt, P. H., 2002, A&A., v.382, p.563-572.

Baranne, A.; Queloz, D.; Mayor, M.; Adrianzyk, G.; Knispel, G.; Kohler, D.; Lacroix, D.; Meunier, J.-P.; Rimbaud, G.; Vin, A, 1996, A&AS., v.119, p.373-390.

Beaulieu, J.-P.; Bennett, D. P.; Fouqué, P.; Williams, A.; Dominik, M.; Jorgensen, U. G.; Kubas, D.; Cassan, A.; Coutures, C.; Greenhill, J.; and 63 coauthors, 2006, Nature, Volume 439, Issue 7075, pp. 437-440.

Benedict, G. F.; McArthur, B. E.; Forveille, T.; Delfosse, X.; Nelan, E.; Butler, R. P.; Spiesman, W.; Marcy, G.; Goldman, B.; Perrier, C.; and 2 coauthors, 2002, ApJ., Volume 581, Issue 2, pp. L115-L118.

Benedict, G. F.; McArthur, B. E., *Are ThерePlanets or Not ?*, 2004, American Astronomical Society, DPS meeting #36, #42.02; Bulletin of the American Astronomical Society, Vol. 36, p.1172.

Benedict G. F., McArthur B. E., Gatewood G., Nelan E., Cochran W. D., Hatzes A., Endl M., Wittenmyer R., Baliunas S. L., Walker G. A. H., Yang S., Kurster M., Els S., Paulson D. B., ***astro-ph/0610247***.

Berton, A.; Gratton, R. G.; Feldt, M.; Henning, T.; Desidera, S.; Turatto, M.; Schmid, H. M.; Waters, R., 2006, PASP., Volume 118, Issue 846, pp. 1144-1164.

Beuzit, J.-L.; Mouillet, D.; Oppenheimer, B.; Monnier., J, *Direct Detection of Exoplanets*, in Proceedings of the conference: *Protostars and Planets V*, Waikoloa (Hawaii, USA), 24-29 October 2005. Edited by B. Reipurth, D. Jewitt, and K. Keil. University of Arizona Press, Tucson, 2006, in press.

Bond, I. A.; Udalski, A.; Jaroszyński, M.; Rattenbury, N. J.; Paczyński, B.; Soszyński, I.; Wyrzykowski, L.; Szymański, M. K.; Kubiak, M.; Szewczyk, O.; and 22 coauthors, 2004, ApJ., Volume 606, Issue 2, pp. L155-L158.

Born, Max; Wolf, Emil, **Principles of optics. Electromagnetic theory of propagation, interference and diffraction of light**, Oxford: Pergamon Press, 1965, 3rd (revised) ed.

Bouchy, F.; Pepe, F.; Queloz, D., 2001, A&A., v.374, p.733-739.

Chabrier, G.; Baraffe, I.; Allard, F.; Hauschildt, P., 2000, ApJ., Volume 542, Issue 1, pp. 464-472.

Charbonneau, David; Noyes, Robert W.; Korzennik, Sylvain G.; Nisenson, Peter; Jha, Saurabh; Vogt, Steven S.; Kibrick, Robert I., 1999, ApJ., Volume 522, Issue 2, pp. L145-L148.

Charbonneau, David; Allen, Lori E.; Megeath, S. Thomas; Torres, Guillermo; Alonso, Roi; Brown, Timothy M.; Gilliland, Ronald L.; Latham, David W.; Mandushev, Georgi; O'Donovan, Francis T.; Sozzetti, Alessandro, 2005, ApJ., Volume 626, Issue 1, pp. 523-529.

Charbonneau D., Brown T. M., Burrows A., Laughlin G., ***astro-ph/0603376*** (Review Chapter for Protostars and Planets V).

Chauvin, G.; Lagrange, A.-M.; Dumas, C.; Zuckerman, B.; Mouillet, D.; Song, I.; Beuzit, J.-L.; Lowrance, P., 2004, A&A., v.425, p.L29-L32.

Chauvin, G.; Lagrange, A.-M.; Zuckerman, B.; Dumas, C.; Mouillet, D.; Song, I.; Beuzit, J.-L.; Lowrance, P.; Bessell, M. S., 2005, A&A., Volume 438, Issue 3, pp.L29-L32.

Colavita, M. Mark; Swain, Mark R.; Akeson, Rachel L.; Koresko, Christopher D.; Hill, Reginald J., 2004, PASP., Volume 116, Issue 823, pp. 876-885.

Collier Cameron A., Bouchy F., Hebrard G., Maxted P., Pollacco D., Pont F., Skillen I., Smalley B., Street R. A., West R. G., Wilson D. M., Aigrain S., Christian D. J., Clarkson W. I., Enoch B., Evans A., Fitzsimmons A., Gillon M., Haswell C. A., Hebb L., Hellier C., Hodgkin S. T., Horne K., Irwin J., Kane S. R., Keenan F. P., Loeillet B., Lister T. A., Mayor M., Moutou C., Norton A. J., Osborne J., Parley N., Queloz D., Ryans R., Triaud A. H. M. J., Udry S., Wheatley P. J., ***astro-ph/0609688*** (MNRAS submitted).

Dekany, Richard G., *Second Backaskog Workshop on Extremely Large Telescopes*. Edited by Ardeberg, Arne L.; Andersen, Torben. Proceedings of the SPIE, Volume 5382, pp. 12-20, 2004.

Deming, Drake; Seager, Sara; Richardson, L. Jeremy; Harrington, Joseph, 2005, Nature, Volume 434, Issue 7034, pp. 740-743.

Des Marais, David J.; Harwit, Martin O.; Jucks, Kenneth W.; Kasting, James F.; Lin, Douglas N. C.; Lunine, Jonathan I.; Schneider, Jean; Seager, Sara; Traub, Wesley A.; Woolf, Neville J, 2002, Astrobiology, Volume 2, Issue 2, pp. 153-181.

Fusco, T.; Rousset, G.; Beuzit, J.-L.; Mouillet, D.; Dohlen, K.; Conan, R.; Petit, C.; Montagnier, G., *Astronomical Adaptive Optics Systems and Applications II*. Edited by Tyson, Robert K.; Lloyd-Hart, Michael. Proceedings of the SPIE, Volume 5903, pp. 178-189, 2005.

Gisler, Daniel; Schmid, Hans Martin; Thalmann, Christian; Povel, Hans Peter; Stenflo, Jan O.; Joos, Franco; Feldt, Markus; Lenzen, Rainer; Tinbergen, Jaap; Gratton, Raffaele; and 14 coauthors, *Ground-based Instrumentation for Astronomy*. Edited by Alan F. M. Moorwood and Iye Masanori. Proceedings of the SPIE, Volume 5492, pp. 463-474, 2004.

Gould, A.; Udalski, A.; An, D.; Bennett, D. P.; Zhou, A.-Y.; Dong, S.; Rattenbury, N. J.; Gaudi, B. S.; Yock, P. C. M.; Bond, I. A.; and 26 coauthors, 2006, ApJ., Volume 644, Issue 1, pp. L37-L40.

Gratton, R. G.; Bonanno, G.; Bruno, P.; Cali, A.; Claudi, R. U.; Cosentino, R.; Desidera, S.; Diego, F.; Farisato, G.; Martorana, G.; and 2 coauthors, 2001, Experimental Astron., 12, 107-143.

Guillot, T.; Showman, A. P., 2002, A&A., v.385, p.156-165.

Guyon, O., 2003, A&A., v.404, p.379-387.

Hinz, P. M.; Angel, J. R. P.; Hoffmann, W. F.; McCarthy, D. W., Jr.; McGuire, P. C.; Cheselka, M.; Hora, J. L.; Woolf, N. J., 1998, Nature, 395, 251-253.

Jenkins, Jon M.; Caldwell, Douglas A.; Borucki, William J., 2002, ApJ., Volume 564, Issue 1, pp. 495-507.

Lecavelier des Etangs A., ***astro-ph/0609744*** (to be publihed in A&A.).

Lenzen, Rainer; Close, Laird; Brandner, Wolfgang; Hartung, Markus; Biller, Beth, *Science with Adaptive Optics*, Proceedings of the ESO Workshop Held at Garching, Germany, 16-19 September 2003. Edited by W. Brandner and M. E. Kasper. 387 p. Library of Congress Catalog Card No. 200592215. ISBN: 3-540-25034-4. Published by Springer, Berlin 2005, p.46.

Lyot, Bernard, 1939, MNRAS., Vol. 99, p.580.

Marcy, Geoffrey W.; Butler, R. P.; 1992, PASP, Publications (ISSN 0004-6280), vol. 104, no. 674, p. 270-277.

Marois, Christian; Doyon, René; Nadeau, Daniel; Racine, René; Riopel, Martin; Vallée, Philippe; Lafrenière, David, 2005, PASP., Volume 117, Issue 833, pp. 745-756.

Mattox, J. R.; Halpern, J. P.; Caraveo, P. A., 1998, ApJ., v.493, p.891.

Mayor, M.; Pepe, F.; Queloz, D.; Bouchy, F.; Rupprecht, G.; Lo Curto, G.; Avila, G.; Benz, W.; Bertaux, J.-L.; Bonfils, X.; and 22 coauthors, 2003, The Messenger (ISSN0722-6691), No.114, p. 20-24.

Mayor, M.; Queloz, D., 1995, Nature V.378, NO.6555/NOV23, P. 355.

Monnier J. D. ,2002, in Eurowinter School: *Observing with the Very Large Telescope Interferometer* (G. Perrin and F. Malbet, eds.), pp. 213-226.

Mullally, F.; Winget, D. E.; Kepler, S. O., 2005, American Astronomical Society Meeting 207, #68.08; Bulletin of the American Astronomical Society, Vol. 37, p.1267.

Mullally, F.; Winget, D. E.; Kepler, S. O., *New Horizons in Astronomy*: Frank N. Bash Symposium ASP Conference Series, 2006,Vol. 352, Proceedings of the Conference Held 16-18 October, 2005 at The University of Texas, Austin, Texas, USA, p.265.

Neuhäuser, R.; Guenther, E. W.; Wuchterl, G.; Mugrauer, M.; Bedalov, A.; Hauschildt, P. H., 2005, A&A., Volume 435, Issue 1, pp.L13-L16.

O'Donovan F. T., Charbonneau D., Mandushev G., Dunham E. W., Latham D. W., Torres G., Sozzetti A., Brown T. M., Trauger J. T., Belmonte J. A., Rabus M., Almenara J. M., Alonso R., Deeg H. J., Esquerdo G. A., Falco E. E., Hillenbrand L. A., Roussanova A., Stefanik R. P., Winn J. N., ***astro-ph/0609335*** (accepted for publication in ApJL.).

Oppenheimer, B. R.; Sivaramakrishnan, A.; Makidon, R. B, **The Future of Small Telescopes in the New Millennium**. Volume III - Science in the Shadows of Giants. Edited

by Terry D. Oswalt. Astrophysics and Space Science Library, Volume 289, Kluwer Academic Publishers, Dordrecht, 2003., p.155.

Oppenheimer, Ben R.; Digby, Andrew P.; Newburgh, Laura; Brenner, Douglas; Shara, Michael; Mey, Jacob; Mandeville, Charles; Makidon, Russell B.; Sivaramakrishnan, Anand; Soummer, Remi; and 7 coauthors, *Advancements in Adaptive Optics*. Edited by Domenico B. Calia, Brent L. Ellerbroek, and Roberto Ragazzoni. Proceedings of the SPIE, Volume 5490, pp. 433-442, 2004.

Paczynski, B., 1986, ApJ., Part 1 (ISSN 0004-637X), vol. 304, p. 1-5.

Pepe, Francesco; Mayor, Michel; Delabre, Bernard; Kohler, Dominique; Lacroix, Daniel; Queloz, Didier; Udry, Stephane; Benz, Willy; Bertaux, Jean-Loup; Sivan, Jean-Pierre, Proc. SPIE Vol. 4008, p. 582-592, *Optical and IR Telescope Instrumentation and Detectors*, Masanori Iye; Alan F. Moorwood; Eds.

Perryman, M. A. C.; Lindegren, L.; Kovalevsky, J.; Hoeg, E.; Bastian, U.; Bernacca, P. L.; Crézé, M.; Donati, F.; Grenon, M.; van Leeuwen, F.; and 9 coauthors, 1997, A&A., 323, L49-L52.

Perryman, M. A. C., 2000, Rep. Prog. Phys., 63, 1209-1272.

Perryman, M. A. C.; de Boer, K. S.; Gilmore, G.; Høg, E.; Lattanzi, M. G.; Lindegren, L.; Luri, X.; Mignard, F.; Pace, O.; de Zeeuw, P. T., 2001, A&A., v.369, p.339-363.

Perryman M., Hainaut O., Dravins D., Leger A., Quirrenbach A., Rauer H., Kerber F., Fosbury R., Bouchy F., Favata F., Fridlund M., Gilmozzi R., Lagrange A-M., Mazeh T., Rouan D., Udry S., Wambsganss J., ***astro-ph/0506163*** (ESA-ESO Working Groups Report No. 1, A printed version (A5 booklet) is available in limited numbers from Space Telescope-European Coordinating Facility (ST-ECF) on request: stdesk@eso.org).

Queloz, D.; Mayor, M.; Naef, D.; Santos, N.; Udry, S.; Burnet, M.; Confino, B, *Extrasolar Planets to Cosmology: The VLT Opening Symposium*: Proceedings of the ESO Symposium Held at Antofagasta, Chile, 1-4 March 1999, ESO ASTROPHYSICS SYMPOSIA. ISBN 3-540-67163-3. Edited by J. Bergeron and A. Renzini. Springer-Verlag, 2000, p. 548.

Quirrenbach, Andreas; Henning, Thomas; Queloz, Didier; Albrecht, Simon; Bakker, Eric J.; Baumeister, Harald; Bizenberger, Peter; Bleuler, Hannes; Dandliker, Rene; de Jong, Jeroen A.; and 24 coauthors, *New Frontiers in Stellar Interferometry*, Proceedings of SPIE Volume 5491. Edited by Wesley A. Traub. Bellingham, WA: The International Society for Optical Engineering, 2004.

Readhead, A. C. S.; Nakajima, T. S.; Pearson, T. J.; Neugebauer, G.; Oke, J. B.; Sargent, W. L. W., 1988, AJ., (ISSN 0004-6256), vol. 95, p. 1278-1296.

Sato, Bun'ei; Fischer, Debra A.; Henry, Gregory W.; Laughlin, Greg; Butler, R. Paul; Marcy, Geoffrey W.; Vogt, Steven S.; Bodenheimer, Peter; Ida, Shigeru; Toyota, Eri; and 11 coauthors, 2005, ApJ., Volume 633, Issue 1, pp. 465-473.

Segransan, Damien; Beuzit, Jean-Luc; Delfosse, Xavier; Forveille, Thierry; Mayor, Michel; Perrier-Bellet, Christian; Allard, F., Proc. SPIE Vol. 4006, p. 269-276, *Interferometry in Optical Astronomy*, Pierre J. Lena; Andreas Quirrenbach; Eds., 2000.

Sivaramakrishnan, Anand; Koresko, Christopher D.; Makidon, Russell B.; Berkefeld, Thomas; Kuchner, Marc J., 2001, ApJ., Volume 552, Issue 1, pp. 397-408.

Sobolev, V. V., **Light Scattering in Planetary Atmospheres**, Oxford: Pergamon Press, 1975, ed.

Traub, W. A.; Jucks, K. W., **Atmospheres in the Solar System: Comparative Aeronomy**. Geophysical Monograph 130. Edited by Michael Mendillo, Andrew Nagy, and J.H. Waite. Washington, D.C.: American Geophysical Union, 2002, p.369.

Traub, Wesley A.; Levine, Marie; Shaklan, Stuart; Kasting, James; Angel, J. Roger; Brown, Michael E.; Brown, Robert A.; Burrows, Christopher; Clampin, Mark; Dressler, Alan; and 16 coauthors, *Advances in Stellar Interferometry*. Edited by Monnier, John D.; Schöller, Markus; Danchi, William C.. Proceedings of the SPIE, Volume 6268, pp., 2006.

Udalski, A.; Szymanski, M.; Kaluzny, J.; Kubiak, M.; Krzeminski, W.; Mateo, M.; Preston, G. W.; Paczynski, B., 1993, Acta Astronomica, vol. 43, no. 3, p. 289-294.

Udalski, A.; Jaroszyński, M.; Paczyński, B.; Kubiak, M.; Szymański, M. K.; Soszyński, I.; Pietrzyński, G.; Ulaczyk, K.; Szewczyk, O.; Wyrzykowski, Ł.; and 23 coauthors, 2005, ApJ., Volume 628, Issue 2, pp. L109-L112.

Vérinaud, C.; Hubin, N.; Kasper, M.; Antichi, J.; Baudoz, P.; Beuzit, J.-L.; Boccaletti, A.; Chalabaev, A.; Dohlen, K.; Fedrigo, E.; and 24 coauthors. *Advances in Adaptive Optics II*. Edited by Ellerbroek, Brent L.; Bonaccini Calia, Domenico. Proceedings of the SPIE, Volume 6272, pp., 2006.

Wolszczan, A.; Frail, D. A., 1992, Nature (ISSN 0028-0836), vol. 355, Jan. 9, p. 145-147.

Wolszczan, A., 1994, SCIENCE V.264, NO.5158/APR22, P. 538.

Wolszczan, A., 1997, The Pulsar Planets Update in D R Soderblom, ed., *Planets Beyond the Solar System and the Next Generation of Space Missions*, ASP Conf. Series 119 135–138 San Francisco.

# 3 Simultaneous Differential Imaging

Simultaneous Differential Imaging (SDI) is a high contrast differential technique by which subtraction of simultaneous images reduces the Noise[17] produced by atmospheric and instrumental phase aberrations.

The most important problem for high contrast imaging instruments aimed to the direct detection of extrasolar planets is the Background Noise[18]. Coronagraphy represents the first remedy to this Noise, attenuating the coherent diffraction pattern of the on-axis PSF. At high SR levels, the diffraction pattern dominates much of the on-axis PSF. This is the case of space-based instruments for which SR goes ideally to unity, and where Coronagraphy can achieve strong attenuation with respect to off-axis signals whose direction is contained in the Isoplanatic Angle[19]. However, with the SR levels obtained from ground by the present XAO[20] devices, the coronagraphic efficiency is limited by the presence of a rapidly changing halo of *Speckles* generated by phase distortions at the level of the telescope Entrance Pupil. In addition, phase aberrations inside the optical train - not corrected by AO - produced for example by temporal variations of the optical alignment, or by different optical paths in a frozen optical alignment (hereafter non-common path aberrations), produce Speckles (hereafter *Super-Speckles*) of a much longer lifetime than the ones produced by the atmospheric turbulence. Speckles and Super-Speckles are the major sources of Noise for high contrast imaging instruments equipped with AO-devices.

SDI (Smith 1987, Racine et al. 1999, Marois et al. 2000, Sparks and Ford 2002, Marois et al. 2004, Biller et al. 2004, Berton et al. 2006) is a calibration technique. Images are acquired simultaneously at adjacent wavelengths in a spectral range where the planetary and stellar spectra differ appreciably. Then, fine tuned Data Reduction Software (DRSW) allows to create several chromatic images of the same FOV around the central star. The images subtraction should remove the Speckle Noise - assumed to be similar in any single simultaneous image after suitable chomatical re-scaling - which in turn dominates over any other optical pattern contained within the Control Radius[21] boundary.

## 3.1 Planet features useful for Simultaneous Differential Imaging

In principle, SDI calibration technique becomes a powerful method for extrasolar planets direct imaging only when specific wavelength ranges for the observations of a target star are selected. As described in Section 1.3, Sudarsky et al. (2000) modeled albedo and reflection spectra for a full range of extrasolar giant planets, distinguishing the theoretical spectral albedos in five classes, defined only by the different range of atmospheric temperature of the

---

[17] In this Dissertation the term Noise indicates the Root Mean Square of residuals with respect to the average value over temporal realizations of a given optical signal.

[18] For the definition of Background Noise see (Section 2.4.1).

[19] For the definition of Isoplanatic Angle see: **Introduction to Adaptive Optics**, SPIE Tutorial Text in Optical Engineering Vol. TT41

[20] In XAO devices the reference star for WFS analysis is the target star.

[21] For the definition of Control Radius see (Section 2.4.3.2). In literature this quantity is often called Outer Working Angle (OWA).

planet. This classification has been improved in Sudarsky et al. (2003), obtaining the spectral profile of the whole energy (i.e. the sum of the reflected and internal - blackbody-like - radiations) emitted by the atmospheres of irradiated extrasolar giant planets[22]. What appears from these theoretical works is that planetary atmospheres spectra are dominated by a forest of lines in a wide range of wavelengths, from the VISible up to the NIR (see Figure 3-1). In the synoptic work made by Burrows et al. (2004), spectral profile models are improved introducing both environmental parameters like the spectral type and distance of parent star, and physical parameters of the planet itself like its mass and age. They obtained several diagnostics, like the ratio between the planetary spectral flux and the one proper to the parent star (see Figure 3-2 and Figure 3-3). This observable in particular is extremely useful for the selection of wavelength ranges suitable for the SDI technique, which in turn works exploiting differences of simultaneous images taken in a set of chromatic bands, where the candidate planet gets a forest of features, while the parent star could be featureless as the one represented in Figure 3-4.

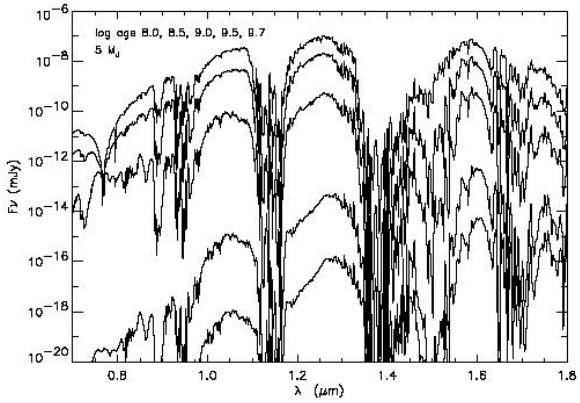


**Figure 3-1: Spectra (flux densities in [mJy]) of 5 $M_{JUPITER}$ planets with $log_{10}$ Age: 8.5, 9.0, 9.5 and 9.7 [yr] (from top to bottom). The effective temperatures span between ~200-600 K and the wavelength range is 0.7-1.8 [micron]. From models of Burrows et al. (2003).**

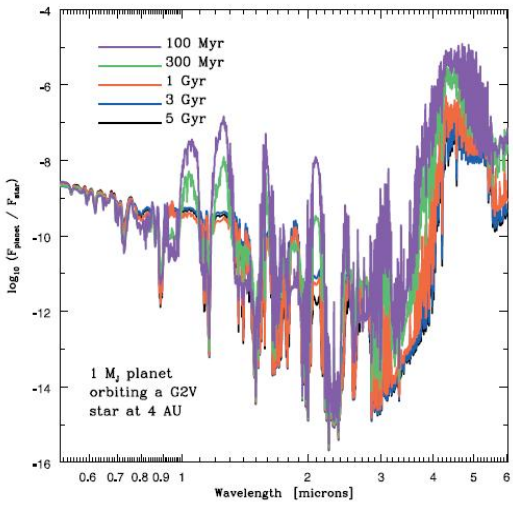


[22] However, as discussed by Baraffe et al. (2002), spectral profile models should not be considered reliable for very young planets (age < 10 [Myr]), due to the strong dependence on their - unknown - initial conditions.

**Figure 3-2: Planet-to-star flux ratio from 0.5 to 6.0 [micron] for a $M_{JUPITER}$ planet orbiting a G2V star at 4 AU as a function of the planet age: 0.1, 0.3, 1.3 and 5 [Gyr], from Burrows et al. (2004).**

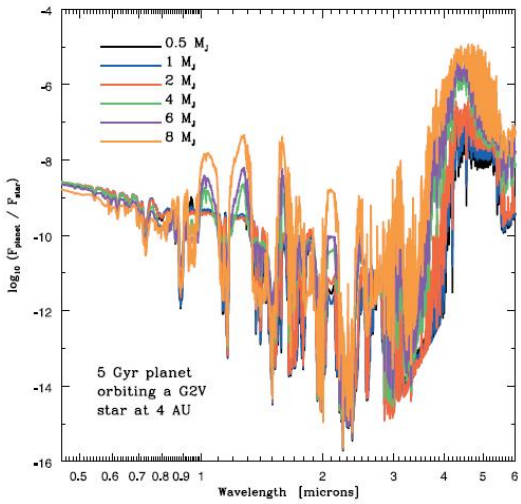


**Figure 3-3: Planet-to-star flux ratio from 0.5 to 6.0 [micron] for a 5 [Gyr] planet orbiting a G2V star at 4 AU as a function of the planet mass: 0.5, 1, 2, 4, 6, and 8 $M_{JUPITER}$, from Burrows et al. (2004).**

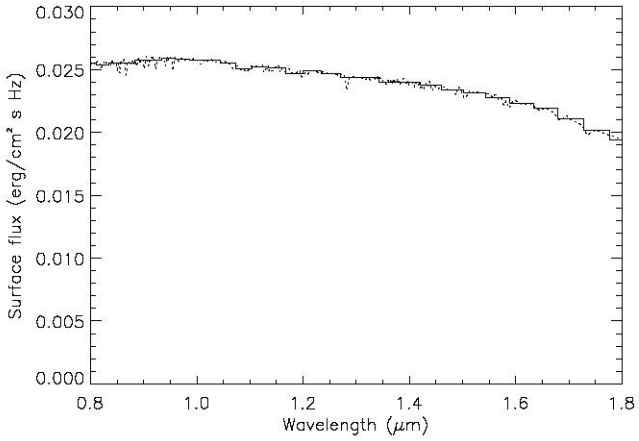


**Figure 3-4: NIR spectrum of a G2V star sampled with to different spectral steps corresponding to R=15 (solid line) and R=375 (dotted line). The plot does not include the telluric absorptions proper of the wavelengths range 0.8-1.8 [micron]. Notice the featureless profile of this stellar spectrum at different spectral resolutions. By courtesy of the CHEOPS[23] team.**

For ground-based observations aimed to SDI image analysis, the best window selection in the range 0.5-6.0 [micron] depends on the level of Sky Noise[24] with respect to the Background Noise of the star itself; actually this is not a request of SDI only, rather a constraint for any high contrast imaging technique working from ground. Sky Noise strongly limits SDI observations down to the K-band at last (i.e. $\lambda$<2.2 [micron]). However, by the models of Sudarsky et al. (2003), it appears clear that at temperatures T <1500 K the NIR

[23] CHEOPS was consortium of German, Italian, Swiss, Dutch and Portuguese Astronomical Institutes funded for an 18 months Phase-A study dedicated to the next VLT Planet Finder instrument (http://www.mpia-hd.mpg.de/CHEOPS/).

[24] For the definitions of Sky Noise see (Section 2.4.1).

planetary spectra are dominated by methane and water absorptions and the K-band is strongly depressed, specifically by the methane absorptions. This fact destroys any spectral feature, frustrating *de-facto* the aims of SDI. In principle, the K-band is suitable for SDI image analysis for planetary atmospheres with T >1500 only. This is due essentially to the carbon chemistry: the higher the atmosphere effective temperature is the higher the carbon percentage converted in carbon dioxide is. In this specific condition, the planetary spectrum is wealthy of features, and then attractive for SDI, for such high temperatures.

Dedicated studies, as the one undertaken by the CHEOPS team, shows that the best wavelengths bands for SDI image analysis of extrasolar planets from ground are the following: R, I, z', J, and H, covering the range 0.80-1.70 [micron]. As Figure 3-5 and Figure 3-6 explain, even after Speckle Noise subtraction, the Contrast[25] as a function of separation to the central star is nearly flat and low for wavelengths beyond the H-band; this happens because the Sky Noise dominates over these wavelength bands. As a conclusion, the achievable Contrast is highly reduced beyond the H-band for planets with atmospheric effective temperature T <1500K. Moreover the VISible edge of a planetary spectrum should contain polarized light (actually the fractional polarization from self-luminous planets is expected to be very small, typically lower than 1%, but significant asymmetries in clouds distribution can induce higher polarization). On this topic the CHEOPS team - as first - and now implemented in the SPHERE project (see Section 4), proposed an instrument for the next VLT Planet Finder that should be able to make accurate Polarimetric Differential Imaging (P-DI) in the wavelength range 0.60-0.90 [micron]: ZIMPOL (cfr. Gisler et al. 2004).

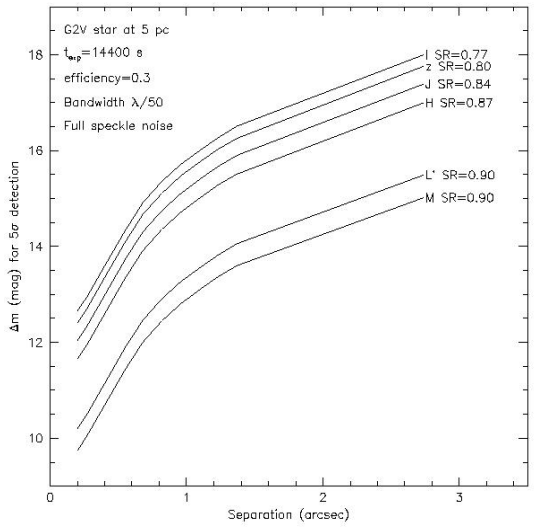


**Figure 3-5: Simulation of the Contrast (5σ detection threshold) vs. separation to the center for a G2V star a 5 pc in 4 hours observing time, efficiency 0.3, and spectral step equal to λ/50 without Speckle Noise subtraction: in this case a relation scale is valid over all the wavelength bands up to the M one. Curves are computed in different wavelengths band below the K-band limit with realistic SR levels for the AO-compensation of the signal coming from this model star (by courtesy of the CHEOPS team).**

[25] For the definitions of Constrast see (Section 2)

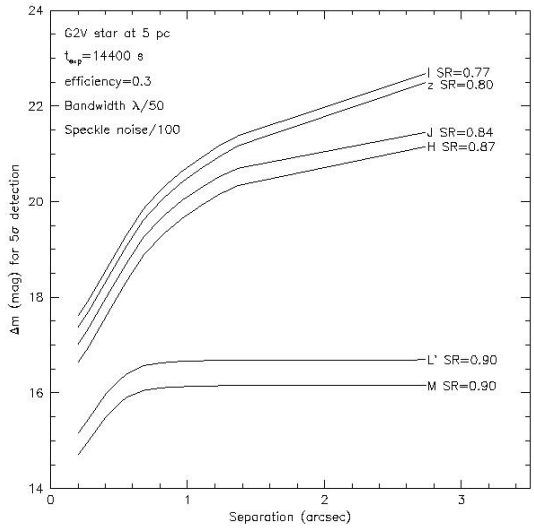


**Figure 3-6: Simulation of the Contrast (5σ detection threshold) vs. separation to the center for the same star of Figure 3-5 with Speckle Noise subtraction: in this case it comes clear that Sky Noise dominate L' and M bands and that the achievable Contrast vs. separation is nearly flat. Curves are computed in different wavelength windows below the K-band with realistic SR levels for the AO-compensation of the signal coming from this model star (by courtesy of the CHEOPS team).**

Summarizing, SDI image analysis supported by ground-based telescopes and an AO-compensation system, should be a useful technique for the direct detection of extrasolar planets with ages >100 [Myr], and having atmospheres with temperature T <1500 K, for selected observations in the I, z', J, H bands, or having atmospheres with temperature T >1500 K, for selected observations up to the K-band. At longer wavelengths (the MIR range) the Sky Noise dominates over the Background Noise of the target star, impeding further possibilities to this calibration technique.

## 3.2 Characterization of the telescope PSF with AO-compensation

Atmospheric turbulence severely limits the spatial resolution of a ground based telescope. AO is a powerful technique to overcome this limitation and to reach the diffraction limit condition.

AO compensates - in real-time - for the random fluctuation of the wavefront induced by the turbulent atmosphere. The turbulent wavefront is measured by Wave Front Sensor and optically corrected by a Deformable Mirror (DM). DM is characterized by the number of sub-mirrors that can be rapidly moved independently one to each others in order to compensate the phase differences of the Electric Field (EF) - that is the distortions of the wavefront of a beam coming from the scientific source - at the level of the telescope Entrance Pupil. This compensation allows to record high spatial resolution long exposure images. However, even if the scientific source (hereafter: the object) spatial frequencies are preserved up to the diffraction limit of the telescope, they are often severely attenuated since AO-correction is only partial. A degraded PSF still blurs the object.

In the following, the theoretical estimation of the object PSF is presented by the Fourier Transform (FT) formalism which describes the Fraunhofer propagation of the EF between the telescope Entrance Pupil Plane and the telescope Focal Plane (cfr. Born and Wolf 1965).

### 3.2.1 Computation of the telescope PSF before AO-compensation

The computation of the telescope PSF before AO-compensation requires to introduce the statistics of the phase ($\Phi$) of the EF across the Entrance Pupil. $\Phi$ is a random field described by two functions:

$$B_{\Phi}(f) = \langle \Phi(\rho) \cdot \Phi(\rho + f) \rangle \qquad \textbf{Equation 3-1}$$

or the correlation function of the phase and

$$D_{\Phi}(f) = \langle [\Phi(\rho) - \Phi(\rho + f)]^2 \rangle \qquad \textbf{Equation 3-2}$$

or the structure function of the phase. The symbol < > denotes the expectation over turbulence realizations, the term $\rho$ is an a-dimensional coordinate across the Entrance Pupil that ranges between **[-1, 1]**, the term **f** represents a spatial frequency normalized to the telescope cutoff frequency $\mathbf{f_C=(F\cdot\lambda)^{-1}}$, where **F** is the telescope Focal Ratio and $\lambda$ is the wavelength at which the WFS measures the phase variations of the EF.

The Optical Transfer Function (OTF) of the telescope- i.e. the FT of the telescope PSF - is given by:

$$OTF(f) = \int_{-1}^{1} [P(\rho) \cdot P(\rho + f)] \cdot \exp\left\{-\frac{1}{2} \cdot D_{\Phi}(f)\right\} \cdot d\rho \qquad \textbf{Equation 3-3}$$

where **P(f)** is the Entrance Pupil Transmission Function. In the case of homogeneous transmission by the telescope optics, the Entrance Pupil Transmission Function gets the functional form of a top-hat function ($\Pi$) with unitary size[26]:

$$P(f) = \Pi(f) \equiv \begin{cases} 1, & \text{if } |f| \le \frac{1}{2} \\ 0, & \text{if } |f| > \frac{1}{2} \end{cases} \qquad \textbf{Equation 3-4}$$

Then, the telescope PSF before AO-compensation is:

$$PSF(x) = FT[OTF(f)] \qquad \textbf{Equation 3-5}$$

The term **x** represents the spatial coordinate on the telescope Focal Plane normalized to the diffraction limited spatial resolution: $\mathbf{x_{DL}=F\cdot\lambda}$.

### 3.2.2 Computation of the telescope PSF after AO-compensation

The computation of the PSF after AO-compensation should take into account the residual phase distortions of the EF across the Entrance Pupil. This residual phase signal can be represented as a new random field ($\mathbf{\Phi_{RES}}$) described by its correlation and structure functions (cfr. Fusco et al. 2000).

Conan (1994) and Véran (1997) have shown that $\mathbf{\Phi_{RES}}$ is a random field that remains quasi-stationary. With this assumption the OTF expression becomes:

---

[26] When spatial frequencies unit is $[mm]^{-1}$, this top-hat function has size equal to $\mathbf{f_C}$.

$$OTF(f) = OTF_0(f) \cdot \exp\left\{-\frac{1}{2} \cdot D_{\Phi_{RES}}(f)\right\} \qquad \textbf{Equation 3-6}$$

$$OTF_0(f) = P \oplus P(f)$$

**$OTF_0$** - defined as the auto-correlation of the Entrance Pupil Transmission Function - is the telescope OTF, while the exponential term is called Residual Atmospheric OTF. Then - according to the convolution theorem - the AO-compensated telescope PSF is the convolution between the FT of the telescope OTF and the residual atmospheric OTF (**RAOTF**).

$$PSF(x) = FT[OFT_0(f) \cdot RAOTF(f)] = \{PSF_0 \otimes FT[RAOTF(f)]\}(x) \qquad \textbf{Equation 3-7}$$

For a circular telescope Entrance Pupil without Central Obscuration parameter[27] (**ε**), the term **$PSF_0$** is proportional to the Bessel-J-Function of order one (cfr. Born and Wolf 1965):

$$PSF_0(x) = I_C \cdot \left(\frac{2 \cdot J_1(\pi \cdot x)}{\pi \cdot x}\right)^2 \qquad \textbf{Equation 3-8}$$

For a circular telescope Entrance Pupil with Central Obscuration parameter (**ε**), the term **$PSF_0$** is equal to (cfr. Schroeder 1987):

$$PSF_0(x) = I_C \cdot \left(\frac{1}{\left(1-\varepsilon^2\right)^2}\right) \cdot \left(\frac{2 \cdot J_1(\pi \cdot x)}{\pi \cdot x} - \varepsilon \cdot \frac{2 \cdot J_1(\varepsilon \cdot \pi \cdot x)}{\pi \cdot x}\right)^2 \qquad \textbf{Equation 3-9}$$

In both cases the term **$I_C$** represents the central intensity of the EF reaching the telescope Focal Plane.

Facing with the residual phase random field **$\Phi_{RES}$**, the term dominating the OTF becomes the atmospheric OTF, more precisely the structure function contained is this term: **$D_{\Phi RES}(f)$**. According to the formalism of Fusco et al. (2000), **$D_{\Phi RES}(f)$** is the spatially averaged residual phase structure function:

$$D_{\Phi_{RES}}(f) = \frac{\int_{-1}^{1} \left\langle \left[\Phi_{RES}(\rho) - \Phi_{RES}(\rho + f)\right]^2 \right\rangle \cdot \left[P(\rho) \cdot P(\rho + f)\right] \cdot d\rho}{\int_{-1}^{1} \left[P(\rho) \cdot P(\rho + f)\right] \cdot d\rho} \qquad \textbf{Equation 3-10}$$

This averaged signal becomes zero for **f=1** when the Tip Tilt Mirror (TTM) is acting on the turbulent wavefront. This means that at the telescope cutoff frequency, the term **RAOTF** goes to zero just when the AO-system works in a closed loop, or equivalently it means that in telescope Focal Plane the PSF reaches its diffraction limit inside the region comprised between the boundary **[-λ·F, λ·F]**.

Differently, for normalized spatial frequencies with absolute value **|f|<1**, AO-corrections made by the DM is not able to reduce to zero the spatially averaged residual phase structure function. This means that for these spatial frequencies the term **RAOTF** is not zero, or equivalently that in the Focal Plane the telescope PSF does not reach its diffraction limit out

[27] In a two mirrors telescope the Central Obscuration parameter is defined as the ratio between the clear apertures of the smallest and the largest mirror.

the region comprised in the boundary **[-λ·F, λ·F]**. Then, outside this diffraction limited range, the right expression of the telescope PSF - still inside the AO Control Radius - remains the one of Equation 3-7.

### 3.2.3 Definition of the Speckle pattern field

Inside the AO Control Radius, the Speckle pattern field can be defined as the FT of the residual atmospheric OTF i.e.:

$$Sp(x) = FT[RAOFT(f)] \qquad \textbf{Equation 3-11}$$

A heuristic interpretation of the Speckle pattern field in term of the Fried's coherence length[28] (**$r_0$**) and of the telescope Entrance Pupil size (**D**) is given by Racine et al. (1999). More in detail, they noticed that the short-exposure image of a point source, focused by the telescope optics on a given detector, can be interpreted as the interference pattern of light from many coherent patches - of typical diameter **$r_0$** - distributed over the full aperture of the telescope. For a single **$r_0$**-size sub-pupil where phase coherence is preserved, the focal plane image should be a diffraction limited PSF of width **$\sim\lambda/r_0$**. Two such sub-pupils with the same phase coherence and separated by a distance **$\sim D$**, constitute a two-beam interferometer. Then, the PSF they produce should be a pattern of linear interference fringes normal to line joining the sub-pupils, modulated by the diffraction pattern of a single sub-pupil, and of width **$\sim\lambda/D$**. As a result of the randomly differential-phase variation between these two coherent sub-pupils, they move within the broad PSF envelope. Introducing others sub-pupils produce different patterns of interference fringes. When these patterns interfere constructively, they finally produce what actually is measured in the telescope Focal Plane, that is a pattern of enhanced bright Speckle of width **$\sim\lambda/D$**. Following the work of Roddier et al. (1982), Racine et al. (1999) give the numerical density (per unit area) of the Speckle pattern for a given telescope Entrance Pupil of size **D**:

$$n_{Sp} = \frac{0.342}{\pi \cdot \left(\frac{\lambda}{D}\right)^2} \qquad \textbf{Equation 3-12}$$

What is important to note in Equation 3-12 is that - adopting the quantum approach for the propagating EF - the Speckle signal produces a constant flux on the focal plane because its number density remains constant over time. This behaviour indicates that photo-events generated by the Speckle pattern are not independent, as the ones proper of the central object, and they do not follow the Poisson statistic. Then, a new definition of Noise should be given for this quantum-statistic ensemble (see Section 3.3). Moreover, in AO-compensated images, a fraction of the object photo-events flux (**$F_S$**) equal to the SR is transferred into the a bright central Speckle with size **$\sim 2\lambda/D$**, leaving the rest of the photo-events flux - proper to the object - equal to **$(1\text{-}SR)\cdot F_S$**. This Speckle flux, averaged by time, produces a smooth long-exposure halo (cfr. Racine at al. 1999).

[28] For the definition of the Fried's coherence length see: **Introduction to Adaptive Optics**, SPIE Tutorial Text in Optical Engineering Vol. TT41.

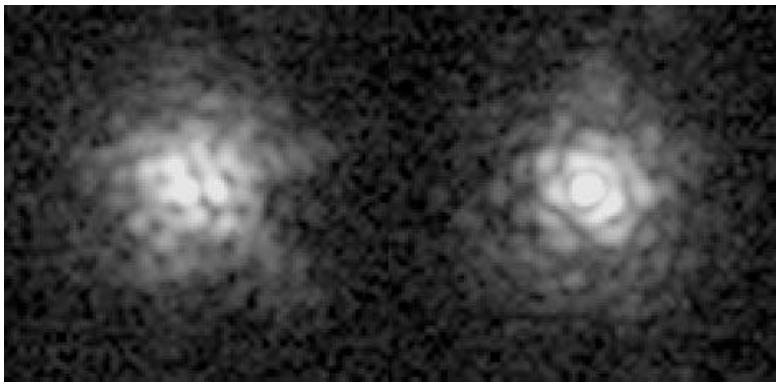

**Figure 3-7: Short-exposure (0.1 sec) natural (left) and AO-compensated (right) images of a star obtained with the CFHT "bonnette" AO-system at $\lambda$=1.6 [micron] and $D/r_0$~4. The grey scale is logarithmic in intensity (from Racine et al. 1999). Notice that the increasing Speckle brightness toward the PSF center and the appearance of the bright diffraction limited core with size ~2$\lambda$/D.**

Finally, in addition to the Speckle pattern field produced by the residual - not AO-compensated - phase distortions, a Super-Speckle pattern field - due to differential phase aberrations downstream of the AO-system - will be always present. The big difference between Super-Speckle and Speckle pattern fields is the time-scale of variations. Ideally, for instrumental setups with extreme optical quality, the Super-Speckle pattern field varies more slowly than the first one; this is why it is often called *Quasi-Static-Speckle pattern*.

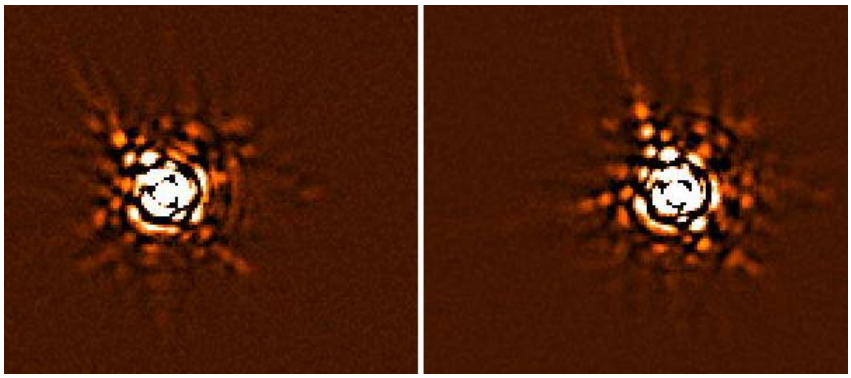

**Figure 3-8: Quasi-static Speckle pattern. The images show the high spatial frequency content of long exposures taken with NACO at the VLT separated by about one hour (from Vérinaud et al. 2006).**

### 3.2.4 Computation of the PSF beyond the AO Control Radius

Following the definition of Section 2.4.3.2, the monochromatic Control Radius is **$\lambda$/2d,** where **d** is the inter actuator spacing as projected on the telescope primary mirror. This angular scale defines the boundary of the DM corrections on the phase **$\Phi$** - proper to the object EF - across the telescope Entrance Pupil. This means that, for angular separations greater than **$\lambda$/2d** on the telescope Focal Plane, AO-systems are not able to correct variations of this random field.

A useful parameterization of the AO-uncorrected halo of the telescope PSF is given again by Racine et al. (1999), using a convenient Moffat's profile for angular separations from the telescope optical axis ($\theta$) verifying the condition **$|\theta|>\lambda$/2d:**

$$PSF_{halo}(\theta) = \frac{0.488}{W_{halo}^2} \cdot \left[ 1 + \frac{11}{6} \cdot \left( \frac{\theta}{W_{halo}} \right)^2 \right]^{-\frac{11}{6}}$$ **Equation 3-13**

In this formula $W_{halo}$ represents the angular position at which the normalized Encircled Energy (EE) contained of this PSF profile is 25 %.

## 3.3 Speckle Noise

The shape of Speckle pattern field change randomly over small fractions of second. Dividing the acquisition intervals of a Focal Plane detector in $\tau_0$ unit ($\tau_0$ being defined as the inverse of the Greenwood's temporal frequency[29]), after each $\tau_0$ interval, and in a fixed area of the detector, the number of photo-events corresponding to the Speckle pattern signal changes, but the statistical variation of the recorded photo-events number is not caused by the intrinsic random nature of the Speckle pattern; at contrary it is due to the variance of the relative number of photo-events due the Speckle pattern itself in a specific patch of the Focal Plane detector. Substantially, in the angular range of the PSF where AO compensates partially for the phase distortions of the EF across the telescope Entrance Pupil - i.e. the AO Control Radius - Speckle Noise arises as the RMS of the number density of the photo-events due to the Speckle signal. In other words, as the Speckle pattern evolves, Speckles grow and fade across a fixed boundary of the PSF area and the total flux in this area fluctuates (cfr. Racine et al. 1999).

The enormous complexity of the Speckle Noise forces to avoid any analytical treatment of it and to plunge in the numerical simulations domain, where atmospheric parameters ($\mathbf{r_0}$, $\tau_0$,...) together with telescope, AO-system and Coronagraph specifications ($\lambda$, **F**, **SR**, **OWA**, **IWA**,…)[30] are inputs to Codes by which realistic screens of the residual phase distortions are generated; then Speckle pattern fields are obtained via phase screens Monte Carlo extractions and the RMS of the number density of photo-events - i.e. the Speckle Noise - is obtained over a fixed pixels patch of a simulated detector. The simulated Speckle Noise is thus compared with the ones stored during observation at the telescope. The comparison between simulated and real Speckle Noise fields allows to test various calibration techniques aimed to decrease the impact of this pattern, in order to reach strong signal attenuation (or *high contrast regime*) in the AO-compensated part of the telescope PSF. The purposes of calibration techniques like SDI (see Section 3.4) and S-SDI (see Section 3.5) is to obtain direct images of faint companions around target stars in the Galaxy. The challenge is to obtain direct images of the faintest population i.e. the one of extrasolar planets.

[29]For the definition of the Greenwood temporal frequency see: **Introduction to Adaptive Optics**, SPIE Tutorial Text in Optical Engineering Vol. TT41.

[30] For the definition of all the abbreviations adopted in this Section see the opening list.

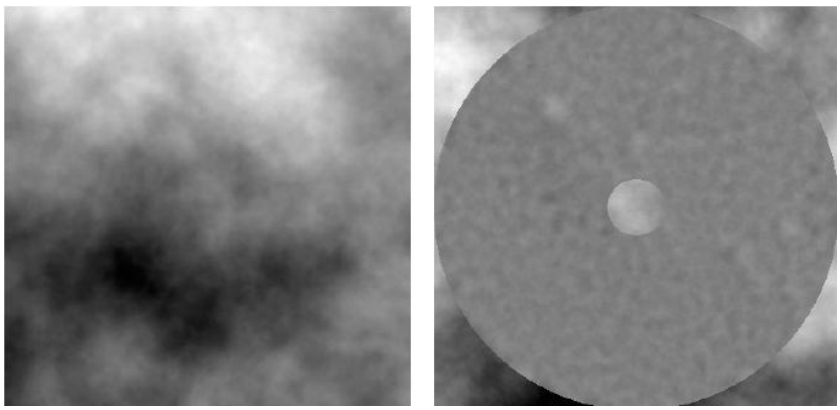

**Figure 3-9: Example of adopted phase screen in the Speckle Noise simulator Code described in Berton et al. (2006), by courtesy of the CHEOPS team. At left: a phase screen produced by software CAOS (cfr. Carbillet et al. 2004) representing a perturbed wavefront not corrected by Adaptive Optics. At right: the same phase screen AO-compensated.**

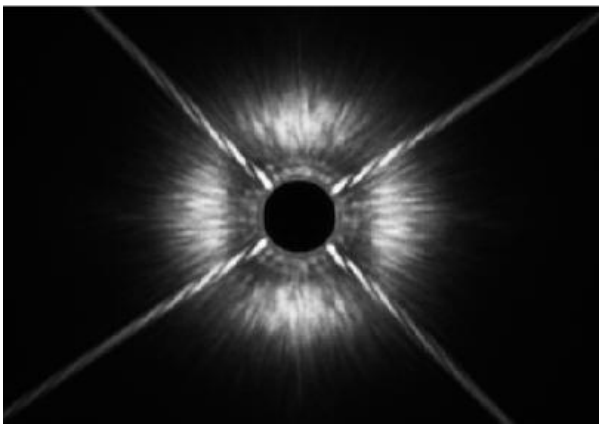

**Figure 3-10: Example of simulated Speckle pattern with coronagraphic spatial filtering of the coherent part of the central PSF with the Speckle Noise simulator Code described in Berton et al. (2006), by courtesy of the CHEOPS team. The object is a G0V star, the Entrance Pupil size is 8 m and its shape is proper of a VLT telescope in the Nasmyth configuration, the integration time is 0.5 [sec] and the adopted Entrance Pupil phase screens assumes SR~0.8.**

What comes out of these Numerical Simulations is that Speckle Noise dominates by a factor $10^2$- $10^4$ over other Noise contributions in the AO-compensated region of a telescope PSF, depending on the distance of the target star and its spectral type. Figure 3-11 explains clearly this fact: the comparison of the Background (or Photon) Noise related to the central star with the Speckle Noise indicates that the second one is the major source of Noise for calibration techniques aimed to reach a high contrast regime. Moreover, in the same Figure it is shown that - at the level of simulations - Photon Noise threshold can be reached with these calibration techniques over an adequate range of separations from the central star suitable for the direct detection of extrasolar planets. Notice that the simulations considered in the preparation of Figure 3-11 assume a Speckle patter field due to atmospheric turbulence only.

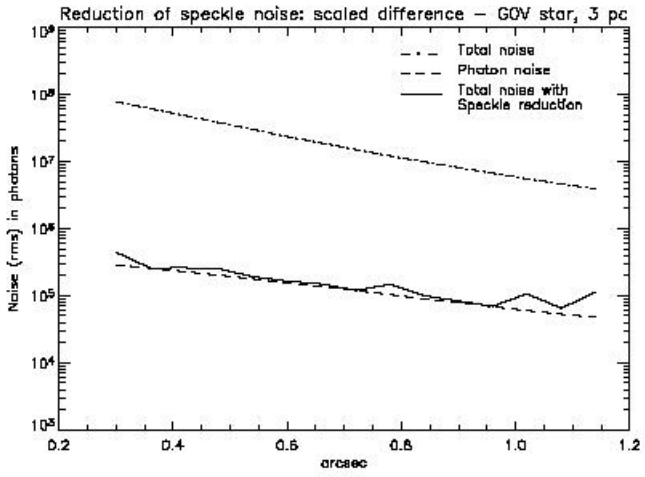


**Figure 3-11: Comparison between the speckle noise (dash-dotted line), the photon noise (dashed line), and the noise in the differential image (solid line) obtained using the Speckle Noise simulator Code described in Berton et al. (2006) - by courtesy of the CHEOPS team - as a function of separation for a simulated G0V star at 3 pc from Earth. The ratio between the Speckle and Photon Noises is $10^2$. Notice that the simulations considered in the preparation of this figure assume a Speckle patter field due to atmospheric turbulence only.**

## 3.4 SDI at the diffraction limit

In details, SDI is an instrumental method which can be used to calibrate (first step) and then remove (second step) the Speckle Noise (see Section 3.3) in the limited portion of the telescope Focal Plane, where an AO-system is able to compensate for distortions of the phase random field (**Φ**) and to restore totally (inside the angular range ~**2λ/D**) or partially (outside the angular range ~**2λ/D** but still inside the angular range ~**2λ/d**) the diffraction limited condition of the telescope PSF (see Section 3.2.2). As discussed in Section 3.1, the second step of SDI - i.e. the simultaneous image acquisition at adjacent wavelengths in a spectral range where the planetary and stellar spectra differ appreciably - is suitable from ground-based observations in the wavelength range 0.80-1.70 [micron] for all the realm of planets having atmospheres with T <1500 K and in the K-band too, for the warmest, that is those having atmospheres with T >1500 K.

Let be **S(λ)** (in [erg·sec$^{-1}$·cm$^{-2}$]) - the spectral signal corresponding to a fixed angular position **θ** around the central target star which verifies the condition: **|θ|<λ/d**. Generally, this spectral signal can be expressed as the sum of the spectral signal of the central star corresponding to this angular position: **s(λ)**, and the spectral signal of a low-mass companion candidate (hopefully an extrasolar planet) proper - specifically - to this angular position: **p(λ)**. Then, fixing a wavelength range **[$\lambda_1$-$\lambda_2$]** inside the window 0.80-1.70 [micron], the following relations hold:

$$S(\lambda_1) = s(\lambda_1) + p(\lambda_1)$$
$$S(\lambda_2) = s(\lambda_2) + p(\lambda_2)$$

**Equation 3-14**

Basic SDI assumption is that after suitable flux normalization and chromatic re-scaling, the following relations hold for the boundary wavelengths of the range above:

$$p(\lambda_2) = 0$$
$$s(\lambda_1) = s(\lambda_2)$$

**Equation 3-15**

Then, the difference between $\mathbf{S(\lambda_1)}$ and $\mathbf{S(\lambda_2)}$ should return - in principle - the spectral signal $\mathbf{p(\lambda_1)}$ only, i.e. the one proper to the low-mass (or extrasolar planet) candidate.

The main difference between SDI and Spectroscopic-SDI (or S-SDI) lies on the definition of the wavelength $\lambda_1$ and $\lambda_2$. For instruments making SDI, $\lambda_1$ and $\lambda_2$ represent actually the central wavelengths of two narrow-band chromatic filters, which bandwidths $\Delta\lambda_1$ and $\Delta\lambda_2$. While, for S-SDI, $\lambda_1$ and $\lambda_2$ are properly wavelengths and the range $[\lambda_1-\lambda_2]$ represents the spectral step by which a suitable Disperser spectrally samples the total signal $\mathbf{S(\lambda)}$. A general presentation of S-SDI is given in Section 3.5, while Sections 5 and 6 describe all the optical aspects of the first instrument commissioned by ESO which exploits this new calibration technique: SPHERE/IFS.

While working with narrow-band filters, a number of precautions are required for optimal results. As suggested by Marois et al. (2000), the important items are substantially three:

- The scale length of an image taken with one narrow-band filter has to be re-scaled before confronting it with a second image taken with a different narrow-band filter. This is due to the fact that both the images are dominated by the Speckle Noise and this latter is chromatic because its scale depends linearly on wavelength (the heuristic explanation of this fact is that the size of a single monochromatic Speckle signal is $\sim\lambda/D$).
- Any narrow-band filter separating two adjacent spectral bands should have trasmissivity as similar as possible.
- The difference between the central wavelengths ($\lambda_i$ , $\lambda_j$) of two adjacent narrow-band filters with bandwidth $(\Delta\lambda_i , \Delta\lambda_j)$ should be as small as possible.

The last item is the most critical due to the fact the chromatism of the Speckle pattern always induces a certain amount of phase errors depending on the difference between the narrow-band filters central wavelength: $\delta\lambda_{ij}$. Following the approach of Marois et al. (2000), a residual wavefront distortion - which appears as an instantaneous Speckle pattern field on the telescope Focal Plane - can be described through a linear optical path difference ($\delta$), or by its relative chromatic phase error: $\Phi=2\pi\delta/\lambda_i$, on the telescope Entrance Pupil plane. Then, defining the Noise RMS of this chromatic phase error as $\sigma_\Phi(\lambda)$, and adopting the Maréchal's approximation for the Strehl Ratio: $SR(\lambda)=\exp[-\sigma^2_\Phi(\lambda)]$, the following relation for the flux residual between images taken with two narrow-band filters holds (cfr. Marois et al. 2000):

$$\frac{\Delta S_{ij}}{S_i} = 2 \cdot \sigma^2_\Phi(\lambda_i) \cdot \frac{\delta\lambda_{ij}}{\lambda_i}$$

**Equation 3-16**

Specifically, Equation 3-16 represents the relative flux residual coming out from the Speckle Noise subtraction of simultaneous images taken with the filters labeled as: **i, j**. Marois et al. (2000) - as first - proposed to alleviate the problem of the Speckle Chromatism with more complex image processing receipts, like e.g. the *Double Difference* method. Specifically, it foresees to make differences among images taken at 3 wavelengths: $\lambda_i$, $\lambda_j$, $\lambda_k$ and to combine them as follows:

$$\Delta S = (S_i - S_j) - k \cdot (S_i - S_k)$$

$$k \equiv \frac{SR_i - SR_j}{SR_i - SR_k}$$ **Equation 3-17**

The Double Difference method is able to keep low the residual flux due to the Speckle Chromatism and it should be adopted by any DRSW built to manage with SDI image processing. Moreover, general prescriptions for DRSW dealing with the Speckle Chromatism - in the specific case of S-SDI - have been proposed by Sparks and Ford (2002) (see Section 3.5.2). However, as described in details in Section 5, Speckle Chromatism can be compensated even directly, with specific precautions leading to an optimization of the optical design, when Integral Field Spectroscopy is adopted for SDI purposes. On the contrary, any SDI instrument suffers from differential aberrations as the optical signal is chromatically separated before reaching the detector and a certain amount of phase diversity, due to the non-common path of the beams, will always be present. Moreover, these aberrations do not depend on the optical quality level both of the incoming signal and of the instrumental setup: ideally they should be present also if the incoming signal were Speckle-free or if the instrumental setup got **SR**=1. Thus, these are non-common path static aberrations, which generate a differential RMS wavefront error - $\Delta(\sigma_\Phi)$ - among SDI chromatic Exit Pupils. Adopting again the Maréchal's approximation for the Strehl Ratio, it is possible to transfer this RMS wavefront error on a relative flux variation on the detector/s plane:

$$\frac{\Delta S_{ij}}{S_{ij}} \propto 2 \cdot \Delta_{ij}(\sigma_\Phi^2)$$ **Equation 3-18**

Specifically, Equation 3-18 indicates that the relative flux residual, obtained with simultaneous difference, is proportional to the delta-phase wavefront error Variance on the Exit Pupils, corresponding to the chromatic filters **i, j**. As a conclusion, non-common path static aberrations represent a pathology which severely limits the performances of the standard[31] SDI instrumentation in obtaining high contrast imaging regimes, suitable for the direct detection of extrasolar planets. However, SDI devices have produced already a number of important scientific results. For example: the discovery of AB Dor C (Close et al. 2005) which is the tightest (0.16 [arcsec] separation) low-mass companion detected by direct imaging, detailed surface maps of Titan (Hartung et al. 2004), the discovery of ε Indi Ba-Bb, the nearest binary brown dwarfs (McCaughrean et al. 2004), and evidence of orbital motion for Gl 86 B, the first known white dwarf companion to an extrasolar planet host star (Mugrauer and Neuhäuser 2005). All these observational successes are due to the SDI facilities installed at the VLT (NACO-SDI) and at the MMT (cfr. Biller et al. 2006). Both these instruments use a double Wollaston Prism and a 4Q chromatic filter to take 4 simultaneous images at 3 wavelengths, close to the 1.62 [micron] methane band head found in the spectrum of cool brown dwarfs and expected in extrasolar giant planet spectra (see Figure 3-12). By performing a difference of images in these narrow-band filters, Speckle Noise can be significantly attenuated, resulting in Photon Noise limited data (see Figure 3-13). The achieved H-band Contrast is **C**>2.5x10$^4$ that corresponds to a magnitude difference of 11.5 mag. for a T6 spectral type. In principle, these facilities could image (5σ

[31] The instrument proposed by Marois et al. (2004) should be mentioned, for completeness, as a non-standard SDI device which is able - in principle - to attenuate non-common paths static aberrations through a fine-tuned optical approach (see references of this article in Section 3.6).

detection threshold) a 2-4 $M_{JUPITER}$ planet a 5 AU around a 30 [Myr] star at 10 pc from Earth (cfr. Biller et al. 2006).

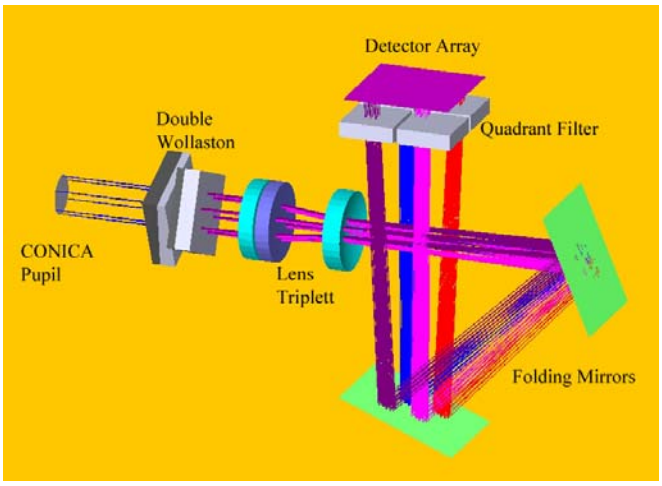


**Figure 3-12: A 3D-view of NACO-SDI optical design, by courtesy the CHEOPS team. The double Wollaston Prism separates the beam coming from the AO-Camera Focal Plane in 4 parts. Then, the Camera re-images the Focal Plane of the telescope on 4 distinct 1024 x 1024 array detectors. Before the focus, a 4Q chromatic narrow-band filter is inserted to obtain simultaneous images in 3 different wavelengths.**

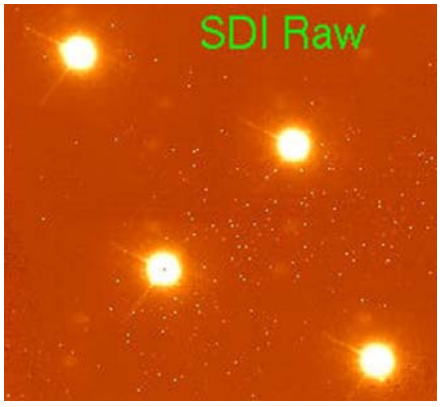


**Figure 3-13: Raw images on the focus of NACO-SDI, by courtesy of the CHEOPS team. The simultaneous difference between them strongly attenuates the Speckle Noise.**

For completeness, another SDI facility is currently mounted at CFHT and OMM telescopes i.e. the TRIDENT Camera (see Figure 3-14). This instrument is based on a Hawaii-1 1024 x 1024 HgCdTe array detector and it mounts a classic Lyot Coronagraph (cfr. Malbet 1996) upstream. TRIDENT can detect (6σ detection threshold) a methanated low-mass companion with $\Delta H$=9.5 mag. at separation 0.5 [arcsec] from the star in 1 hour observing time. Instrument rotation and reference-star subtraction improve the detection limit by a factor of 2 and 4, respectively (cfr. Marois et al. 2005).

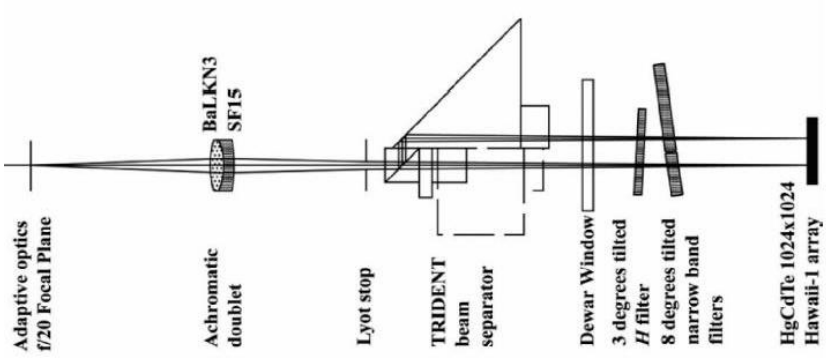


**Figure 3-14: Optical sketch of the TRIDENT Camera mounted at CFHT and OMM. After the Lyot Stop, the beam separator uses a combination of 2 polarizing beam splitters, 2 right-angle Prisms, and a first order quarter-wave retarder to generate 3 optical beams, each one organized in a "L"-shape reproducing - as a whole - the shape of a trident.**

## 3.5 Integral Field Spectroscopy at the diffraction limit: S-SDI

Integral Field Spectroscopy (IFS), coupled with Extreme Adaptive Optics (XAO) and Coronagraphy, represents - in principle - a powerful technique for the detection and characterization of extrasolar planets (Vérinaud et al. 2006). The simplest explanation for this statement is a matter of methodology: SDI was originally proposed for two wavelengths only and for a simple difference operation. Marois et al. (2000) showed than that the Speckle Noise reduction can be much more efficient if observations at three wavelength are available, using the Double Difference method (see Section 3.4). Starting from here, it is reasonable to assume that a larger number of images at different wavelengths, taken with a small regular spectral step, can result in even better reduction of Speckle Noise with S-SDI calibration technique. This thought suggests the use of IFS for collecting data simultaneously at a large number of different wavelengths, given by the total spectral length and the spectral resolution of a suitable disperser. Specifically, the purpose of IFS for the direct detection of extrasolar planets - then working in diffraction limited condition - is to exploit the spectral features of the sub-stellar companions (hopefully an extrasolar planet) in order to increase the Contrast on the stellar background and then to use S-SDI for attenuating the Speckle Noise at the level of the Photon Noise (cfr. Berton et al. 2006).

Before choosing an IFS concept, optical analysis based on deep understanding of how to handle the residual Speckles pattern and the Coherent/Incoherent cross-talks among spectra (see Section 5) is required. More in detail, the behavior of the residual Speckle pattern field has to be analyzed in terms of its spectral and spatial Power Spectral Densities, while 2D-simulations of the optical propagation from the re-imaged telescope Focal Plane up to the IFS Entrance Slits plane are mandatory in order to estimate the impact of Coherent/Incoherent cross-talks in the final matrix of spectra generated by an IFS device. This kind of analysis defines the basic technical requirements of such an instrument, while other technical requirements depend directly on the specificities of different optical concepts able to realize Integral Field Spectroscopy[32]. Within the SPHERE project, experiments with an IFS prototype were also done, allowing to verify the concepts developed in this Dissertation.

[32] Hereafter the terms Integral Field Spectroscopy (IFS) and 3D-Spectroscopy are synonymous.

### 3.5.1 Requirement and Options

3.5.1.1 Requirement for the spatial sampling of the re-imaged telescope Focal Plane

According to Racine et al. (1999) and the SDI arguments of Section 3.4, in AO-compensated images, the fraction of the spectral signal of the central star (**s(λ)**), corresponding to an angular position **θ** and verifying the condition: **|θ|<λ/d**, will be **1-SR(θ)** times the diffraction limited central value. Differently, the spectral signal due to a candidate planet (**p(λ)**) in this specific angular position will be **SR(θ)** times its diffraction limited value. Then, for a given star vs. planet Contrast (**C**) and a given Strehl Ratio **SR(θ)**, the following relation characterizes the actual measured flux-Contrast on the detector/s of a SDI instruments:

$$\frac{s(\lambda_1)}{p(\lambda_1)} = \frac{1-SR(\theta)}{SR(\theta)} \cdot C \qquad \textbf{Equation 3-19}$$

Equation 3-19 indicates that for a given Contrast (**C**=$10^8$ in the NIR domain for of a Jupiter-like planet, while **C**=$10^{10}$ domain in the case of an Earth-like planet, see Figure 2-1) the signal of the star - thus its Photon Noise - can be attenuated with respect to the planet signal only if a suitable AO-system compensates for the residual Speckles pattern.

In the case of IFS, Equation 3-19 should be expanded as follows:

$$\frac{s(\lambda_1)}{p(\lambda_1)} = \frac{1-SR(\theta)}{SR(\theta)} \cdot C \cdot \left( \frac{N_{Im}^{P}}{N_{Im}^{S}} \right)^2 \qquad \textbf{Equation 3-20}$$

Where $\mathbf{N_{Im}^{S}}$ is defined as the number of spaxels[33] that spatially sample the monochromatic central PSF, while $\mathbf{N_{Im}^{P}}$ is defined as the number of spaxels that spatially sample the planet monochromatic signal where this latter is higher than the Photon Noise of the central star, after the Speckle Noise attenuation procedure.

Equation 3-20 indicates that for a given Constrast and an AO-compensation, the detection capability of an IFS instrument is - in principle - much higher then for standard SDI instruments. Then, IFS should realize a sound improvement on the high contrast imaging thresholds reachable by ground-based observations. This capability lies basically on the spatial sampling of the central PSF through the parameter $\mathbf{N_{Im}}$. As a conclusion, the Nyquist's[34] sampling condition on the IFU plane is needed for:

- Lowering the measured flux ratio on the IFS detector/s, for a given star vs. planet Contrast and AO-compensation capability.
- Correctly sampling the spatial profile of a planetary spectral feature.

---

[33] The term *spaxel* indicates a spatial pixel proper to the IFS sub-system called Integral Field Unit (IFU). IFU in turn indicates the matrix of spaxels which should be placed on the re-imaged telescope Focal Plane, working as an optical field-stop array.

[34] For the definition of the Nyquist's sampling condition (alias Whittaker-Shannon Sampling Theorem) see Goodman, Joseph W., **Introduction to Fourier Optics**, 2nd ed., Publisher: New York, NY: McGraw-Hill, 1996. Series: McGraw-Hill series in electrical and computer engineering; Electromagnetic. ISBN: 0070242542.

As an example, during the Phase-A study conducted by the CHEOPS team, it was found that, for a Contrast value **C**=$10^8$ on the sky, a flux ratio ~$10^4$ should be reachable on the IFS detector/s plane, when the Nyquist's sampling condition is verified on the IFU plane. Specifically, this conclusion was obtained adopting the following set of parameters: range of angular separations from the central star $0.50<\theta<2.50$ [arcsec], range of wavelengths $0.95<\lambda<1.35$ [micron] and average Strehl Ratio value **SR**=0.90.

3.5.1.2 Options for the optical design

What is extremely demanding for 3D-Spectroscopy is the need of a conspicuous number of pixels on the detector plane where the matrix of spectra is acquired and a specific DRSW generates a certain number (equal to the spectral resolution of a suitable disperser) of monochromatic images in order to make S-SDI. This issue is particularly important when spectral and spatial information is recorded simultaneously in the detector plane, such as in Image Slicer or TIGER-type instruments. The Image Slicer option (see Figure 3-15 a) is more efficient in terms of detector pixels usage, since no separation between spectra from adjacent pixels is required. The number of detector pixels ($\mathbf{N_{Det}^2}$) required for a given number of spaxel ($\mathbf{N_{Im}^2}$) and spectral samples ($\mathbf{N_{Spec}}$) is given by the following relation:

$$N_{Det} \approx N_{Im} \cdot \sqrt{N_{Spec}} \qquad \textbf{Equation 3-21}$$

In the TIGER-type option (see Figure 3-15 b), where spectra are interleaved in a more intricate manner, a separation between spectra is necessary. For a separation of $\mathbf{N_{Sep}}$ spectral samples, the required number of detector pixels becomes:

$$N_{Det} \approx N_{Im} \sqrt{N_{Spec} \cdot N_{Sep}} \qquad \textbf{Equation 3-22}$$

For a typical separation of 5-10 pixels, depending upon detailed design and cross-talk requirements, the TIGRE-type is up to 3 times hungrier in terms of linear detector dimension than the Image Slicer option.

For the Fourier Transform Spectrograph (FTS, see Figure 3-15 c) the situation would be of course different. Here, the spectral information is obtained by scanning the optical path difference between the arms of a Mach-Zehnder interferometer. The detector is therefore entirely dedicated to the spatial dimensions, so that:

$$N_{Det} \approx N_{Im} \qquad \textbf{Equation 3-23}$$

This constitutes an enormous advantage for the FTS option, both in terms of detector real-estate (the detector cost is a major part of present-day instruments) and instrumental dimensions and complexity, which is strongly related to the size and resolution of the final image, i.e. the number of detector pixels, $\mathbf{N_{Det}}$. An interferometric setup and a cryogenic scanning mechanism certainly add complexity to the system (cfr. Vérinaud et al. 2006).

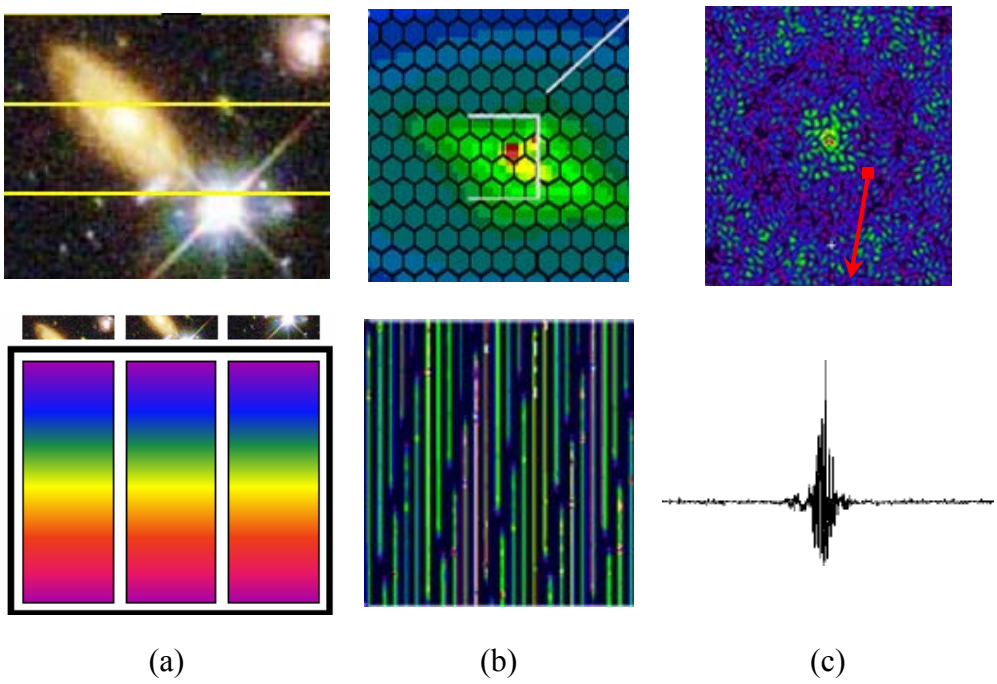


**Figure 3-15: Schematic comparison of three Integral Field Spectrograph concept: Image Slicer Spectrograph (a), TIGER-type Spectrograph (b), FTS (c), from Vérinaud et al. (2006).**

However, the Image Slicer presents a serious drawback when a Speckle-dominated signal feeds the IFU. In fact - as Figure 3-16 shows clearly - in this concept a bi-dimensional FOV is divided by mirrors, in the spaxels plane, and then re-formatted in a mono-dimensional pseudo long slit; this latter representing the Entrance Slit Line of the IFS. Monochromatic Exit Slits will be then obtained downstream, by using a standard Collimator, Disperser and Camera optical system. What appears extremely painful in the case of a Speckle-dominated signal is to measure the non-common path aberrations acting on the bundle of monochromatic signals proper to a fixed spaxel on the FOV, and then reaching the detector pixels with an unknown budget of chromatic differential phase aberrations. This specific issue was indicated a show stopper for the Image Slicer option by the VLT-PF[35]team. On the contrary, the FTS option does not present show stoppers, as described in Vérinaud et al. (2006), and it would be the subject of further analyses in the next Planet Finder feasibility study - promoted by ESO - for the European-ELT. However, possible drawbacks for the FTS option could come by the fact that the signal proper to a fixed spaxel in the FOV is not spread over the detector pixels. This issue represents- in principle - a sound limitation for possible targets of such a Planet Finder instrument, just because candidate stars of a dedicated survey are the most shiny in the Galaxy. Serious strategies for the signal reduction at the level of the single spaxel - all over the acquisition time needed for the Speckle Noise attenuation - should be then mandatory for a possible FTS optimized to this science case.

[35] VLT-PF was consortium of French and English Astronomical Institutes funded for an 18 months Phase-A study dedicated to the next VLT Planet Finder instrument.

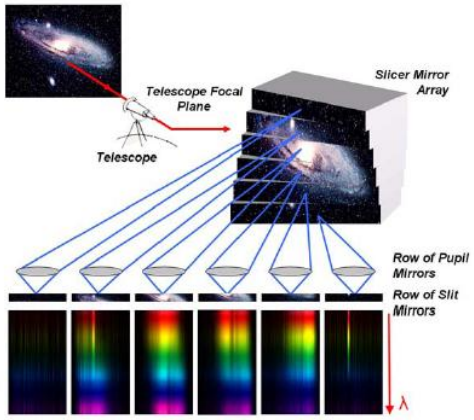


**Figure 3-16: The principle of an Image Slicer. The slicer mirror array, located on the re-imaged telescope Focal Plane, divides the FOV and re-images the telescope Exit Pupils along a line on the pupil mirrors. Each pupil mirror then re-images its corresponding slice of the FOV on its corresponding slit mirror located at the Spectrograph Focal Plane. The re-formatted FOV acts as the Entrance Slit in the Spectrograph where all the slices are aligned as a pseudo long slit (cfr. Prieto and Vivès 2006).**

Finally the TIGER optical concept, i.e. the one using as IFU a matrix of lenses (cfr. Bacon et al. 1995), avoids all possible drawbacks affecting the other optical options. More in detail, the issue of the chromatic differential phase aberrations is - in principle - completely avoided for a TIGER-type concept, properly because the original bi-dimensional FOV is spatially sampled by the matrix of lenses, then it is re-formatted in a bi-dimensional configuration yet, i.e. the Entrance Slit Plane of the IFS (see Figure 3-17). Furthermore, as widely described in Section 5, it comes out that a new version of such a Spectrograph is the only solution able to take into account for all the effect (Shape Distortion, Speckle Chromatism, Coherent and Incoherent CrossTalks) appearing when IFS is performed in diffraction limited condition, for high contrast imaging purposes. The name we (K. Dohlen, R. Gratton and me) assigned to this new IFS optical concept is Bigre[36].

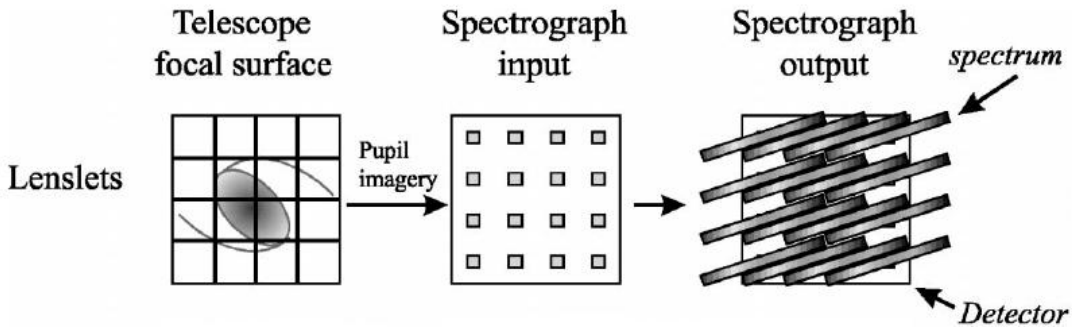


**Figure 3-17: The TIGER optical concept as reduced by Lee et al. (2001). The IFS Entrance Slit Plane becomes a matrix of micro-pupils corresponding to different parts of the original FOV.**

[36]. "Bigre" was the first word uttered by G. Courtes - the inventor of the TIGER concept - after our attempt to explain him all the problems of diffraction limited IFS (Shape Distortion, Speckle Chromatism, Coherent and Incoherent CrossTalks) and their possible resolution using this new optical concept. "Bigre" is the French exclamation with a meaning similar to the English: "Bligh-me" or the Italian: "Accidenti".

### 3.5.2 Speckle Chromatism in the specific case of 3D-Spectroscopy

Speckle Chromatism, that is the chromatic dependence of Speckles, is a general feature of any type of Differential Imaging technique based on the spectral properties of an optical signal described by Equation 3-7.

In the specific case of 3D-Spectroscopy, the incoming signal is spatially sampled - according to the Nyquist's criterion (see Section 3.5.1.1) - in the IFU plane. Then, following Equations 3-7, 3-11, and according to the formalism adopted in Section 3.5.1.1, the spaxel with radial coordinate ($\theta$), is fed by the following signal:

$$S(\theta) = [(s+p) \otimes Sp](\theta) \qquad \textbf{Equation 3-24}$$

where **s(θ)**, **p(θ)** are the diffraction limited signals of the star and the planet respectively, while **Sp(θ)** is the Speckle pattern.

Equation 3-24 is not valid - at the level of the single pixel - once the total signal **S** is dispersed chromatically in the Exit Slits plane. This is due to the fact that the single Speckle located at the radial position $\theta$ gets a chromatic dependence **~λ/D** already on the spaxel plane which is responsible for its chromatic shift - with respect to the optical axis - across the same spaxel. This fact indicates that a single Speckle - located at the position $\theta$ - contributes to the total signal **S** of several spaxels around the angular position $\theta$. Finally - as indicated by Sparks and Ford (2002) - the Chromatism of the Speckle pattern is measured on the detector pixels corresponding to the radial coordinate $\theta$, as a modulation of the spectrum ($s_\theta(\lambda)+p_\theta(\lambda)$) corresponding to that position in the field of view (see Figure 3-18).

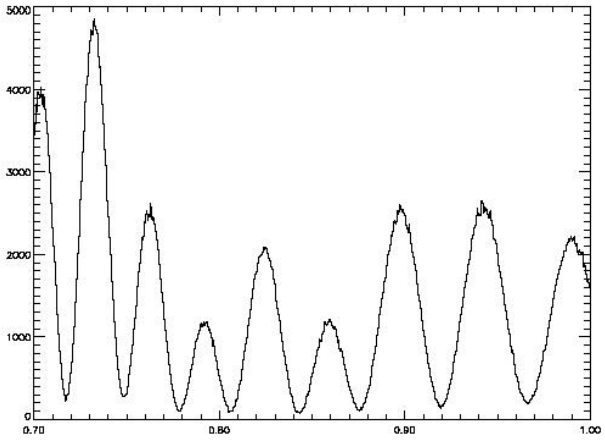


**Figure 3-18: Spectral plot for the light feeding a spaxel near the position θ of a simulated Jovian planet. The modulation induced on the intrinsic spectrum by the Speckle Chromatism is clearly visible (from Sparks and Ford 2002).**

The behaviour of Speckle Chromatism is well described making a cut through the entire data cube **[θ, λ, S(θ,λ)]** obtainable with a 3D-Spectrograph. As Figure 3-19 (top panel) shows, the spectrum of a single Speckle pattern **Sp(θ,λ)** - which spectral dependence is proportional to **λ/D** - is spread through a diagonal line, then covering an entire range of angular position **[$\theta_1$,$\theta_2$]**. Thus, the Spectrum of a Speckle modulates the signal: **s(θ,λ)+p(θ,λ)**. Moreover, as indicated by the analysis of Sparks and Ford (2002), the period (**P**) of the modulation is proportional to the angular position $\theta$ and to the wavelength ($\lambda$) according the following relation:

$$P(\theta,\lambda) \propto \frac{\lambda/D}{\theta}$$ **Equation 3-25**

Equation 3-25 indicates that **P** depends linearly on the wavelength; this fact is shown in Figure 3-18. Moreover, **P** depends inversely to the angular position $\theta$, indicating that the spatial frequency of this modulation increases for spectra corresponding to spaxels which are far from the optical axis.

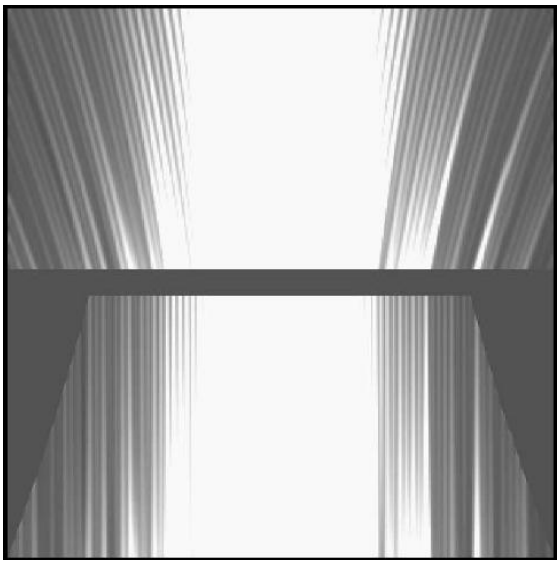

**Figure 3-19: Cuts through the original data cube with one spatial dimension (horizontal axis) and one spectral dimension (vertical axis). In the original cube (top panel) the rings diverge outward with wavelength, while in the spatially re-sampled cube (bottom panel), they form a straight lines running vertically in the plot (from Sparks and Ford 2002).**

Finally, Sparks and Ford (2002) indicate that for 3D-Spectroscopy the Speckle Chromatism can be attenuated imposing a pixel-dependent chromatical re-scaling on the data cube. Such a spatial re-sampling of the date cube is shown in Figure 3-19 (bottom panel).

### 3.5.3 S-SDI as powerful improvement of standard SDI

The reasons why an S-SDI is preferable to SDI can be then summarized with three items:

- With a whole spectrum available, more spectral features of the planet can be studied. Having two, three, or a finite number of filters that were chosen to observe a specific absorption band, spectral information coming from the other features are inexorably lost. With a spectrum, one can actually combine the data on and off different absorption bands in order to increase the S/N (if there are other features in the planetary spectrum).
- The availability of data at many wavelengths can allow the development of various algorithms and specific methods for the DRSW which can improve the Speckle Noise attenuation.
- Using IFS there is the possibility of detecting extrasolar planets, and characterizing these objects. In fact, the data available after the subtraction of stellar light allow the study of the spectrum of the planet and its main features, which can be very different, according to mass, age, temperature, etc. S-SDI calibration technique can then also be very useful in observing planets that have already been discovered in other ways.

A detailed planetary spectral features analysis is then necessary in order to choose the best spectral region for observations and to optimize the spectral resolution and spectral coverage

of an IFS instrument. Models of giant planets, such as those of Burrows et al (2004), indicate the NIR as the best spectral region for ground observations (see Section 3.1). These bands can be studied at very low spectral resolutions (**R>15,** see Figure 3-20 and Figure 3-21). The methane-dominated spectra are characterized by *emission peaks* which indicate the portions of the spectrum that are not affected by absorption; these are expected to be constant in wavelength, but their intensities are expected to change from object to object. At the same spectral resolution and in the same wavelength range, the spectrum of a solar-type star is nearly featureless (see Figure 3-4). Then, combination of strong planetary features and very smooth stellar spectra makes this range optimal for the S-SDI calibration technique. Difficulties of S-SDI simulations when a TIGER-type IFS is adopted are of two types:

- Proper to the Instrument Simulator. In the case of Berton et al. (2006), the simulated IFS is a TIGER-type composed of hexagonal lenses. The adopted spatial sampling is 0.014 [arcsec/spaxel], the covered FOV is 3.5 x 3.5 [arcsec$^2$]. Moreover a circular mask is applied to every lens in order to have axial symmetry in every re-imaged micro-pupil. Each IFU-lens samples - according the Nyquist's condition - the telescope PSF and creates its own smaller PSF on the IFS Entrance Slit Plane. The size of this micro-PSF depends on the pitch of the lenses array. After chromatical dispersion, a matrix of dispersed Exit Slits appears on the final screen (see Figure 3-22).
- Proper to the Data Reduction SoftWare. Before making simultaneous difference it is necessary to extract all the data related to any single spectral step from all the matrix of spectra, in order to rebuild a set of monochromatic images. Then, the chromatic re-scaling allows making the simultaneous difference of images separated by one spectral step. Finally the sum of all these differential images attenuates the Speckle Noise at the Photon Noise threshold (see Figure 3-11). For example, the subtraction algorithm adopted by Berton et al. (2006) is a pure Double Difference, giving the results showed in Figure 3-23 and Figure 3-24.

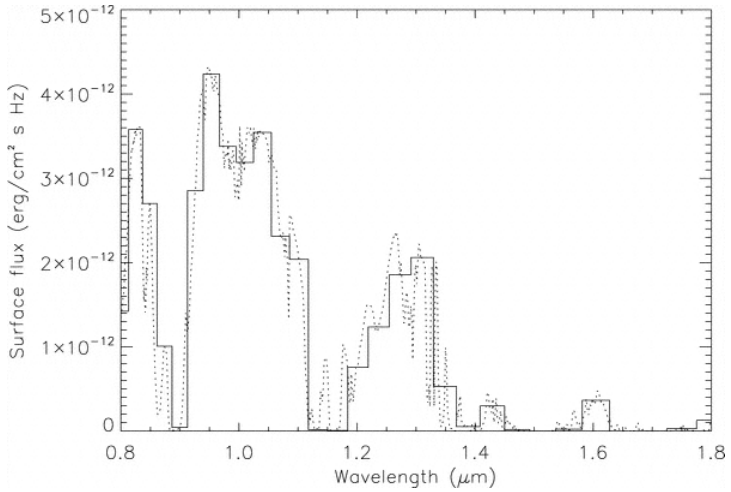


**Figure 3-20: Model of a NIR spectrum in the range 0.80-1.80 [micron] of a 1 $M_{JUPITER}$ planet orbiting a solar-type star (G2V) which is 1 [Gyr] old, with a separation of 10 AU. The spectral emission is mainly intrinsic, with a negligible component of reflected light. The solid spectrum has a spectral resolution R=15 while the dotted one R=375, from Berton et al. (2006).**

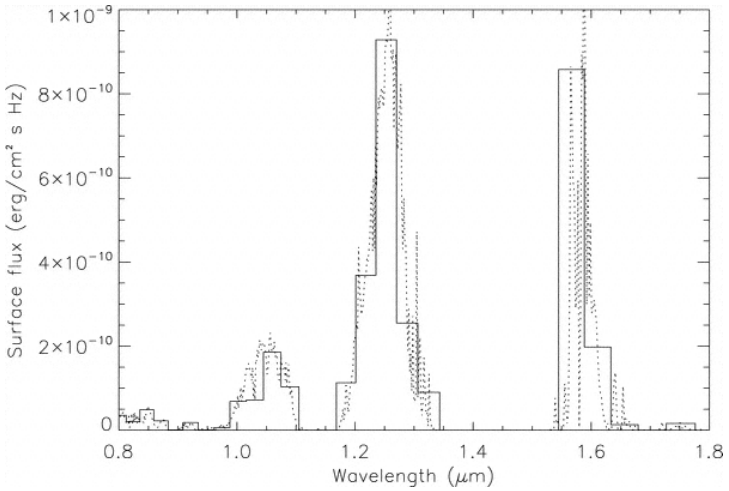


**Figure 3-21: Model f a NIR spectrum of the same planet of Figure 3-20, but at separation of 1 AU. The spectral emission is still mainly intrinsic, with a negligible component of reflected light. The solid spectrum has still a spectral resolution R=15 and the dotted one R=375, from Berton et al. (2006).**

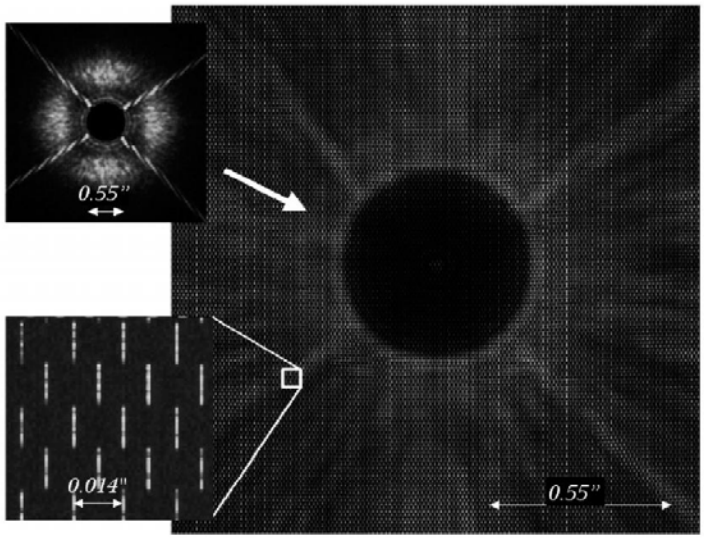


**Figure 3-22: Final output of an IFS observation of a star in the case of the Entrance Pupil proper to the VLT Nasmyth configuration. Top-left: example of telescope PSF before AO-compensation and Coronagraph spatial filtering, after the simulation of the TIGER-type IFU and the disperser, a large image is obtained. Bottom left: details of the spectra. Separations are expressed in [arcsec]. The spectral range is 0.95-1.70 [micron] and the spectral resolution R=15, so the length of a single spectrum is about 20 pixels (from Berton et al. 2006).**

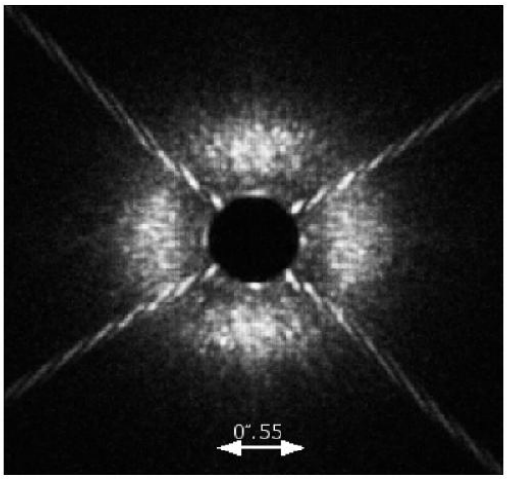


**Figure 3-23: Rebuilt monochromatic image obtained using the DRSW of Berton et al. (2006). As explained in the text, from the spectra of Figure 3-22, a set of images such as this are obtained before SDI procedure.**

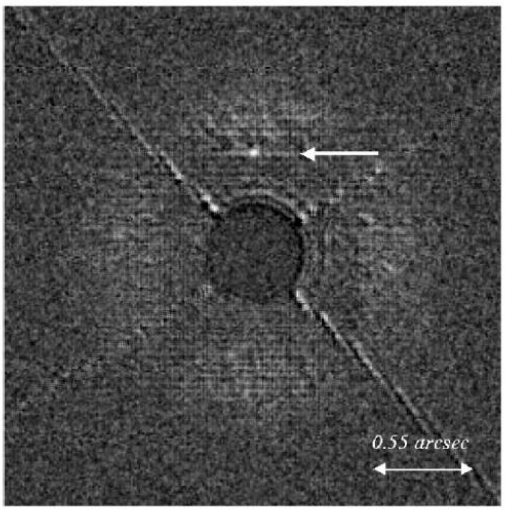


**Figure 3-24: Results of the simultaneous difference operated after a correct chromatic re-scaling of the monochromatic images. A brown dwarf of 30 $M_{JUPITER}$ finally arises from the Noise (S/N=30), on the top of this simulated image (from Berton et al. 2006).**

### 3.5.4 First high contrast imaging with an Integral Field Spectrograph

Presently, Integral Field Spectroscopy for high contrast imaging is not only a matter of simulations and optical designs optimizations, searching the best optical solution which cure all the optical effects appearing in the diffraction limited regime (cfr. this Dissertation). In fact, AO-supported astronomical observations with IFS and aimed to stellar Astrophysics have been tested recently by McElwain et al. (2006), which did science on the system GQ Lup.

The IFS adopted by McElwain et al. (2006) was OSIRIS (a TIGER-type instrument working in diffraction limited condition, cfr. Larkin et al. 2006), which is mounted on the Keck-II telescope on Mauna Kea (Hawaii). They obtained the spectrum of the faint companion of

this star - i.e. GQ Lup b (see Figure 3-25) - with spectral resolution R~2000 in the J and H-band.

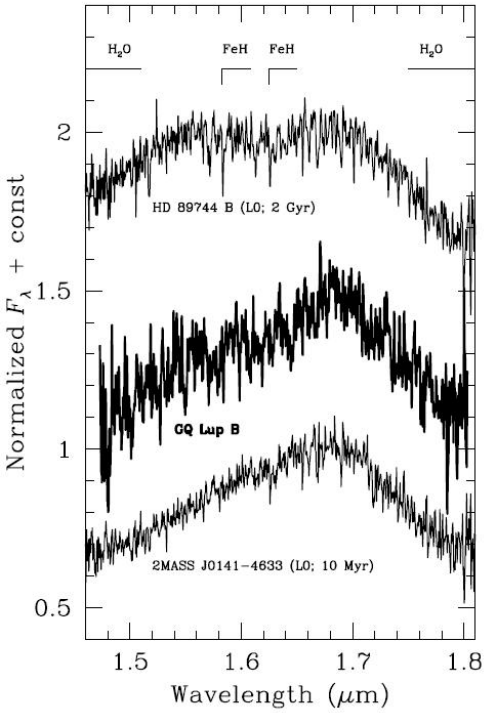


**Figure 3-25: The H-band spectrum of GQ Lup b compared to the spectra of L0 dwarfs of different ages. The peaked continuum shape of the spectrum of GQ Lup b strongly resembles to that of ~10 [Myr] old 2MASS J01415823-4633574, indicating similarity in low surface gravity and spectral type. All the spectra are normalized to unity at 1.68 [micron], (cfr. McElwain et al. (2006).**

In this specific case, diffraction limited IFS allowed to update the spectroscopic classification of GQ Lup b, its estimated age and the heliocentric distance of the primary. With these parameters, McElwain et al. (2006) found that the mass of GQ Lup b lies in the range 0.010-0.040 $M_{SUN}$. This result represents a strong observational constraint against theoretical models of planetary formation suggesting a nearly planetary mass of this object, as the one proposed by Wuchterl et al. (2003).

## 3.6 Bibliography


Bacon, R.; Adam, G.; Baranne, A.; Courtes, G.; Dubet, D.; Dubois, J. P.; Emsellem, E.; Ferruit, P.; Georgelin, Y.; Monnet, G.; and 3 coauthors, 1995, A&AS., v.113, p.347.

Baraffe, I.; Chabrier, G.; Allard, F.; Hauschildt, P. H., 2002, A&A., v.382, p.563-572.

Berton, A.; Gratton, R. G.; Feldt, M.; Henning, T.; Desidera, S.; Turatto, M.; Schmid, H. M.; Waters, R., 2006, PASP., Volume 118, Issue 846, pp. 1144-1164.

Biller, Beth A.; Close, Laird; Lenzen, Rainer; Brandner, Wolfgang; McCarthy, Donald W.; Nielsen, Eric; Hartung, Markus, *Advancements in Adaptive Optics*. Edited by Domenico B. Calia, Brent L. Ellerbroek, and Roberto Ragazzoni. Proceedings of the SPIE, Volume 5490, pp. 389-397, 2004.

Biller B. A., Close L. M., Masciadri E., Lenzen R., Brandner W., McCarthy D., Henning T., Nielsen E., Hartung M., ***astro-ph/0601062*** (Presented at IAU Colloquium 200, *Direct Imaging of Exoplanets: Science and Techniques*. For high resolution figures, see IAUC 200 conference proceedings).

Bakos G. A., Noyes R. W., Kovacs G., Latham D. W., Sasselov D. D., Torres G., Fischer D. A., Stefanik R. P., Sato B., Johnson J. A., Pal A., Marcy G. W., Butler R. P., Esquerdo G. A., Stanek K. Z., Lazar J., Papp I., Sari P., Sipocz B., ***astro-ph/0609369*** (accepted for publication in ApJ.).

Born, Max; Wolf, Emil, **Principles of optics. Electromagnetic theory of propagation, interference and diffraction of light**, Oxford: Pergamon Press, 1965, 3rd (revised) ed.

Burrows, Adam; Sudarsky, David; Lunine, Jonathan I., 2003, ApJ., Volume 596, Issue 1, pp. 587-596.

Burrows, Adam; Sudarsky, David; Hubeny, Ivan, 2004, ApJ, Volume 609, Issue 1, pp. 407-416.

Carbillet, Marcel; Vérinaud, Christophe; Guarracino, Mario; Fini, Luca; Lardiere, Olivier; Le Roux, Brice; Puglisi, Alfio T.; Femenia, Bruno; Riccardi, Armando; Anconelli, Barbara; and 3 coauthors, *Advancements in Adaptive Optics*. Edited by Domenico B. Calia, Brent L. Ellerbroek, and Roberto Ragazzoni. Proceedings of the SPIE, Volume 5490, pp. 637-648, 2004.

Close, Laird M.; Lenzen, Rainer; Guirado, Jose C.; Nielsen, Eric L.; Mamajek, Eric E.; Brandner, Wolfgang; Hartung, Markus; Lidman, Chris; Biller, Beth, 2005, NATURE, Volume 433, Issue 7023, pp. 286-289.

Conan, J.-M., Thesis (Ph.D.), Université Paris XI Orsay, 1994.

Fried D. L., 1982, J. Opt. Soc. Am. 72(1), 52.

Fusco, T.; Conan, J.-M.; Mugnier, L. M.; Michau, V.; Rousset, G., 2000, A&AS., v.142, p.149-156.

Gisler, Daniel; Schmid, Hans Martin; Thalmann, Christian; Povel, Hans Peter; Stenflo, Jan O.; Joos, Franco; Feldt, Markus; Lenzen, Rainer; Tinbergen, Jaap; Gratton, Raffaele; and 14 coauthors, *Ground-based Instrumentation for Astronomy*. Edited by Alan F. M. Moorwood and Iye Masanori. Proceedings of the SPIE, Volume 5492, pp. 463-474, 2004.

Hartung, M.; Herbst, T. M.; Close, L. M.; Lenzen, R.; Brandner, W.; Marco, O.; Lidman, C, 2004, A&A., v.421, p.L17-L20.

Larkin, James; Barczys, Matthew; Krabbe, Alfred; Adkins, Sean; Aliado, Ted; Amico, Paola; Brims, George; Campbell, Randy; Canfield, John; Gasaway, Thomas; and 16 coauthors, *Ground-based and Airborne Instrumentation for Astronomy*. Edited by McLean, Ian S.; Iye, Masanori. Proceedings of the SPIE, Volume 6269, pp., 2006.

Lee, David; Haynes, Roger; Ren, Deqing; Allington-Smith, Jeremy, 2001, PASP., Volume 113, Issue 789, pp. 1406-1419.

Malbet, F., 1996, A&AS., v.115, p.161.

Marois, Christian; Doyon, René; Racine, René; Nadeau, Daniel, 2000, PASP., Volume 112, Issue 767, pp. 91-96.

Marois, Christian; Racine, René; Doyon, René; Lafrenière, David; Nadeau, Daniel, 2004, ApJ., Volume 615, Issue 1, pp. L61-L64.

McCaughrean, M. J.; Close, L. M.; Scholz, R.-D.; Lenzen, R.; Biller, B.; Brandner, W.; Hartung, M.; Lodieu, N., 2004, A&A., v.413, p.1029-1036.

McElwain M. W., Metchev S. A., Larkin J. E., Barczys M., Iserlohe C., Krabbe A., Quierrenbach A., Weiss J., Wright S., ***astro-ph/0610265*** (accepted for publication to ApJ).

Mugrauer, M.; Neuhäuser, R., 2005, MNRAS., Volume 361, Issue 1, pp. L15-L19.

Prieto, E.; Vivès, S., 2006, NewAR., Volume 50, Issue 4-5, p. 279-284.

Racine, Rene', 1996, PASP., v.108, p.699.

Racine, René; Walker, Gordon A. H.; Nadeau, Daniel; Doyon, René; Marois, Christian, 1999, PASP., Volume 111, Issue 759, pp. 587-594.

Roddier, F.; Gilli, J. M.; Lund, G, 1982, JOpt., vol. 13, p. 263-271.

Schroeder, Daniel J., **Astronomical Optics**, San Diego: Academic Press, 1987.

Smith, W. Hayden, 1987, PASP., Publications (ISSN 0004-6280), vol. 99, Dec. 1987, p. 1344-1353.

Sparks, William B.; Ford, Holland C., 2002, ApJ., Volume 578, Issue 1, pp. 543-564.

Sudarsky, David; Burrows, Adam; Pinto, Philip, 2000, ApJ., Volume 538, Issue 2, pp. 885-903.

Sudarsky, David; Burrows, Adam; Hubeny, Ivan, 2003, ApJ., Volume 588, Issue 2, pp. 1121-1148.

Véran, J. P., Thesis (Ph.D.), École Nationale Supérieure des Télécommunications, France, 1997.

Vérinaud, C.; Hubin, N.; Kasper, M.; Antichi, J.; Baudoz, P.; Beuzit, J.-L.; Boccaletti, A.; Chalabaev, A.; Dohlen, K.; Fedrigo, E.; and 24 coauthors. *Advances in Adaptive Optics II*. Edited by Ellerbroek, Brent L.; Bonaccini Calia, Domenico. Proceedings of the SPIE, Volume 6272, pp., 2006.

Wuchterl, G.; Tscharnuter, W. M., 2003, A&A., v.398, p.1081-1090.

# 4 The SPHERE project

The Planet Finder instrument for ESO VLT telescope, scheduled for first light in 2010, aims to detect giant extrasolar planets in the vicinity of bright stars and to characterise the objects found through spectroscopic and polarimetric observations. The observations will be done both within the Y, J, H and Ks atmospheric windows by the aid of a Dual Imaging Camera (IRDIS) and an Integral Field Spectrograph (IFS), while in the R, I atmospheric windows using a Dual Imaging Polarimeter Camera (ZIMPOL). The instrument employs an XAO[37] turbulence compensation system (SAXO), Focal Plane Tip-Tilt correction, and Interferential Coronagraphs. In this Section[38] the science goals of the instrument are described and its top level requirements are deduced. The system architecture is presented, including an overall description of ZIMPOL and IRDIS sub-systems. Expected performances are presented in terms of a semi-analytic performance-estimation tool for sensitivity analysis at the level of the single sub-systems. Instead, the detailed description of the IFS sub-system is specific argument of Sections 5 and 6.

## 4.1 Science case

After review of the two competing phase A studies: CHEOPS (cfr. Feldt et al. 2005) and VLT-PF (cfr. Mouillet et al. 2004), ESO has launched a contract for designing and building an instrument benefiting from both studies. This instrument, dedicated to Spectro-Polarimetric High contrast Exoplanet REsearch (SPHERE) includes the eXtreme AO-system (SAXO, cfr. Fusco et al. 2006), the Coronagraphic device (cfr. Mawet et al. 2006), and the Differential Imaging Camera (IRDIS, cfr. Dohlen et al. 2006) from the VLT-PF consortium and the Dual Imaging Polarimeter (ZIMPOL, cfr. Gisler et al. 2004) and the Integral Field Spectrograph (IFS, cfr. this Dissertation) proposed by the CHEOPS consortium. Following the merging of the two concepts, the science operation model has been revisited to take into account the specificities and complementarities of the different focal instruments.

The prime objective of SPHERE is the discovery and study of new planets orbiting stars by direct imaging of the circumstellar environment. The challenge consists in the very large Contrast of luminosity between the star and the planet (larger than ~12.5 magnitudes or ~$10^5$ flux ratio), at very small angular separations. The whole design of SPHERE is therefore optimized towards high contrast performance in a limited field of view and at short distances from the central star. Both evolved and young planetary systems will be detected, respectively through their reflected light (ZIMPOL mode) and through the intrinsic planet emission (IRDIS and IFS modes). Both components of the NIR-arm of SPHERE will provide complementary detection capacities and characterization potential, in terms of field of view, Contrast of luminosity, and spectral domain.

Within a core of ~100 target stars separated in several age bins, the SPHERE team expects to find about 10 planets with masses between a few tenths up to about tens $M_{JUPITER}$ with the NIR-arm. Moreover, SPHERE will be in the position to screen about 20 nearby stars for the presence of planets in their reflected VISible light with ZIMPOL. Notice that any detection by either of the two arms would immediately result in a characterization of the atmosphere

[37] For the definition of all the abbreviations adopted in this Section see the opening list.

[38] This Section is a summary of the work presented by K. Dohlen: *SPHERE, a Planet Finder instrument for the VLT* during the SPIE conference: *Astronomical Telescopes and Instrumentation*, 24-31 May 2006, Orlando, Florida, USA; by courtesy of the Author.

of the extrasolar planet. A larger comprehensive survey of additional ~300 targets will finally lead to a statistically relevant sample of planets with masses between a few tenths up to about tens $M_{JUPITER}$, in the distance bin between 1 and 20 AU in a sample of more than 400 nearby stars.

With such a prime objective, it is obvious that many other research fields will benefit from the large contrast performance of SPHERE: proto-planetary disks, brown dwarfs, evolved massive stars and marginally, solar system and extragalactic science. These domains will nicely enrich the scientific impact of the instrument.

## 4.2 Observational modes

Two basic observing modes have been defined in order to draw maximum benefit of the unique instrumental capacities of SPHERE:

- **NIR survey.** This is the main observing mode which will be used for 80% of the observing time. It combines the SDI mode - proper to IRDIS - in H band with the S-SDI mode - proper to the IFS - in the Y-J bands, by the aid of dichroic beam separation after the Coronagraph. This configuration permits to benefit simultaneously from the optimal capacities of both Dual Imaging over a large field (out to ~5 [arcsec] radius) and spectral imaging in the inner region (out to at least 0.7 [arcsec] radius). In particular, it allows to reduce the number of false alarms and to confirm potential detections obtained in one channel by data from the other channel. This will be a definitive advantage in case of detections very close to the limits of the system.
- **VISible survey.** The polarimetric capacities of ZIMPOL will provide unique performance for reflected light very close to the star, down to the level required for the first direct detection in the VISible of old close-in extrasolar planets, even if on a relatively small number of targets. ZIMPOL also provides classical imaging in the VISible, offering unique high-Strehl performance in an era when the Hubble Space Telescope (HST) will probably have been decommissioned.

## 4.3 System architecture

### 4.3.1 Global overview

The proposed design of SPHERE is divided into four sub-systems as illustrated in Figure 4-1[39]: the Common Path Optics and the three science channels: ZIMPOL, IRDIS and IFS. The Common Path includes pupil stabilizing fore optics where polarimetric half-wave plates are also provided, the SAXO eXtreme Adaptive Optics system with a VISible WaveFront Sensor, and NIR coronagraphic devices in order to feed IRDIS and IFS with a highly stable coronagraphic Image in the NIR. ZIMPOL shares the VISible channel with the WaveFront Sensor and includes its own Coronagraphic system. A photon sharing scheme has been agreed between IFS and IRDIS, allowing IFS to exploit the NIR range up to the J band, judged optimal for the S-SDI mode, while leaving the H-band to SDI mode proper of IRDIS.

The instrument and all its sub-systems will be mounted on an optical bench situated on one of the VLT Nasmyth platforms. The bench will be actively damped by a pneumatic servo-controlled system and equipped with a dust cover.

[39] All the figures presented in this Section are provided by courtesy of the SPHERE team.

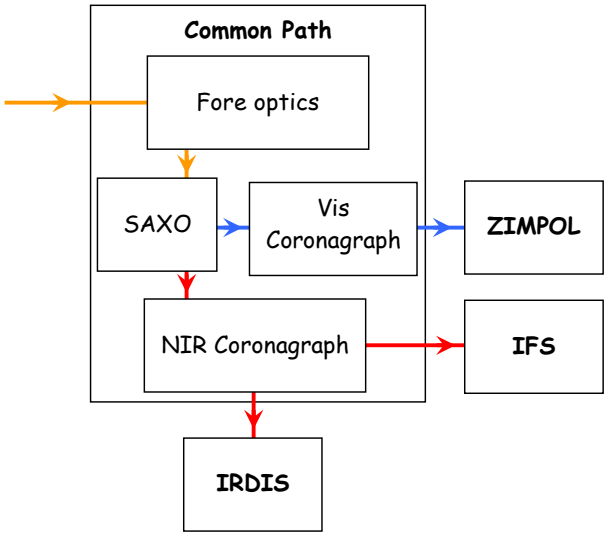


**Figure 4-1: Global concept of the SPHERE instrument indicating its 4 sub-systems: Common Path, ZIMPOL, IRDIS and IFS. It also includes the main functionalities within the Common Path sub-system. Optical beams are red for NIR, blue for VISible and orange for Common Path.**

### 4.3.2 Common Path optics

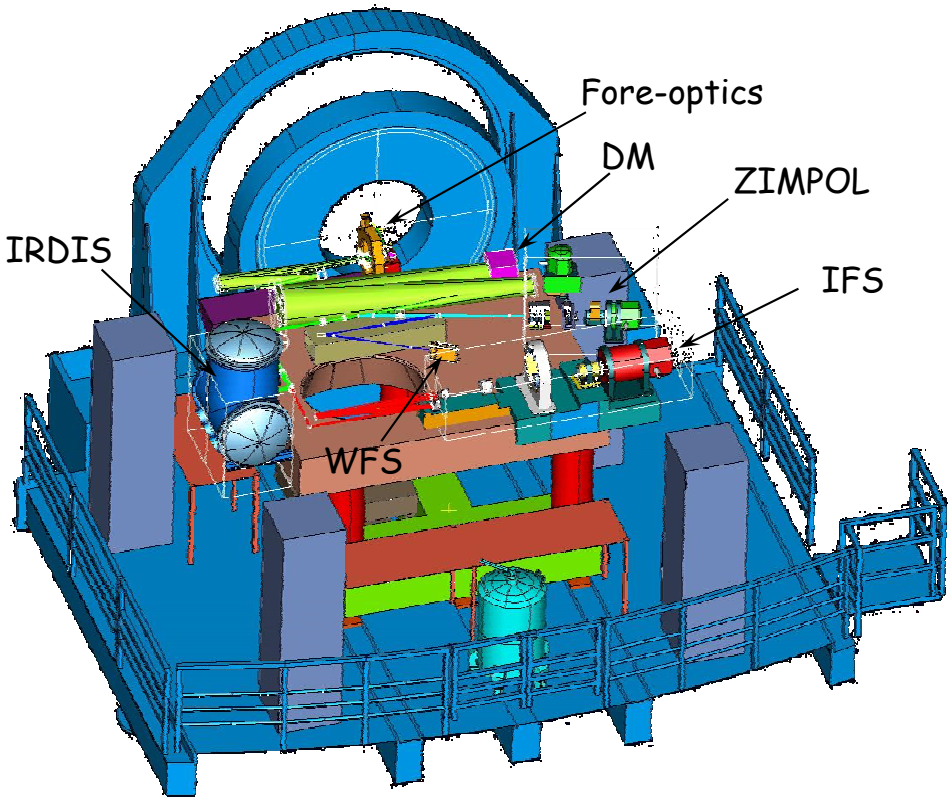


**Figure 4-2: Implementation of SPHERE on the VLT Nasmyth platform**

Figure 4-2 shows current design of SPHERE on the Nasmyth platform, indicating the main feature of the Common Path optics and how it feeds the other sub-systems and the AO sensors. In order to optimize bench stiffness, a compact bench layout is chosen. Access to

critical optics (ADCs, WFS,…) is ensured by a *man-hole* in the bench. Other critical components are located near the edges of the table and accessed by the aid of walkways. The optical design of the Common Path is based on the use of three toroidal mirrors manufactured by spherical polishing of pre-stressed substrates. This gives perfect optical correction and provision for all the necessary pupil and image planes while benefiting from the excellent surface quality (and cost) offered by spherical polishing techniques.

### 4.3.3 The XAO system SAXO

The SPHERE Adaptive optics for eXoplanet Observation (SAXO) is basically the same as the eXtreme AO system proposed by the VLT-PF team (cfr. Mouillet et al. 2004). A global trade-off combining optical design, technological aspects, cost and risk issues, leads to the use of a 41 x 41 actuator DM of 180 [mm] diameter with an inter-actuator stroke >±1 [micron] and a maximum stroke >±3.5 [micron], and a 2-axis TTM with ±0.5 [milliarcsec] resolution. The WFS is a 40 x 40 lenslet Shack-Hartmann sensor, with a spectral range between 0.45 and 0.95 [micron] equipped with a focal plane filtering device with variable size, from **λ/d** to **3λ/d** at 0.7 [micron] (where **d** is the projected micro-lens diameter), for aliasing control. A temporal sampling frequency of 1.2 kHz is achieved using a 240 x 240 pixels electron multiplying CCD detector with a Read-Out-Noise $<1e^{-}$ and a 1.4 Excess Photon Noise factor. The global AO loop delay is maintained below $10^{-3}$ [sec].

The SAXO loop structure is shown in Figure 4-3. Image and Pupil stability are essential in high contrast instruments. Differential image movements due to thermo-mechanical effects and ADC mechanism precision are therefore measured in real-time using an auxiliary NIR Tip-Tilt sensor located close to the Coronagraph Focus and corrected via a Differential TTM in the WFS arm. Likewise, Pupil run-out is measured by analysis of the WFS sub-pupil intensity along the Pupil edge and corrected by a Pupil TTM close to the telescope Focal Plane at the entrance of the instrument. Non-common path aberrations are measured off-line using a phase diversity algorithm and compensated on-line by reference slope adjustments.

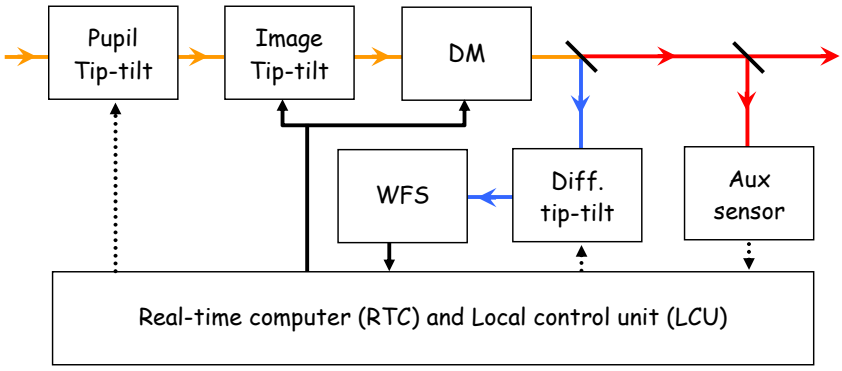


**Figure 4-3: Sketch of the SAXO loop structure.**

In Figure 4-3, the broad-band beam in orange, NIR beam in red, and VISible beam in blue. Electrical signals are shown in black, solid for high-bandwidth ( ~1 [kHZ]) signals, and dotted for low-bandwidth (1-10 [Hz]) signals. The VISIble WFS and RTC generate fast signals for DM and Image TTM control, as well as a slow signal for lateral Pupil alignment via Pupil TTM. Slow differential Image motion between the VISible and NIR beams is detected using a Focal Plane auxiliary sensor located close to the Coronagraph Focus, feeding into the Differential-TTM located in the VISible beam.

### 4.3.4 Coronagraphs

Efficient Coronagraphy is important for reaching the science goals of SPHERE. Its action is two-fold: reduce by a factor of at least 100 the intensity of the stellar peak, and eliminate the diffraction features due to the Pupil edges. Coronagraphy is a quickly evolving research field and it is felt to be important to leave the instrument open for future evolutions by allowing exchangeable masks both in the Coronagraphic Focus and in its Entrance and Exit Pupils.

The base-line Coronagraph suite will include an achromatic four-Quadrant Phase Mask Coronagraph (4QPMC) based on precision mounting of four Half-Wave Plates (HWP), and both a Classical Lyot Coronagraph (CLC) and an Apodized Lyot Coronagraph (ALC). The 4QPMC has recently been demonstrated in the VISible (see Figure 4-4 and Figure 4-5), where the main difficulties of precision edge-polishing and mounting of the HWPs have been addressed and excellent performance has been demonstrated (cfr. Mawet et al. 2006). Extension of these techniques to the NIR is ongoing. While the CLC option, with mask diameter of about **10λ/D** (where **D** is the telescope diameter) is within the realm of classical manufacturing, the ALC option requires an Apodizer in the Coronagraph Entrance Pupil. Prototyping is ongoing, and a promising technology using graded metal deposition has been identified by the SPHERE team. Other options include the classical 4QPMC (cfr. Rouan et al. 2000) which has the advantage of being very well mastered and intensively tested with the laboratory experiments at various wavelengths (VISible, NIR, MIR) and on the sky with VLT/NACO (cfr. Boccaletti et al. 2004).

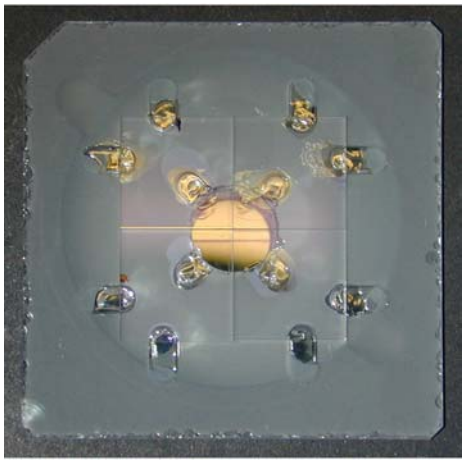

**Figure 4-4: Prototype of the HWP proper to the 4QPMC proposed by the SPHERE team (from Mawet et al. 2006).**

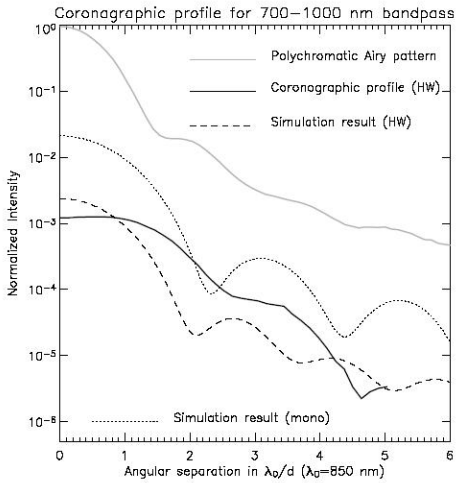


**Figure 4-5: Experimental and simulated PSF profiles obtained with the 4QPMC proposed by the SPHERE team. The grey solid curve is the reference experimental PSF in the range 0.7-1.0 [micron]. The continuous black line is the experimental post-Coronagraph PSF profile. The dashed line is the result of simulations taking into account of the waveplates phase residuals and de-focus errors. For comparison, the simulations result obtained with a monochromatic mask - used in the same conditions - is shown by the dotted curve (from Mawet et al. 2006).**

### 4.3.5 ZIMPOL

The Zurich Imaging Polarimeter (ZIMPOL) sub-system constitutes the P-DI facility of SPHERE, working in the wavelengths range 0.60 to 0.90 [micron]. The instrument principle (cfr. Gisler et al. 2004) is based on fast modulation, using ferro-electric retarder, and demodulation of the polarization signal, using a modified CCD array, as illustrated in Figure 4-6. Key advantages of this technique are the simultaneous detection of two perpendicular polarizations (the modulation is faster than seeing variations), and the recording of both images on the same pixel. Thanks to this approach, a polarimetric precision of $10^{-5}$ or even better should be achieved. The CCD will cover a Nyquist sampled field of 3 [arcsec$^2$] and it is foreseen that the FOV can be moved around the bright star so that a field with a radius of 4 [arcsec] can be covered. In addition to P-DI, ZIMPOL provides the possibility for high resolution imaging in the visual range using a set of broad and narrow band filters. This capacity will be unique in the post-HST era of the years 2010.

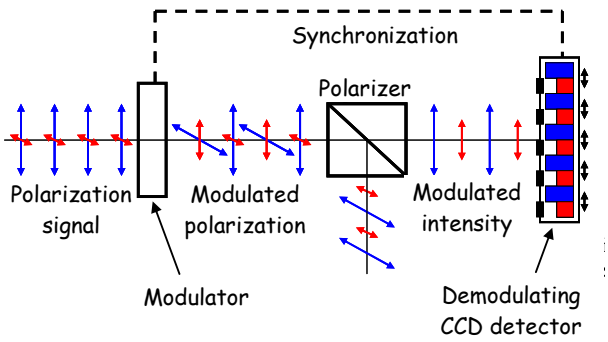


**Figure 4-6: Basic polarimetric principle of ZIMPOL.**

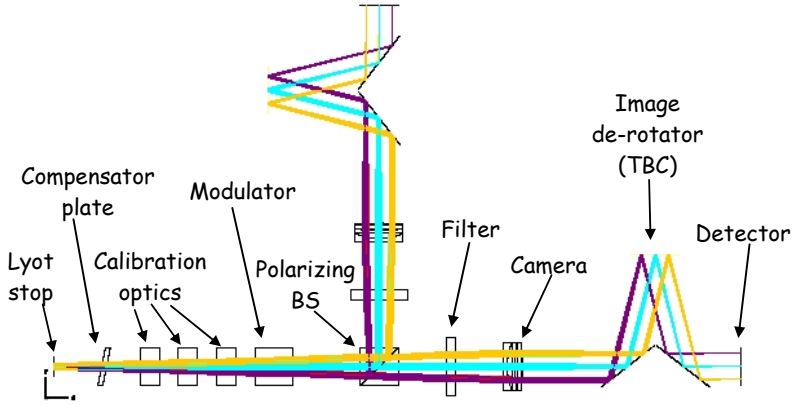


**Figure 4-7: Current optical design of ZIMPOL.**

The optical design of ZIMPOL - from the Lyot Stop to the detectors - is shown in Figure 4-7. After the Pupil, follows a tilted polarization compensator plate minimizing the instrument polarization for ZIMPOL. Selectable retarder plates and polarizers allow for calibration of the remaining instrument polarization. The following modulator package consists of two components, a rotating zero order half wave plate and a ferro-electric polarization modulator. Further downstream, a polarizing beam splitter produces two beams, both of which are equipped with a filter wheel, camera lens and detector.

### 4.3.6 IRDIS

The Infra-Red Dual-beam Imaging and Spectroscopy (IRDIS) sub-system constitutes the SDI facility of SPHERE. The main specifications for IRDIS include a spectral range from 0.95 to 2.32 [micron] and an image scale of 12.25 [milliarcsec] consistent with Nyquist's sampling of the telescope PSF at 0.95 [micron]. The SDI mode of IRDIS provides images in two neighboring spectral channels with minimized differential aberrations ($\sigma_\Phi$<10 [nm]). Moreover, ten different chromatic filter couples are defined corresponding to different features in models of extrasolar planets spectra, as discussed in Section 3.1.

SDI is done using a beam-splitter combined with a mirror, producing two beams in parallel. Each beam has its own Camera doublet and band-limiting filter. The main challenge is to achieve the required 10 [nm] differential aberrations requirement, but an error budget based on high-quality classical polishing technology is found to satisfy the requirement. This option has been favoured over the alternative Wollaston-based option because it eliminates spectral blurring problems, which would limit the useful FOV, and allows the use of high-quality materials with high homogeneity.

The optical design of IRDIS is shown in Figure 4-8. The IRDIS Entrance Pupil is the Coronagraph Exit Pupil where a Lyot Stop Wheel is placed. This latter is located in a collimated beam of diameter 10 [mm] and constitutes the main optical interface parameter with the Common Path optics. The Lyot Stop Wheel also contains a Prism and a Grism for long-slit spectroscopy. It is preceded by a common filter wheel carrying narrow, medium and broad band filters for direct imaging. A second filter wheel carrying dual imaging filter pairs is located down-stream of the beam-separation unit. This mechanism also carries a Pupil-imaging lens. The detector will be mounted on a two axis translation stage to allow dithering for flat-field improvement. The development of this stage is based on NACO heritage.

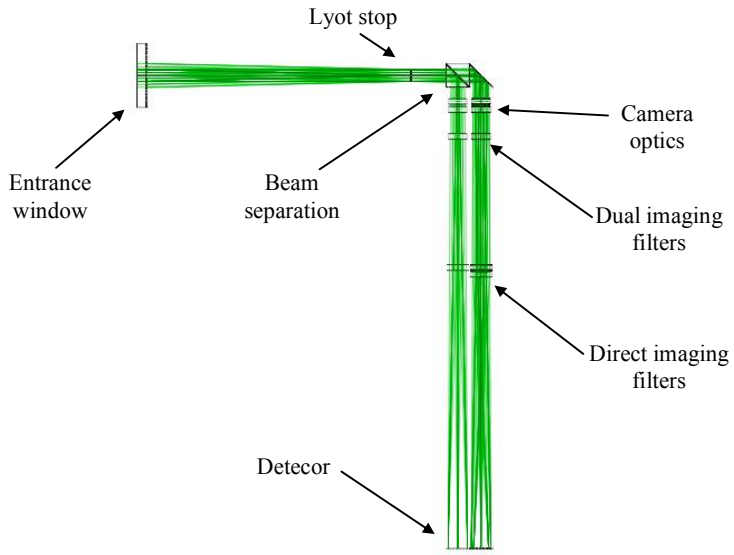


**Figure 4-8: Current optical design of IRDIS.**

### 4.3.7 IFS

Section 5 and 6 are dedicated specifically to this subject, this latter being the core of this Dissertation.

## 4.4 Performance analysis

Several Codes for performances simulation have been developed by CHEOPS and VLT-PF teams during the Phase A studies of the SPHERE instrument. All these efforts are being gathered into a single instrument simulator developed on the CAOS platform (cfr. Carbillet et al. 2004) in order to provide to the community with a tool able to predict the instrument performances at the level of each single sub-system. As Figure 4-9 shows, the action of the Coronagraph on a perturbed wavefront and the influence of post-Coronagraph aberrations are simulated. The Coronagraph Entrance wavefront is affected by time-variable residuals of the AO correction of atmospheric turbulence, as well as quasi-static instrumental aberrations. Instrumental aberrations include actual phase maps representing the VLT mirrors, and estimated phase maps of instrument optics generated using a Power Spectral Density with an inverse square-law radial profile, assumed to represent typical high-quality optical surfaces (cfr. Duparré et al. 2002). In the specific case of IFS, three Fourier Transform (FT) passages are needed to obtain the correct bi-dimensional screen representing the input to the IFS performances simulator Code described in Berton et al. (2006).

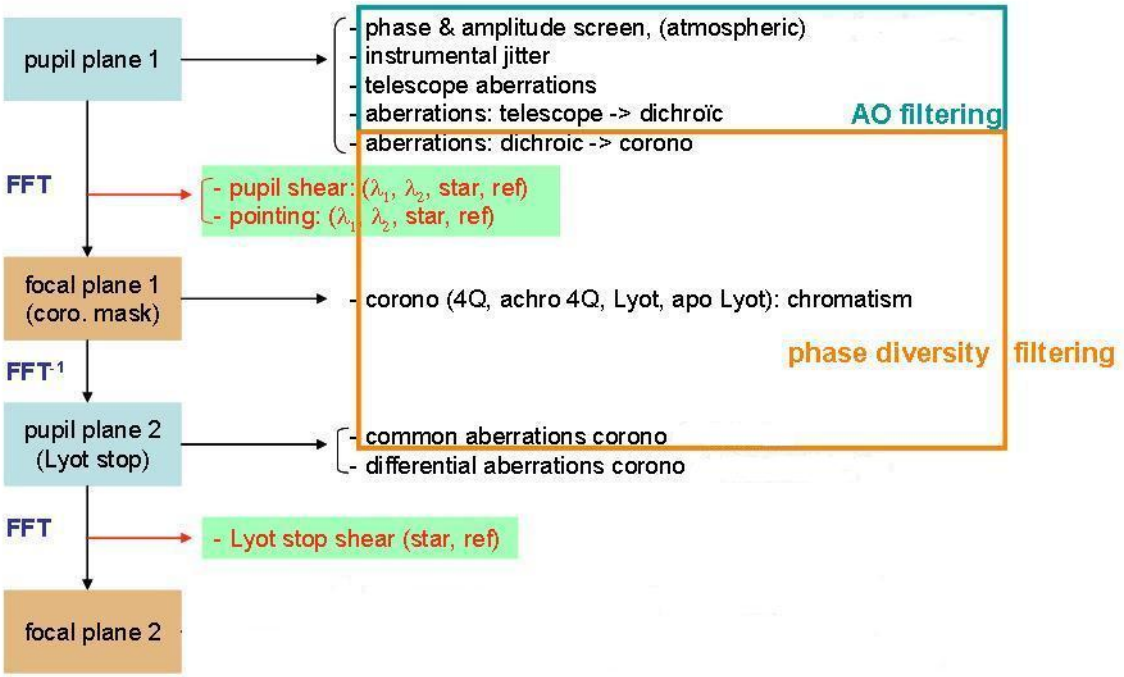


**Figure 4-9: Block diagram for the SPHERE performances simulator Code. Modules are distinguished only for common procedures. The module "focal-plane 2" represents the performances simulator Code implemented - respectively - for ZIMPOL, IRDIS and IFS.**

## 4.5 Bibliography


Boccaletti, A.; Riaud, P.; Baudoz, P.; Baudrand, J.; Rouan, D.; Gratadour, D.; Lacombe, F.; Lagrange, A.-M., 2004, PASP., Volume 116, Issue 825, pp. 1061-1071.

Carbillet, Marcel; Vérinaud, Christophe; Guarracino, Mario; Fini, Luca; Lardiere, Olivier; Le Roux, Brice; Puglisi, Alfio T.; Femenia, Bruno; Riccardi, Armando; Anconelli, Barbara; and 3 coauthors, *Advancements in Adaptive Optics*. Edited by Domenico B. Calia, Brent L. Ellerbroek, and Roberto Ragazzoni. Proceedings of the SPIE, Volume 5490, pp. 637-648, 2004.

Dohlen, K.; Beuzit, J-L.; Feldt, M.; Mouillet, D.; Puget, P.; Antichi, J.; Baruffolo, A.; Baudoz, P.; Berton., A.; Boccaletti., A.; and 26 coauthors, *Ground-based and Airborne Instrumentation for Astronomy*. Edited by McLean, Ian S.; Iye, Masanori. Proceedings of the SPIE, Volume 6269, pp., 2006.

Duparré, A., Ferre-Borrull, J., Gliech, S., Notni, G., Steinert, J., Bennett, J. M., *Surface characterization techniques for determining the root-mean-square roughness and power spectral densities of optical components*, 2002, Appl. Opt. 41, 154.

Feldt M., Henning T., Hippler S., Gratton R., Turatto M., Neuhäeuser R., Schmid H. M., Waters R., ***The CHEOPS project: CHaracterizing Exo-planets by Opto-infrared Polarimetry and Spectroscopy***, in *Exploring the cosmic frontiers: Astrophysical instruments for the 21st century*, Proc. ESO Astrophysics Symposium, 2005.

Fusco, T.; Petit, C.; Rousset, G.; Sauvage, J.-F.; Dohlen, K.; Mouillet, D.; Charton, J.; Baudoz, P.; Kasper, M.; Fedrigo, E.; and 9 coauthors, *Advances in Adaptive Optics II*. Edited by Ellerbroek, Brent L.; Bonaccini Calia, Domenico. Proceedings of the SPIE, Volume 6272, pp., 2006.

Gisler, Daniel; Schmid, Hans Martin; Thalmann, Christian; Povel, Hans Peter; Stenflo, Jan O.; Joos, Franco; Feldt, Markus; Lenzen, Rainer; Tinbergen, Jaap; Gratton, Raffaele; and 14 coauthors, *Ground-based Instrumentation for Astronomy*. Edited by Alan F. M. Moorwood and Iye Masanori. Proceedings of the SPIE, Volume 5492, pp. 463-474, 2004.

Mawet, D.; Riaud, P.; Baudrand, J.; Baudoz, P.; Boccaletti, A.; Dupuis, O.; Rouan, D, 2006, A&A., Volume 448, Issue 2, pp.801-808.

Mouillet, D.; Lagrange, A. M.; Beuzit, J.-L.; Moutou, C.; Saisse, M.; Ferrari, M.; Fusco, T.; Boccaletti, A., ***High Contrast Imaging from the Ground: VLT/Planet Finder***, in *Extrasolar Planets: Today and Tomorrow*, Jean-Philippe Beaulieu, Alain Lecavelier des Etangs and Caroline Terquem (eds), ASP Conf. Proc. 321, 2004, p.39

Rouan, D.; Riaud, P.; Boccaletti, A.; Clénet, Y.; Labeyrie, A., 2000, PASP., Volume 112, Issue 777, pp. 1479-1486.

# 5 SPHERE Integral Field Unit

In classical TIGER design optimized for seeing limited conditions (Bacon et al. 1995 and Bacon et al. 2001) the micro-lenses (hereafter spaxels[40]) composing the IFU are much bigger than the projected size of telescope PSF-FWHM, providing therefore resolved images of the telescope Entrance Pupil (see Figure 5-1), which in turn represent the Slits of a 3D-Spectrograph.

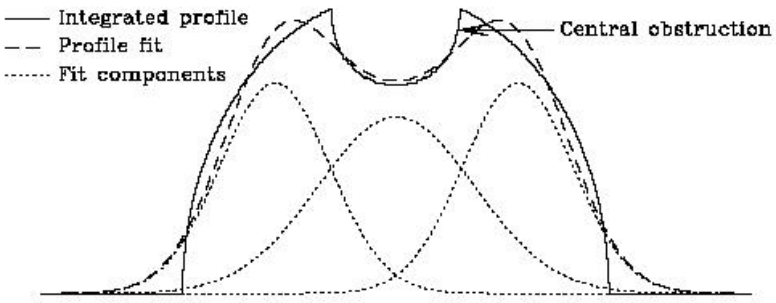


**Figure 5-1: Profile of IFS Slit Function (solid line) of the single re-imaged WHT Entrance Pupil obtained with the TIGER Integral Field Unit of the SAURON 3D-Spectrograph. The dashed line represents the fit obtained with three (dotted lines) Gaussian functions (from Bacon et al. 2001).**

In the case of high contrast imaging, the Nyquist's spatial sampling condition imposed on the re-imaged telescope Focal Plane implies a specific value for the single spaxel size, according to the following formalism.

The spaxel size the IFU with pitch[41] - equal to $\mathbf{D_L}$ - gives the spatial sampling frequency ($\mathbf{f_S}$):

$$f_S \equiv \frac{1}{D_L}$$ **Equation 5-1**

hence the spatial Nyquist frequency ($\mathbf{f_{NY}}$) turns to be:

$$f_{NY} = \frac{1}{2 \cdot D_L}$$ **Equation 5-2**

For an image with a fixed Focal Ratio - indicated as **F** - the imaging theory[42] implies:

$$f_C \equiv \frac{1}{\lambda_{min} \cdot F}$$ **Equation 5-3**

---

[40] For the definition of spaxel see Section 3.5.1.1.

[41] The pitch of an array of spaxels is defined as the center-to-center-distance among adjacent ones. For a filling factor close to unity this quantity equals the size of the single spaxel which is indicated as $\mathbf{D_L}$.

[42] Cfr. Goodman, Joseph W., **Introduction to Fourier Optics**, 2nd ed., Publisher: New York, NY: McGraw-Hill, 1996. Series: McGraw-Hill series in electrical and computer engineering; Electromagnetic. ISBN: 0070242542

where $\mathbf{f_C}$ is the spatial cutoff frequency of the Telescope and $\boldsymbol{\lambda_{min}}$ is the minimum wavelength in the working range of a fixed Focal Plane instrument.

Combining Equation 5-1 and Equation 5-2 in order to satisfy the Nyquist's criterion:

$$f_{NY} > f_C \qquad \textbf{Equation 5-4}$$

the correct spatial sampling on the re-imaged telescope Focal Plane implies the value of the Input Focal Ratio ($\mathbf{F_{IN}}$) as follows:

$$F_{IN} > \frac{2 \cdot D_L}{\lambda_{min}} \qquad \textbf{Equation 5-5}$$

Equation 5-5 assures that the single spaxel is smaller than the size of the Airy Disk of the telescope PSF, and so the resulting re-imaged Electric Field distribution (**E**) proper to the telescope Entrance Pupil, is no longer spatially resolved. Specifically, in the case of a spaxel with circular aperture $D_L$ (cfr. Born and Wolf 1965) the Electric Field distribution takes itself the following normalized form:

$$E_P(s) = \left[ \frac{2 \cdot J_1(\pi \cdot s)}{\pi \cdot s} \right] \qquad \textbf{Equation 5-6}$$

$\mathbf{J_1}$ is the Bessel-J-Function of order one, the variable (**s**) is defined as the spatial coordinate on all the planes of the IFS optics where the telescope Entrance Pupil is re-imaged, in unit of $\mathbf{F_{OUT} \cdot \lambda}$, where $\mathbf{F_{OUT}}$ is defined as the spaxel Output Focal Ratio both for the TIGER and BIGRE cases. Equation 5-6 indicates that in the case of diffraction limited 3D-Spectroscopy the re-imaged Electric Field is no longer a bounded signal, and then the related Intensity distribution does not recover the form of the Intensity distribution across the telescope Entrance Pupil, as in the case of Figure 5-1. This behaviour forces us to describe the optical propagation from the re-imaged telescope Focal Plane up to the IFS Slits Plane adopting the Fourier Transform formalism. Through this approach, the standard TIGER and the new BIGRE devices are described in Sections 5.1, 5.2 respectively.

## 5.1 3D-Spectroscopy at the diffraction limit with a TIGER IFU

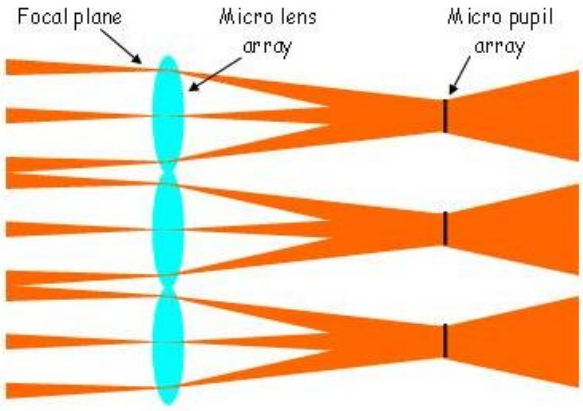


**Figure 5-2: Optical concept of a TIGER IFU: the IFS Slits Plane is filled with an array of micro-images of the telescope Entrance Pupil.**

In the case of a TIGER IFU the spaxel is a thick lens with only one surface getting optical power (see Figure 5-2[43]). This surface lies on the re-imaged telescope Focal Plane and samples a portion of the telescope PSF, according the Nyquist's criterion. The IFS Slit Function (**SF**), which in this case is the Intensity distribution over the re-imaged MicroPupil, is equal to the Airy Pattern corresponding to a circular aperture with a size equal to the spaxel one. This fact is explained through the following formalism.

Once introduced in the optical train, any single spaxel acts essentially as a diaphragm isolating a portion of the incoming Electric Field. A diaphragm in turn is defined by its monochromatic object transmission function ($\mathbf{T_L}$). In the case of homogeneous transmission, the spaxel transmission function gets the functional form of a top-hat function ($\Pi$) with size equal to the spaxel one:

$$T_L(x) = \Pi(x) \equiv \begin{cases} 1, & \text{if } |x| \le \frac{1}{2} \\ 0, & \text{if } |x| > \frac{1}{2} \end{cases} \qquad \textbf{Equation 5-7}$$

The variable (**x**) represents the radial coordinate on the re-imaged telescope Focal Plane in unit of $\mathbf{D_L}$.

From the optical point of view, each spaxel makes an image of the Electric Field signal, received by the telescope Entrance Pupil, on its corresponding MicroPupil Plane. Then, each spaxel acts as a liner spatial filter between two optically conjugated Planes: the telescope Entrance Pupil Plane and the MicroPupil Plane which is imaged by the single spaxel. This means that the Electric Field signal on each MicroPupil Plane is obtained by the convolution of the Electric Field signal on the Telescope Entrance Pupil and the spaxel transmission function. Moreover, the Nyquist's sampling of the diffraction limited telescope PSF implies that the telescope Entrance Pupil is unresolved by the single spaxel. In this optical condition, the Electric Field distribution on the telescope Entrance Pupil is not always resolved and becomes analytically a Dirac-Delta function ($\delta_{\mathbf{DIRAC}}$).

Then, the normalized monochromatic Electric Field distribution on the MicroPupil Plane corresponding to the single spaxel becomes:

$$E_P(s) = \delta_{DIRAC}(s) \otimes FT[T_L(x)] = FT[T_L(x)] = \frac{2 \cdot J_1(\pi \cdot s)}{\pi \cdot s} \qquad \textbf{Equation 5-8}$$

As a conclusion, for a TIGER spaxel the normalized monochromatic IFS Slit Function becomes:

$$SF(s) = |E_P(s)|^2 = \left[ \frac{2 \cdot J_1(\pi \cdot s)}{\pi \cdot s} \right]^2 \qquad \textbf{Equation 5-9}$$

Figure 5-3 shows a linear profile of such an IFS Slit Function; this is obtained by imposing, to the TIGER IFU a set of specifications that fulfil some of the SPHERE/IFS Top Level Requirements described in Table 5-2.

[43] In Figure 5-2 the TIGER concept is schematized by considering single thin lenses (cyan objects) with both powered optical surfaces. In the real world, a TIGER IFU is made with an array of thick lenses, each one having only one powered optical surface, that is the one which lies on the telescope re-imaged Focal Plane.

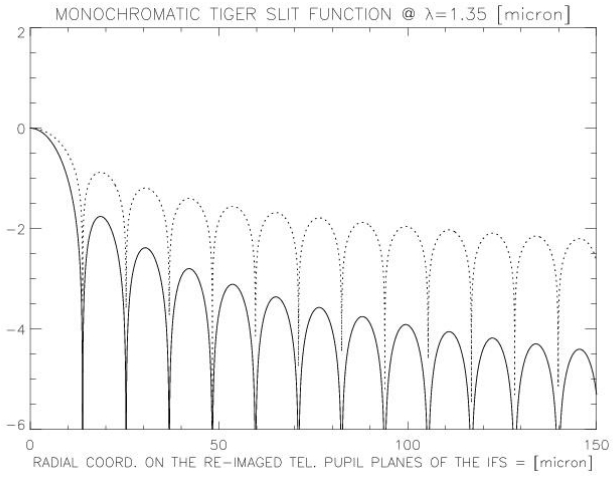


**Figure 5-3: Simulated profile of a monochromatic IFS Slit Function @ λ=1.35 [micron] in the case of the TIGER spaxel. Normalization is done with respect to the central value and the ordinate scale is logarithmic. The adopted Output Focal Ratio is $F_{OUT}$=8.**

The concept of TIGER spaxel, optimized for the Nyquist's spatial sampling of the re-imaged telescope Focal Plane, is shown in Figure 5-4.

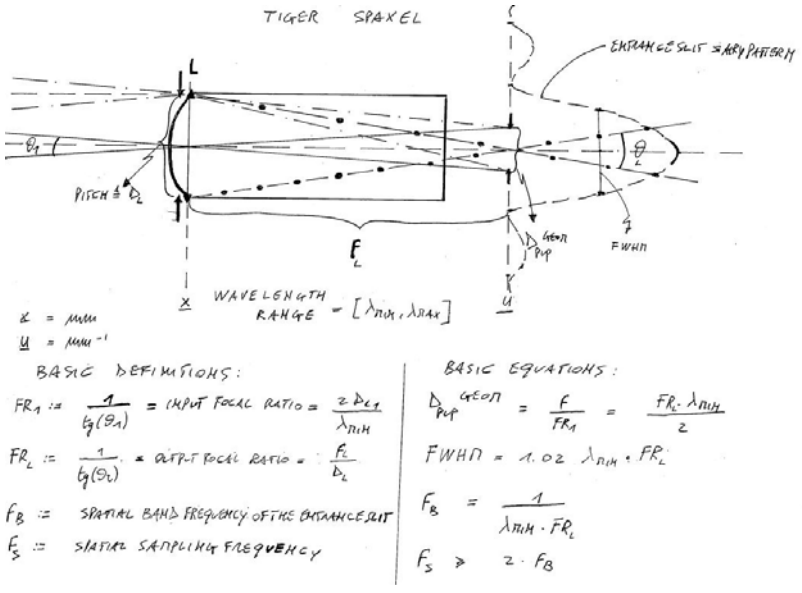


**Figure 5-4: TIGER spaxel in a nutshell.**

Basic definitions

- Minimum wavelength of the range of the 3D-Spectrograph ≡ $\lambda_{min}$
- Output Focal Ratio ≡ $F_{OUT}$
- Spatial sampling frequency on the IFS Detector Plane ≡ $f_S$
- Spatial Nyquist frequency on the IFS Detector Plane ≡ $f_{NY}$
- Spatial cutoff frequency ≡ $f_C$
- Size of the Detector pixel ≡ $d_{pixel}$

- IFS optical magnification ≡ $\mathbf{m_{IFS}}$

Basic equations

The case of the TIGRE spaxel, the shape of the monochromatic IFS Slit Function imposes to sample it at the Nyquist's limit, once re-imaged by the IFS optics on the Detector Plane.

The spatial cutoff frequency of the re-imaged IFS Slit Function is:

$$f_C = \frac{1}{\lambda_{min} \cdot F_{OUT} \cdot m_{IFS}} \qquad \textbf{Equation 5-10}$$

and the spatial sampling frequency on the IFS Detector Plane is:

$$f_S \equiv \frac{1}{d_{pixel}} \qquad \textbf{Equation 5-11}$$

The Nyquist's criterion imposes:

$$f_{NY} \equiv \frac{f_S}{2} > f_C \qquad \textbf{Equation 5-12}$$

Hence, the minimum output focal ratio can be expressed as:

$$F_{OUT} \geq \frac{2 \cdot d_{pixel}}{\lambda_{min} \cdot m_{IFS}} \qquad \textbf{Equation 5-13}$$

The basic specification of a TIGER spaxel is expressed by Equation 5-13. Specifically, it gives a lower limit for the Output Focal Ratio which depends on the Nyquist's sampling constraint on the IFS Detector Plane. Differently, the Output Focal Ratio upper limit results from the value of Incoherent CrossTalk between adjacent IFS Exit Slits Function (ES), which will be discussed in Section 5.4.

## 5.2 3D-Spectroscopy at the diffraction limit with a BIGRE IFU

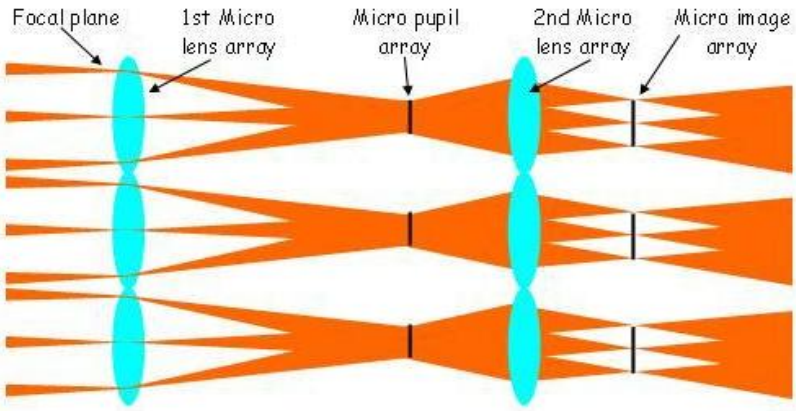


**Figure 5-5: Optical concept of a BIGRE IFU: the IFS Slits Plane is filled with an array of micro-images of the telescope Focal Plane.**

As in the case of TIGER case, the first surface of the BIGRE spaxel acts essentially a diaphragm isolating a portion of the incident Electric Field, which, differently to the TIGER

case, is re-focalized by the second surface of the spaxel (see Figure 5-5[44]). The first surface lies on the re-imaged telescope Focal Plane and samples the telescope PSF, according to the Nyquist's criterion. This surface re-images inside the lens the Electric Field received by the telescope Entrance Pupil, producing a MicroPupil that is an Airy Pattern, as in the case of the TIGER spaxel. While, differently to the TIGER case, the second surface re-images part of the light contained in this MicroPupil Plane, producing a de-magnified image of the first surface outside the lens, in the IFS Slit Plane. In this case then, the IFS Slit Function is the image of the first surface of the spaxel obtained through an optically thick lens whose surfaces have different optical power. Moreover, the resulting image respects the Fraunhofer optical propagation between the MicroPupil Plane and the IFS Slit Plane. This fact is explained through the following formalism.

Starting from Equation 5-8, the normalized monochromatic Electric Field distribution on the IFS Slit Plane is the Fourier Transform of the Electric Field distribution on the MicroPupil, which in turn is imaged inside the thick lens by its first optical surface:

$$E_S(w) = FT[E_P(s)] \qquad \textbf{Equation 5-14}$$

The variable (**w**) is defined as the spatial coordinate on all the planes of the IFS where the telescope Focal Plane is re-imaged, in unit of $\mathbf{F_{OUT}}\cdot\boldsymbol{\lambda}$.

The Electric Field distribution proper to the IFS Slit is modified by the transmission through the Spectrograph system due to the finite size of the Spectrograph Pupil. This can be expressed as a spatial filtering of the Intermediate Pupil Electric Field by a top-hat transmission function, the Spectrograph Pupil Mask (**SPM**). In this case, the normalized monochromatic Electric Field distribution on the IFS Detector plane gets the following functional form:

$$E_D(w) = FT[E_P(s)\cdot SPM(s)] = FT[E_P(s)\cdot \Pi(s/S_{SPM})] \qquad \textbf{Equation 5-15}$$

where $\mathbf{S_{SPM}}$ is the size of the Spectrograph Pupil Mask ($\mathbf{D_{SPM}}$) in unit of $\mathbf{F_{OUT}}\cdot\boldsymbol{\lambda}$.

Then, the normalized monochromatic IFS Slit Function for a BIGRE spaxel becomes then:

$$SF(w) = \left| FT\left\{ \left[ \frac{2\cdot J_1(\pi\cdot s)}{\pi\cdot s} \right] \cdot SPM(s) \right\} \right|^2 \qquad \textbf{Equation 5-16}$$

Figure 5-6 shows a linear profile of such an IFS Slit Function. This latter is obtained by imposing to the BIGRE IFU a set of specifications that fulfil the SPHERE/IFS Top Level Requirements described in Table 5-2.

[44] In Figure 5-5 the BIGRE concept is schematized by couples of thin lenses (cyan objects). In the real world, a BIGRE IFU is made with an array of thick lenses, each one having two powered optical surfaces.

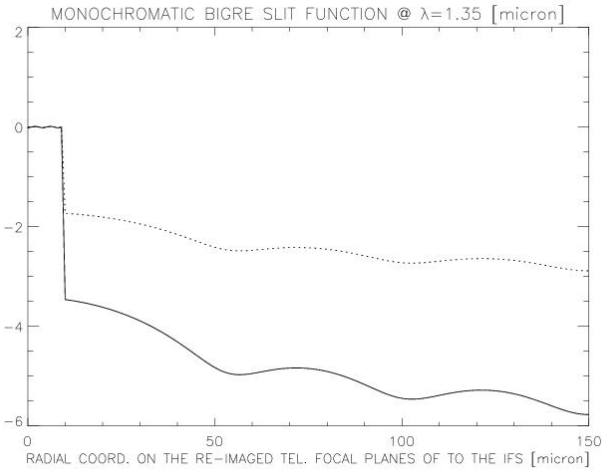


**Figure 5-6: Simulated profile of a monochromatic IFS Slit Function @ λ=1.35 [micron] in the case of the BIGRE spaxel. Normalization is done with respect to the central value and the ordinate scale is logarithmic. The adopted spaxel Output Focal Ratio is $F_{OUT}$=8.13 and $D_{SPM}$=30.72 [mm].**

The concept of BIGRE spaxel, optimized for the Nyquist's spatial sampling of the re-imaged telescope Focal Plane, is shown in Figure 5-7.

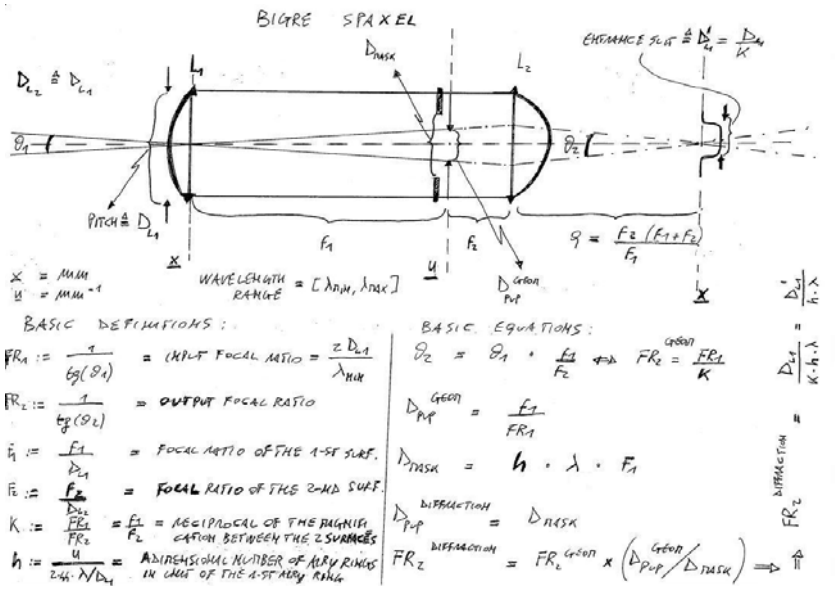


**Figure 5-7: BIGRE spaxel in a nutshell.**

Basic definitions

- Minimum wavelength of the range of the IFS ≡ $\boldsymbol{\lambda_{min}}$
- Central wavelength of the range of the IFS ≡ $\boldsymbol{\lambda_C}$
- Size of the single spaxel ≡ $\mathbf{D_L}$
- Input Focal Ratio ≡ $\mathbf{F_{IN}}$
- Output Focal Ratio ≡ $\mathbf{F_{OUT}}$
- Focal Ratio of the first optical surface of the BIGRE ≡ $\mathbf{F_1}$
- Focal length of the first optical surface of the BIGRE ≡ $\mathbf{f_1}$

- Focal Ratio of the second optical surface of the BIGRE ≡ $\mathbf{F_2}$
- Focal length of the second optical surface of the BIGRE ≡ $\mathbf{f_2}$
- Focal length of the optics downstream the second optical surface of the BIGRE= $\mathbf{f_{OUT}}$
- De-magnification factor between the two surfaces ≡ **K**
- Size of the Geometrical MicroPupil ≡ $\mathbf{D_{MP}}$
- Size of the MicroPupil Pupil Mask ≡ $\mathbf{D_{MPM}}$
- Size of the MicroPupil Pupil Mask in unit of $\mathbf{F_1 \cdot \lambda_C \equiv H}$
- Size of the Spectrograph Pupil Mask ≡ $\mathbf{D_{SPM}}$
- Size of the Spectrograph Pupil Mask in unit of $\mathbf{F_{OUT} \cdot \lambda_C \equiv S_{SPM}}$
- Size of the Detector pixel ≡ $\mathbf{d_{pixel}}$
- IFS optical magnification ≡ $\mathbf{m_{IFS}}$

Basic equations

The parameter **K** is defined as follows

$$K \equiv \frac{F_1}{F_2}$$ **Equation 5-17**

and determines the diameter of the IFS Slit through the following equation:

$$D_{SF} = \frac{D_L}{K}$$ **Equation 5-18**

Then, the size of the re-imaged IFS Slit will be:

$$D_{ES} = D_{SF} \cdot m_{IFS}$$ **Equation 5-19**

Thus, the correct spatial sampling of the re-imaged IFS Slit on the Detector plane is given by the following relation:

$$2 \cdot d_{pixel} \geq D_{ES} = \frac{D_L \cdot m_{IFS}}{K}$$ **Equation 5-20**

By Equation 5-5 the Input Focal Ratio is:

$$F_{IN} = \frac{2 \cdot D_L}{\lambda_{min}}$$ **Equation 5-21**

From the paraxial perspective, Input and Output Focal Ratios are related as follows:

$$F_{OUT}^{GEOMETRICAL} = \frac{F_{IN}}{K}$$ **Equation 5-22**

and the Geometric MicroPupil size is fixed as follows:

$$D_{MP} = \frac{f_1}{F_{IN}}$$ **Equation 5-23**

From the diffractive perspective, the Output Focal Ratio is fixed only when the size of the MicroPupil Mask is fixed on the MicroPupil Plane. This fact depends properly to the unbounded nature of the MicroPupil profile that is - as in the TIGER case - an Airy Pattern. The size of the MicroPupil Mask can be parameterized in term of **H**, $\lambda_C$ and $F_1$ as follows:

$$D_{MPM} = H \cdot \lambda_c \cdot F_1$$ **Equation 5-24**

The Diffractive Output Focal results from the following equation:

$$F_{OUT}^{DIFFRACTIVE} \equiv F_{OUT}^{GEOMETRICAL} \cdot \frac{D_{MP}}{D_{MPM}} = \frac{D_L}{K \cdot H \cdot \lambda_c} \equiv F_{OUT}$$ **Equation 5-25**

The true Output Focal Ratio will then the Diffractive one i.e.:

$$F_{OUT} \equiv F_{OUT}^{DIFFRACTIVE}$$ **Equation 5-26**

The Output Focal Ratio is the basic specification of a BIGRE spaxel. Through Equation 5-25, it is expressed in terms of the parameter $\mathbf{D_L}$, **K**, **H**, which in turn depend on the allowed level of Coherent CrossTalk between couples of monochromatic IFS Slit Functions.

Finally, the size of $\mathbf{D_{SMP}}$ can be expressed in term of the focal length of the second optical surface of the BIGRE and the focal length of the optics that - downstream to the BIGRE spaxels - re-image all the MicroPupils in a single Spectrograph Pupil:

$$D_{SMP} = D_{MPM} \cdot \frac{f_{OUT}}{f_2}$$ **Equation 5-27**

## 5.3 Optical quality of the single IFS Slit

Following (Section 3.2.1), realistic XAO systems - as SPHERE/SAXO (see Section 4.3.3) - are able to partially correct for the phase distortions proper to the signal feeding the telescope Entrance Pupil. In this condition (cfr. Equations 3-7, 3-1, 3-24), the actual profile of the signal (**S**) transmitted by a single spaxel described as follows:

$$S(x,\lambda) = [S_0 \otimes Sp](x,\lambda)$$

$$Sp(x,\lambda) \equiv FT[RAOTF(f,\lambda)]$$ **Equation 5-28**

$\mathbf{S_0(x,\lambda)}$ is defined by Equation 3-24 (the variable **x** here indicates the spatial coordinate on the telescope Focal Plane normalized to the diffraction limited spatial resolution at the entrance of single spaxel: $\mathbf{F_{IN} \cdot \lambda}$), while $\mathbf{RAOTF(f,\lambda)}$ is defined by Equation 3-6 (the variable **f** here indicates the spatial frequency normalized to the telescope cutoff frequency evaluated at the entrance of the single spaxel: $\mathbf{(F_{IN}.\lambda)^{-1}}$).

Equation 5-28 suggests that, both for the TIGER and the BIGRE spaxel types, the shape of the IFS Slit is no longer the one described by Equation 5-9 or Equation 5-16. At contrary, several optical effects have to be taken into account on the IFS Slits Plane, when a TIGER or a BIGRE device is introduced in an optical beam which is affected by a residual Speckle pattern field. These *Diffraction Effects* are described in the following Sub-Sections.

### 5.3.1 Shape Distortion of the single IFS Slit

As indicated by Equation 5-28, the re-imaged telescope Focal Plane is fed with an optical signal which is the convolution of pure diffraction limited signals with a residual Speckle pattern field (see Figure 5-8).

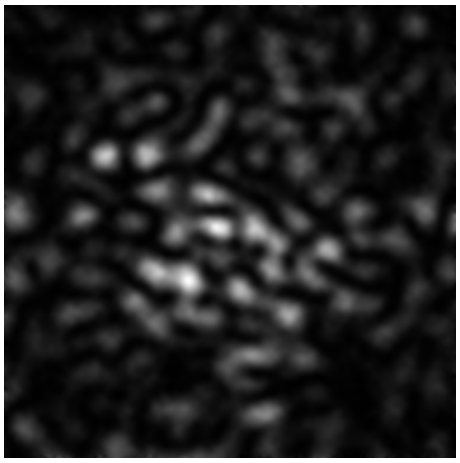

**Figure 5-8: Example of simulated bi-dimensional screen (0.5 [msec] integration time), generated by the SPHERE performance simulator (see Section 4.4). It represents the expected input to the SPHERE Integral Field Unit (by courtesy of the SPHERE team).**

As the VLT-PF team indicated, the residual Speckle pattern field is responsible for the shape distortions of the Slit Functions generated by the spaxels proper to this kind of IFU. Figure 5-9 shows a simulated image, produced by the VLT-PF team, which clearly indicates this effect. This behaviour arises because the spaxel Output Focal Ratio is high enough to allow the single spaxel to re-image its own portion of residual Speckle pattern.

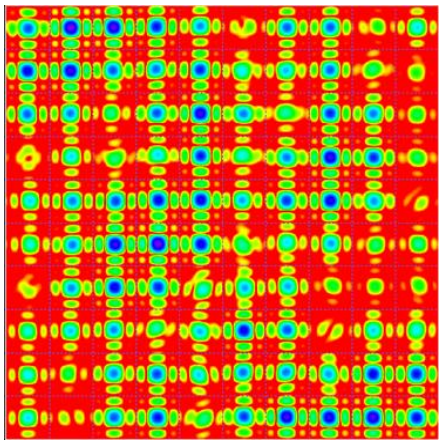

**Figure 5-9: 2D-image of the Slits Functions simulated by the VLT-PF team. The shape of the single TIGER spaxel is square, producing the $SINC^2$ profile proper the FT of a square aperture. Strong distortions due to this effect are clearly visible; the color scale is logarithmic: blue is hot, red is cold.**

This effect can be attenuated adopting low values of $\mathbf{F_{OUT}}$, as indicated by the CHEOPS team, through simulations of a TIGER IFU optimized only to control the impact of the Incoherent CrossTalk on the final Exit Slits. In this case, only Intensity variations remain clearly visible in the simulated screen; however Equation 5-13 indicates that Aliasing of the final Exit Slits can be avoided only when the spaxel Output Focal Ratio is larger than a specific value depending on the minimum wavelength, the pixel size and the optical

magnification on the Detector plane. Then, Aliasing can be a showstopper for a TIGER IFU in the case that the value of spaxel Output Focal Ratio, needed to the decrease the Incoherent CrossTalk pattern, becomes lower than the minimum value needed to sample at the Nyquist's limit the Exit Slits on the Detector plane.

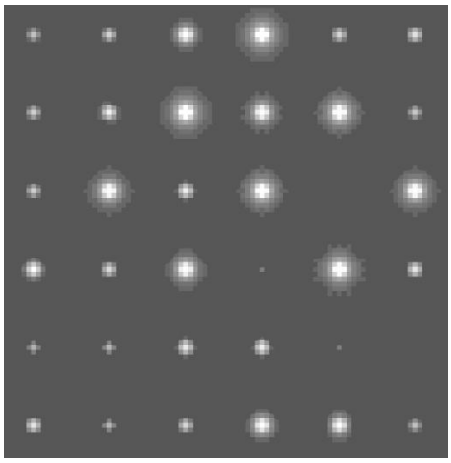

**Figure 5-10: Image of the MicroPupils Plane of the simulated TIGER IFU adopted by the CHEOPS team. The shape of the single spaxel is circular, producing an Airy Pattern profile. The modulation of the FT of the residual Speckle pattern field on the shape of the single MicroPupils is quite small, and only Intensity variations among re-imaged telescope Entrance Pupils are clearly visible in this 2D-screen. The color scale is logarithmic: white is hot, grey is cold.**

The impact of the Shape Distortion on the Slit Functions of such a TIGER IFU has been quantified adopting the Simulation Code described in Berton et al. (2006). As Figure 5-10 shows, when the spaxel Output Focal Ratio is sufficiently small, the shape variations of the Slits become statistically small as well (see Figure 5-11).

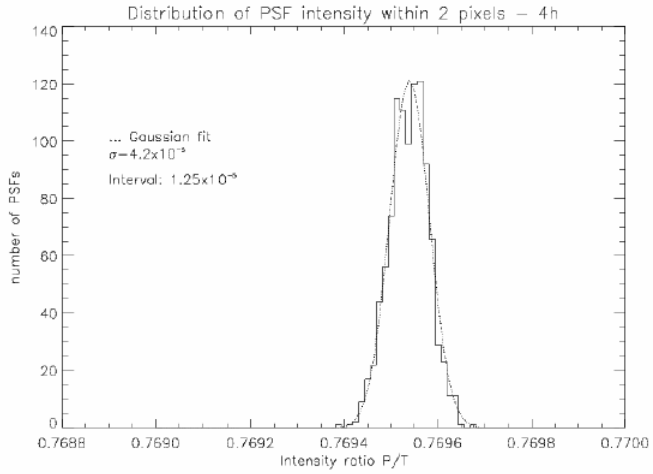


**Figure 5-11: Distribution of the intensities within the 2 central pixels ($d_{pixel}$=18 [micron]) of the IFS Slit Function profile resulting from a simulation of the TIGER IFU optimized by the CHEOPS team. The imposed Output Focal Ratio is $F_{OUT}$=8. Any Intensity value is normalized to the total Intensity incident on the single spaxel; the acquisition time is 4 [hr]. All the spaxels produce a SF central-peak whose Intensity is very close to that given by a Uniform Illumination i.e. the Airy Pattern proper to a circular aperture with size equal to the one of the single spaxel. Overimposed a Gaussian curve that fits the obtained statistical distribution with RMS=4.2x10$^{-5}$.**

In the case of a BIGRE IFU, this Diffraction Effect is avoided properly because the Slit Functions are re-imaged version of the first surface of the spaxels, with a de-magnification factor equal to **K**: the higher is this factor the higher will be the de-magnified image of the first surface of the spaxel, independently on the kind of illumination feeds this surface. This concept has been verified at the OAPD/Lab. for a prototype version of the BIGRE IFU for SPHERE/IFS (see Figure 5-12).

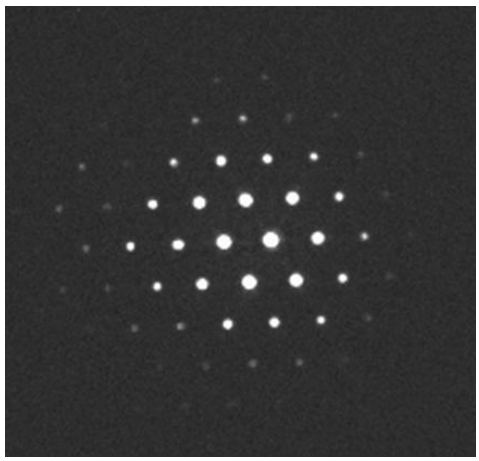

**Figure 5-12: Images of the IFS Slits obtained with the BIGRE IFU, at the OAPD/Lab. The Shape Distortion of the Slit Functions is practically absent and only Intensity variations among different IFS Slits remain. The color scale is logarithmic: white is hot, grey is cold.**

### 5.3.2 Speckle Chromatism on the single final spectrum

As defined in (Section 3.5.2), in the specific case of 3D-Spectroscopy Speckle Chromatism appears on the Detector pixels - once the IFS Slits are chromatically separated by a suitable disperser, and then re-imaged on the IFS Detector Plane - as a modulation of the spectra corresponding to the diffraction limited IFS Slits (cfr. Sparks and Ford 2002). In the 3D-cube, the Speckle Chromatism appears as an inclination of the final spectra (see Figure 5-13).

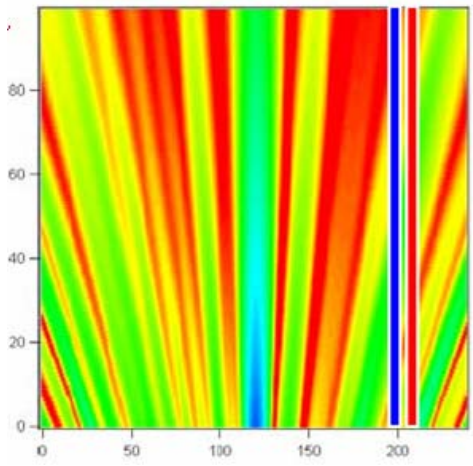


**Figure 5-13: Cuts through the data cube obtained by the chromatical dispersion of the IFS Slits resulting from the prototype TIGER IFU simulated by the VLT-PF team. The spatial dimension is on the horizontal axis, while the spectral dimension is on the vertical axis. The red and blue lines indicate two spectra taken at different radial distances to the optical axis. Moving along these spectra, a variable pseudo-periodic modulation - depending on the wavelength - is clearly visible.**

The correct formalism allowing to take into account for the Speckle Chromatism in a way which is independent on the actual profile of the diffraction limited monochromatic IFS Slit is presented in this Section.

At any given angular position[45] (**θ**) the separation between two consecutive maxima on the spectrum corresponding to this angular position, which is due to the modulation induced by the Speckle Chromatism, that is the pseudo-period (**P**) of this oscillation is given by:

$$P = \frac{\Delta}{N} \qquad \textbf{Equation 5-29}$$

where **Δ** is proportional to the wavelength **λ** and **N** is defined as the a-dimensional radial coordinate corresponding to angular position **θ**, expressed in **λ/D** unit[46]:

$$N \equiv \theta \cdot \frac{D}{\lambda} \qquad \textbf{Equation 5-30}$$

This definition implies that this a-dimensional coordinate is equal to the **N**-th diffraction order of a single monochromatic Speckle pattern. Then, for any angular position **θ**, two consecutive diffraction order (**N, N+1**) [47] of a chromatically dispersed Speckle pattern field, and corresponding to two different wavelengths ($\lambda_1<\lambda_2$), can be written as:

$$\theta = \frac{\lambda_1}{D} \cdot N \qquad \textbf{Equation 5-31}$$

and

$$\theta = \frac{\lambda_2}{D} \cdot (N+1) \qquad \textbf{Equation 5-32}$$

Combining Equations 5-31 and 5-32, a relation between the two consecutive maxima of the chromatically dispersed Speckles pattern field, proper to the a-dimensional radial position **N,** is then fixed:

$$\lambda_1 \cdot N = \lambda_2 \cdot (N+1) \qquad \textbf{Equation 5-33}$$

In order to satisfy the Nyquist's spectral sampling criterion of the chromatically dispersed Speckle pattern, the wavelength difference $\lambda_1$-$\lambda_2$ must be sampled by at least 2 pixels along spectral dispersion axis, that is:

$$\lambda_2 = \lambda_1 - (2 \cdot d\lambda) \qquad \textbf{Equation 5-34}$$

where **dλ** is defined as the portion of spectra sampled by a single spectral pixel[48]:

---

[45] In this formalism, the angular dimension **θ** is used in order to be independent on the physical scales adopted on the IFS Slit Planes of a given 3D-Spectrograph.

[46] **D** indicates the linear size of the telescope Entrance Pupil.

[47] The asymptotic separation between consecutive maxima of diffraction images is adopted.

[48] This definition of *spectral step* is given here fixing the origin of the spectral axis coordinate at the maximum wavelength of a given spectral range suitable for 3D-Spectroscopy.

$$d\lambda \equiv \frac{\lambda_C}{2R}$$ **Equation 5-35**

**R** is the spectral resolution and $\lambda_C$ is the central wavelength of the range covered by the 3D-Spectrograph[49].

Combining Equations 5-33 and 5-34, and approximating the quantity **2N+1** with **2N**, the wavelength $\lambda_1$ is obtained in term of the spectral step and the a-dimensional radial position **N**:

$$\lambda_1 \approx 2N \cdot d\lambda$$ **Equation 5-36**

Then, the spectral step can be expressed in term of the minimum of the two considered wavelength ($\lambda_1$), and the a-dimensional radial position **N**:

$$d\lambda = \frac{\lambda_1}{2N}$$ **Equation 5-37**

Equation 5-37 indicates that the correct spectral step depends on the a-dimensional position **N** i.e. to the physical angular position $\theta$. Then, for a given fixed spectral step $d\lambda$ there is a maximum angular position on the sky - we call this angular position the *Nyquist Radius* - below which the superposition of two consecutive maxima of a chromatically dispersed Speckles pattern field are sampled at the Nyquist limit, while they are undersampled beyond this boundary. Recalling the definition of **N** (cfr. Equation 5-30), the definition of $\theta_{NY}$ for a given working wavelength range $[\lambda_{min}, \lambda_{max}]$ is given as follows:

$$\theta_{NY} \equiv \frac{\lambda_{min}}{D} \cdot N_{NY}$$ **Equation 5-38**

According to Equation 5-37, the minimum wavelength diffraction order which corresponds to this angular position can be expressed as:

$$N_{NY} = \frac{\lambda_{min}}{2 \cdot d\lambda}$$ **Equation 5-39**

Then, combining Equations 5-38, 5-39 the Nyquist Radius will be:

$$\theta_{NY} = \frac{\lambda_{min}^2}{2 \cdot d\lambda \cdot D}$$ **Equation 5-40**

Recalling the definition of spectral step (see Equation 5-35) the Nyquist Radius can be finally written as follows:

$$\theta_{NY} = \frac{\lambda_{min}^2 \cdot R}{D \cdot \lambda_C}$$ **Equation 5-41**

Equation 5-41 expresses the minimum angular position below which the correct spectral sampling of a chromatically dispersed Speckle pattern field is verified in terms of the spectral resolution **R**, the minimum wavelength $\lambda_{min}$ of a given working range $[\lambda_{min},\lambda_{max}]$, and the telescope Entrance Pupil size **D**. As conclusion, the Nyquist Radius is a property

[49] Constant spectral sampling is assumed.

independent to the shape of the monochromatic IFS Slit. In this sense, the Nyquist Radius is not linked to the choice of Integral Field Unit. At contrary, this quantity depends directly on telescope and 3D-Spectrograph optical characteristics.

## 5.4 Coherent and Incoherent CrossTalks

Adopting the formalism of Goodman (1996), any spaxel of an Integral Field Unit is a linear optical system. In the case of TIGER and BIGRE, this linear system is the lens which transmits on the IFS Slits Plane two different kinds of signals:

- A Coherent signal i.e. the one composed by the sum of the diffraction limited signals of the star and the planet: $\mathbf{S_0(x)}$, cfr. Equation 5-28.
- An Incoherent signal, i.e. the one represented by the residual Speckles pattern field: **Sp(x)**, cfr. again Equation 5-28.

At level of Electric transmission, Coherent and Incoherent Electric Fields are then transmitted linearly in a different way through two adjacent spaxels. Specifically, when the Object illumination is Coherent, the linear responses of adjacent spaxels vary in unison, and therefore their signals, once transmitted and re-imaged on the IFS Slits Plane, must be added in complex amplitude. At contrary, when the Object illumination is Incoherent, the linear responses of two adjacent spaxels are statistically independent. This means that their signals, once transmitted and re-imaged on the IFS Slits Plane, must be added in real Intensity. Finally, once dispersed and re-imaged by the IFS optics, monochromatic Slits corresponding to adjacent spaxels will suffer from a certain amount of interference or *Coherent CrossTalk*. Furthermore, any monochromatic Slit will be affected by a spurious amount of signal due to its adjacent spectra. This latter effect is called *Incoherent CrossTalk*. Figure 5-14 explains these concepts in an evident way.

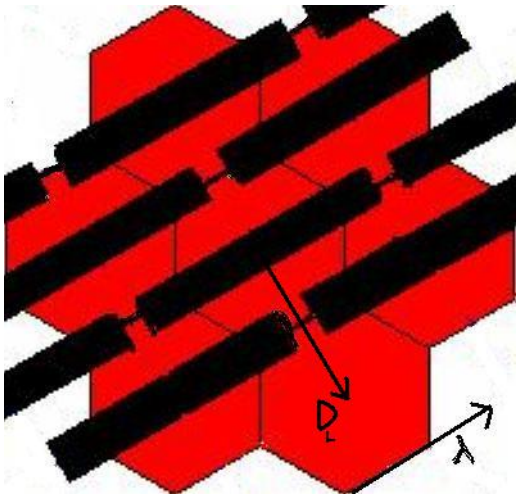


**Figure 5-14: Sketch of the final spectra (black rectangles) superimposed on an array of 7 (red) hexagonal spaxels, inside of a lenses-based IFU[50]. In this picture, Coherent CrossTalk is the interference signal between monochromatic IFS Slits corresponding to adjacent lenses i.e. separated by a distance equal to $D_L$; while Incoherent CrossTalk is the spurious signal registered over a fixed monochromatic IFS Slit and due to its adjacent spectra.**

[50] With a real 3D-Spectrograph, the spectral axis - indicated in the Figure with a black arrow - can be defined orienting the IFS Disperser with respect to a reference frame fixed on to the IFU.

### 5.4.1 Coherent CrossTalk: the formalism

Let be $\mathbf{E_1}$ the complex Electric Field of the Coherent signal transmitted by spaxel **1** on the IFS Slits Plane.

Let be $\mathbf{dE_2}$ the stray part of the complex Electric Field of the Coherent signal transmitted by spaxel **2** (spaxel **2** being adjacent to spaxel **1**) and evaluated in the position of the Slit corresponding to spaxel **1**.

$\mathbf{E_1}$ and $\mathbf{dE_2}$ are complex quantities that differ according their phase difference.

The effective Coherent Intensity measured on the IFS Slit and corresponding to position of spaxel **1** will be then:

$$I_1^C \equiv \left|E_1 + dE_2\right|^2 \qquad \textbf{Equation 5-42}$$

In the worst case, the phase difference is $\boldsymbol{\pi \cdot k}$, where **k** is an integer. Ignoring the last term in the binomial expression of Equation 5-42, the Coherent light then becomes:

$$I_1^C = I_1 \pm 2 \cdot \left|E_1\right| \cdot \left|dE_2\right| \qquad \textbf{Equation 5-43}$$

Defining the Intensity of the Electric Fields $\mathbf{E_1}$ and $\mathbf{dE_2}$ as follows:

$$\begin{aligned} I_1 &\equiv \left|E_1\right|^2 \\ dI &\equiv \left|dE_2\right|^2 \end{aligned} \qquad \textbf{Equation 5-44}$$

we can write:

$$I_1^C = I_1 \pm 2 \cdot \sqrt{I_1 \cdot dI} \qquad \textbf{Equation 5-45}$$

Through Equation 5-45 it is possible to define a Coherent CrossTalk coefficient (CCT) as:

$$CCT \equiv \frac{I_1^C - I_1}{I_1} = 2 \cdot \left|\frac{dE_2}{E_1}\right| \qquad \textbf{Equation 5-46}$$

CCT represents the extra amount of Coherent signal on the IFS Slit which corresponds to spaxel **1**.

Is important to point out that this definition of Coherent CrossTalk coefficient considers the maximum interference between two adjacent spaxels, which corresponds to the worst case of phase difference between the Electric Fields $\mathbf{E_1}$ and $\mathbf{dE_2}$. Equation 5-46 is then the upper limit of Coherence CrossTalk budget over the single IFS Slit.

Through Equation 5-46, the effective Coherent Intensity on spaxel **1** can be then written as:

$$I_1^C = I_1 + CCT \cdot I_1 \qquad \textbf{Equation 5-47}$$

Once re-imaged through the IFS optics on the Detector Plane, a monochromatic IFS Slit will get an amount of Coherent light interfering with others monochromatic IFS Slits, located at distances:1,2,3,…..,n times the separation between adjacent spaxels ($\mathbf{D_L}$, see Figure 5-14). Also in this case, the previous formalism gives the upper limit of Coherent CrossTalk affecting the single monochromatic IFS Exit Slit:

$$I_1^C(\lambda) = I_1(\lambda) + CCT(\lambda) \cdot I_1(\lambda) \qquad \textbf{Equation 5-48}$$

Then, the maximum estimate of Coherent CrossTalk is given by measuring the square root of the Coherent Intensity of a single monochromatic IFS Exit Slit at distance equal to the pitch size $\mathbf{D_L}$.

### 5.4.2 Incoherent CrossTalk: the formalism

The amount of spurious Incoherent light can be evaluated directly on the Detector Plane, where a single Exit Slit appears as a spectrum made of a finite number of monochromatic Slits, equal to the spectral step of a suitable Disperser.

As indicated in Figure 5-14, any final spectrum is surrounded by a number (**Ns**) of spectra. This number depends on the configuration (square, hexagonal, …) proper to adopted for the TIGER or BIGRE IFU.

Let be $\mathbf{I_i(\lambda)}$ the Incoherent Intensity proper to the i-th monochromatic IFS Slit on the IFS Detector plane. Due to the presence of $\mathbf{N_S}$ adjacent spectra (4 for a square configuration, 6 for a hexagonal one,…) its effective Incoherent Intensity will be:

$$\mathrm{I_i^I}(\lambda) \equiv \mathrm{I_i}(\lambda) + \sum_{l=1}^{l=N_S} \mathrm{ICT}_l(\lambda) \cdot \mathrm{I}_i^l(\lambda) \qquad \textbf{Equation 5-49}$$

where $\mathbf{ICT_l(\lambda)}$ and $\mathbf{I^l_i(\lambda)}$ are respectively the monochromatic Incoherent CrossTalk coefficient, and the stray Incoherent Intensity of the l-th Slit evaluated at a distance equal to the separation to the i-th one.

The l-th Incoherent CrossTalk coefficient can be defined as follows:

$$\mathrm{ICT_l}(\lambda) \equiv \frac{\mathrm{I_i^l}(\lambda) - \mathrm{I}_i(\lambda)}{\mathrm{I}_i(\lambda)} \qquad \textbf{Equation 5-50}$$

Considering the case of a constant contribution of stray Incoherent Intensity by all the IFS Slits surrounding the i-th one: $\mathbf{I^l_i(\lambda) \equiv I(\lambda)}$, the single Incoherent CrossTalk coefficient can be written as follows:

$$\mathrm{ICT}(\lambda) = \frac{\mathrm{I_i^l}(\lambda) - \mathrm{I}_i(\lambda)}{\mathrm{N_S} \cdot \mathrm{I}(\lambda)} \qquad \textbf{Equation 5-51}$$

Then, differently to the Coherent case, the Incoherent CrossTalk must be considered on the IFS Detector Plane, searching for spectral alignments for which the distance among adjacent spectra could be as small as possible. Once this spectral alignment is found, an estimate of the Incoherent CrossTalk can be given by measuring the Incoherent Intensity of a single monochromatic IFS Slit at the distance equal to the transversal separation among adjacent spectra**.**

## 5.5 Format of the final spectra on the IFS Detector plane

The format of the spectra must allow the best use of the IFS Detector area in such a way that the transversal separation among adjacent spectra ($\delta_S$) remains constant and large enough to reduce Incoherent CrossTalk contamination at acceptable values.

Clearly, the allowed spectra layout on the Detector Plane depends on the shape of a lenses based array. To this aim, the analysis of the square and the hexagonal shapes is presented in this Dissertation, properly because - independently on the TIGER or BIGRE IFU types - these represent the best choices in terms of filling factor.

As shown in Table 5-1, we have taken into account several geometrical configurations giving different values for the length-to-distance ratio $\mathbf{R_S}$ of a spectrum, defined as follows[51]:

$$R_S = \frac{L_S}{\delta_S}$$ **Equation 5-52**

and different values for the Position Angle ($\alpha$) formed by a reference direction with the direction of the spectral dispersion.

| **Square** | $\mathbf{R_S}$ | $\alpha$ | **Hexagonal** | $\mathbf{R_S}$ | $\alpha$ |
|---|---|---|---|---|---|
| **case A** | **1** | **0°** | **case A** | **1.15** | **30°** |
| **case B** | **2** | **45°** | **case B** | **3.46** | **0°** |
| **case C** | **5** | **26.56°** | **case C** | **8.09** | **10.89°** |
| **case D** | **10** | **18.43°** | **case D** | **15.02** | **16.10°** |
| **case E** | **13** | **33.69°** | **case E** | **21.94** | **6.56°** |

**Table 5-1: Alignment of the spectra for Square and Hexagonal configurations of a lenses-based IFU.**

These two configurations are displayed in Figure 5-15 and Figure 5-16.

[51] In Equation 5-52 $\mathbf{L_S}$ represents the allowed length of a spectrum in a fixed spectral alignment.

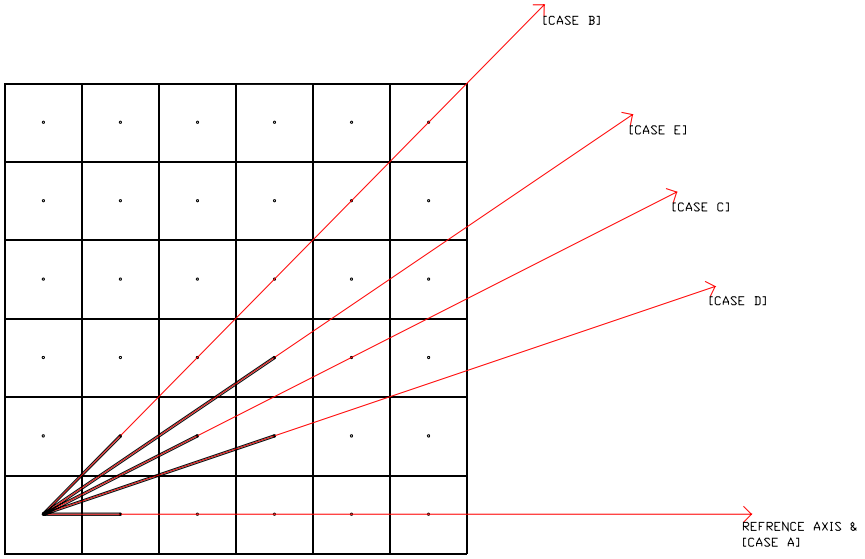


**Figure 5-15: Possible spectra alignment for the Square configuration of lens based IFU. The reference axis is aligned to a side of the square. Notice that the symmetries of a square configuration allow to analyze only alignments having Position Angles $< \alpha \leq \pi/4$.**

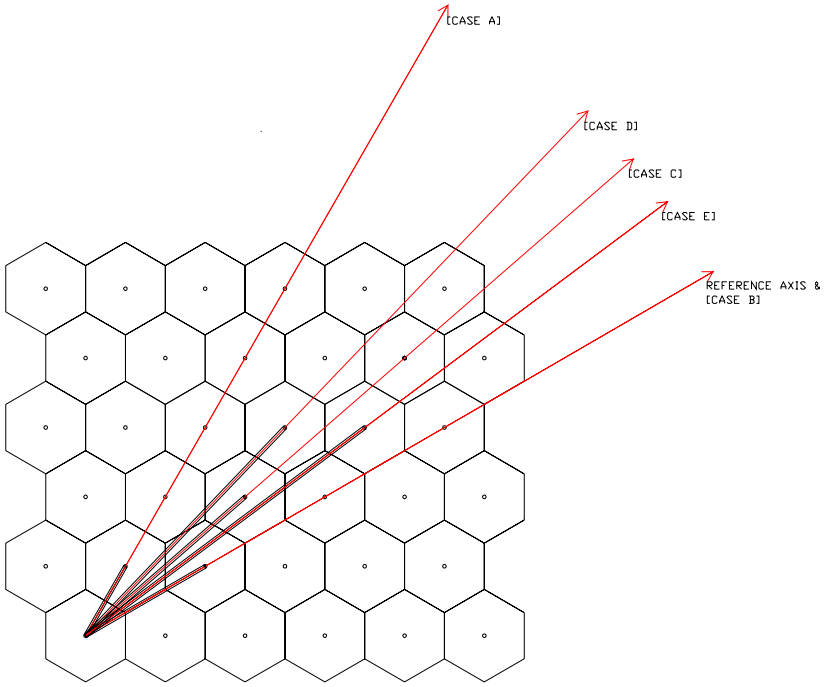


**Figure 5-16: Possible spectra alignment for the Hexagonal configuration of a lens based IFU. The reference axis is aligned to a side of the hexagon. Notice that the symmetries of a hexagonal lens based IFU allow to analyze only configurations having Position Angles $\alpha \leq \pi/6$.**

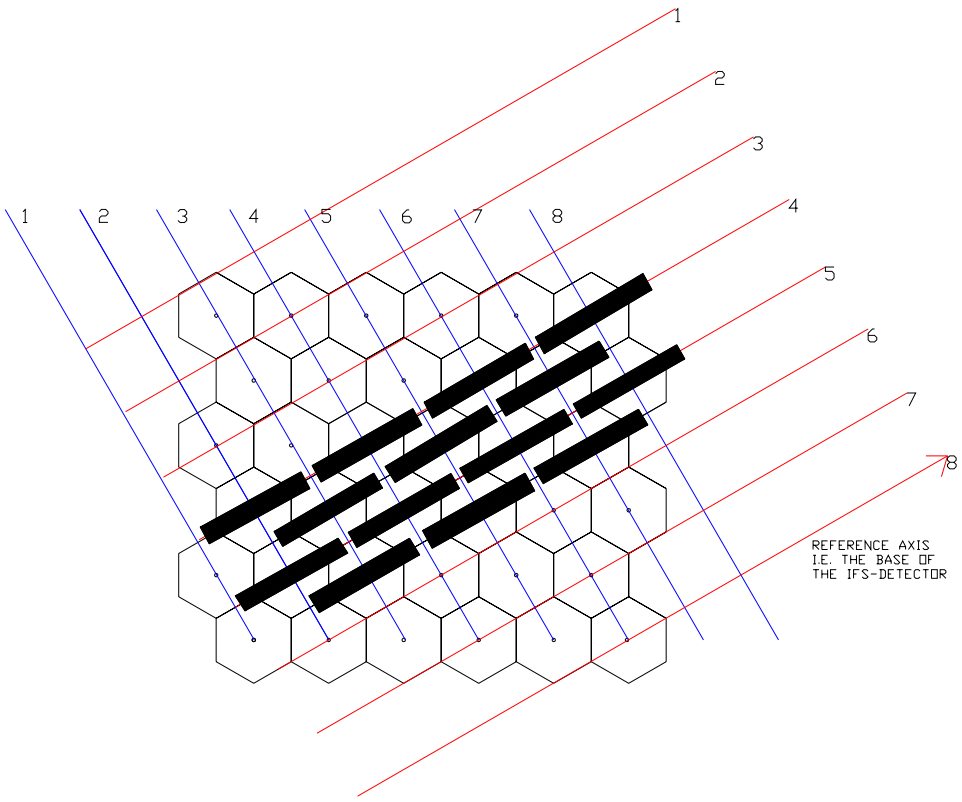


**Figure 5-17: Example of spectra alignment: the considered case in the Hexagonal-B (cfr. Table 5-1).**

The requested value of $\delta_S$ depends then on the limit imposed to the Incoherent CrossTalk coefficient, and it changes varying the alignment resumed in Table 5-1. At contrary, the allowed length of a spectrum depends only on the configuration selected for the layout of the spectra and it must verify the following inequality:

$$L_S - \delta_S \geq l_S \qquad \textbf{Equation 5-53}$$

($\mathbf{l_S}$ being defined as the length of the single spectrum on the Detector Plane). This condition guarantees that the Incoherent CrossTalk of two adjacent spectra, in the direction orthogonal to the dispersion one, do not exceed a specified upper limit.

### 5.5.1 Length of the single spectrum on the Detector plane

Defining the Spectral Purity (**SP**) of the IFS as:

$$SP \equiv \frac{2 \cdot R}{\Gamma} = \frac{\lambda_C}{d\lambda} \cdot \frac{1}{\Gamma} \qquad \textbf{Equation 5-54}$$

Where **R** is the spectral resolution, $\boldsymbol{\lambda_C}$ the central wavelength of the working range, $\mathbf{d\lambda}$ the spectral step and $\boldsymbol{\Gamma}$ the maximum between FWHM of the monochromatic IFS Exit Slit Function on the Detector Plane, evaluated at the central wavelength in pixel unit, and the Nyquist's spectral sampling limit:

$$\Gamma \equiv MAX\{2, FWHM[ES(\lambda_c)]\} \qquad \textbf{Equation 5-55}$$

Then, the spectral step of the IFS will be given by:

$$d\lambda = \frac{\lambda_C}{2 \cdot R} \cdot \frac{1}{\Gamma}$$ **Equation 5-56**

and the length of a spectrum in pixel unit by:

$$l_S = \left( \frac{\lambda_{max} - \lambda_{min}}{\lambda_C} \right) \cdot R \cdot \Gamma$$ **Equation 5-57**

## 5.6 TIGER and BIGRE Integral Field Units vs. SPHERE/IFS TLRs

According the Memorandum of Understanding stipulated with ESO, SPHERE/IFS should provide a spectrum in each point of the observed Field of View, for any star listed in the SPHERE Core Survey Program (see Section 4.2)[52].

| **Top Level Requirements** | **SPHERE/IFS** | **Technical Constraints** | **SPHERE/IFS** |
|---|---|---|---|
| **Wavelength range** | **0.95-1.35 [micron]** | **Detector size** | **$(2048)^2$ pixels** |
| **Field of View** | **$>(1.35)^2$ [arcsec]$^2$** | **Detector pixel size** | **18 [micron]** |
| **Resolution (2 pixels)** | **>15** | **Total Length** | **<2000 [mm]** |
| **Contrast** | **$>10^7$** | | |

**Table 5-2: Top Level Requirements of SPHERE/IFS, and Technical Constraints of the IFS sub-system inside the main SPHERE module.**

As indicated in Table 5-2, SPHERE/IFS should verify basic requirements (TLRs) due to its scientific goal, and a list of Technical Constraints according to the SPHERE main module (see Figure 4-2).

These value allows to fix the basic parameters of a TIGER/BIGRE type of Integral Field Unit which is able to perform high contrast diffraction limited Integral Field Spectroscopy. To this aim, both the Diffraction Effects and the effective level of Coherent and Incoherent CrossTalks are decisive tests for choosing the best solution for the SPHERE/IFU module.

In details, Diffraction Effects affect in a different way the TIGER and the BIGRE types of Integral Field Unit (see Table 5-3), and have to be taken into account in order to guarantee optical qualities suitable for the Spectroscopical-SDI calibration technique (see Section 3.5). Furthermore, a threshold for both the Coherent and Incoherent CrossTalks have to be imposed in the optimization of a TIGER/BIGRE Integral Field Unit, in order to reach the challenging Star vs. Planet Contrast value imposed to SPHERE/IFS: **$C>10^7$**.

| **Diffraction Effect** | **TIGER** | **BIGRE** | **CrossTalk type** | **TIGER** | **BIGRE** |
|---|---|---|---|---|---|
| **Shape Distortion** | **Present** | **Not Present** | **Coherent CrossTalk** | **Present** | **Present** |
| **Speckle Chromatism** | **Present** | **Present** | **Incoherent CrossTalk** | **Present** | **Present** |

**Table 5-3: Scheme of the Diffraction Effects and types of CrossTalk acting on a TIGER/BIGRE Integral Field Unit.**

[52] The VTL facility for the observations with SPHERE will be UT3.

### 5.6.1 Optimization of a TIGER IFU for SPHERE/IFS

Through Equation 5-41, the minimum wavelength $\lambda_{min}$**=0.95 [micron]**, the central wavelength ($\lambda_C$**=1.15 [micron])**, the telescope Entrance Pupil (**D=8 [m]**) and the minimum Field of View (**FOV=1.35$^2$ [arcsec]$^2$**), fix the minimum value of spectral resolution of the IFS Disperser (**R**), by which the Speckle Chromatism can be well attenuated. **R** together with the adopted geometrical configuration for the spectral alignment, the Detector pixel size ($\mathbf{d_{pixel}}$**=18 [micron]**), the IFS optical magnification, the lens pitch and the total number of spaxels, establish maximum filling factor of the Detector pixels. Through Equation 5-13, the Detector pixel size, the IFS optical magnification, and the minimum wavelength, establish the minimum value of the spaxel Output Focal Ratio. Through Equation 3-19, the fixed Star vs. Planet Contrast (**C>10$^7$**), can be converted into the single-spaxel Contrast defined as: **s(λ)/p(λ)**, which in turn depends on the total number of spaxels and the level of Strehl Ratio provided by the AO-system. Considering the average Strehl Ratio provided by SPHERE/SAXO (**SR(λ)≥0.9 ∀λ∈(0.95-1.35) [micron]**, according to the SPHERE TLRs list), and resuming all the previous calculations on a suited system of equations, the minimum value of the single spaxel Contrast returns: **s/p≥10$^3$**. This lower limit allows to fix the upper limit for the CCT and ICT: **CCT≤10$^{-3}$**; **ICT<10$^{-3}$**. Adopting the operative definitions of Coherent and Incoherent CrossTalks (see Sections 5.4.1 and 5.4.2 respectively) it comes out that both CCT and ICT can be estimated by the Intensity value of the monochromatic IFS Slit evaluated at a distance equal to:

- the lens pitch ($\mathbf{D_L}$), in the case of Coherent CrossTalk,
- the spectrum-to-spectrum separation, orthogonally to the spectral dispersion direction ($\delta_S$) in the case of Incoherent CrossTalk.

CCT and ICT can be reduced imposing the lowest values to the Output Focal Ratio. However, $\mathbf{F_{OUT}}$ should be larger than the minimum value by which Aliasing of the IFS Exit Slit is avoided, according Equation 5-13. This fact prevents a TIGER IFU, verifying all the others TLRs, to keep below the **10$^{-3}$** threshold the Coherent and Incoherent CrossTalk coefficients (see Figure 5-18). This fact rules out the TIGER IFU as a final solution for the SPHERE/IFU system**.**

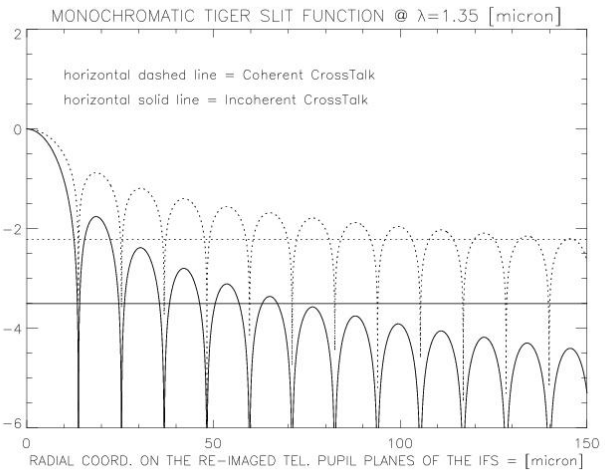


**Figure 5-18: Estimate of the CCT (~10$^{-2.25}$ at 150 [micron]) and ICT (~10$^{-3.5}$ at 75 [micron]) for the same Slit Function shown in Figure 5-3. Normalization is done with respect to the central value and the ordinate scale is logarithmic. These values are not sufficient for reaching the SPHERE/IFS Contrast goal of C>10$^7$.**

### 5.6.2 Optimization of a BIGRE IFU for SPHERE/IFS

As in the TIGER case, through Equation 5-37 the minimum wavelength ($\lambda_{min}$**=0.95 [micron]**) , the central wavelength ($\lambda_C$**=1.15 [micron]**), the telescope Entrance Pupil (**D=8 [m]**) and the minimum Field of View (**FOV=1.35$^2$ [arcsec]$^2$**), fix the minimum value of spectral resolution of the IFS Disperser (**R**), by which the Speckle Chromatism can be well attenuated. As in the TIGER case, **R** together with the adopted geometrical configuration for the spectral alignment, the Detector pixel size ($d_{pixel}$**=18 [micron]**), the IFS optical magnification the lens pitch and the total number of spaxels, establish maximum filling factor of the Detector pixels. Differently to the TIGER case, Coherent and Incoherent CrossTalks coefficients are constrained directly by choosing a suitable vector inside the parameter space **A=⟨$D_L$, K, H, $\lambda_C$⟩**. This is justified by the following considerations:

- **$D_L$** and **K** determine the relative separation of two arbitrary IFS Slits,
- **$D_{SPM}$** determines the amount of spatial filtering of the single IFS Slit Function and depends on **K** and **H**. Thus, a suitable vector in the sub-space **B=⟨$D_L$, K, H, $\lambda_C$=1.15 [micron]⟩** can be found directly searching for vectors verifying the conditions:
- **CCT≤10$^{-3}$**
- **ICT<10$^{-3}$**

In the domain **C={($D_L$, K, H, $\lambda_C$=1.15 [micron]) ∈ B | CCT ≤10$^{-3}$ and ICT<10$^{-3}$}**, the final solution is established once the constraint on the maximum Detector filling factor, together with the condition of correct spatial sampling of the final IFS Slit Function is verified; this procedure fixes the final IFS optical magnification factor. Finally, the spaxel Output Focal Ratio is determined through Equation 5-25.

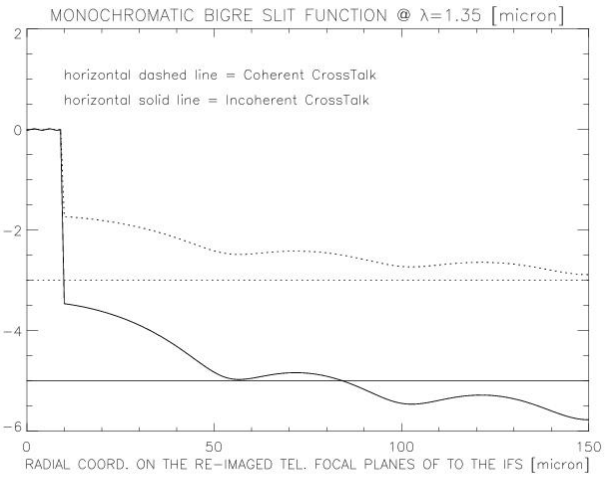


**Figure 5-19: Estimate of the CCT (~10$^{-3}$ at 150 [micron]) and ICT (~10$^{-6}$ at 75 [micron]) for the same Slit Function shown in Figure 5-6. Normalization is done with respect to the central value and the ordinate scale is logarithmic. The values are sufficient (Coherent CrossTalk) or well beyond (Incoherent CrossTalk) the limits allowing to reach the SPHERE/IFS Contrast goal of C>10$^7$.**

As shown in Figure 5-19, a BIGRE IFU can be fine-tuned for matching all the Top Level Requirements and the Technical specification listed in Table 5-2.

The BIGRE IFU is the solution adopted for the SPHERE/IFU system.

## 5.7 The BIGRE Integral Field Unit for SPHERE/IFS

The solution found for the SPHERE/IFU system is an optimized BIGRE lenses array.

The 3D-view of the Optical design is shown in Figure 5-20. The adopted solution for the SPHERE/IFU system is summarized in Figure 5-21.The geometrical configuration adopted for the alignment on the spectra on the IFS Detector is the **Hexagonal case C** (cfr. Figure 5-16) with the following specifications:

- the pitch size of the single BIGRE spaxel is $\mathbf{D_L=161.5\ [micron]}$
- the maximum achievable spectral resolution is: **R=54**
- the length of the single spectrum is: $\mathbf{l_S=37.50\ pixels}$
- the transversal separation among adjacent spectra is: $\mathbf{\delta_S=2.90\ pixels}$
- the optical magnification of the IFS optical system is $\mathbf{m_{IFS}=1.68}$

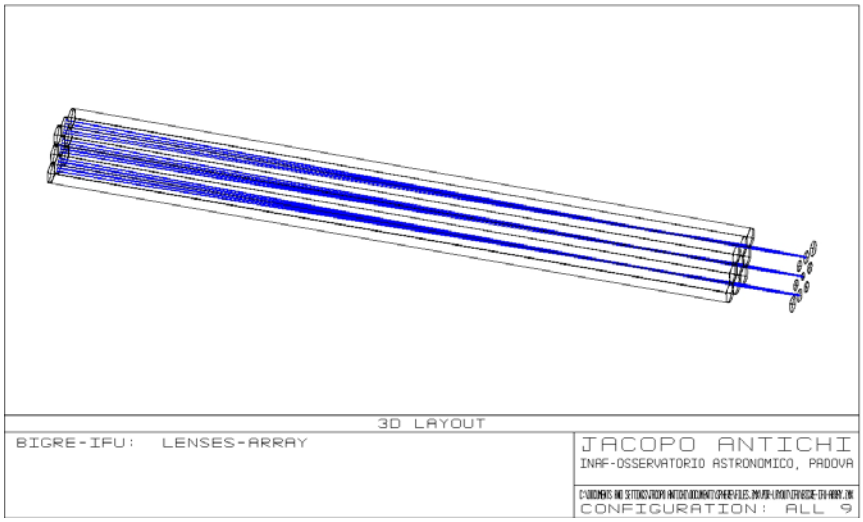


**Figure 5-20: Optical design of the BIGRE IFU to be mounted on SPHERE/IFS.**

CONCEPT-BIGRE-IFS  Hexagonal C case

**Common Path properties**

| | | | | |
|---|---|---|---|---|
| d-EnP | 8.00 | m | Telescope entrance pupil | D |
| FR-AO (computed) | 316 | | Input IFU focal ratio | FR_AO=2 P sqrt(0.866)/l1 |
| s-res (computed) | 1.225E-02 | arcsec | Nyquist spatial sampling at minimum wavelength | S_res=l1/(2 D) |

**IFS Specifications**

| | | | | |
|---|---|---|---|---|
| FoV | 1.770 | arcsec | field of view | FOV |
| min-w | 0.95 | micron | minimum wavelength | l1 |
| mid-w | 1.07 | micron | reference wavelength for coherent cross talk computati | l2 |
| max-w | 1.35 | micron | maximum  wavelength | l3 |
| 2-pixel spectral resolution | 54 | | wavelength divided by two pixel (in wavelength units) | R_2p |
| True spectral resolution (computed) | 50 | | wavelength divided by instrumental profile | R=2 R_2p/sqrt[(P M m/(k d_p))^2+1] |
| Linear dispersion (computed) | 0.0106 | micron/pixel | spectral linear resolution | Dis=(l2+l1)/[2 (2 R_2p)] |

**Detector Properties**

| | | | | |
|---|---|---|---|---|
| d-pixel | 18.00 | micron | pixel size | d_p |
| d-detector | 2048 | pixel | size of detector | d_d |

**IFU Parameters**

| | | | | |
|---|---|---|---|---|
| IFU-pitch | 161.50 | micron | microlens size | P |
| IFU-mask-factor | 0.95 | | lens mask in unit of pitch | M |
| IFU-index | 1.5055 | | refraction index of IFU at 1.15 micron (BK7) | n |
| K-factor | 7.4 | | ratio of IFU internal focal lengths | k |
| FR2 | 3 | | IFU-second lens focal ratio | FR2 |
| N-lenslets (side) (computed) | 145 | | IFU-linear lens number | N_lens = FOV / S_res |
| Area-lens (computed) | 22587 | micron^2 | Area of an hexagonal lens in pitch unit | A_lens=0.866*P^2 |
| d-IFU (computed) | 30.72 | mm | IFU-diagonal length | d_IFU = sqrt(2) sqrt(A_lens) N_lens |
| FR1 (computed) | 22.2 | | IFU-first lens focal ratio | FR1 = k FR2 |
| F1 (computed) | 3.585 | mm | IFU-first lens focal length | FL1 = P FR1 |
| F2 (computed) | 0.485 | mm | IFU-second focal length | FL2 = P FR2 |
| F1-med (computed) | 5.398 | mm | IFU-first lens spectral length in the medium | FL1_med = n FL1 |
| F2-med (computed) | 0.729 | mm | IFU-second lens spectral length in the medium | FL2_med = n FL2 |
| R1 (computed) | 1812 | micron | IFU first lens curvature radius | R1 = (n-1) FL1 |
| R2 (computed) | 245 | micron | IFU second lens curvature radius | R2 = (n-1) FL2 |
| Back Focal Distance (computed) | 0.550 | mm | IFU-back focal distance | BFD = FL2 (FL1+FL2) / FL1 |
| IFU-thickness (computed) | 6.127 | mm | IFU-thickness | t_IFU = FL1_med + FL2_med |
| d-EnS (computed) | 20.733 | micron | IFS-entrance-slit size | s = M P / k |
| TSA2-EnS (computed) | 8.78 | micron | Transverse Spherical aberration of second IFU lens | TSA_mu = 2 (0.5 P)^3/(2 R2)^2 |
| TSA2-ExS (computed) | 0.82 | pixels | Transverse Spherical aberration of second IFU lens | TSA_pix = (TSA_mu m)/d_p |
| IFU spatial filter | 2.50 | Airy disks | IFU-intermediate virtual mask (diffractive) | h |
| IFU spatial filter (diff.) (computed | 59.61 | micron | IFU-intermediate virtual mask (diffractive) | pup_IFU_d = h l2 FR1 |
| IFU spatial filter (geom.) (computed | 11.33 | micron | IFU-intermediate virtual mask (geometric) | pup_IFU_g = FL1 / FR_AO |

**IFS parameters**

| | | | | |
|---|---|---|---|---|
| m-IFS | 1.680 | | IFS magnification | m |
| FR-coll-geom (computed) | 42.76 | | IFS Collimator Geometrical Focal Ratio | FR_coll_g = FR_AO/k |
| FR-coll-diff (computed) | 8.13 | | IFS Collimator Diffractive Focal Ratio | FR_coll_d = P/(k h l2) |
| f-coll (computed) | 249.68 | mm | IFS Collimator Focal Length | FL_coll = FR_coll d_IFU |
| coll-beam (computed) | 30.72 | mm | IFS Intermediate Pupil Diameter | B = FL_coll / FR_coll |
| d-coll (computed) | 61.44 | mm | IFS Collimator Diameter | d_coll = B + d_IFU |
| d-cam (computed) | 103.21 | mm | IFS Camera Diameter | d_cam = m d_coll |
| IFS-l-actual (computed) | 1338.30 | mm | Approximate IFS Total length | l_IFS = 2 (f_coll + f_cam) |

**Spectrum format parameters**

| | | | | |
|---|---|---|---|---|
| Sp. length (computed) | 37.57 | pixels | Length of the spectrum | l_sp = (l3 - l1)/Dis |
| Sp. Sep (Hexagonal-C) (computed) | 4.93 | pixels | distance between 2 adjacent spetrum columns | sep_sp = 0.327 m P /d_p |
| Sp. Space (Hexagonal-C) (computed) | 39.88 | pixels | space available for a spectrum along its length | l_sp_max = sqrt(7) m P/d_p |
| Sp. Area (Hexagonal-C) (computed) | 196.57 | pixels | area available for a spectrum | Area_sp = sep_sp l_sp_max |
| Detector filling factor (computed) | 0.9789 | | fraction of the detector filled by the spectra | fill = Area_sp N_lens^2 / d_d^2 |

**Sampling parameters**

| | | | | |
|---|---|---|---|---|
| Super-sampling (computed) | 2.18 | pixels | Size of the projection of the entrance slit in pixel | Sam_super=sqrt[(P M m/(k d_p))^2+1] |
| Hyper-sampling (computed) | 1.83 | arcsec | Nyquist radius | Ny_r = l1^2 R_2p m / [D 0.5 (l1+l3)] |
| Hyper-sampling (computed) | 2.593 | arcsec | Side of square within the Nyquist sample radius | Ny_side = sqrt(2) Ny_r |

**Checks**

| Paramater | Value | Criterion | Results of test |
|---|---|---|---|
| IFU Thickness: | 6.127 | < 12 | Acceptable |
| IFU Transverse spherical aberration: | 0.82 | < 1 | Acceptable |
| IFU Fresnel propagation criterion: | 59.61 | < 80.75 | Acceptable |
| IFS Collimator focal ratio: | 8.13 | > 6 | Acceptable |
| IFS Total length: | 1338.30 | < 2000 | Acceptable |
| Spectrum length: | 37.57 | < 37.88 | Acceptable |
| Format fit into detector: | 0.9789 | < 1 | Acceptable |
| Incoherent cross talk: | 1.76E-04 | < 1.00E-03 | Acceptable |
| Coherent cross talk: | 6.28E-04 | < 1.00E-03 | Acceptable |
| Super-sampling criterion: | 2.18 | > 2 | Satisfied |
| Hyper-sampling criterion: | 2.593 | > 1.770 | Satisfied |

**Figure 5-21: Viewgraph of the spreadsheet by which the BIGRE solution for the SPHERE/IFU system has been obtained. The checks at the bottom (colored in green) consider all the constraints imposed by the SPHERE/IFS TLRs and the Technical Constraints inside the SPHERE main module. Notice that the spreadsheet contains - as Outputs - the basic specifications of the SPHERE/IFS optical design.**

## 5.8 SPHERE/IFU prototype

A complete prototype of the Integral Field Unit for SPHERE/IFS has been realized at the OAPD/Laboratory.

To simplify issues related to the Detector, the adopted wavelength range was the VISible domain where a commercial CCD-Detector could be used. This implied a tuned re-scaling of the IFU parameters by the use of the spreadsheets shown in Figure 5-21.

The main characteristics of the prototype BIGRE IFU are reported in Table 5-4, while its optical design in Figure 5-22.

| **Specification type** | **Specification tolerance** |
|---|---|
| **Wavelength range** | **0.55-0.80 [micron]** |
| **Refraction index of the lens** | **1.4585 @ 0.633 [micron] (SUPRASIL)** |
| **Pitch** | **200.0±0.1 [micron]** |
| **Curvature Radius: 1st lens surface** | **2.000±0.100 [mm]** |
| **Curvature Radius: 2nd lens surface** | **0.367±0.014 [mm]** |
| **Center thickness of the lens** | **7.53±0.28 [mm]** |

**Table 5-4: Main parameters of the BIGRE IFU adopted for the prototyping of SPHERE/IFU.**

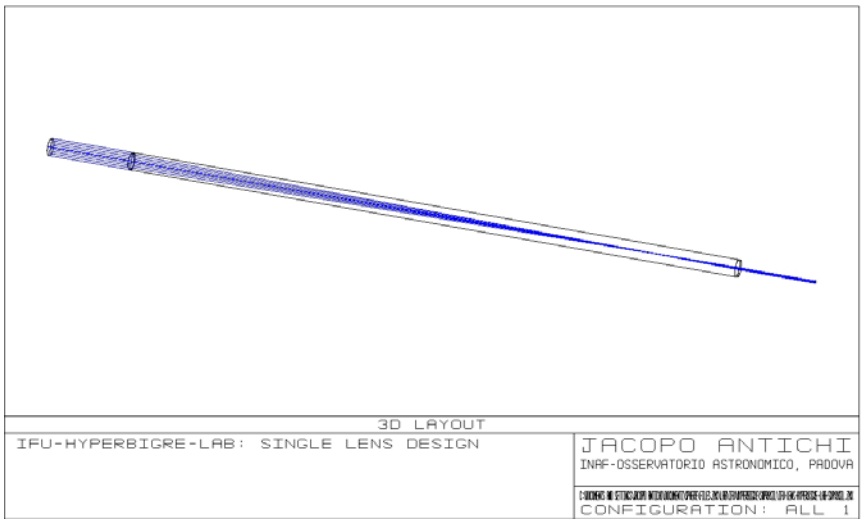


**Figure 5-22: Optical design of a single BIGRE lens for the prototyping of SPHERE/IFU.**

The IFU prototype has a rectangular shape of **16.4 [mm]** and contains **70×70** lenses.

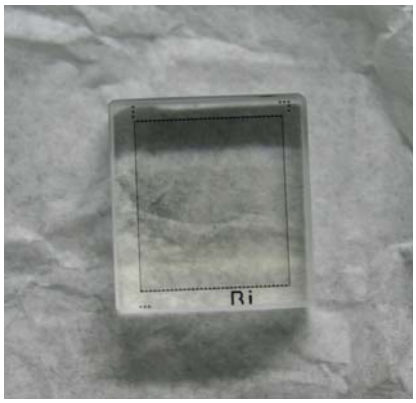

**Figure 5-23: Photo-image of the adopted IFU prototype realized by microoptic systems gmbh [ams]**

In front of the IFU prototype, a specific mask was deposited in order to render the first surface of any single lens a circular aperture (see Figure 5-24).

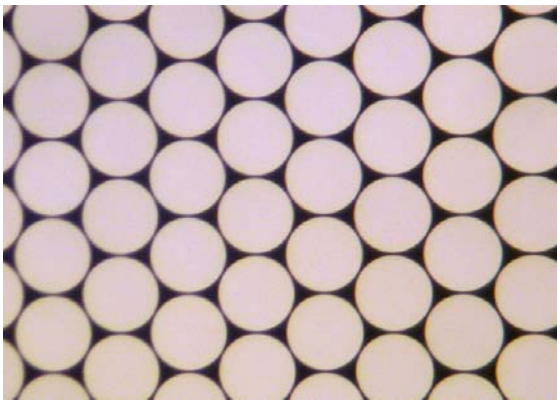

**Figure 5-24: Microscope-image of a portion of the prototype IFU. The deposited mask, that renders the shape of first surface of the lenses circular, is clearly visible.**

The lens pitch has been obtained measuring the distance between the central peaks of the autocorrelation of the microscopic-image of the lenses array. The autocorrelation map is shown in Figure 5-25.

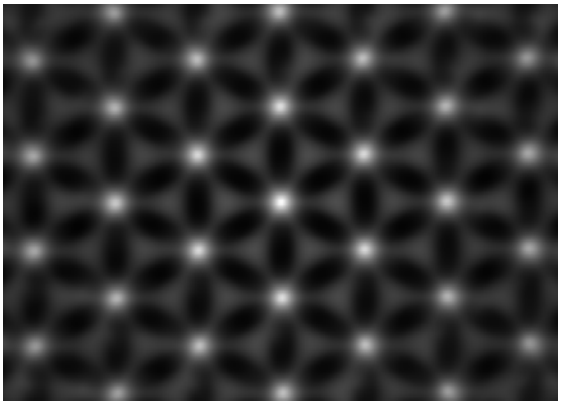

**Figure 5-25: Autocorrelation of the microscope-image of the prototype IFU.**

In order to realize a prototype for the IFS Slits, a suited optical setup has been realized (see Figure 5-26).

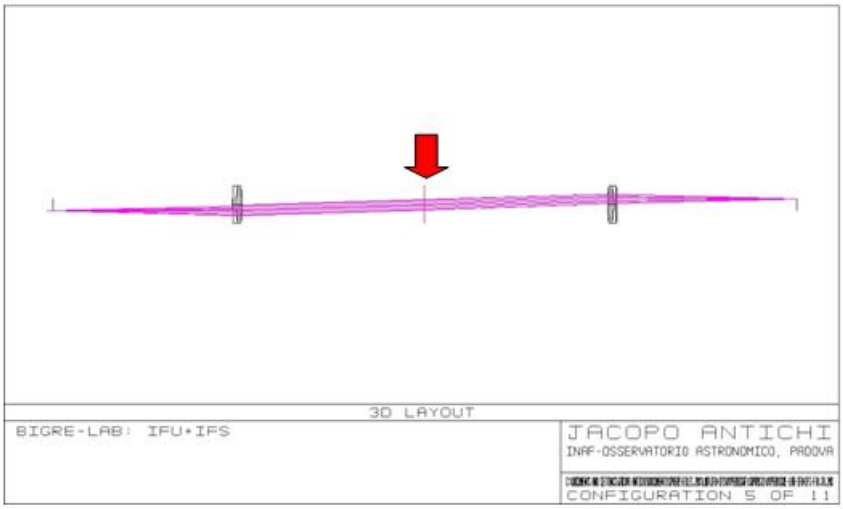


**Figure 5-26: Optical design of the 3D-Spectrograph adopted for the prototyping. The red arrow indicates the position of the Spectrograph Pupil Mask.**

With this optical setup, images of the IFS Slits Plane as generated by the BIGRE spaxels had been obtained (see Figure 5-27).

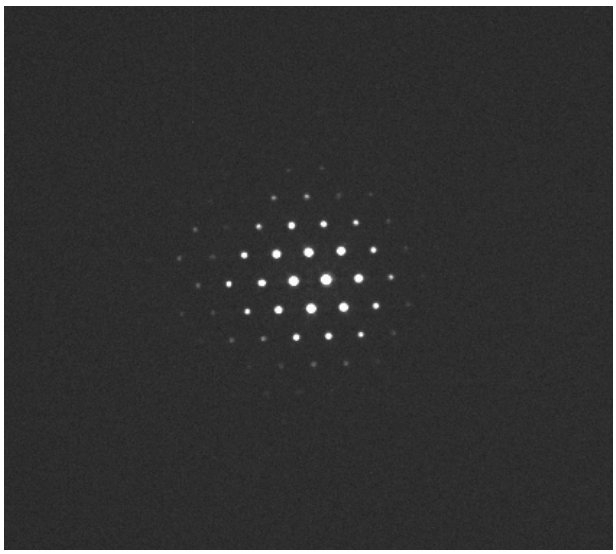

**Figure 5-27: CCD-image of the IFS Slits Plane obtained with the IFU prototype.**

As clearly visible in Figure 5-28, the BIGRE works as theoretically predicted. Specifically the Intensity profile on the Spectrograph Pupil Plane is an Airy Pattern with size matching the one foreseen by the formalism developed in this Dissertation. Moreover a Spectrograph Pupil Mask can be inserted in this position in order to control the spatial filtering of the final Exit Slits directly on this Pupil position, by using a top-hat transmission function with suited size: $\mathbf{D_{SPM}}$.

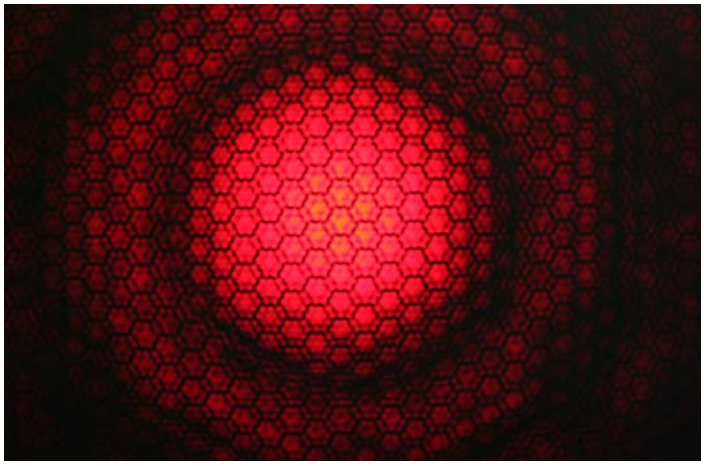

**Figure 5-28: Photo-image of the Spectrograph Pupil Plane of the IFS prototype. This is optically conjugated with the MicroPupils Plane that forms inside the thick lenses of the BIGRE IFU. The diffractive hexagonal pattern due to the Coherent CrossTalk among hexagonal spaxels is also visible.**

### 5.8.1 CrossTalk measures

An experiment was setup to measure the Incoherent CrossTalk on the IFS Slits Plane and the Intensity peaks of the interference signal generated by two adjacent spaxel (see Figure 5-29). The IFS was illuminated with a spatially filtered He-Ne laser source (**$\lambda_C$=0.683 [micron]**) whose monochromaticity enhances the visibility of the interference patterns. In order to show the faint structures due to CrossTalk, 100 images were summed up; furthermore the spots in the central part of the image were saturated.

For the measure of the Coherent CrossTalk two different optical setups have been considered:

- **Setup A**: a Spectrograph Pupil Mask with size equals **$D_{SPM}$=10.79 [mm],** corresponding to a number of Pupil Airy rings **H=2.5**, is inserted in the Spectrograph Pupil Plane.
- **Setup B**: without Spectrograph Pupil Mask.

The spaxel Output Focal Ratio for the BIGRE prototype is **$F_{OUT}$=23.17**, and the focal length length of the optics downstream the second optical surface - i.e. the IFS Collimator prototype - is **$f_{OUT}$=250 [mm]**.

The comparison between the two optical setups allows to check the BIGRE optical concept confronting measures of Coherent CrossTalk with the theoretical expectation.

The measures of Coherent CrossTalk has been obtained using the not saturated spots, evaluating the ratio between the central Intensity of each spot and the Intensity of the hexagonal-like structure surrounding it. According Section 5.4.1, the obtained quantity is proportional to the Coherent CrossTalk Coefficient.

For **Setup A**, which reproduces the expected setup of SPHERE/IFS, the averaged value of this quantity (**$2x10^{-4}$**) is well in agreement with the expected Coherent Cross Talk coefficient foreseen for this prototype.

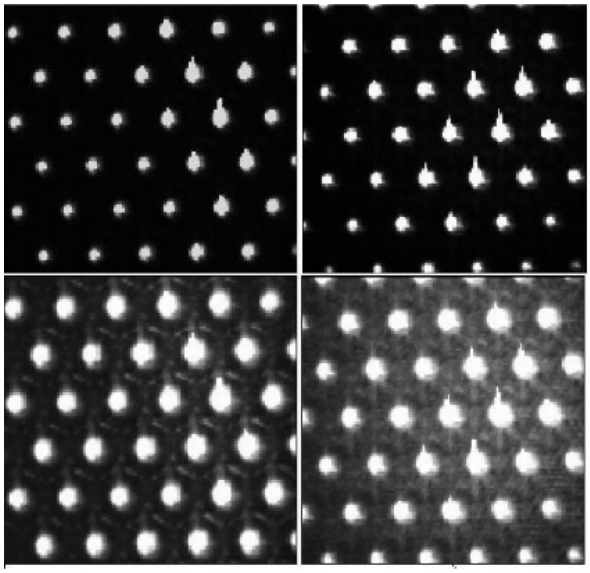

**Figure 5-29: Intensity map (on a logarithmic scale) of the re-imaged IFS Slits Plane of the prototype SPHERE/IFU. The top-panels show full images of Setup A (left) and Setup B (right); while the bottom-panels are Intensity-zoomed parts for the Setup A (left) and Setup B (right). Faint hexagonal-like structures are visible in those images obtained with Setup-A, due to the Coherent Cross Talk of the grid. The same hexagonal-like structures are clearly visible in the images proper to Setup B, but they have a much higher Intensity. The Intensity difference of these hexagonal-like structures depends on the Spectrograph Pupil Mask: when SPM is inserted (Setup A) the Coherent CrossTalk level on the IFS Slits Plane decreases. Notice that in order to show the extremely faint structures due to CrossTalk, the spots corresponding to the IFS Slits were saturated. Charge transfer inefficiency in the Detector causes the apparent presence of light along Detector columns.**

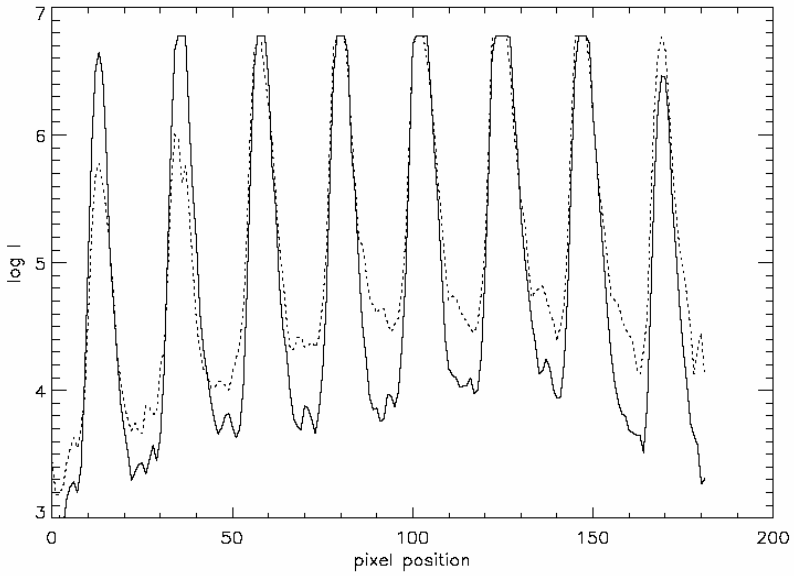


**Figure 5-30: Plot along a CCD-row passing across centers of consecutive re-imaged IFS Slits, obtained with the SPHERE/IFU prototype when the Spectrograph Pupil Mask is inserted (continuous line), or excluded (dashed line). Notice that the spots at coordinate X>350 are saturated.**

### 5.8.2 Achievement of the spectra

To obtain finally the spectra, a suitable Disperser has been then inserted in the IFS Spectrograph Pupil Plane, and a geometrical configuration for the alignment of the spectra has been chosen, according the prescription for the allowed levels of Incoherent CrossTalks.

For the IFS prototype, the Hexagonal-B configuration (see Figure 5-17) verifies the requested specification.

The final spectra are clearly visible in Figure 5-31.

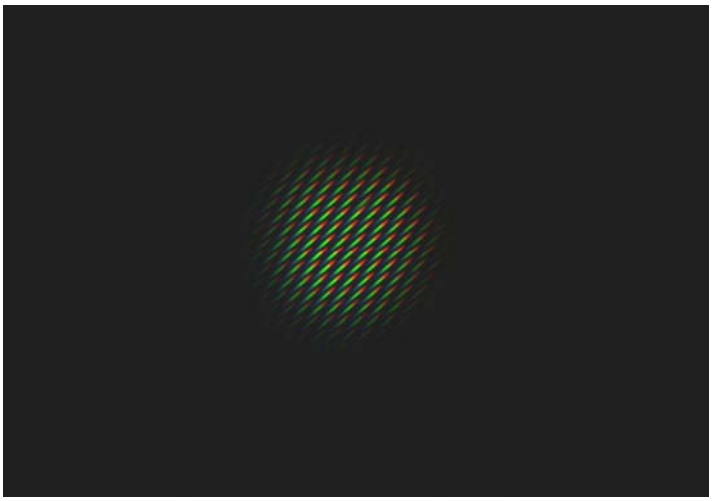

**Figure 5-31: CCD-image of the final spectra obtained with the IFS prototype realized at the OAPD/Lab.**

## 5.9 Bibliography

Bacon, R.; Adam, G.; Baranne, A.; Courtes, G.; Dubet, D.; Dubois, J. P.; Emsellem, E.; Ferruit, P.; Georgelin, Y.; Monnet, G.; and 3 coauthors, 1995, A&AS., v.113, p.347.

Bacon, R.; Copin, Y.; Monnet, G.; Miller, Bryan W.; Allington-Smith, J. R.; Bureau, M.; Carollo, C. M.; Davies, Roger L.; Emsellem, Eric; Kuntschner, Harald; and 3 coauthors, 2001, MNRAS., Volume 326, Issue 1, pp. 23-35.

Berton, A.; Gratton, R. G.; Feldt, M.; Henning, T.; Desidera, S.; Turatto, M.; Schmid, H. M.; Waters, R., 2006, PASP., Volume 118, Issue 846, pp. 1144-1164.

Born, Max; Wolf, Emil, **Principles of optics. Electromagnetic theory of propagation, interference and diffraction of light**, Oxford: Pergamon Press, 1965, 3rd (revised) ed.

Goodman, Joseph W., **Introduction to Fourier Optics**, 2nd ed., Publisher: New York, NY: McGraw-Hill, 1996. Series: McGraw-Hill series in electrical and computer engineering; Electromagnetic. ISBN: 0070242542.

Sparks, William B.; Ford, Holland C., 2002, ApJ., Volume 578, Issue 1, pp. 543-564

# 6 SPHERE Integral Field Spectrograph

The basic optical characteristic of SPHERE/IFS is to image the array of Slits, generated by the BIGRE IFU and chromatically separated by a proper dispersing device, on the IFS Detector Plane. The final exit Slits form then the array of spectra of this 3D-Spectrograph (see Figure 6-1).

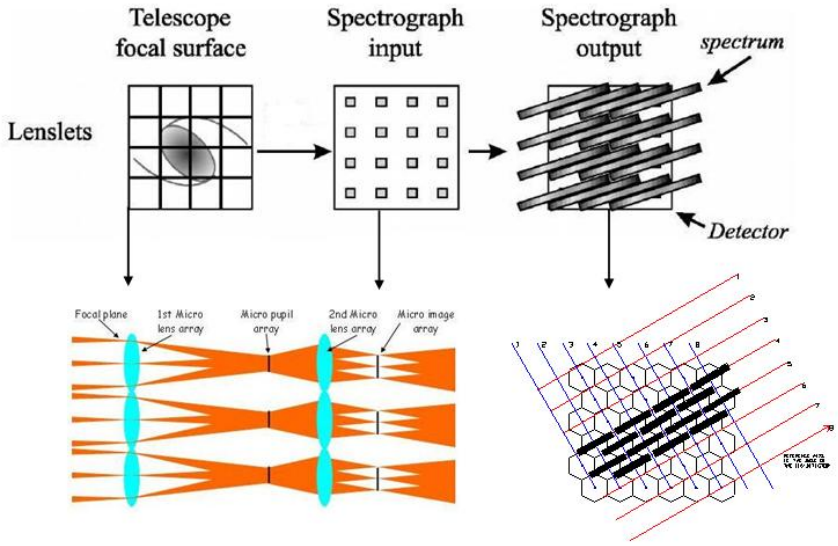


**Figure 6-1: Geometry of the Entrance Slits array produced by the BIGRE IFU system together with an example of spectra alignment on the IFS Detector Plane.**

The BIGRE optical system is located on a re-imaged Focal Plane inside the SPHERE Common Path (see Section 4.3.2). Furthermore, the input telecentricity[53] guarantees that the condition of Fraunhofer optical propagation holds between all the conjugate optical planes of the IFS.

In order to build an instrument with the highest optical stability together with good optical quality, the optimized IFS is a fully dioptric optical design composed by several sub-systems (see Table 6-1) located all along a unique optical axis (see Figure 6-2). Furthermore, the Camera optics are distinguished in two main sub-system: Warm and Cryogenic. The Warm optics get the same temperature of all the remaining part of SPHERE/IFS, which in turn shares the same environmental temperature of the SPHERE Common Path optics. Specifically, inside SPHERE/IFS the second surface of the Camera Singlet optics (see Figure 6-3) acts as the Dewar Window that isolates the Cryogenic sub-system, where the IFS IR-Detector is located. The only cooled-optics is a Low Pass chromatic-Filter that cuts the transmissions beyond the maximum working wavelength of SPHERE/IFS i.e. **$\lambda$=1.35 [micron]**. Finally, the instrumental background radiation is kept under control by imposing a distance between Dewar Window and Detector Plane equal to **150 [mm]**.

[53] Telecentricity is the property of an optical system to keep chief rays, i.e. those passing through the center of the Entrance/Exit Pupil, parallel to its optical axis (cfr. http://en.wikipedia.org/wiki/Telecentric_effect).

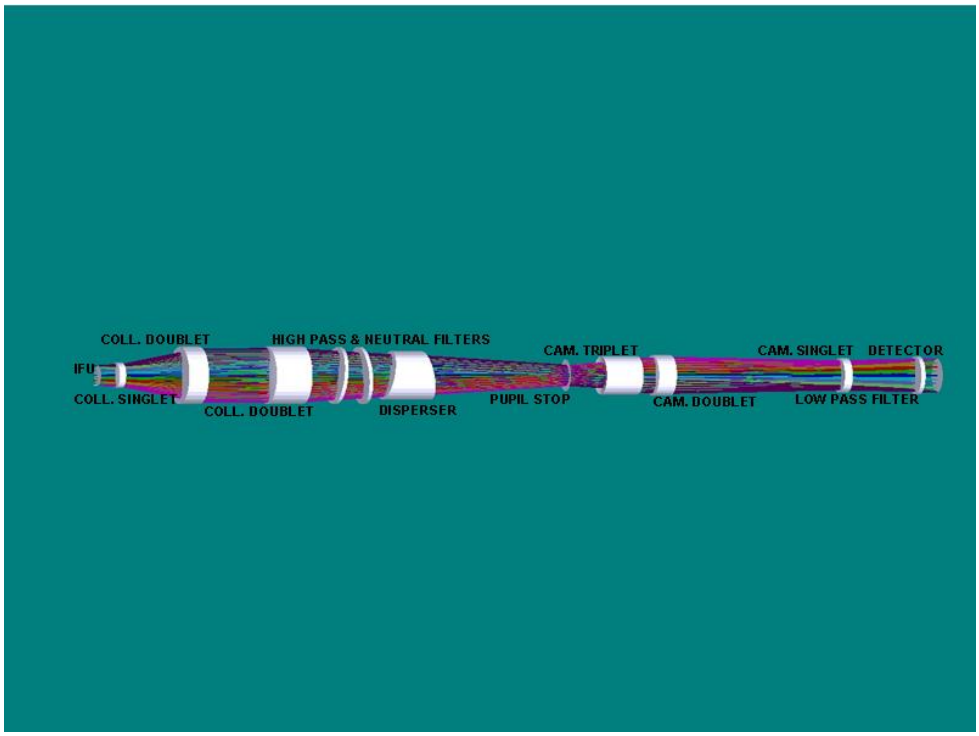


**Figure 6-2: 3D-representation of the SPHERE Integral Field Spectrograph.**

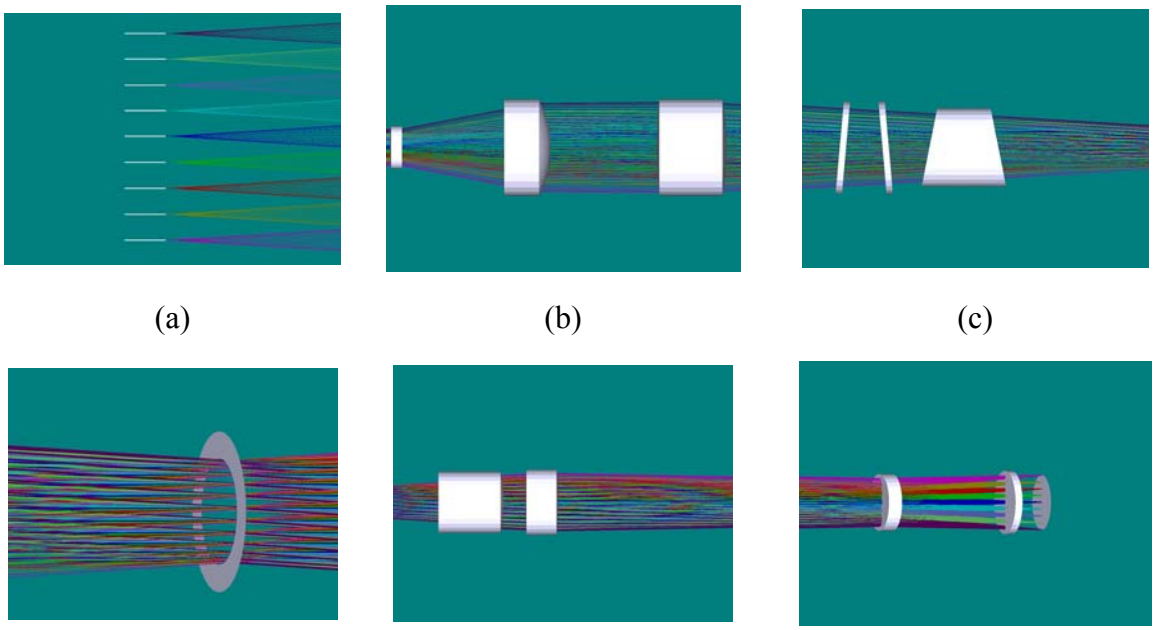


**Table 6-1: Scheme of the SPHERE/IFS main sub-systems: a) the BIGRE IFU sub-system; b) the IFS Collimator sub-system; c) the IFS Dispersion sub-system; d) the Pupil Stop sub-system; e) the IFS Warm Camera sub-system; f) the IFS Cryogenic Camera sub-system.**

## 6.1 Description of the ongoing IFS optical layout

The IFS optical design (see Figure 6-3) has been optimized exploiting the ray-tracing Code Zemax.

The adopted strategy was to optimize the IFS Collimator optics (see Section 6.2) and IFS Camera optics (see Section 6.4) separately, by imposing distinct Focal Ratios to these main IFS sub-system according the ones written in Table 6-2.

After the merging of these optimized sub-systems, the selected BIGRE IFU device (with optimized specifications, according to the spreadsheet shown in Figure 5-21) has been inserted in the optical train, in order to obtain the final SPHERE/IFS optical design.

An optimized Disperser (with the optimized specifications obtained in Section 6.6) has been finally inserted in the optical train, in order to realize the ray-tracing of the spectra generated by this 3D-Spectrograph.

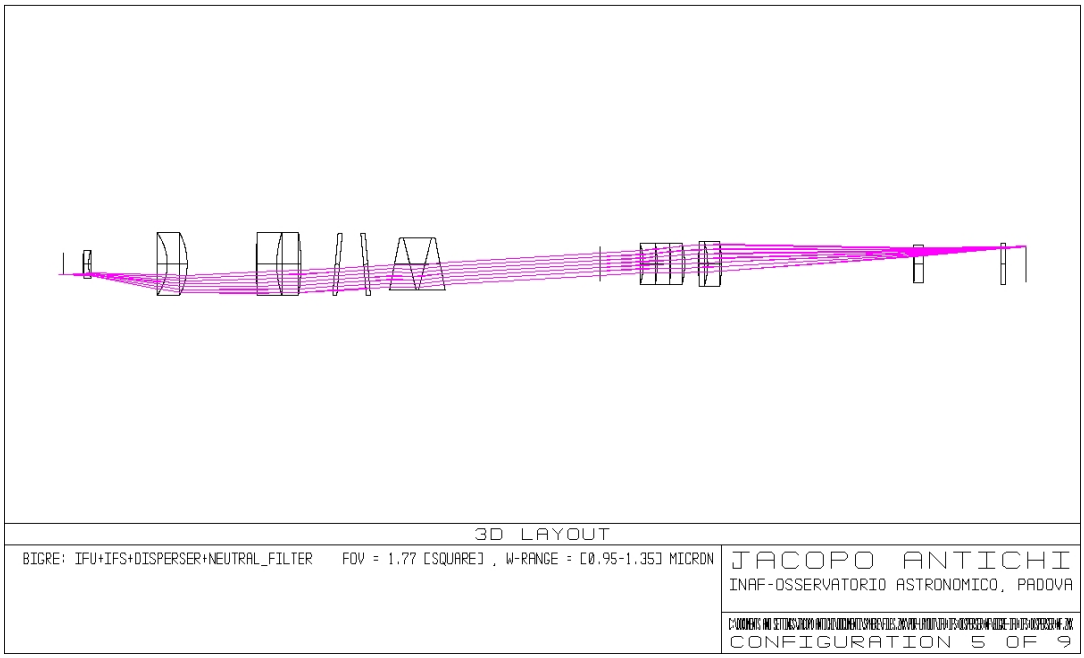


**Figure 6-3: Optical design of SPHERE/IFS: optical path of the extreme off-axis configuration; the total length of the system is: 1403.773 [mm].**

For the ray-tracing of a set of Input Parameters - summarized in Table 6-2 - are requested. Then, the optical design optimization returns the IFS Output Parameters that are summarized in Table 6-3.

| Input Parameter | Symbol | Value |
|---|---|---|
| IFS working wavelength range | $[\lambda_{min}, \lambda_{max}]$ | 0.95-1.35 [micron] |
| Size of the single BIGRE spaxel | $D_L$ | 161.5 [micron] |
| Input Focal Ratio on the BIGRE sub-system | $F_{IN}$ | 316 |
| Output Focal Ratio of the BIGRE sub-system | $F_{OUT}$ | 8.13 |
| Focal Ratio of the IFS Collimator sub-system | $F_{coll}$ | 8.13 |
| Camera vs. Collimator sub-systems magnific. | $m_{IFS}$ | 1.68 |
| Focal Ratio of the IFS Camera sub-system | $F_{cam}$ | 13.66 |
| Scale on the re-imaged telescope Focal Plane | $\Sigma_{IFU}$ | 0.01225 [arcsec/spaxel] |
| Covered Field of View | FOV | $(1.77)^2$ $[arcsec]^2$ |
| Total number of spaxels inside the BIGRE IFU | $N_{Im}^2$ | $(145)^2$ |
| Diagonal size of the BIGRE IFU | $diag_{IFU}$ | 30.72 [mm] |
| Focal length of the IFS Collimator sub-system | $f_{coll}$ | 249.68 [mm] |
| Focal length of the IFS Camera sub-system | $f_{cam}$ | 419.46 [mm] |
| Pixel size of the IFS Detector | $d_{pixel}$ | 18 [micron] |

**Table 6-2: Input Parameters for the ray-tracing optimization of the SPHERE/IFS optical design.**

| Optical Element | Location | Material | Thickness | Diagonal size |
|---|---|---|---|---|
| IFU | | BK7 | 6.127 [mm] | 30.72 [mm] |
| Single lens | Collimator. | S-FTM16 | 8.000 [mm] | 40.00 [mm] |
| Double lens | Collimator | CaF2+S-FTM16 | 43.160 [mm] | 90.00 [mm] |
| Double lens | Collimator | SFTM16+CaF2 | 65.000 [mm] | 90.00 [mm] |
| High-Pass Chromatic Filter | After Collimator | BK7 | 6.000 [mm] | 90.00 [mm] |
| Neutral Density Filter | After High-Pass Chromatic Filter | BK7 | 6.000 [mm] | 90.00 [mm] |
| Disperser | After Neutral Filter | FK54+LAFN21+ FK54 | 66.000 [mm] | 76.00 [mm] |
| Pupil Stop | After Disperser | None | 0 [mm] | 33.00 [mm] |
| Triple lens | Warm Camera | S-FTM16+CaF2+ S-FTM16 | 60.000 [mm] | 60.00 [mm] |
| Double lens | Warm Camera | CaF2 S-FTM16 | 33.396 [mm] | 64.00 [mm] |
| Dewar Window | Warm Camera | S-FTM16 | 12.140 [mm] | 54.00 [mm] |
| Low-Pass Chromatic Filter | Cryogenic Camera | S-FTM16 | 7.000 [mm] | 60.00 [mm] |

**Table 6-3: Optical elements of the SPHERE/IFS layout.**

## 6.2 Optimization of the IFS Collimator

The IFS Collimator optics (see Figure 6-4) have been optimized considering this sub-system has a Camera which focalizes collimated beams spanning the entire Field of View of SPHERE/IFS (**1.77$^2$ [arcsec]$^2$**) with the fixed focal ratio: **$F_{coll}$=8.13**.

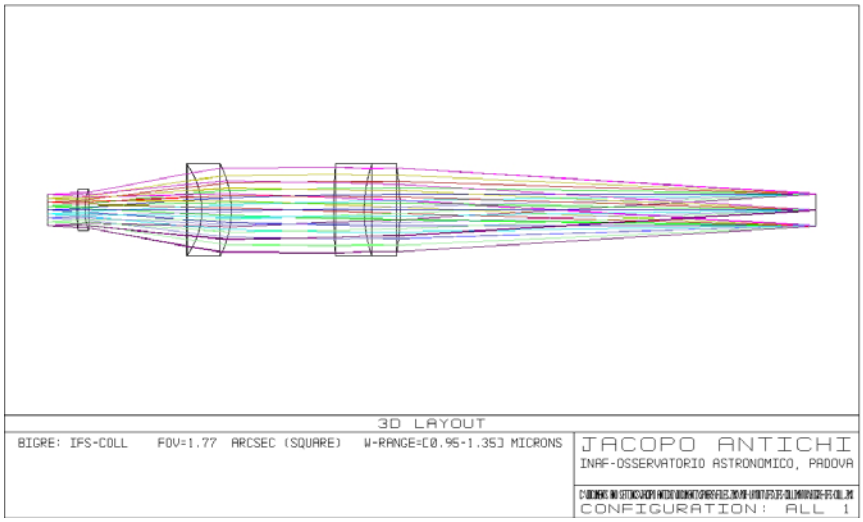


**Figure 6-4: Optical design of the SPHERE/IFS/Collimator.**

The optical quality of the optimized Collimator is well within the diffraction limit, as Figure 6-5 indicates.

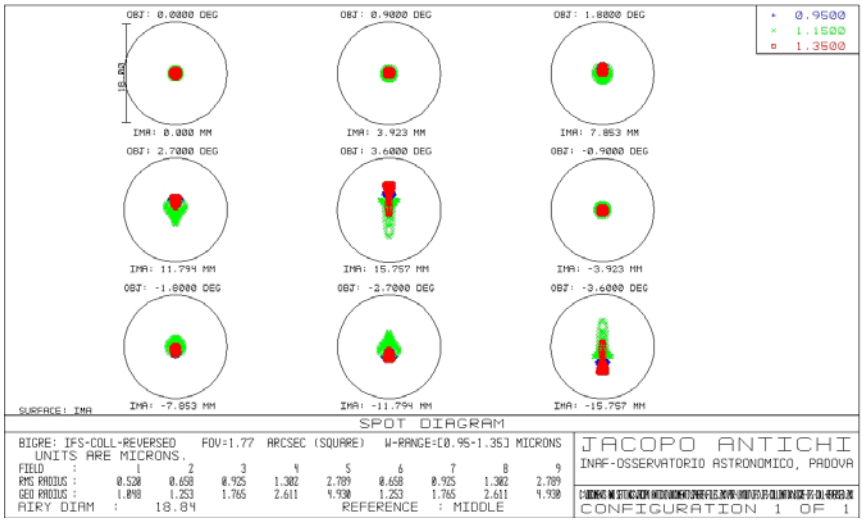


**Figure 6-5: Spot diagrams of the SPHERE/IFS/Collimator from the on-axis configuration to the extreme off-axis configurations whose correspond to a diagonal FOV equal to ± 1.25 [arcsec].**

In this optical condition, the achieved level of Strehl Ratio can be measured through the level of RMS Wavefront Error across the IFS Collimator Exit Pupil (see Figure 6-6).

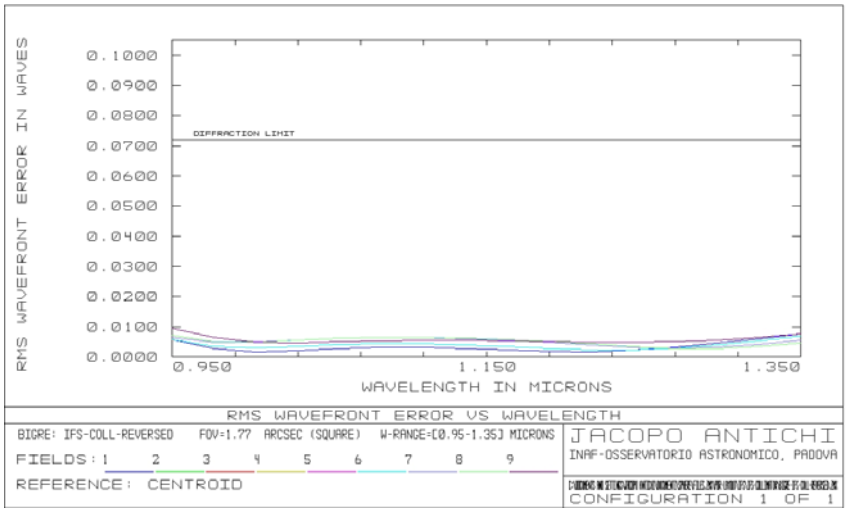


**Figure 6-6: RMS Wavefront Error vs. Wavelength diagram. Adopting the Maréchal's approximation (cfr. Born and Wolf 1965), the achieved Strehl Ratio is SR≈0.997.**

## 6.3 Tolerance analysis for the IFS Collimator

ADOPTED WAVELENGTH = 0.95 [micron]

ADOPTED COMPENSATOR: paraxial focus

CRITERION: WFE-RMS

NOMINAL WFE-RMS = 0.0230 (wavelength unit)

THRESHOLD ON THE DELTA WFE-RMS = 30%

THRESHOLD ON THE WFE-RMS = 1.3 * 0.0230 = 0.03

FIRST MODE ADOPTED: INVERSE-LIMIT

The Sensitivity Matrix changes until the following condition is reached:

DELTA WFE-RMS ≤ 30%

SECOND MODE ADOPTED: SENSITIVITY

The Sensitivity Matrix in changed term by term until the following condition is reached:

90% of the extractions should verify DELTA WFE-RMS ≤ 30%
, adopting the following statistical setup:

DISTRIBUTION OF RAYS STARTING FROM THE OBJECT PLANE: Uniform

NUMBER OF MONTE CARLO RUNS = 500

**IFS-COLL-REVERSED: FOV=1.77$^2$ [ARCSEC$^2$](SQUARE); W-RANGE = 0.95-1.35 [MICRON]**

**SURFACE DATA SUMMARY:**

| Surf | Type | Comment | Radius | Thickness | Glass | Diameter |
|---|---|---|---|---|---|---|
| OBJ | STANDARD | | Infinity | Infinity | | 0 |
| STO | STANDARD | | Infinity | 0 | | 30.72 |
| 2 | STANDARD | | Infinity | 406.77 | | 30.72 |
| 3 | STANDARD | | 282.81 | 35 | CAF2 | 90 |
| 4 | STANDARD | | -139.02 | 30 | S-FTM16 | 90 |
| 5 | STANDARD | | -480.78 | 100 | | 90 |
| 6 | STANDARD | | 98.97 | 28.87 | S-FTM16 | 90 |
| 7 | STANDARD | | 76.14 | 14.29 | CAF2 | 90 |
| 8 | STANDARD | | Infinity | 100 | | 90 |
| 9 | STANDARD | | -56.83 | 8 | S-FTM16 | 40 |
| 10 | STANDARD | | -156.19 | 28.64 | | 40 |
| IMA | STANDARD | | Infinity | | | 31.52067 |

**TOLERANCE DATA LISTING:**

| Num | Type | Int1 | Int2 | Int3 | Nominal | Min | Max | Units |
|---|---|---|---|---|---|---|---|---|
| 1 | (COMP) | 10 | 0 | | | 0.00000E+000 | 0.00000E+000 | |
| 2 | (TWAV) | | | | | 9.50000E-001 | | Microns |
| 3 | (TOFF) | | | | | | | |
| 4 | (TRAD) | 3 | | | 2.82810E+002 | -5.00000E-001 | 5.00000E-001 | Millimeters |
| 5 | (TRAD) | 4 | | | -1.39020E+002 | -2.00000E-001 | 2.00000E-001 | Millimeters |
| 6 | (TRAD) | 5 | | | -4.80780E+002 | -6.00000E-001 | 6.00000E-001 | Millimeters |
| 7 | (TRAD) | 6 | | | 9.89700E+001 | -4.00000E-002 | 4.00000E-002 | Millimeters |
| 8 | (TRAD) | 7 | | | 7.61400E+001 | -7.00000E-002 | 7.00000E-002 | Millimeters |
| 9 | (TFRN) | 8 | | | | -1.00000E-001 | 1.00000E-001 | Fringes |
| 10 | (TRAD) | 9 | | | -5.68300E+001 | -5.00000E-002 | 5.00000E-002 | Millimeters |
| 11 | (TRAD) | 10 | | | -1.56190E+002 | -3.00000E-001 | 3.00000E-001 | Millimeters |
| 12 | (TOFF) | | | | | | | |
| 13 | (TTHI) | 2 | 3 | | 4.06770E+002 | -3.00000E-001 | 3.00000E-001 | Millimeters |
| 14 | (TTHI) | 3 | 4 | | 3.50000E+001 | -1.00000E-001 | 1.00000E-001 | Millimeters |
| 15 | (TTHI) | 4 | 5 | | 3.00000E+001 | -1.00000E-001 | 1.00000E-001 | Millimeters |
| 16 | (TTHI) | 5 | 6 | | 1.00000E+002 | -5.00000E-002 | 5.00000E-002 | Millimeters |
| 17 | (TTHI) | 6 | 7 | | 2.88700E+001 | -1.00000E-001 | 1.00000E-001 | Millimeters |
| 18 | (TTHI) | 7 | 8 | | 1.42900E+001 | -1.00000E-001 | 1.00000E-001 | Millimeters |
| 19 | (TTHI) | 8 | 9 | | 1.00000E+002 | -1.00000E-001 | 1.00000E-001 | Millimeters |
| 20 | (TTHI) | 9 | 10 | | 8.00000E+000 | -1.00000E-001 | 1.00000E-001 | Millimeters |
| 21 | (TOFF) | | | | | | | |
| 22 | (TEDX) | 3 | 5 | | | -1.00000E-003 | 1.00000E-003 | Millimeters |
| 23 | (TEDY) | 3 | 5 | | | -1.00000E-003 | 1.00000E-003 | Millimeters |
| 24 | (TETX) | 3 | 5 | | | -1.00000E-002 | 1.00000E-002 | Degrees |
| 25 | (TETY) | 3 | 5 | | | -1.00000E-002 | 1.00000E-002 | Degrees |
| 26 | (TEDX) | 6 | 8 | | | -1.00000E-003 | 1.00000E-003 | Millimeters |
| 27 | (TEDY) | 6 | 8 | | | -1.00000E-003 | 1.00000E-003 | Millimeters |
| 28 | (TETX) | 6 | 8 | | | -1.00000E-002 | 1.00000E-002 | Degrees |
| 29 | (TETY) | 6 | 8 | | | -1.00000E-002 | 1.00000E-002 | Degrees |
| 30 | (TEDX) | 9 | 10 | | | -1.00000E-002 | 1.00000E-003 | Millimeters |
| 31 | (TEDY) | 9 | 10 | | | -1.00000E-002 | 1.00000E-003 | Millimeters |
| 32 | (TETX) | 9 | 10 | | | -1.00000E-002 | 1.00000E-002 | Degrees |
| 33 | (TETY) | 9 | 10 | | | -1.00000E-002 | 1.00000E-002 | Degrees |

**NOMENCLATURE:**

TRAD = TOLLERACE  ON THE  RADIUS OF CURVATURE
TFRN = TOLLERANCE ON THE  SURFACE FLATNESS: +/-0.1 FRINGES = LAMBDA/20 @ λ=0.95 [MICRON]
TTHI = TOLLERANCE ON THE  THICKNESS BETWEEN THE INDICATED SUPERFACE AND THE NEXT ONE
TEDX = TOLLERANCE ON DECENT. X OF THE GROUP OF OPTICS COMPRISED BETWEEN THE INDICATED SURF.
TEDY = TOLLERANCE ON DECENT. Y OF THE GROUP OF OPTICS COMPRISED BETWEEN THE INDICATED SURF.
TETX = TOLLERANCE ON TILT    X OF THE GROUP OF OPTICS COMPRISED BETWEEN THE INDICATED SURF.
TETY = TOLLERANCE ON TILT    Y OF THE GROUP OF OPTICS COMPRISED BETWEEN THE INDICATED SURF.

## 6.4 Optimization of the IFS Camera

The IFS Camera optics (see Figure 6-7) have been optimized considering that this sub-system focalizes the IFS Intermediate Pupil (**33.00 [mm]**) with the fixed optical magnification: $\mathbf{m_{IFS}=1.68}$. This condition constraints then the Focal Ratio of the IFS Camera optics: $\mathbf{F_{cam}=13.66}$.

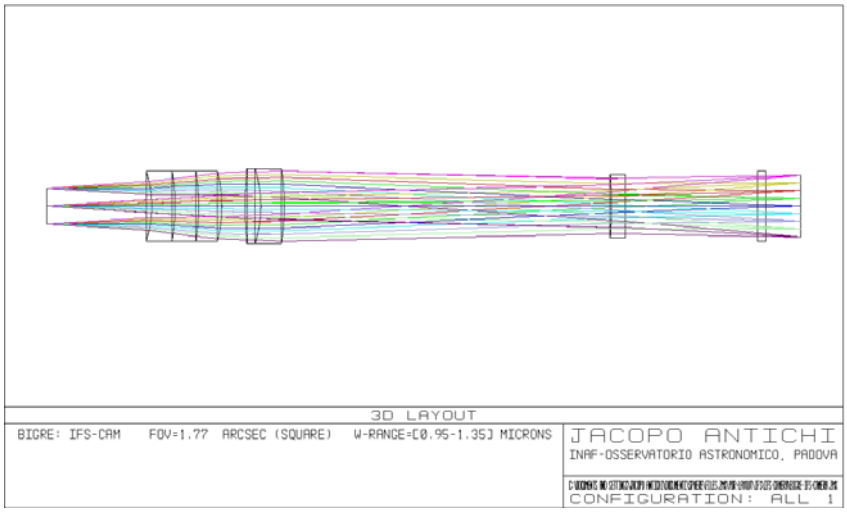


**Figure 6-7: Optical design of the SPHERE/IFS/Camera.**

The optical quality of the optimized Camera is well within the diffraction limit, as Figure 6-8 indicates.

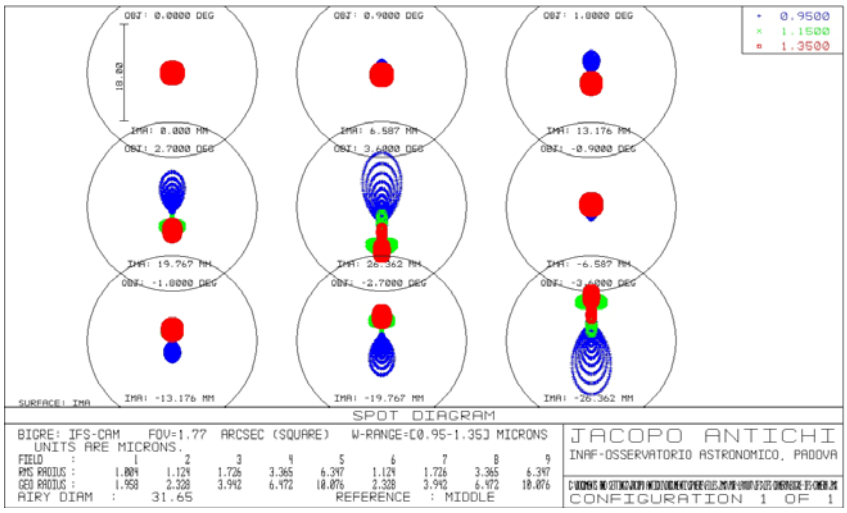


**Figure 6-8: Spot diagrams of the SPHERE/IFS/Camera from the on-axis configuration to the extreme off-axis configurations corresponding to a diagonal FOV range of ± 1.25 [arcsec].**

In this optical condition, the achieved level of Strehl Ratio can be measured through the level of RMS Wavefront Error across the IFS Camera Exit Pupil (see Figure 6-9).

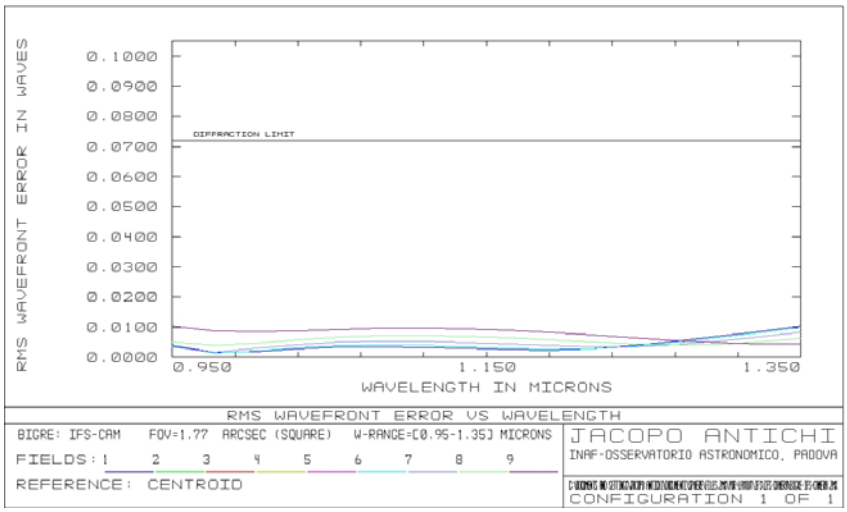


**Figure 6-9: RMS Wavefront Error vs. Wavelength diagram. Adopting the Maréchal's approximation (cfr. Born and Wolf 1965), the achieved Strehl Ratio is SR≈0.996.**

## 6.5 Tolerance analysis for the IFS Camera

ADOPTED WAVELENGTH = 0.95 [micron]

ADOPTED COMPENSATOR: paraxial focus

CRITERION: WFE-RMS

NOMINAL WFE-RMS = 0.0209 (wavelength unit)

THRESHOLD ON THE DELTA WFE-RMS = 20%

THRESHOLD ON WFE-RMS = 1.2 * 0.0209 = 0.0250 (wavelength unit)

FIRST MODE ADOPTED: INVERSE-LIMIT

The Sensitivity Matrix changes until the following condition is reached:

DELTA WFE-RMS ≤ 20%

SECOND MODE ADOPTED: SENSITIVITY

The Sensitivity Matrix in changed term by term until the following condition is reached:

90% of the extractions should verify DELTA WFE-RMS ≤ 20%
, adopting the following statistical setup:

DISTRIBUTION OF RAYS STARTING FROM THE OBJECT PLANE: Uniform

NUMBER OF MONTE CARLO RUNS = 500

**IFS-CAM: FOV=1.77$^2$ [ARCSEC$^2$](SQUARE); W-RANGE = 0.95-1.35 [MICRON]**

**SURFACE DATA SUMMARY:**

| Surf | Type | Comment | Radius | Thickness | Glass | Diameter |
|---|---|---|---|---|---|---|
| OBJ | STANDARD | | Infinity | Infinity | | 0 |
| STO | STANDARD | | Infinity | | 90 | 30.72 |
| 2 | STANDARD | | -94.87 | 20 | S-FTM16 | 60 |
| 3 | STANDARD | | -168.41 | 20 | CAF2 | 60 |
| 4 | STANDARD | | -205.26 | 20 | S-FTM16 | 60 |
| 5 | STANDARD | | -117.19 | 20 | | 60 |
| 6 | STANDARD | | 352.34 | 13.37 | CAF2 | 64 |
| 7 | STANDARD | | -105.24 | 20 | S-FTM16 | 64 |
| 8 | STANDARD | | -222.18 | 279.99 | | 64 |
| 9 | STANDARD | | -345.31 | 12.14 | S-FTM16 | 54 |
| 10 | STANDARD | | Infinity | 113 | | 54 |
| 11 | STANDARD | | Infinity | 7 | S-FTM16 | 60 |
| 12 | STANDARD | | Infinity | 30 | | 60 |
| IMA | STANDARD | | Infinity | | | 52.74331 |

**TOLERANCE DATA LISTING:**

| Num | Type | Int1 | Int2 | Int3 | Nominal | Min | Max | Units | Comments |
|---|---|---|---|---|---|---|---|---|---|
| 1 | (COMP) | 12 | 0 | | | 0.00000E+000 | 0.00000E+000 | | |
| 2 | (TWAV) | | | | | 9.50000E-001 | | Microns | |
| 3 | (TOFF) | | | | | | | | |
| 4 | (TRAD) | 2 | | | -9.48700E+001 | -1.00000E-001 | 1.00000E-001 | Millimeters | |
| 5 | (TRAD) | 3 | | | -1.68410E+002 | -3.00000E-001 | 3.00000E-001 | Millimeters | |
| 6 | (TRAD) | 4 | | | -2.05260E+002 | -3.00000E-001 | 3.00000E-001 | Millimeters | |
| 7 | (TRAD) | 5 | | | -1.17190E+002 | -1.00000E-001 | 1.00000E-001 | Millimeters | |
| 8 | (TRAD) | 6 | | | 3.52340E+002 | -5.00000E-001 | 5.00000E-001 | Millimeters | |
| 9 | (TRAD) | 7 | | | -1.05240E+002 | -1.00000E-001 | 1.00000E-001 | Millimeters | |
| 10 | (TRAD) | 8 | | | -2.22180E+002 | -2.00000E-001 | 2.00000E-001 | Millimeters | |
| 11 | (TRAD) | 9 | | | -3.45310E+002 | -6.00000E-001 | 6.00000E-001 | Millimeters | |
| 12 | (TFRN) | 10 | | | | -1.00000E-001 | 1.00000E-001 | Fringes | |
| 13 | (TFRN) | 11 | | | | -1.00000E-001 | 1.00000E-001 | Fringes | |
| 14 | (TFRN) | 12 | | | | -1.00000E-001 | 1.00000E-001 | Fringes | |
| 15 | (TOFF) | | | | | | | | |
| 16 | (TTHI) | 1 | 2 | | 9.00000E+001 | -1.00000E-001 | 1.00000E-001 | Millimeters | |
| 17 | (TTHI) | 2 | 3 | | 2.00000E+001 | -1.00000E-001 | 1.00000E-001 | Millimeters | |
| 18 | (TTHI) | 3 | 4 | | 2.00000E+001 | -1.00000E-001 | 1.00000E-001 | Millimeters | |
| 19 | (TTHI) | 4 | 5 | | 2.00000E+001 | -1.00000E-001 | 1.00000E-001 | Millimeters | |
| 20 | (TTHI) | 5 | 6 | | 2.00000E+001 | -3.00000E-001 | 3.00000E-001 | Millimeters | |
| 21 | (TTHI) | 6 | 7 | | 1.33700E+001 | -1.00000E-001 | 1.00000E-001 | Millimeters | |
| 22 | (TTHI) | 7 | 8 | | 2.00000E+001 | -1.00000E-001 | 1.00000E-001 | Millimeters | |
| 23 | (TTHI) | 8 | 9 | | 2.79990E+002 | -3.00000E-001 | 3.00000E-001 | Millimeters | |
| 24 | (TTHI) | 9 | 10 | | 1.21400E+001 | -1.00000E-001 | 1.00000E-001 | Millimeters | |
| 25 | (TTHI) | 10 | 11 | | 1.13000E+002 | -1.00000E-001 | 1.00000E-001 | Millimeters | |
| 26 | (TTHI) | 11 | 12 | | 7.00000E+000 | -1.00000E-001 | 1.00000E-001 | Millimeters | |
| 27 | (TOFF) | | | | | | | | |
| 28 | (TEDX) | 2 | 5 | | | -1.00000E-003 | 1.00000E-003 | Millimeters | |
| 29 | (TEDY) | 2 | 5 | | | -1.00000E-003 | 1.00000E-003 | Millimeters | |
| 30 | (TETX) | 2 | 5 | | | -1.00000E-002 | 1.00000E-002 | Degrees | |
| 31 | (TETY) | 2 | 5 | | | -1.00000E-002 | 1.00000E-002 | Degrees | |
| 32 | (TEDX) | 6 | 8 | | | -1.00000E-003 | 1.00000E-003 | Millimeters | |
| 33 | (TEDY) | 6 | 8 | | | -1.00000E-003 | 1.00000E-003 | Millimeters | |
| 34 | (TETX) | 6 | 8 | | | -1.00000E-002 | 1.00000E-002 | Degrees | |
| 35 | (TETY) | 6 | 8 | | | -1.00000E-002 | 1.00000E-002 | Degrees | |
| 36 | (TEDX) | 9 | 10 | | | -1.00000E-003 | 1.00000E-003 | Millimeters | |
| 37 | (TEDY) | 9 | 10 | | | -1.00000E-003 | 1.00000E-003 | Millimeters | |
| 38 | (TETX) | 9 | 10 | | | -1.00000E-002 | 1.00000E-002 | Degrees | |
| 39 | (TETY) | 9 | 10 | | | -1.00000E-002 | 1.00000E-002 | Degrees | |
| 40 | (TEDX) | 11 | 12 | | | -1.00000E-003 | 1.00000E-003 | Millimeters | |
| 41 | (TEDY) | 11 | 12 | | | -1.00000E-003 | 1.00000E-003 | Millimeters | |
| 42 | (TETX) | 11 | 12 | | | -1.00000E-002 | 1.00000E-002 | Degrees | |
| 43 | (TETY) | 11 | 12 | | | -1.00000E-002 | 1.00000E-002 | Degrees | |

**NOMENCLATURE:**

TRAD = TOLLERACE  ON THE  RADIUS OF CURVATURE
TFRN = TOLLERANCE ON THE  SURFACE FLATNESS: +/-0.1 FRINGES = LAMBDA/20 @ λ=0.95 [MICRON]
TTHI = TOLLERANCE ON THE  THICKNESS BETWEEN THE INDICATED SUPERFACE AND THE NEXT ONE
TEDX = TOLLERANCE ON DECENT. X OF THE GROUP OF OPTICS COMPRISED BETWEEN THE INDICATED SURF.
TEDY = TOLLERANCE ON DECENT. Y OF THE GROUP OF OPTICS COMPRISED BETWEEN THE INDICATED SURF.
TETX = TOLLERANCE ON TILT    X OF THE GROUP OF OPTICS COMPRISED BETWEEN THE INDICATED SURF.
TETY = TOLLERANCE ON TILT    Y OF THE GROUP OF OPTICS COMPRISED BETWEEN THE INDICATED SURF.

## 6.6 Optimization of the IFS Disperser

In order to provide the requested spectral resolution (**R=54**), the best choice appears to be an Amici Prism device. This choice is driven by the Prism direct vision characteristic and fairly uniform dispersion, and because grating based devices (e.g. Grism) at very low resolution give troubles with their zero order.

The Amici Prism is a device built with three Prisms: in the classical scheme, there are two Prisms with low dispersion (made with the same glass) with a third Prism in between with high dispersion. Angles are chosen so that the emerging ray at a selected wavelength $\lambda_C$ is not deviated (see Figure 6-10). An example of the use of an Amici Prism for low spectral resolution IR-spectroscopy is the NICS spectrograph at TNG (cfr. Oliva 2003).

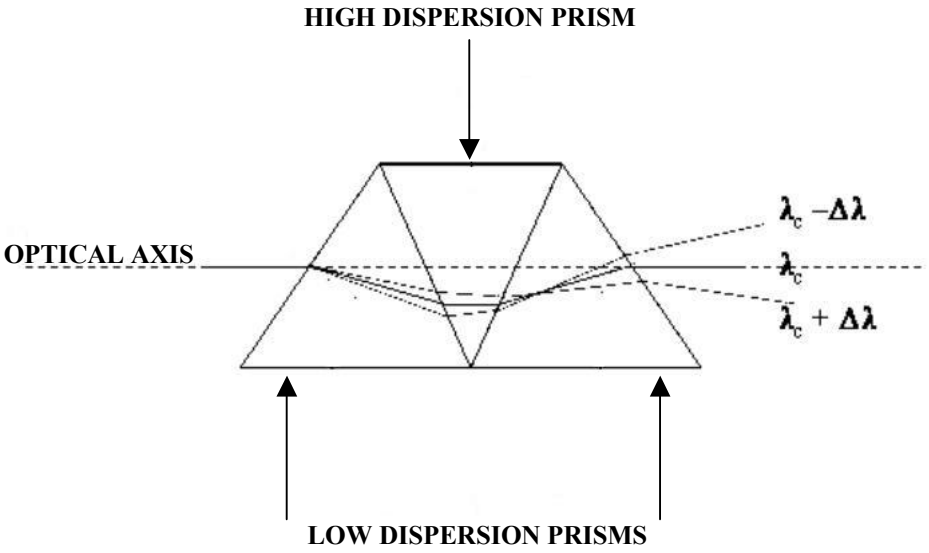


**Figure 6-10: Optical concept of the Amici Prism.**

The method to select the pair of glasses to be used, and the geometry of the Amici Prism is described in the following part of this Section.

The direct vision condition of the Amici Prism comes directly from the minimum deviation condition for the wavelength $\lambda_C$:

$$n_{2,1} = \frac{\sin\left(\frac{D_{MIN} + A}{2}\right)}{\sin\left(\frac{A}{2}\right)} \qquad \textbf{Equation 6-1}$$

where $\mathbf{D_{MIN}}$ is the angular deviation between the incident and the emerging ray at the given wavelength; **A** is the vertex angle of the Prism and $\mathbf{n_{2,1} \equiv n_{2C}/n_{1C}}$ is the relative refractive index corresponding to $\lambda_C$. This condition defines the direct vision geometry of this Prism.

With reference to Figure 6-11, the geometrical relationships between the different angular elements of the Prism are:

$$i_2 = \frac{D_{min} + A}{2} = r_3$$

$$D_{min} = 2 \cdot \arcsin\left( \frac{n_{2C}}{n_{1C}} \cdot \sin\left( \frac{A}{2} \right) \right) - A$$

**Equation 6-2**

$$\tan(B) = \frac{n_1 \cdot \sin(i_2) - \sin\left( \frac{A}{2} \right)}{n_1 \cdot \cos(i_2) - \cos\left( \frac{A}{2} \right)}$$

Considering a generic $\lambda \neq \lambda_C$, the following relationships between the Prism vertex angle **A**, the incident angle $\mathbf{i_i}$, where index (**i**) corresponds to the Prism faces from left to right, and the refractive angle $\mathbf{r_i}$ hold:

$$i_1 = \left( B - \frac{A}{2} \right)$$

$$r_1 = \arcsin\left[ \frac{\sin(i_1)}{n_1(\lambda)} \right]$$

$$i_2 = B - r_1$$

$$r_2 = \arcsin\left[ \frac{n_1(\lambda)}{n_2(\lambda)} \cdot \sin(i_2) \right]$$

$$i_3 = A - r_2$$

$$r_3 = \arcsin\left[ \frac{n_2(\lambda)}{n_1(\lambda)} \cdot \sin(i_3) \right]$$

$$i_4 = B - r_3$$

**Equation 6-3**

$$r_4 = \arcsin\left[ n_1(\lambda) \cdot \sin(i_4) \right]$$

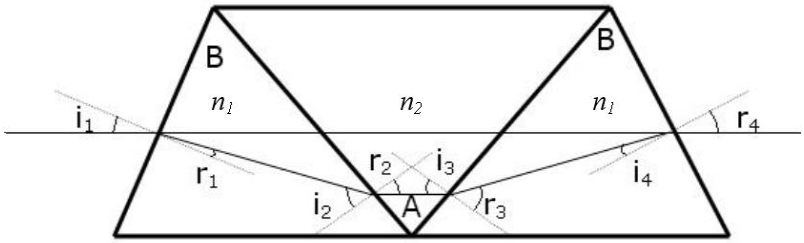


**Figure 6-11: Geometrical optics of the Amici Prism.**

The angular deviation of the generic wavelength will be $\Theta=r_4-i_1$ and the angular dispersion $\rho \equiv dP/d\lambda=dr_4/d\lambda$ can be expressed in terms of spectral resolution **R**, the Detector pixel size $d_{pixel}$ and the Focal Length of the IFS Camera optics $f_{cam}$:

$$\rho(\lambda) = \frac{2 \cdot R \cdot d_{pixel}}{f_{cam} \cdot \lambda}$$ **Equation 6-4**

Equations 6-2, 6-3, and 6-4 allow then to find the right couple of glass **($n_1$ , $n_2$)**, and the right couple of Prism vertex angles **(A , B)** by which the condition of low spectral resolution (**R=54**) is verified in the whole wavelength range of SPHERE/IFS.

For what concerns the linear size of the Amici Prism, it is important to define correctly its vertical section both for the acceptance of the whole optical footprint - at the position where the Prism is placed along the optical axis (see Figure 6-3) - and to avoid that the shortest wavelength of the dispersed beam will not meet the second refractive surface of the Prism (see Figure 6-12).

The vertical size of the Prism will be $h>H_{MIN}+D_{BEAM}$ where $D_{BEAM}$ is the beam footprint at the position of the Prism along the optical axis, and the horizontal size **L** of the entire Prism is simply twice the base of its first:

$$L = 2 \cdot H \cdot [\tan(i_1) + \tan(B - i_1)]$$ **Equation 6-5**

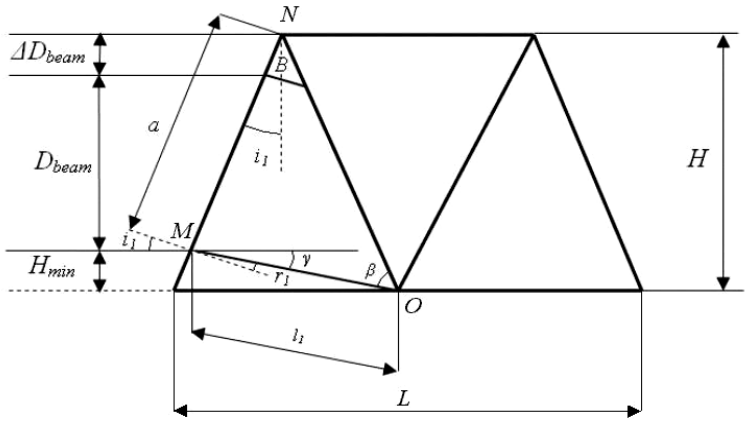


**Figure 6-12: Vertical section of the Amici Prism: $H_{MIN}$ is the maximum vertical deviation of the rim-ray inside the first Prism.**

The Amici Prism solution for SPHERE/IFS is resumed in the following in Table 6-4.

| Glass 1 | Glass 2 | A | B | L [mm] |
|---|---|---|---|---|
| FK54 | LAFN21 | 13.77 [deg] | 10.99 [deg] | 66.000 |

**Table 6-4: Key optical parameters of the Amici Prism for SPHERE/IFS.**

By this optimization, the Amici Prism of SPHERE/IFS can be inserted in the ray-tracing Code in order to realize a complete (see Figure 6-13) and optimized (see Figure 6-14) optical design of the IFS system, and finally to obtain the ray-tracing of a single spectrum of this low-resolution 3D-Spectrograph (see Figure 6-15).

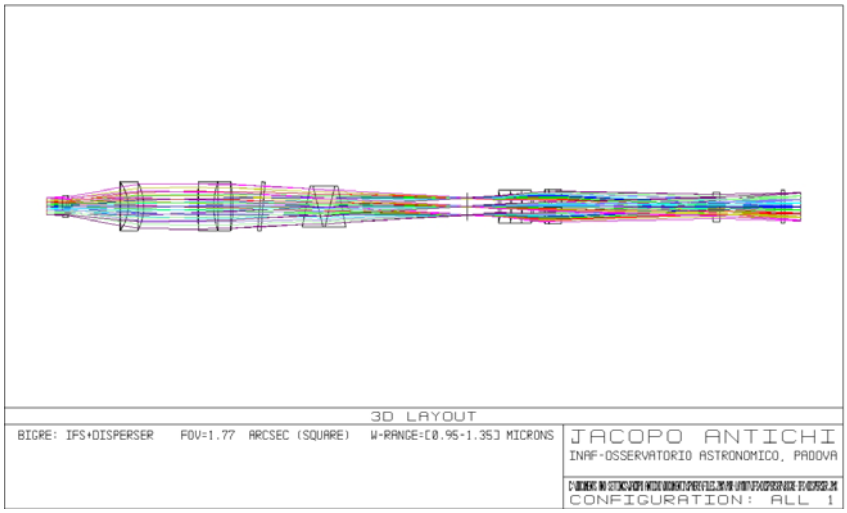


**Figure 6-13: Optical design of IFS with the Amici Prism included.**

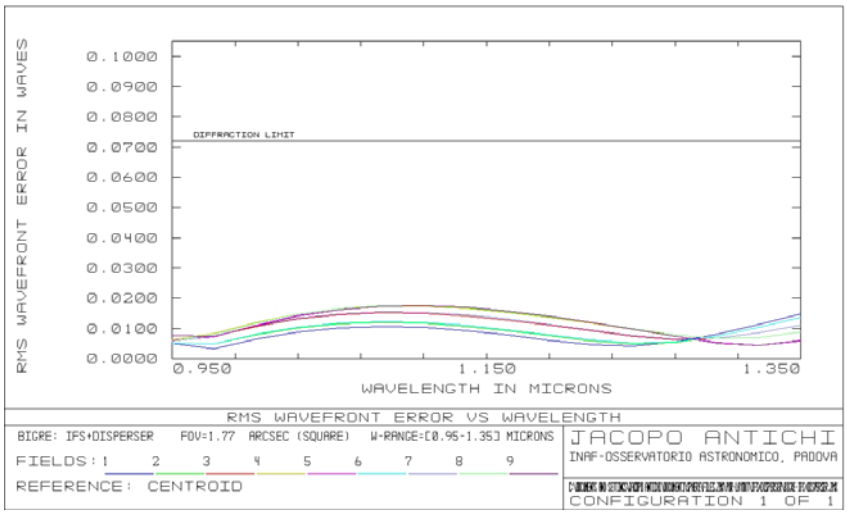


**Figure 6-14: RMS Wavefront Error vs. Wavelength diagram of the overall IFS optical layout, with the Amici Prism inserted. Adopting the Maréchal's approximation (cfr. Born and Wolf 1965), the achieved Strehl Ratio SR≈0.987.**

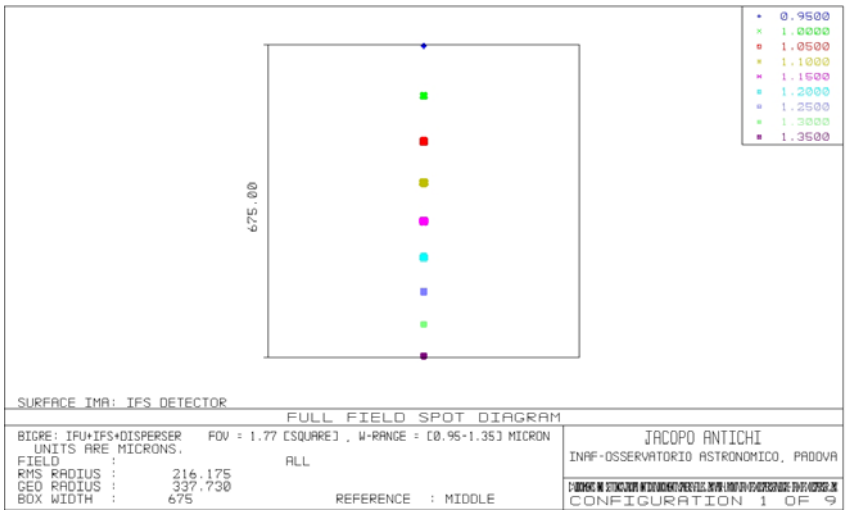


**Figure 6-15 Ray-tracing of a single spectrum imaged; the length of the spectrum is 675 [micron] that corresponds to the spectral length $l_S$=37.5 pixels (cfr. Section 5.7).**

## 6.7 Transmission of the IFS optics

The estimate of the transmission of the IFS should take into account several components:

- the mask deposited on the first surface of the BIGRE IFU sub-system,
- the transmission of all the glasses adopted in the IFS optical design,
- the total number of air-glass surfaces of the overall (IFU+IFS) system.

The mask deposited on the BIGRE lenses array (see Figure 6-16) renders the shape of the first surface of each lens contained in the array circular. This mask allows to remove the straylight from the lenslet edges and to customize each spaxel to a circular shape.

The adopted mask hole is fixed to be 95% of the lens pitch; this allows to remove the straylight generated by the edges the lenses shape of the BIGRE IFU adopted for SPHERE/IFS which is hexagonal, and to customize each spaxel to a circular shape with good transmission level: **0.819** for a mask hole equal to $\mathbf{0.95 \cdot D_L}$, contained in a hexagonal lens with pitch equal to $\mathbf{D_L}$.

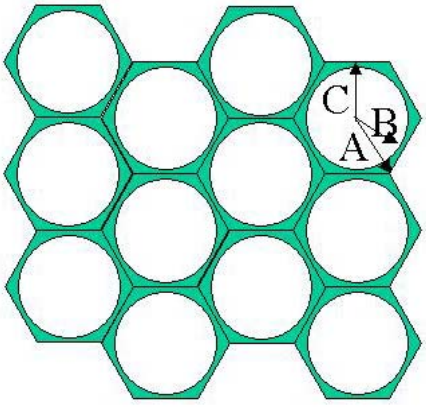


**Figure 6-16: Sketch of the circular-apertures mask adopted for the BIGRE IFU sub-system. B is the radius of the mask hole (B=76.71 [micron]), C is half of the lens pitch (C=80.75 [micron]) and A is a side of the hexagon (A=93.24 [micron]).**

The transmission of all the glasses of the IFS is summarized in Table 6-5.

| Transmission | Thickness | λ=0.95 [micron] | λ=1.15 [micron] | λ=1.35 [micron] |
|---|---|---|---|---|
| BK7 | 18.127 [mm] | 0.999 | 0.996 | 0.992 |
| S-FTM16 | 146.036 [mm] | 0.986 | 0.986 | 0.954 |
| CaF2 | 82.660 [mm] | 1.000 | 1.000 | 1.000 |
| FK54 | 44.000 [mm] | 0.985 | 0.986 | 0.986 |
| LAFN21 | 22.000 [mm] | 0.995 | 0.994 | 0.990 |

**Table 6-5: Transmission of the glasses adopted for the IFS optical design. The thicknesses are distinguished by glass type and the transmission of each glass is evaluated for the minimum, the central and the maximum wavelength of the working range of SPHERE/IFS.**

The total Efficiency of the IFS is summarized in Table 6-6.

| Components | λ=0.95 [micron] | λ=1.15 [micron] | λ=1.35 [micron] |
|---|---|---|---|
| IFU mask | 0.819 | 0.819 | 0.819 |
| Glasses Transmission | 0.965 | 0.962 | 0.924 |
| 22 AR-C Surfaces[54] | 0.802 | 0.802 | 0.802 |
| Total Efficiency | 0.634 | 0.632 | 0.607 |
| SPHERE/IFS TLR | >0.600 | >0.600 | >0.600 |

**Table 6-6: Transmission of all the system components and total Efficiency evaluated for the minimum, the central and the maximum wavelength of the working range of SPHERE/IFS.**

[54] In this Dissertation a standard 1% energy loss for any air-glass reflection is adopted.

## 6.8 Thermal and Pressure analyses

Sensitivity of the IFS optics to thermal and pressure variations have been estimated by repeating the ray-tracing with variable environment conditions. The effects of Temperature and Pressure have been considered separately

Temperature has been changed over the range: **0-20 [deg]**, which are the expected ranges of environment condition at Paranal (i.e. the location of the SPHERE instrument) and in Laboratories.

Pressure has been changed over the range: **0.69-1.00 [atm]**, which are the expected pressure boundaries for the environment condition at Paranal and in Laboratories.

Focus variation of the IFS have been compensated by moving the Warm Camera Doublet.

After re-focusing, the optical quality is nearly identical to that obtained in nominal conditions both for temperature variations (see Figure 6-17 and Figure 6-18) and pressure variations (see Figure 6-19 and Figure 6-20).

Specifically:

- Temperature variation of **20 [deg]** causes a de-focusing of **-1.002 [mm]** which is compensated by the displacement of the Warm Camera Doublet by **+0.632 [mm]** towards the IFS Detector Plane.
- Pressure variation of **0.31 [atm]** causes a de-focusing of **-0.458 [mm]** which is compensated by the displacement of the Warm Camera Doublet by **+0.289 [mm]** towards the IFS Detector Plane.

The range of the re-focusing movement has then to be: **(-0.50 , +1.50) [mm]**.

Re-focusing is required to maintain the optical quality level whenever temperature changes by more than **0.4 [deg]** or pressure by more than **0.014 [atm]**; the movement has to be accurate to within **+/-5 [micron]**.

When re-focusing, on the IFS Detector the image expands/contracts. Specifically, at the corner of the FOV, the change is of **8 [micron],** when temperature is changed over the range **0-20 [deg]** and re-focusing is made. In order to maintain the displacement of the image at the Detector corner less than **0.2 pixels** (required from for the DRSW), the temperature (pressure) should not change more than **9.0 [deg]** (**0.3 [atm]**). If temperature (pressure) changes more than **9 [deg]** (**0.3 [atm]**) during the target acquisition, this should be taken into account by the DRSW.

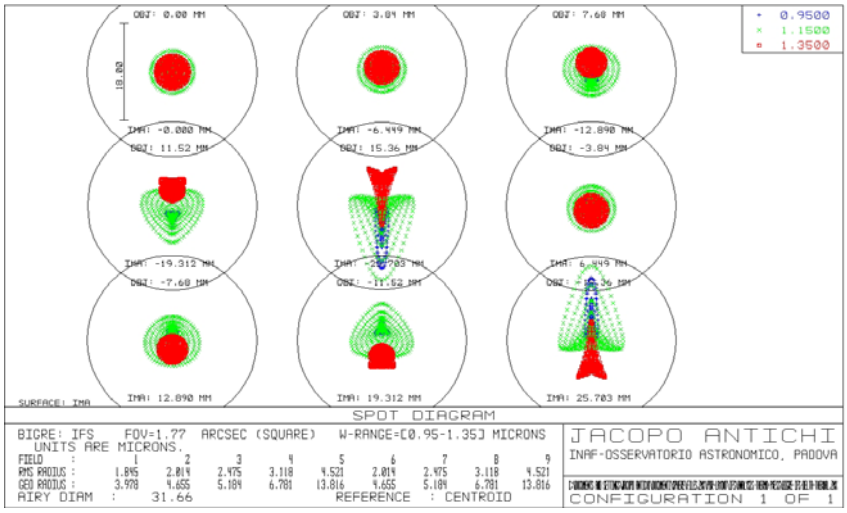


**Figure 6-17: Spot diagrams of the entire SPHERE/IFS optics, from the on-axis to the extreme off-axis configurations, after re-focusing for a temperature delta of 20 [deg].**

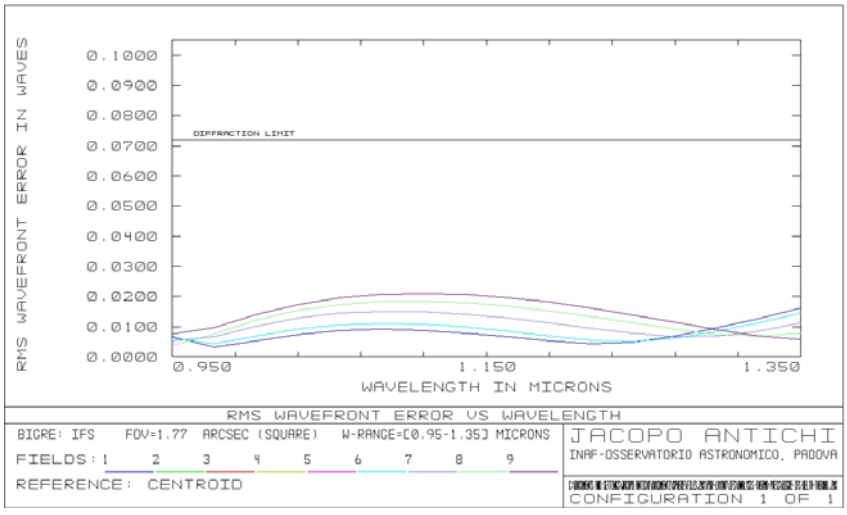


**Figure 6-18: RMS Wavefront Error vs. Wavelength diagram after re-focusing for a temperature delta of 20 [deg]. Adopting the Maréchal's approximation (cfr. Born and Wolf 1965), the achieved Strehl Ratio is SR≈0.982.**

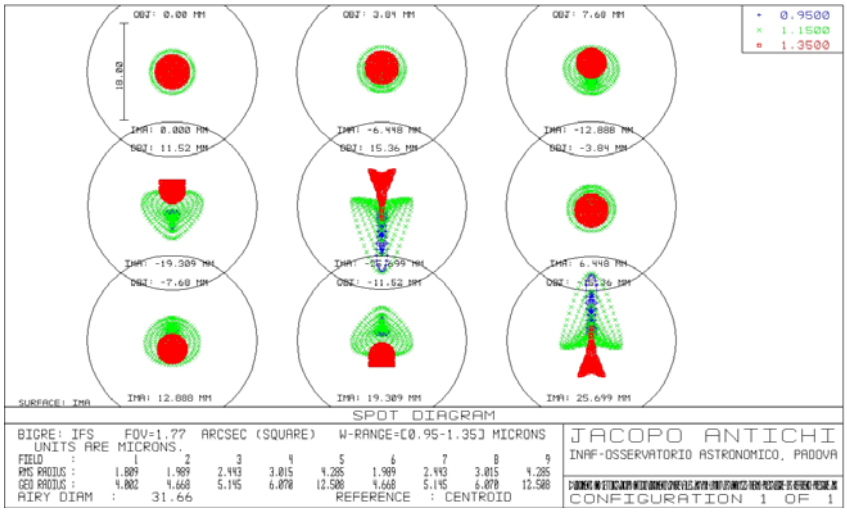


**Figure 6-19: Spot diagrams of the entire SPHERE/IFS optics, from the on-axis to the extreme off-axis configurations, after re-focusing for a pressure delta of 0.31 [atm].**

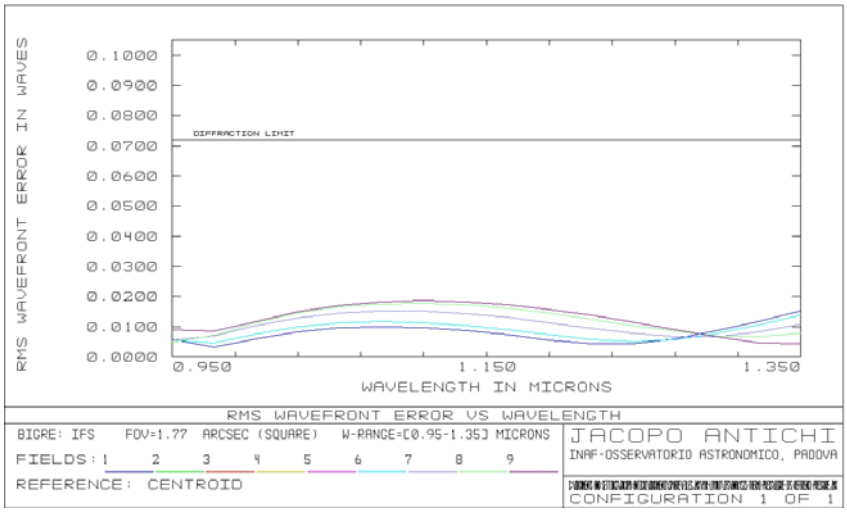


**Figure 6-20: RMS Wavefront Error vs. Wavelength diagram after the re-focusing for a temperature delta of 0.31 [atm]. Adopting the Maréchal's approximation (cfr. Born and Wolf 1965), the achieved Strehl Ratio is SR≈0.986.**

## 6.9 Dithering analysis

Dithering of images on the IFS Detector is required to keep the noise due to flat fielding below specifications.

Moving part of the Camera (either the Triplet or the Doublet, or both) is the easiest solution from the opto-mechanical point of view; the alternative solutions of moving either the Detector or all the Cryogenic optics are less easy, in the first case because a cryo-movement is required, and in the second case because the mass to be moved is large.

The requested amount of dithering on the Detector plane is **10 pixels** (that is **+/-5 pixels**) both in X and Y directions, orthogonally to the IFS optical axis Z.

Adopting a physical pixel size of **18 [micron]**, the dithering movement should be **180 [micron]** both in X and Y directions, that is **+/-90 [micron]** both in X and Y directions once the dithering movement is projected - through the IFS Camera optics - on the Detector plane.

Several decentering possibilities have been analyzed in order to obtain the requested image-shift on the IFS Detector plane:

1. Decentering of the Warm Camera Triplet
2. Decentering of both all the Warm Camera optics: Triplet and Doublet
3. Decentering of the Warm Camera Doublet

In the case (1), it turns that an image-shift of **90 [micron]** on the Detector is obtained with a decentering budget equal to **3.7 [mm]**. Optical quality check (i.e. the variation on the $WFE_{RMS}$ vs. wavelength diagram) indicates that this option is to be excluded in order to preserve the optical quality achieved in the optimized layout. In the case (2), it turns that an image-shift of **90 [micron]** on the Detector is obtained with a decentering budget equal to **72 [micron]**. Optical quality check (i.e. the variation on the $WFE_{RMS}$ vs. wavelength diagram) indicates that this option maintains the optical quality at the level achieved in the optimized layout: **Delta-SR=0.04%** (ref. **SR=0.987**). In the case (3), it turns that an image-shift of **90 [micron]** on the Detector is obtained with a decentering budget equal to **74 [micron]**. Optical quality check (i.e. the variation on the $WFE_{RMS}$ vs. wavelength diagram) indicates that this option maintains the optical quality very at the level achieved in the optimized layout: **Delta-SR=0.42%** (ref. **SR=0.987**). Options (2) and (3) are then optically equivalent. However, from the opto-mechanical point of view, option (3) is better because the mass to be moved is smaller. Option (3) - see Figure 6-21 - is then to be considered the solution for the dithering of SPHERE/IFS, with a requested Decentering Budget of the Warm Camera Doublet equal to **+/-74 [micron]**. The optical quality level of this solution is shown in Figure 6-22, while the opto-mechanical design of the Warm Camera sub-system, equipped with two distinct motors, for dithering and re-focusing respectively, is shown in Figure 6-23 and Figure 6-24.

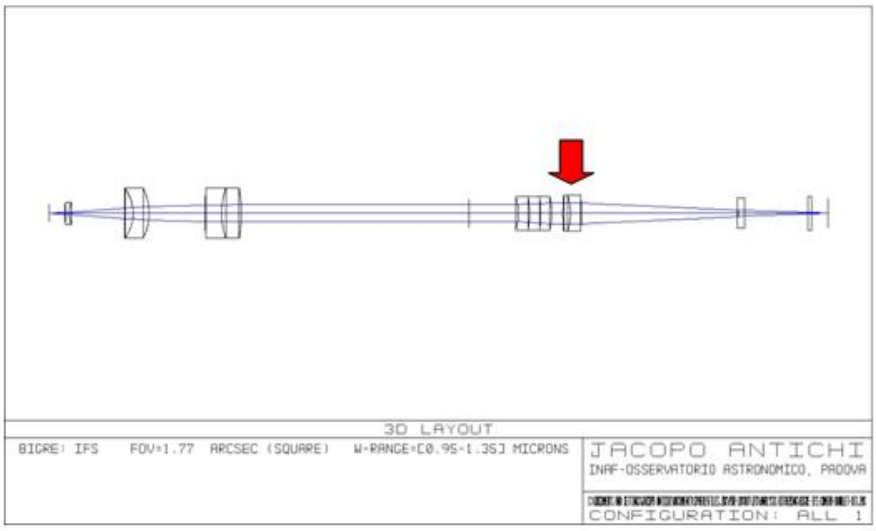


**Figure 6-21: Dithering solution for SPHERE/IFS: the Warm Camera Doublet is moved back and forth on the XY plane, orthogonally to the optical axis of the system, with a maximum excursion of ±74 [micron]. The red arrow indicates the optical element to be equipped with suitable piezo and standard motors.**

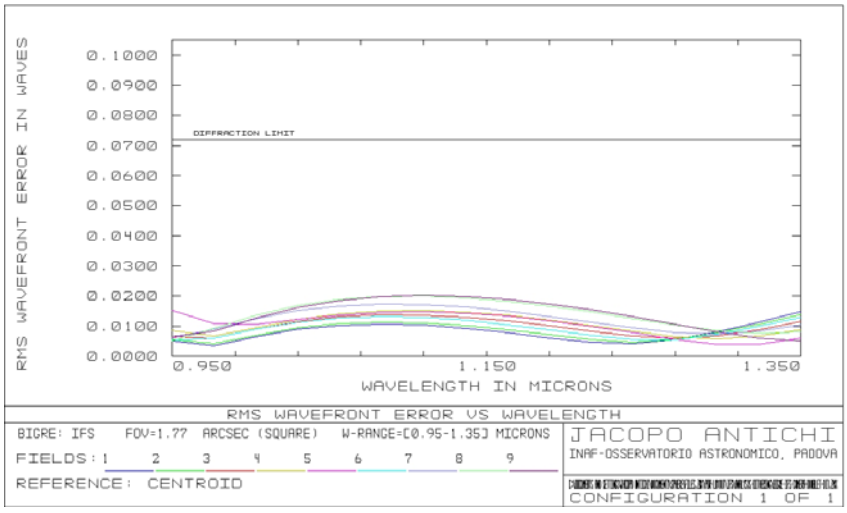


**Figure 6-22: RMS Wavefront Error vs. Wavelength diagram corresponding to a decentring of ±90 [micron] on the IFS Detector Plane. The Strehl Ratio level remains as good as the one obtained in the optimized IFS layout. Adopting the Maréchal's approximation (cfr. Born and Wolf 1965) the Strehl Ratio level is SR≈0.983 with respect to SR≈0.987.**

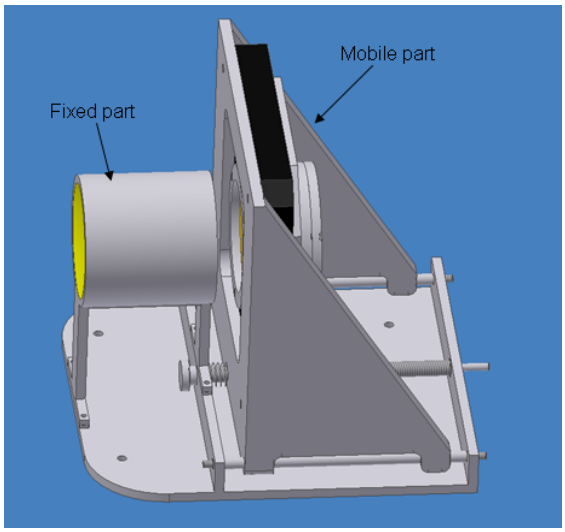


**Figure 6-23: Opto-mechanical sketch of the Warm Camera sub-system divided in two main parts: a fixed one containing the Triple lens, and a mobile one containing the Double lens.**

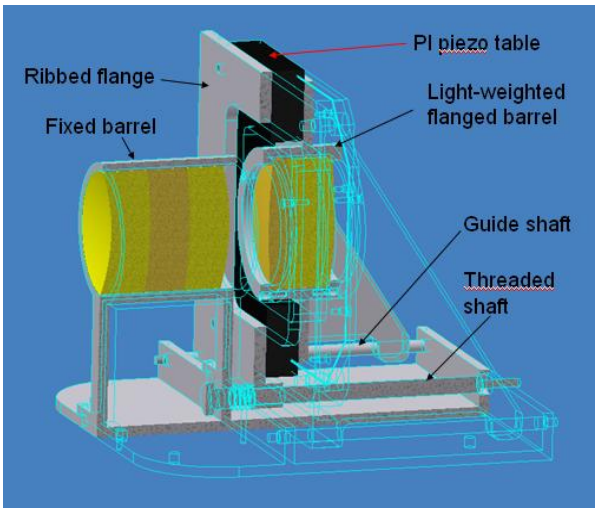


**Figure 6-24: Detailed opto-mechanical sketch of the of the Warm Camera sub-system. The mobile part mounts two kinds of motors: a piezo-motor (colored in black) for the dithering movement of the Doublet, and a standard motor which moves the Doublet along the optical axis for re-focusing.**

## 6.10 Ghost analysis

Ghost analysis of IFS has been performed considering separately the elements in converging and diverging beams, and on the parallel beam.

For the elements on the converging and diverging beams, we used the tool: **Ghost focus generator of** Zemax. Results are shown is Table 6-7. By this analysis, significant ghosts are excluded. The ghost focus closest to the IFS Focal Plane is due to double internal reflection within the Low-Pass Chromatic Filter which creates a ghost with a RMS of about **0.230 [mm]**; since the intensity of this ghost is expected to be about $\mathbf{10^{-4}}$ and should be spread over a couple of hundred of pixels, its contribution should be negligible. In principle more worrying should be ghosts generated by double reflections involving the Detector itself, since the Detector reflectivity is at least one order of magnitude larger than the reflectivities of the air-glass surfaces when AR-C is adopted. However, in the IFS design none of the elements on the converging and diverging beams creates ghosts with RMS smaller than a few millimeter when coupled to the Detector, so the total effect is simply a higher level of background.

Different considerations should be done for those optical elements that are on the collimated part of the beam (Disperser, High-Pass Chromatic Filter, and Neutral Density Filter). When coupled to the Detector surface, these elements would form on-focus ghosts with intensities of the order of a few $\mathbf{10^{-3}}$, which is unacceptable. To avoid this effect, optical surfaces on the collimated beam should be tilted respect to the optical axis, so that the reflected beam falls outside of the camera first element. In the proposed design, both the Chromatic and Neutral Density Filters are tilted by **5 [deg]**, and get distance larger than **400 [mm]** from the Warm Camera first element. This is enough to guarantee that ghosts can not be seen by the Detector. The surfaces of the Disperser are tilted by design with larger angles, so that the Amici Prism can be located somewhat closer to the Warm Camera first element, but still at distance larger than **300 [mm]** from it.

The IFU sub-system itself causes several ghosts that can not be eliminated from the optical design. In principle, some of them can be eliminate by tilting the IFU itself; however a tilting larger than **10 [deg]** is required. Such a tilt causes several problems that can not be handled properly. The worst ghost is due to reflection back from the Detector surface and then again on the fist surface of the IFU. This ghost is on-focus and its intensity is expected to be proportional to the product of the reflectivity of the Detector and of the first surface of the IFU times the cube of the IFS efficiency (see Table 6-6). The spectrum given by this ghost is dispersed three times the original one due to the three passages through the Amici Prism. If these factors are considered, the ghost is expected to be few $\mathbf{10^{-4}}$ as intense as the original image, and will show up with a very complex - practically not eliminable - pattern. Additional ghost is provided by the second surface of the IFU. This is slightly off-focus and it has similar position, intensity and spectral dispersion than the ghost due to first IFU surface. We will consider these ghosts as additional CrossTalk sources.

| Surf. | 2 | 3 | 4 | 5 | 6 | 7 | 8 | 9 | 10 | 11 | 12 | 13 | 14 | 15 | 16 | 17 | 18 | 19 | 20 | 21 |
|---|---|---|---|---|---|---|---|---|---|---|---|---|---|---|---|---|---|---|---|---|
| **1** | 0.700 | 0.238 | 0.288 | 0.288 | 0.333 | ∞ | 24.89 | None | ∞ | ∞ | ∞ | ∞ | ∞ | ∞ | ∞ | 38.90 | 12.50 | 6.72 | 6.49 | 4.96 |
| **2** | | ∞ | ∞ | ∞ | ∞ | ∞ | ∞ | None | ∞ | ∞ | ∞ | ∞ | ∞ | ∞ | ∞ | ∞ | ∞ | 13.54 | 12.85 | 9.06 |
| **3** | | | ∞ | ∞ | 0.360 | ∞ | 13.46 | None | ∞ | ∞ | ∞ | ∞ | ∞ | ∞ | ∞ | ∞ | 37.98 | 31.41 | 31.18 | 29.66 |
| **4** | | | | 0.144 | ∞ | ∞ | ∞ | None | ∞ | ∞ | ∞ | ∞ | ∞ | ∞ | ∞ | ∞ | ∞ | ∞ | ∞ | ∞ |
| **5** | | | | | ∞ | ∞ | ∞ | None | ∞ | ∞ | ∞ | ∞ | ∞ | ∞ | ∞ | ∞ | ∞ | ∞ | ∞ | ∞ |
| **6** | | | | | | ∞ | ∞ | None | ∞ | ∞ | 61.49 | ∞ | ∞ | ∞ | ∞ | ∞ | 29.04 | 31.19 | 31.27 | 31.88 |
| **7** | | | | | | | ∞ | None | ∞ | ∞ | ∞ | ∞ | ∞ | ∞ | ∞ | ∞ | ∞ | ∞ | ∞ | ∞ |
| **8** | | | | | | | | None | ∞ | ∞ | ∞ | ∞ | ∞ | ∞ | ∞ | ∞ | ∞ | 49.50 | 48.08 | 40.61 |
| **9** | | | | | | | | | None | None | None | None | None | None | None | None | None | None | None | None |
| **10** | | | | | | | | | | 47.19 | 51.76 | ∞ | 173.4 | ∞ | 119.7 | 117.4 | 31.56 | 81.40 | 83.37 | 96.71 |
| **11** | | | | | | | | | | | 6.47 | 102.9 | 88.48 | 248.1 | 95.52 | 54.34 | 16.64 | 34.05 | 34.73 | 39.36 |
| **12** | | | | | | | | | | | | 98.29 | 73.48 | 230.1 | 88.82 | 43.62 | 13.94 | 26.25 | 26.73 | 30.00 |
| **13** | | | | | | | | | | | | | 176.5 | 212.6 | 45.63 | 130.8 | 30.56 | 98.36 | 101.1 | 119.6 |
| **14** | | | | | | | | | | | | | | 301.0 | 127.2 | 21.75 | 1.09 | 29.05 | 30.25 | 38.39 |
| **15** | | | | | | | | | | | | | | | 70.23 | 220.5 | 39.87 | 174.2 | 180.4 | 225.6 |
| **16** | | | | | | | | | | | | | | | | 98.65 | 21.41 | 77.59 | 79.85 | 95.29 |
| **17** | | | | | | | | | | | | | | | | | 4.73 | 9.43 | 9.99 | 13.76 |
| **18** | | | | | | | | | | | | | | | | | | 5.86 | 6.09 | 7.64 |
| **19** | | | | | | | | | | | | | | | | | | | **0.230** | 1.78 |
| **20** | | | | | | | | | | | | | | | | | | | | 1.55 |

**Table 6-7: Ghost RMS spot radii on the IFS Detector surface expressed in [mm]. The minimum value is 0.230 [mm], arising from the ghost reflection of surface 20 then 19, whose in turn correspond to the Low Pass Chromatic Filter optics located in front of the Detector (see Figure 6-2). The symbol (∞) is adopted to indicate RMS sizes ≥1000 [mm], while the term 'None' indicates the dummy surface corresponding to the Pupil Stop sub-system (see Figure 6-2).**

## 6.11 Bibliography

Born, Max; Wolf, Emil, **Principles of optics. Electromagnetic theory of propagation, interference and diffraction of light**, Oxford: Pergamon Press, 1965, 3rd (revised) ed.

Oliva, E., Memorie della Società Astronomica Italiana, 2003, v.74, p.118.

# 7 The European ELT perspective

One of the most ambitious science objectives of the European ELT is the characterization of all the extrasolar systems detected with the VLT Planet Finder and to extend the capabilities of direct detection up to a statistically meaningful sample of stars. Beyond this, the rocky planets detection, with possibly Earth-like features, is the ultimate and most challenging goal of the Planet Finder proposed by ESO i.e. EPICS.

Presently EPICS is the name of a feasibility study of a Planet Finder Instrument foreseen for the OWL case[55] by ESO, with the direct collaboration of the VLT-PF and CHEOPS teams now merged in the SPHERE project, which will realize the VLT Planet Finder.

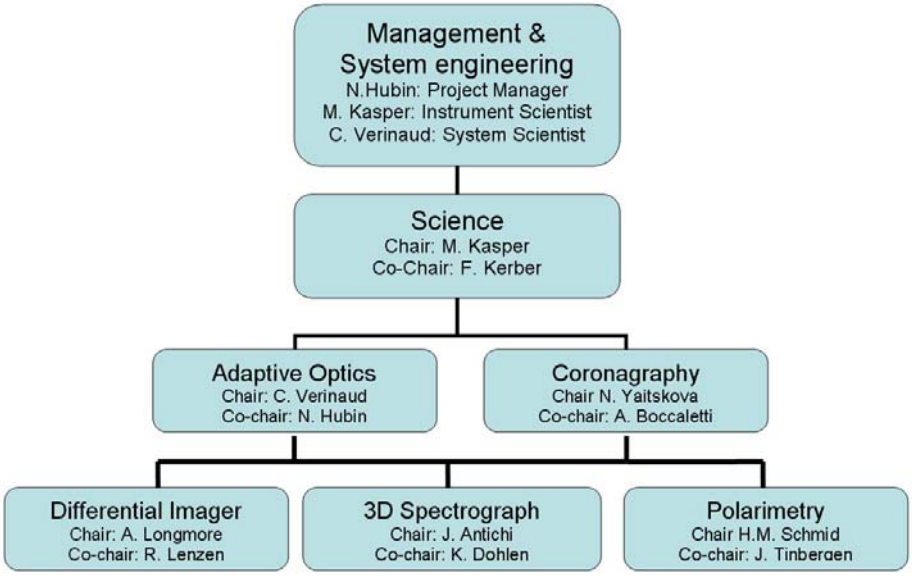


**Figure 7-1: EPICS organization**

The joint study by ESO and VLT-PF/CHEOPS teams was done over 6 month: from 15th April up to October 31st 2005 (cfr. Vérinaud et al. 2006). The synergy with the ESO Instrumental Astronomy team and the SPHERE expertises allowed to conceive the optical design of OWL in a way customized entirely for the EPICS goal i.e. the detection of extremely faint companions around main sequence stars close to the Sun.

[55] OWL is the old ELT concept proposed by ESO as the European biggest facility for Astronomy never conceived, with telescope aperture equals 100 [m].

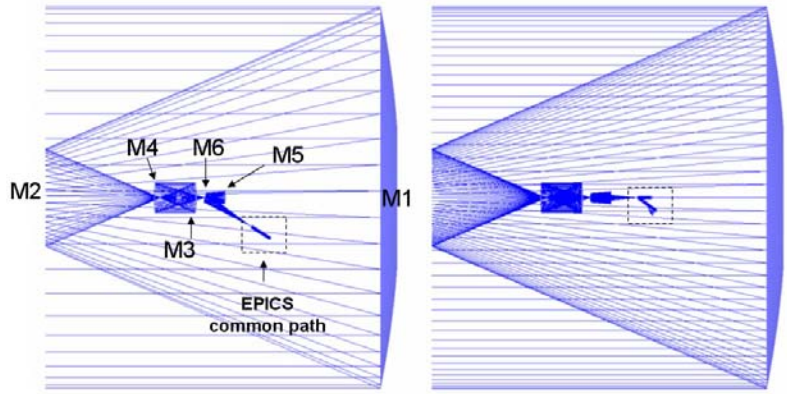


**Figure 7-2: EPICS common path location in OWL optical set-up. The right image is 90 [deg] rotated along the telescope optical axis with respect to the left image. The telescope mirrors are indicated with the symbol 'M' and enumerated from starting from the primary one.**

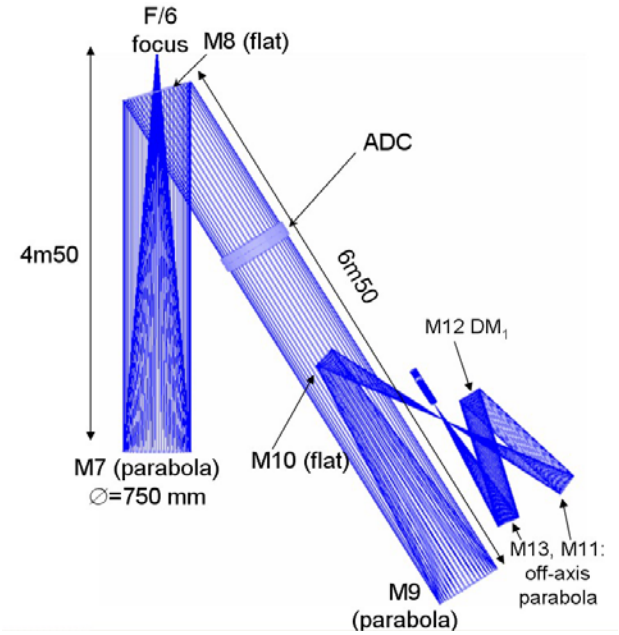


**Figure 7-3: Zoom on EPICS common path at F=6 focus.**

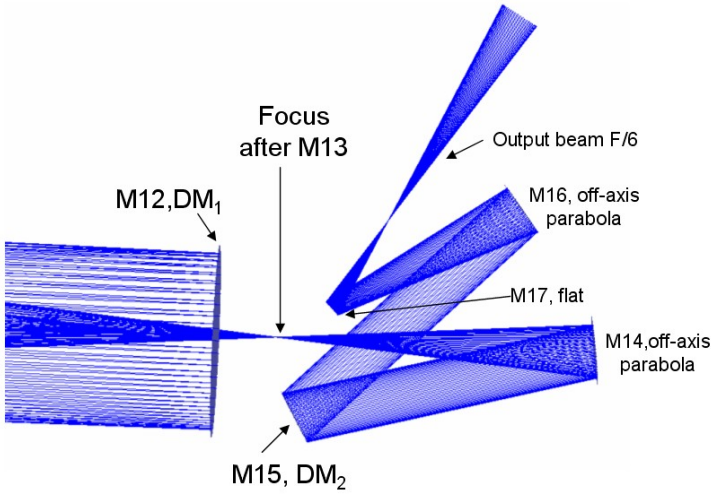


**Figure 7-4: Zoom of the proposed implementation for the telescope deformable mirrors.**

## 7.1 The science milestone: rocky planets

The primary science goal of EPICS required the detection of faint point sources in proximity of a bright star with an object-star Contrast down to about **C**=2.10$^{-10}$ at 0.05 [arcsec] from the star, as Figure 7-5 indicates. Moreover, to observe a planet and to characterize its atmosphere, EPICS was conceived to be sensitive at the wavelengths of $H_2O$, $CO_2$, $CH_4$ and $O_2$ molecular absorption lines.

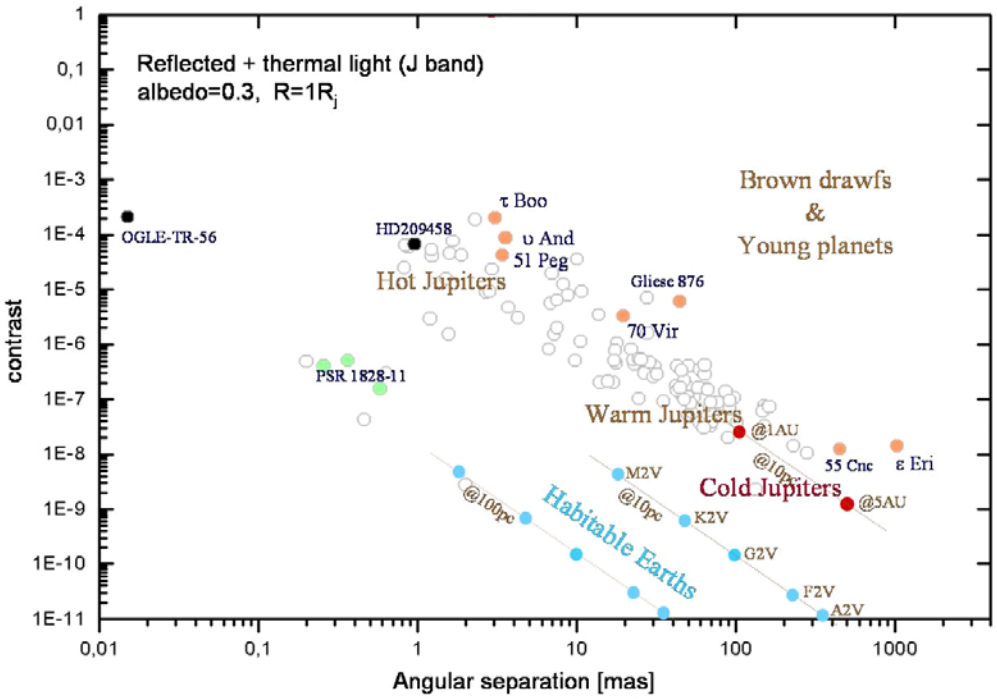


**Figure 7-5: Contrast vs. angular separation for different types of planets (by courtesy O. Lardiere).**

EPICS has been designed also to permit a significant breakthrough in the detection and characterization of cold gas giant planets. The better Contrast of Jupiter like planets (the Jupiter Contrast with respect to the Sun is **C**=10$^{-9}$) and larger separation, permits an easier detection, and opens the door to high resolution spectroscopy. In particular, radial velocity measurements and the analysis of atmospheric composition and dynamics of close-in giant planets will be possible. The Contrast between a Jupiter mass planet at 0.5 AU and its star is around 10$^{-7}$, so it roughly corresponds to the stellar AO residuals. At 10 pc distance from Earth, assuming a G2V star, its magnitude would be around 22.5 and the photon flux at resolution of 50.000 would be about 0.5 photons per second and spectral bin (assuming a 16% overall quantum efficiency). Therefore, a reasonably high SN for high resolution spectroscopy appears feasible in observing times of a couple of hours.

The target stars for which EPICS has been optimized are main sequence star of spectral types G, K and M, selected in order to have access to about 100 stars for each spectral type, that is:

- 25 pc for G-stars ($m_V \approx 7$)
- 20 pc for K-stars ($m_V \approx 8.5$)
- 15 pc for M-stars ($m_V \approx 9$-16 for M0 to M5). There are about 50 M-stars with $m_V<10$ and 100 M-stars with $m_I<10$ observable at low latitudes.

This sets the Top-Level Requirements in terms of Contrast vs. separation and of limiting magnitude for the AO system:

- **C**=2 $10^{-10}$ at 40 [mas]: G star at 25 pc, Mv=7
- **C**=8 $10^{-10}$ at 25 [mas]: K star at 20 pc, Mv=8
- **C**=8 $10^{-9}$ at 15 [mas]: M star at 15 pc, Mv=10

In order to further examine imaging of rocky planets with OWL/EPICS in a general context, we consider in Table 7-1 detection of rocky planets in the Habitable Zone, that is of planets similar to our own Earth, with different techniques. Separation is generally considered to be of the order of 1 AU for solar type stars. In this Table we compare the accuracy required for detection with that achievable with the various techniques. In the last column we list the main sources of concern in the various observing techniques. Specifically, in Column 2, we use a color code: green means that the technique can reach the required accuracy; red means that this is not possible

| Method | | Achievable Accuracy | Required Accuracy | Problems |
|---|---|---|---|---|
| **Radial Velocities** | | **>0.1 [m.sec$^{-1}$]** | **0.03 [m·sec$^{-1}$]** | **Jitter, Pulsations** |
| **Astrometry (Space)** | | **10 [microarcsec]** | **1 [microarcsec]** | **Stellar diameter, Activity** |
| **Transits** | **Ground** | **1 mmag** | **0.1 mmag** | **Scintillation, False Alarms, No follow-up, Rare** |
| | **Space** | **0.01 mmag** | | |
| **Gravitational Micro-lenses** | | **1 mmag** | **1 mmag** | **Unique event, No follow up, Very rare** |
| **Direct imaging stellar/planet Contrast** | **VLT** | **$10^{8}$** | **$10^{10}$** | **Differential Techniques, Coronagraphy, Nulling Interferometry** |
| | **30 m** | **$10^{9}$** | | |
| | **OWL** | **$10^{10}$** | | |
| | **Space** | **$10^{10}$** | | |

**Table 7-1: Detection of an extra-solar Earth with different techniques**

An exam of Table 7-1 reveals that those indirect techniques, where the planet presence is revealed by the reflex motion of the central star, are not well suited for observation of rocky planets in the Habitable Zone: this is essentially due to problems related to time variations and asymmetries in the flux emitted from stars, and are then difficult to overcome even by significant technological progresses. This limits substantially the available techniques, and gives much more weight to the imaging techniques. Also, Transits and Gravitational Micro-lens, while are likely sensible enough to detect rocky planets in the near future, are severely limited by the rarity of the alignment conditions required for detection, and by the size of the

field used in the searches: in both cases, rocky planets in the Habitable Zone detected will likely be at distances much larger than 100 pc from the Sun, so that detailed studies are beyond capabilities of even ELTs and of those space instruments expected to be working in the next 15-20 [years]. It is then clear that direct imaging will likely play a crucial role in the extrasolar rocky planet science.

## 7.2 Instrument concept

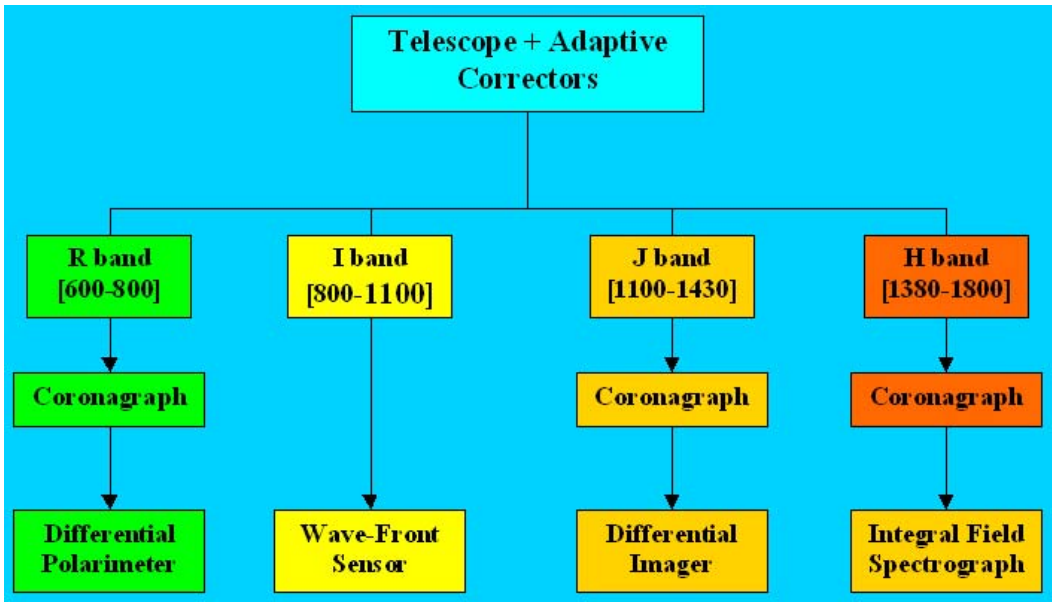


**Figure 7-6: EPICS will be composed of three spectral channels for the scientific instruments and one for the WaveFront Sensor.**

A total of four spectral channels (3 for science and one for wave-front sensing) are defined. Each scientific channel will be equipped with its own Coronagraph.

- The **R band** is dedicated to the Polarimetric Differential Imager for detecting rocky planets and to the follow-up observations for the detection of $O_2$.
- The **J band** is equipped with a Differential Imager using pairs of filters that will be sensitive to both $CH_4$ and $H_2O$ absorption bands.
- The **H band** will be equipped with an Integral Field Spectrograph. The main features that can be detected in this band are $CH_4$ and $CO_2$.

The **I band** is reserved for the WaveFront Sensor. This band has been chosen because of the lesser scientific interest for planet detection. Its location, spectrally speaking, between the visible and NIR instruments, is optimal with respect to important atmospheric chromatic limitations for XAO on ELTs. Moreover no light is taken from the scientific channels. The EPICS concept is summarized in Figure 7-6.

## 7.3 Adaptive Optics

Adaptive optics is one of the major components of EPICS, and the success of the instrument depends closely on the performance of the real-time correction of atmospheric turbulence.

For EPICS, the AO system has been optimized, in the NIR, to provide a high efficiency for the rejection of the starlight halo for angular separations ranging from 30 [mas] to 200 [mas], corresponding to the expected locations of rocky planets in the Habitable Zone around stars of the three spectral types defined. To achieve this, the proposed concept is based on a double stage: a first system is an extrapolation of the concept developed in the SPHERE project with a classical Shack-Hartmann (500x500 sub-apertures) controlling a $1.7\times10^5$ actuators system at 1 [kHz]. This system is not enough to provide a sufficient rejection of starlight for the most challenging science goal. A second system in cascade with the first one, is based on $1.5\cdot10^4$ actuators controlled at 3 [kHz] with a Pyramid sensor (150x150 sub-apertures). Thanks to the high speed and to low noise propagation for low spatial frequencies in the pyramid sensor measurements, more than an order of magnitude of halo rejection is obtained in the central part of the field of view (see Table 7-2). This translates in a net gain of more than a factor of 10 in integration time for the detection of rocky planets in the Habitable Zone with respect to the single stage only.

The main reason for this double stage scheme is a computing power issue. Fast reconstruction algorithms exist for a Shack-Hartmann WFS but not yet for a Pyramid Sensor. A 500x500 Pyramid Sensor at 3 [KHz] would have been ideal in terms of noise propagation, but the only way to reconstruct the command, at least today, through classical matrix-vector multiplication, would have required an increase of more than a factor of 200 of computing power with respect to the 150x150 system foreseen for EPICS/XAO.

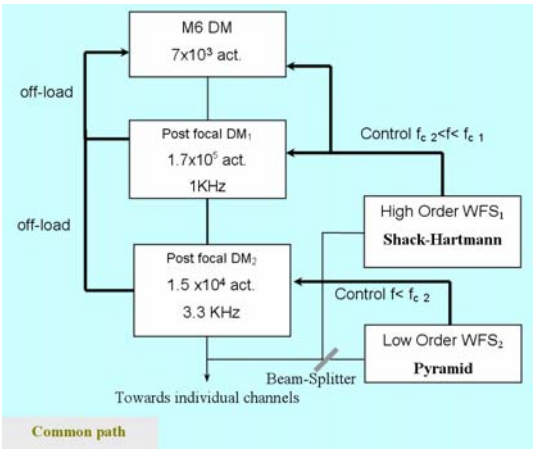


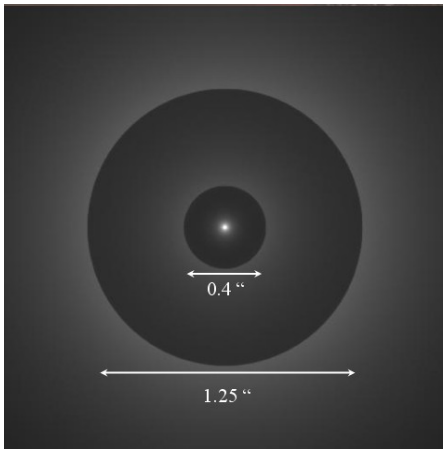


**Table 7-2: EPICS double stage AO system concept (left). Example of simulated coronagraphic image expected with this system (right). Wave-length: 1220 [nm]. Seeing: 0.5 [arcsec], G2V star at 10 pc ($M_v$=5.0). The image has been scaled for better rendering. The large outer corrected field (due to 1st stage correction) is 1.25 [arcsec] in diameter. The inner corrected field (due to 2nd stage correction) is 0.38 [arcsec] in diameter.**

## 7.4 Coronagraphy

Coronagraphy is another major component of EPICS. It has been foreseen to mount 3 Coronagraphs, each optimized for a given scientific channel. Extremely high performance is required to remove the diffraction effects due to a segmented Entrance Pupil as big as the one of OWL. The following Coronagraph concepts have been proposed:

- Prolate Apodized Lyot Coronagraph
- Gauss-Lyot reticulated Coronagraph

Both are Lyot Coronagraphs that are well suited for an ELT, if more than 10λ/D separation angle is expected. A major complication is the problem of segmentation that needs to be carefully treated if high performance is expected. For this specific problem a detailed study has been undertaken for a double stage Gauss-Lyot Coronagraph with complex reticulated stops (in amplitude and phase). Results show a theoretically extremely high extinction of this system.

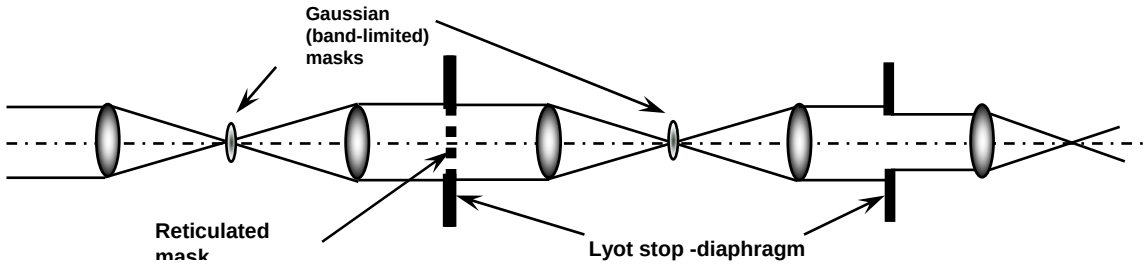


**Figure 7-7: Double stage Gauss-Lyot reticulated Coronagraph.**

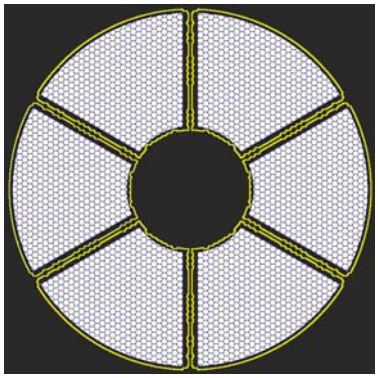

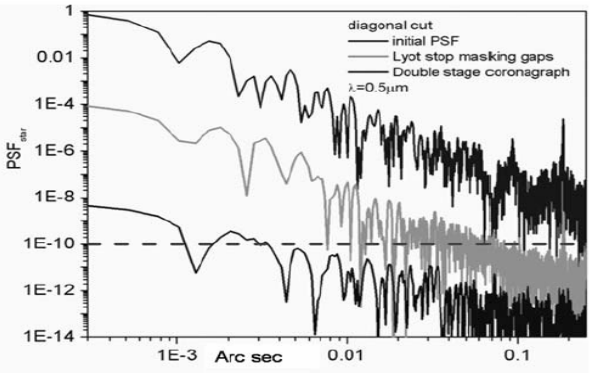


**Table 7-3: (Left) Gauss-Lyot reticulated Coronagraph: reticulated Lyot Stop corresponding to the primary mirror. (Right) performance at 500 [nm] on OWL Entrance Pupil without phase errors.**

## 7.5 Top Level Requirements for the EPICS/Instruments

- TLR-1: The instrument covers the wavelength range 0.6-1.75 [micron]

For the detection of terrestrial planets the wavelength range 700-900 [nm] is most interesting with its $O_2$ band. Gas giant spectra are expected to be dominated by the methane features in J- and H-band. Wavelengths shorter than 700 [nm] might be interesting because of a higher degree of polarization.

- TLR-2: The total field of view in all observing modes is at least 2 [arcsec] in diameter at VISible wavelengths and 4 [arcsec] in diameter in the NIR. A FOV of 2 [arcsec] in diameter corresponds to 1 AU at 1 pc, large enough to cover rocky planets at all distances from the hosting star. The bigger field in the NIR accounts for the larger separation at which giant planets are searched. A FOV of 4 [arcsec] in diameter covers the Solar System (apart from Neptune and Pluto) at distances smaller than 10 pc.
- TLR-3: The Inner Working Angle in all observing modes working at visible wavelengths is smaller than 30 [mas] (goal 15 [mas]). This IWA corresponds to 0.3 AU at 10 pc,

small enough to cover the inner Solar System at 10 pc or to resolve the Earth out to 25 pc. The atmospheres of close-in and therefore bright giant planets could be studied at very small angular separations.

- TLR-4: The spatial sampling will fulfill at least the Nyquist's criterion at all working wavelengths.

## 7.6 Instruments

Specifications for the three instruments able to perform the various calibration techniques: P-DI SDI, and S-SDI, were derived from the EPICS TLRs. The parallel instrumental development of all these calibration techniques reflects the situation of the SPHERE project where special investigations have been pursued on the question of all the Diffraction Effect arising in the case of imaging dominated by the Speckle Noise. Some preliminary design has been produced, and in the specific case of S-SDI proposed facility, the accuracy of the optical concept presented in EPICS lacks of all the breakthroughs described in this Dissertation, by which we defined and characterized completely a new optical concept suited for high contrast diffraction limited Integral Field Spectroscopy: BIGRE, see (Section 5.2). Then, the concept design of the 3D-Spectrograph in EPICS suffered of an evident level of immaturity we got during the period of this feasibility study.

### 7.6.1 Differential Polarimeter

A Differential Polarimeter concept based on the CHEOPS proposal for VLT Planet Finder has been studied for EPICS (see Table 7-4, right). Different modes of operation can be used to detect the polarization signal of an extrasolar planet against the starlight halo. For extremely high contrast application, very precise calibration can be obtained by inserting a polarimetric switch upstream in the optical train.

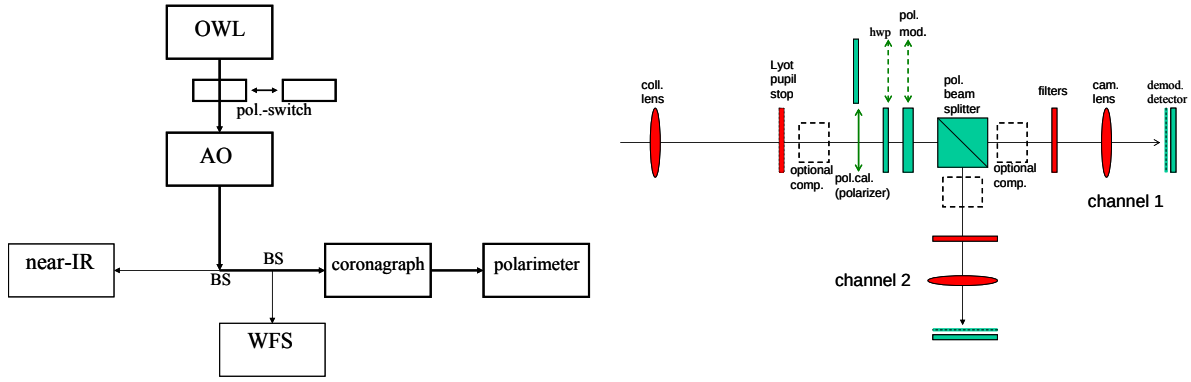


**Table 7-4: Differential Polarimeter concept for EPICS.**

The high precision imaging Polarimeter measures the polarization of the incoming light at the position of the fast polarization modulator package. According to the recommended concept for EPICS (Table 7-4, left) the high precision imaging Polarimeter is located after the AO system, the dichroic beam splitter and the WFS beam splitter. However an open issue is whether the modulator package should be located in front of or after the Coronagraph; the final decision should depend on the adopted Coronagraph machine in the final EPICS Planet Finder.

### 7.6.2 Wave-length splitting Differential Imager

A dichroic based Differential imager with 4 simultaneous channels and high throughput (>90%) has been designed (see Table 7-5). The choice of the wave-lengths for the filters permits to be sensitive to both $CH_4$ and $H_2O$ in the J band.

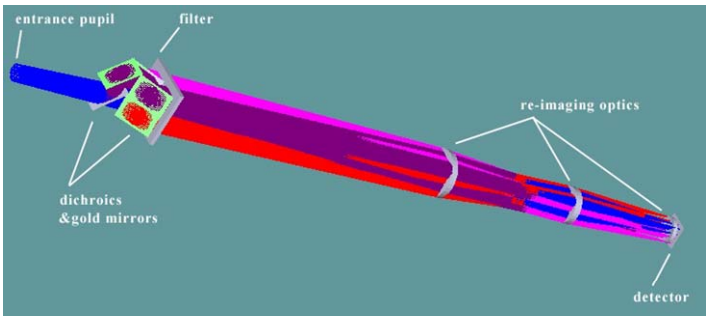


| Filter | Central wavelength | FWHM | λ/Δλ |
|---|---|---|---|
| 1 ('on-line') | 1140 nm | 75 nm | ~ 15 |
| 2 | 1220 nm | 80 nm | ~ 15 |
| 3 | 1300 nm | 85 nm | ~ 15 |
| 4 ('on-line') | 1385 nm | 90 nm | ~ 15 |

**Table 7-5: Dichroic-based 4 channels differential imager: at left the proposed optical design, at right the specifications of the adopted Chromatic Filters.**

The proposed optical concept exploits a double Wollaston Prism concept which is illustrated in Table 7-6. Within the collimated beam, near the Pupil image, to minimize differential static aberrations, a double Wollaston device is introduced. The collimated beam is required to minimize astigmatic effects of the thick Wollaston cubes.

The first Wollaston Prism is of similar designed to the standard Wollaston concept, however, the crystal axis are rotated by 45 [degree] relative to the splitting direction. Thus, there are two beams leaving the first Wollaston Prism, which are inclined against each other. The second Wollaston Prism is a regular one, with a splitting angle perpendicular to the first one, which splits again into two beams of orthogonal direction. As the polarization direction is 45 [degree] against the splitting direction of the second Wollaston, all four resulting beams are of identical intensity, which is about ¼ of the incoming intensity.

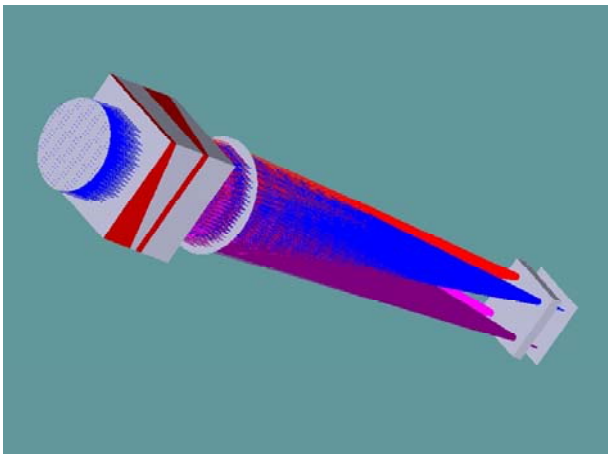

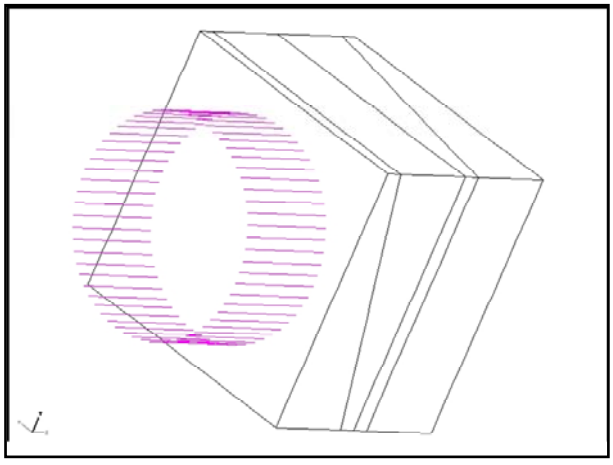

**Table 7-6: 3D overview of the DI optical concept using crossed Wollaston Prisms. Crystal axis are parallel to the wedge edge of the first Wollaston Prism, and rotated by 45 [degree] for the second Wollaston Prism.**

### 7.6.3 Integral Field Spectrograph

The work made by the 3D-Spectroscopy working group of EPICS (cfr. Figure 7-1) is one of the main arguments of this Dissertation, and will be described in the following part of this Section. The work has been done studying two optical concepts realizing 3D-Spectroscopy:

- A TIGER Integral Field Spectrograph
- A Fourier Transform Integral Field Spectrograph

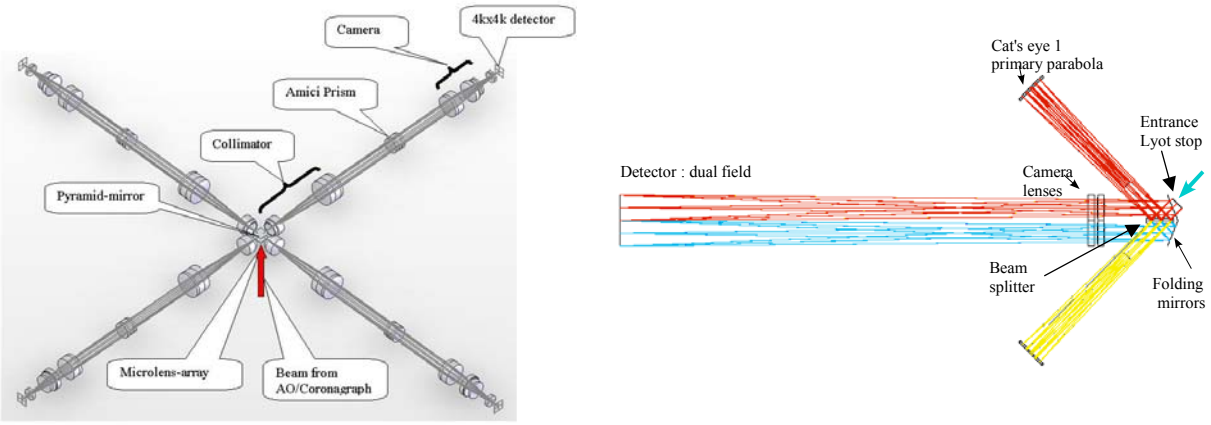


**Table 7-7: Conceptual design of the Integral Field Spectrographs analyzed by the 3D-Specc working group of EPICS. Left: TIGER-type IFS. Right: a Fourier Transform spectrograph.**

As indicated in (Section 3.5), what is extremely demanding for 3D-Spectroscopy is the need of a conspicuous number of pixels on the Detector plane. This issue is particularly important when spectral and spatial information is recorded simultaneously in the Detector plane, such as in the TIGER type instrument. Specifically, Aliasing on the Exit Slit should be avoided for the reconstruction of the monochromatic signals, and the oversampling condition on the spectral direction should be verified inside the scientific FOV, in order to avoid that Speckle Chromatism will be undersampled in this direction (see Section 5.3.2). These requests need a huge amount of pixels that - in principle - an Integral Field FTS does not need.

As described (Section 3.5), with respect to simple Differential Imager obtained through use of Chromatic Filters, the IFS offers a multiplex advantage over the number of usable spectral bands: this is of paramount importance for detection of rocky planets, since their spectra may present a variety of bands, that cannot be predicted in advance. In this contest, a TIGER type IFS design possibly reduces some of the main concerns of Differential Imaging, in particular those related to non common path aberrations, because essentially the same optical path is followed by rays of different wavelength through the IFS.

On the other hand Aliasing cannot occur in FTS systems, since spectral information is obtained via an interferogram. The finite length of the interferogram sets a precise limit to the spectral resolving power, acting as an anti-Aliasing filter, and no higher resolution components of the spectrum can be detected. Still, the effects of temporal variations in speckles may be important. While the single-output FTS (Michelson interferometer) is known to be very sensitive to source intensity variations, this sensitivity is efficiently eliminated in the dual-output version (Mach-Zehnder interferometer) since the sum of the two outputs is equal to the instantaneous source flux.

In the following part of this Dissertation we describe the results obtained in the optimization of a TIGER type Integral Field Spectrograph, because the Author gave a direct contribution on this topic.

### 7.6.3.1 Optical Concept of a TIGER IFS

The number of spaxels shaping the lenses array of a TIGER type IFS has to be equal to the number of angular resolution elements contained in the Field of View. This is because the instrument works at the diffraction limit and the Nyquist's sampling of the Telescope PSF is necessary in order to fully exploit the potentials of S-SDI.

Considering the minimum **FOV=2 [arcsec]** diameter and the telescope angular resolution element (**$\lambda/2D=1.42 \times 10^{-3}$ [arcsec]** at **$\lambda=1.38$ [micron]**, **D=100 [meter]**, the numerical size of the lenses array is **$N_{Im}$=1000x1000**.

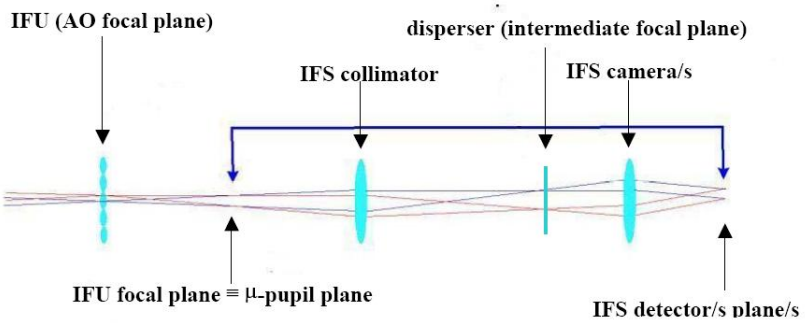


**Figure 7-8: Optical concept of a fully dioptric TIGER type IFS: the lenses array samples at the Nyquist's limit the Telescope PSF, producing an array of MicroPupils which represent the Entrance Slits of a standard dioptric Collimator/Camera system.**

An example of TIGER IFS is the one optimized during the CHEOPS phase-A study for the VLT Planet Finder.

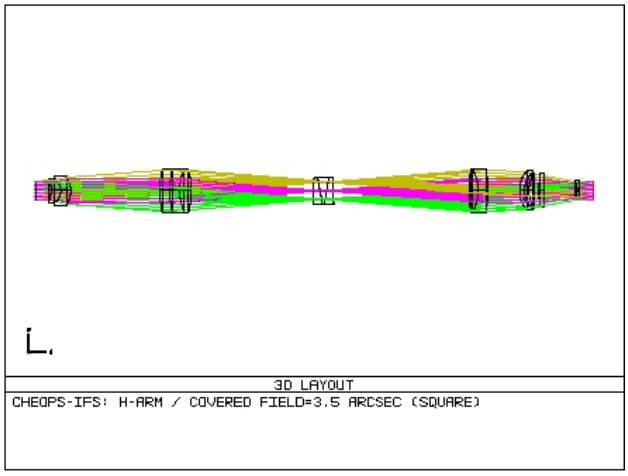


**Figure 7-9: Optical implementation of the H-band CHEOPS IFS. Note that the disperser is placed on an image of the Telescope focal plane. This happens because the IFS object plane is a micro-pupils array which is imaged and dispersed on the Detector pixels**

With the fixed set of EPICS TLRs, the Aliasing budget of a TIGER IFS is large: **λ/D** is sampled with **0.31 pixels** at $\lambda_{min}$. In order to avoid the Aliasing but saving the TIGER IFS concept, one might introduce a magnification factor $\mathbf{m_{IFS}=6.6}$. This Super-TIGER layout solution requires an enormous Detector size : **~176 [4k x 4k]** Detectors.

The layout solution is described in the following Tables, which allow to conceive a design for the TIGER IFS optics following the same strategy of the TIGER IFS proposed in the CHEOPS team.

| TIGER IFS main parameters | TIGER IFS other parameters |
|---|---|
| Input Focal Ratio = 217 | Lens refraction index = 1.5 |
| Lenses array layout = Hexagonal B | Lenses mask diam. = 95% Lenses pitch |
| Lenses array pitch = 150 [micron] | Output Focal Length = 0.6 [mm] |
| Output Focal Ratio = 4 | Lens curvature radius = 300[micron] |
| Lenses number = 1000x1000 | Lens sag = 9.5 [micron] |
| Spectral step = 0.05 [micron/pixel] | Detector/s pixel size = 18 [micron] |
| Spectrum length = 10 pixels | IFS optical magnification = 1 |
| Spectrum area = 60 pixels | |
| Detector size = 4 [4kx4k] | |

**Table 7-8: he TIGER IFS layout solution for EPICS.**

| 3D-SPEC. TLRs | TIGER IFS layout solution |
|---|---|
| Min. wavelength = 1.38 [micron] | 1.38 [micron] |
| Max. wavelength = 1.75 [micron] | 1.75 [micron] |
| Spectral Purity ≥ 15 | 21 |
| Field of View = 2 [arcsec] (diagonal) | 2 [arcsec] (diagonal) |
| Incoherent CrossTalk < $7.5x10^{-5}$ | $7.0x10^{-5}$ |

**Table 7-9: Confront among the 3D-Spectroscopy TLRs and the values obtained in the final layout.**

| 1-QUADRANT TIGER IFS | 4-QUADRANT TIGER IFS |
|---|---|
| Diagonal size of the IFU ≤ 213 [mm] | Diagonal size of the IFU ≤ 106.5 [mm] |
| Collimator Focal Length = 600 [mm] | Collimator Focal Length = 600 [mm] |
| Collimator optics size ≤ 380 [mm] | Collimator optics size ≤ 274 [mm] |
| Collimator corrected field ~20 [deg] | Collimator corrected field ~10 [deg] |
| Camera corrected field ~ 20 [deg] | Camera corrected field ~ 10 [deg] |
| IFS length = 2400 [mm] | IFS length = 2400 [mm] |
| Number of Collimator/Camera arms = 1 | Number of Collimator/camera arms = 4 |
| Single Detector size = 4 [4k x 4k units] | Single Detector size = 1 [4k x 4k units] |

**Table 7-10: Global sketch of the TIGER IFS optics. Two different opto-mechanical configurations are resumed one with no-division/4Q-division of the FOV respectively.**

### 7.6.3.2 Conceptual mechanical design

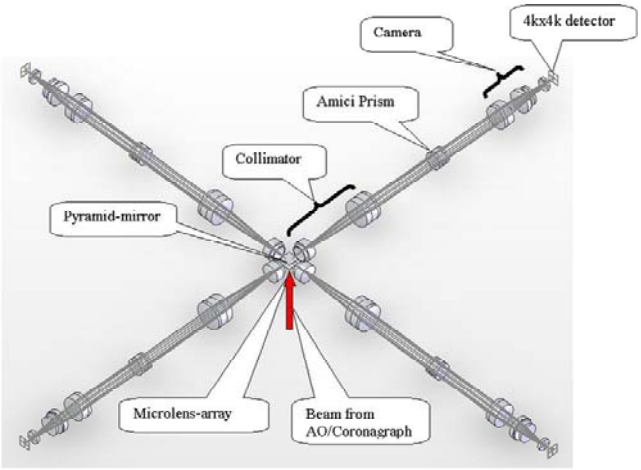


**Figure 7-10: 3D-sketch of EPICS 4Q-TIGER IFS showing the four arms. The light from the AO/Coronagraphic-module comes from bottom. Each arm is fed by a pyramid-mirror. Each arm includes: Collimator, an Amici Prism Disperser, a Camera, and a 4k x 4k Detector. The Detectors should be within cryostats not shown in this figure. The length of each arm is ~2.4 [m]. Suitable folding-flats could be inserted into each arm to modify the geometry of the IFS.**

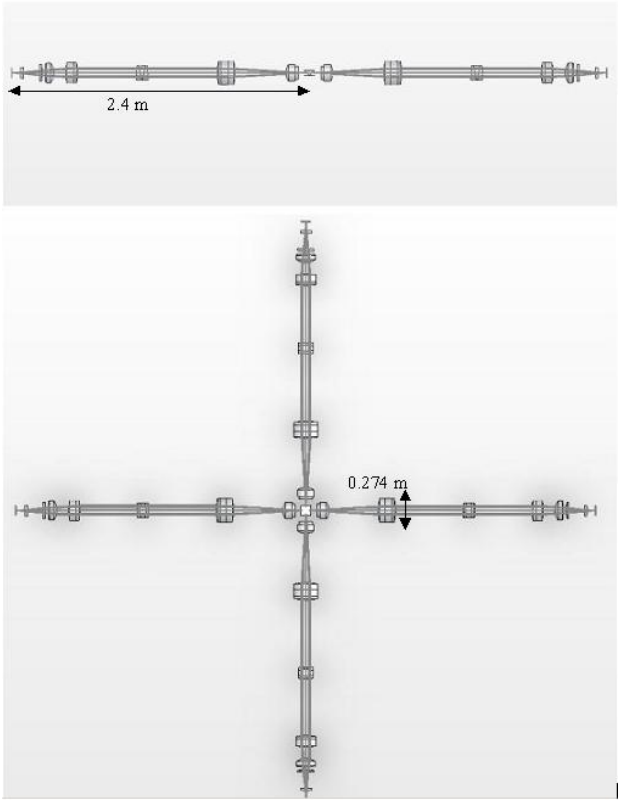


**Figure 7-11: Side and top views of the EPICS 4Q-TIGER IFS.**

7.6.3.3 Simulations

Some simulations have been conducted based on the proposed TIGER IFS layout. The aim of this exercise was not to simulate a detection of an extrasolar planet (and more specifically an Earth-like one) but to test the capability of the TIGER IFS simulator adopted in the CHEOPS-project.

The two figures below show a different scales the pattern of a star on the Detector/s plane (no division of the FOV has been requested in this simulation and no Coronagraph has been inserted in the optical path of the star light.

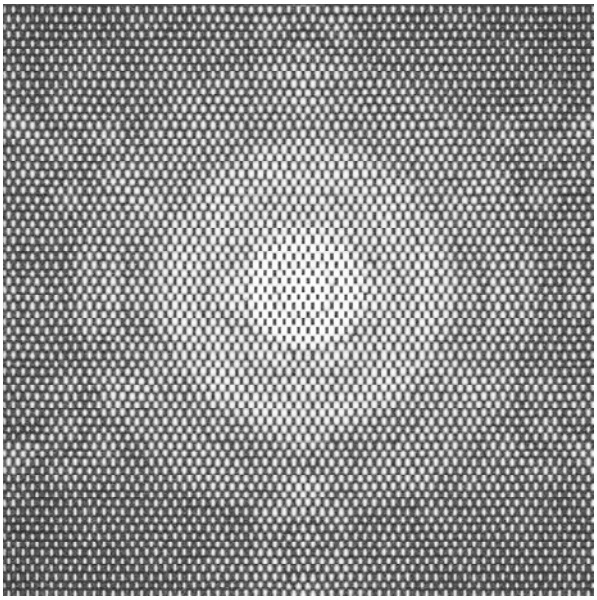

**Figure 7-12: Image of the TIGER IFS spectra of the central star as obtained with the proposed layout covering a 1kx 1k portion of the Detector. Intensities are in log-scale.**

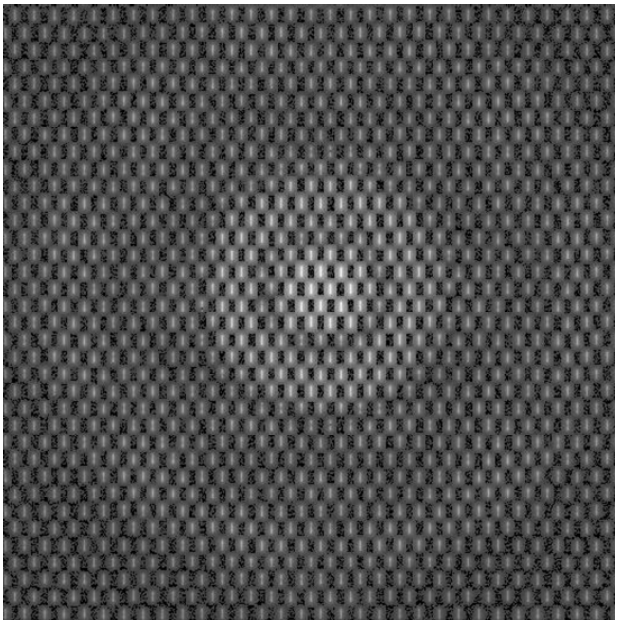

**Figure 7-13: Image of the TIGER IFS spectra of the central star as obtained with the proposed layout covering a 0.5k x0.5k portion of the Detector. Intensities are in log-scale.**

## 7.7 Bibliography

Vérinaud, C.; Hubin, N.; Kasper, M.; Antichi, J.; Baudoz, P.; Beuzit, J.-L.; Boccaletti, A.; Chalabaev, A.; Dohlen, K.; Fedrigo, E.; and 24 coauthors. *Advances in Adaptive Optics II*. Edited by Ellerbroek, Brent L.; Bonaccini Calia, Domenico. Proceedings of the SPIE, Volume 6272, pp., 2006.

# 8 Conclusions

Integral Field Spectroscopy represents a powerful instrument for the detection and characterization of extrasolar giant planets with Constrast values as high as $10^7$. The purpose of high contrast diffraction limited Integral Field Spectroscopy is to exploit all the spectral features proper of extrasolar giant planets atmosphere, in order to perform what - throughout this Dissertation - is indicated as an improvement of the standard Simultaneous Differential Imaging, the Spectroscopical Simultaneous Differential Imaging. Inside the SPHERE project, the Integral Field Spectroscopy channel has been conceived properly to realise - for the first time - this calibration technique.

High contrast diffraction limited 3D-Spectroscopy has been then the leading motivation which allowed us to design the Integral Field Spectrograph foreseen for the coming VLT Planet Finder. Method and results of this work represent the core of this Dissertation.

A new optical concept for the spaxels device adopted in 3D-Spectroscopy has been here newly described, and characterized in the specific case of the SPHERE Integral Field Spectrograph: BIGRE. More in detail, this new optical concept shows itself to be the only solution able to take into account for all the effects appearing when Integral Field Spectroscopy is performed in diffraction limited conditions and for high contrast imaging purposes. The related BIGRE oriented optical design is fully described in this Dissertation.

The future challenge of high contrast diffraction limited Integral Field Spectroscopy is the Contrast threshold of the Earth-like planets, which is around $10^{10}$. Direct detection of these extreme objects has been the subject of an explorative study that ESO promoted in 2005, in order to fix the targets of the future European ELT Planet Finder. This Dissertation presents the contribution we gave to this study, specifically for the 3D-Spectroscopy facility foreseen for this instrument. The work we did is based on the standard TIGER type Integral Field Unit, and has to be conceived as an exercise revealing basic problematics of such an Integral Field Spectrograph. The perspective is to implement a BIGRE spaxel device in a new feasibility study based on the experience acquired with the new BIGRE oriented Integral Field Spectrograph of SPHERE. At the time of the instrument operations, direct detection of extrasolar giant planets would be reality, and the extrasolar planets direct detection ladder should have a sound foundation.